Duct acoustics for air-coupled ultrasonic phased arrays

Dissertation Matthias Rutsch
Zur Erlangung des akademischen Grades Doktor-Ingenieur (Dr.-Ing.)
Genehmigte Dissertation von Matthias Rutsch aus Eberswalde
Tag der Einreichung: 24.06.2022, Tag der Prüfung: 17.01.2023

1. Gutachten: Prof. mont. Mario Kupnik
2. Gutachten: Prof. Gerhard Sessler
Darmstadt, Technische Universität Darmstadt,
Jahr der Veröffentlichung der Dissertation auf TUprints: 2023

TECHNISCHE UNIVERSITÄT DARMSTADT

Electrical Engineering and Information Technology Department

FG Mess- und Sensortechnik

Duct acoustics for air-coupled ultrasonic phased arrays
Dissertation Matthias Rutsch

Accepted doctoral thesis by Matthias Rutsch

Date of submission: 24.06.2022
Date of thesis defense: 17.01.2023

Darmstadt, Technische Universität Darmstadt,
Jahr der Veröffentlichung der Dissertation auf TUprints: 2023

This work is dedicated to my mother.

Erklärungen laut Promotionsordnung

§ 8 Abs. 1 lit. c PromO

Ich versichere hiermit, dass die elektronische Version meiner Dissertation mit der schriftlichen Version übereinstimmt.

§ 8 Abs. 1 lit. d PromO

Ich versichere hiermit, dass zu einem vorherigen Zeitpunkt noch keine Promotion versucht wurde. In diesem Fall sind nähere Angaben über Zeitpunkt, Hochschule, Dissertationsthema und Ergebnis dieses Versuchs mitzuteilen.

§ 9 Abs. 1 PromO

Ich versichere hiermit, dass die vorliegende Dissertation selbstständig und nur unter Verwendung der angegebenen Quellen verfasst wurde.

§ 9 Abs. 2 PromO

Die Arbeit hat bisher noch nicht zu Prüfungszwecken gedient.

Darmstadt, 24.06.2022

M. Rutsch

Acknowledgment

- First of all, I would like to thank my supervisor Prof. Dr. mont. Mario Kupnik. He offered me the great opportunity to do my PhD. In all these years he helped me not only to think scientifically but also to develop my personality.
- I would like to thank Prof. Dr. rer. nat. Dr. hc. Gerhard M. Sessler for reviewing this thesis. He provided me with valuable tips in academia and acoustics.
- I also would like to thank Dr. Thomas Kaindl and Regine Augenstein from P+F. Both supported me and helped me to not only answer academic questions but also to keep an eye on industrial aspects.
- Furthermore, I would like to thank Dr. Alexander Unger. He was a mentor for me from my bachelor time to the beginning of my doctoral time.
- Many thanks to all my great friends and colleagues. It was a huge honer for me to do my PhD with you all. You guys always supported me in good and bad times.
- Additionally, I would like to thank all my undergraduate and graduate students for supporting me in my research.
- Finally, I would like to thank my parents for supporting me all these years and always making sure that I can achieve my goals.

Abstract

Air-coupled ultrasound is used in many applications such as range finding, tactile feedback, flow metering or non-destructive testing. The transducers directivity is a crucial acoustic property for all these applications. For instance, a narrow beam width allows for higher angular resolutions, whereas a wider beam width allows for emitting the sound wave in a bigger area for obstacle detection. However, the transducers dimensions influence its directivity and its resonance frequency. In order to decouple the acoustic aperture from transducer, acoustic waveguides are investigated in this work. This way, grating lobe free phased arrays can be built for unambiguous beamforming.

In this thesis, the wave propagation inside these waveguides, including coupling mechanisms from the transducer till the free-field, are investigated. First, the state of the art of duct acoustics applications in the audible range and the ultrasound range are presented. Afterwards, different duct acoustics models are derived and compared. Each model is validated for $40\,\text{kHz}$, a duct length of $80\,\text{mm}$ and an aperture between $10\,\text{mm}$ and $3.4\,\text{mm}$. The challenge of the simulations is to take higher modes into account while reducing the calculation times. Therefore, analytical and numerical models were investigated. As a result, the boundary element method is the most efficient approach for the given geometry wavelength ratio using the commercial software COMSOL Multiphysics. With this method, free-field calculations on a single Xeon E5-2660 v3 CPU and $256\,\text{GB}$ RAM without the need of a cluster are possible. The model is validated with calibrated measurements in an anechoic chamber. Therefore, an automated measurement system is established where a calibrated measurement microphone moves relative to the transducer, thus characterizing the sound field in front of the transducer. This setup can measure a hemisphere with a radius of up to $6\,\text{m}$ and has a dynamic range of $111\,\text{dB}$.

After the validation of the numerical model, waveguide geometry optimizations were conducted. The analyzed properties were: the influence of a perpendicular output and input surface on the wave propagation inside the waveguide; the size of the output aperture; length variations of the waveguide including temperature dependence; the position of tapering and types of losses due to the waveguide. As a result, the perpendicular input is crucial for fundamental mode propagation, otherwise higher modes occur, because the input diameter is bigger compared to the wavelength. The size of the output surface can be increased for line arrays with an SPL gain of $+10\,\text{dB}$. However, the limit of the aperture size is $3.7 \times \lambda$, otherwise higher modes occur at the output which lead to defocusing of the main lobe. The length of the waveguide can increase the SPL. However, the industrial temperature demands of $-25°\text{C}$ to $75°\text{C}$ have the same influence on the SPL as the length optimization ($\pm 4.8\,\text{dB}$), and, thus, are not investigated in more detail. The positioning of the tapering has just a minor influence of $\pm 0.4\,\text{dB}$. The losses of the waveguide are $-10\,\text{dB}$ with diffraction loss as the dominant part. The losses inside the waveguide (reflection and thermoviscous losses) could not be validated with measurements due to the narrow bandwidth of the transducers, since the incident and reflected wave superposed.

The derived results of the geometry optimization were used to build four line arrays. First, a waveguide with equal length ducts was built as a reference. Second, a Bézier waveguide with plane input surfaces for the transducers was designed. Third, the output aperture was changed from round outputs to rectangular shapes to increase the SPL and sensitivity. Last, a shortened version of the Bézier waveguide was built which has a reduced length of 65%. All four waveguides were simulated using the boundary element

method and validated with the measurement setup. As a result, in both simulation and measurement the shorten waveguide has an increased SPL of $+5$ dB compared to the reference waveguide with equal length ducts. Thus, it is possible to build compact waveguides for air-coupled phased arrays.

Next, the influence of different duct lengths in an acoustic waveguide is analyzed in more detail. Using ducts of different length offers more design freedom for the entire waveguide for compact design, easier assembly and reduced assembly time. However, different lengths must be compensated with additional time delays. Therefore, two waveguides were compared. First, an equal length waveguide was used. Second, a waveguide with Bézier-shaped ducts was used. The time delays, due to varying duct lengths, were measured and simulated with analytic and numerical methods. Afterwards, the directivity patterns of both waveguides were compared. As a result, the time compensation has no significant impact on the beam profile regarding side lobe level and half power beam width. In addition, SPL deviation of the waveguides are within the manufacturing tolerances of the transducers.

The last aspect investigated in this thesis is the water resistance of the waveguide. Since it is designed for air-coupled ultrasound, it can be clogged due to dirt, dust or liquid. Two commonly known solutions for this issue is the use of hydrophobic fabrics or thin films. Therefore, both solutions were compared. First, these two approaches showed no significant impact on the beamforming capabilities of the phased array. In addition, the IP class of the fabric reached IPX7 and the thin film achieved even IPX8. Furthermore, the fabric has a minor insertion loss of just -1.8 dB. In contrast, the film reduces the SPL by -7.5 dB. This loss can be further reduced with special effort to $+0.4$ dB by changing the waveguide geometry and tuning the system to the correct resonance frequency. However, this shows that the film has a high temperature dependence compared to the fabric.

In conclusion, acoustic waveguides enhance the acoustic properties of ultrasonic sensors. The directivity can be decoupled from the transducer and customized for a certain application.

Zusammenfassung

Luftgekoppelter Ultraschall wird in vielen Anwendungen eingesetzt, z. B. zur Entfernungsmessung, taktilen Rückmeldung, Durchflussmessung oder zur zerstörungsfreien Prüfung. Die Richtcharakteristik des Schallkopfs ist eine entscheidende akustische Eigenschaft für all diese Anwendungen. Ein schmaler Schallkegel ermöglicht beispielsweise eine höhere Winkelauflösung, während ein breiterer Schallkegel die Schallwelle in einem größeren Bereich zur Hinderniserkennung abstrahlen kann. Die Abmessungen des Schallwandlers beeinflussen jedoch seine Richtwirkung und seine Resonanzfrequenz. Um die akustische Apertur von dem Waveguide zu entkoppeln, werden in dieser Arbeit akustische Wellenleiter untersucht. Auf diese Weise können gitterkeulenfreie Phased Arrays für eindeutiges Beamforming aufgebaut werden.

In dieser Arbeit werden die Wellenausbreitungen in diesen Wellenleitern, einschließlich der Kopplungsmechanismen vom Wandler bis zum Freifeld, untersucht. Zunächst wird der Stand der Technik von Kanalakustik-Anwendungen im Hörbereich und im Ultraschallbereich vorgestellt. Anschließend werden verschiedene Kanalakustikmodelle abgeleitet und verglichen. Jedes Modell wird für 40 kHz, eine Kanallänge von 80 mm und eine Apertur zwischen 10 mm und $3{,}4$ mm validiert. Die Herausforderung bei den Simulationen besteht darin, höhere Moden zu berücksichtigen und gleichzeitig die Rechenzeiten zu reduzieren. Daher wurden analytische und numerische Modelle untersucht. Im Ergebnis ist die Randelementmethode der effizienteste Ansatz für das gegebene Geometrie-Wellenlängen-Verhältnis unter Verwendung der kommerziellen Software COMSOL Multiphysics. Mit dieser Methode ist es möglich, Freifeldberechnungen auf einer einzelnen Xeon E5-2660 v3 CPU und 256 GB RAM durchzuführen, ohne dass ein Cluster benötigt wird. Das Modell wird mit kalibrierten Messungen in einem schalltoten Raum validiert. Dazu wird ein automatisches Messsystem eingerichtet, bei dem sich ein kalibriertes Messmikrofon relativ zum Schallwandler bewegt und so das Schallfeld vor dem Schallwandler charakterisiert. Dieser Aufbau kann eine Halbkugel mit einem Radius von bis zu 6 m messen und hat einen Dynamikbereich von 111 dB.

Nach der Validierung des numerischen Modells wurden Optimierungen der Wellenleitergeometrie durchgeführt. Die analysierten Eigenschaften waren: der Einfluss einer senkrechten Ausgangs- und Eingangsfläche auf die Wellenausbreitung im Wellenleiter, die Position der Verjüngung und die Arten der Verluste durch den Wellenleiter. Daher ist der senkrechte Eingang für die Ausbreitung der Grundmoden entscheidend, da sonst höhere Moden auftreten, weil der Eingangsdurchmesser im Vergleich zur Wellenlänge größer ist. Die Größe der Ausgangsfläche kann bei Linienarrays mit einem SPL-Gewinn von $+10$ dB vergrößert werden. Die Grenze der Aperturgröße liegt jedoch beim $3{,}7 \times \lambda$, da sonst am Ausgang höhere Moden auftreten, die zu einer Defokussierung der Hauptkeule führen. Die Länge des Wellenleiters kann den Schalldruckpegel erhöhen. Die industriellen Temperaturanforderungen von -25°C bis 75°C haben jedoch den gleichen Einfluss auf den SPL wie die Längenoptimierung ($\pm 4{,}8$ dB) und werden daher nicht näher untersucht. Die Positionierung der Verjüngung hat nur einen geringen Einfluss von $\pm 0,4$ dB. Die Verluste des Wellenleiters betragen -10 dB, wobei die Beugungsverluste den größten Anteil ausmachen. Die Verluste innerhalb des Wellenleiters (Reflexions- und thermoviskose Verluste) konnten aufgrund der geringen Bandbreite der Wandler nicht durch Messungen validiert werden, da sich die einfallende und die reflektierte Welle überlagerten.

Die aus der Geometrieoptimierung abgeleiteten Ergebnisse wurden zum Aufbau von vier Linienarrays verwendet. Zunächst wurde ein Wellenleiter mit gleich langen Kanälen als Referenz gebaut. Zweitens

wurde ein Bézier-Wellenleiter mit ebenen Eingangsflächen für die Wandler entworfen. Drittens wurde die Ausgangsöffnung von runden auf rechteckige Formen geändert, um den Schalldruckpegel und die Empfindlichkeit zu erhöhen. Schließlich wurde eine verkürzte Version des Bézier-Wellenleiters gebaut, die eine um 65% reduzierte Länge aufweist. Alle vier Wellenleiter wurden mit der Randelementmethode simuliert und mit dem Messaufbau validiert. Das Ergebnis ist, dass der verkürzte Wellenleiter sowohl in der Simulation als auch in den Messungen einen um $+5$ dB höheren Schalldruckpegel aufweist als der Referenzwellenleiter mit gleich langen Kanälen. Somit ist es möglich, kompakte Wellenleiter für luftgekoppelte Phased Arrays zu bauen.

Als nächstes wird der Einfluss unterschiedlicher Kanallängen in einem akustischen Wellenleiter genauer analysiert. Die Verwendung von Kanälen unterschiedlicher Länge bietet mehr Gestaltungsfreiheit für den gesamten Wellenleiter und ermöglicht eine kompakte Bauweise, eine einfachere Montage und eine kürzere Montagezeit. Allerdings müssen unterschiedliche Längen mit zusätzlichen Zeitverzögerungen kompensiert werden. Deshalb werden zwei Wellenleiter miteinander verglichen. Zunächst wurde ein Wellenleiter gleicher Länge verwendet. Zweitens wurde ein Wellenleiter mit Bézier-förmigen Kanälen verwendet. Die Zeitverzögerungen, die durch unterschiedliche Kanallängen entstehen, wurden gemessen und mit analytischen und numerischen Methoden simuliert. Anschließend wurden die Richtcharakteristiken der beiden Wellenleiter verglichen. Das Ergebnis ist, dass die Zeitkompensation keinen signifikanten Einfluss auf das Strahlprofil hinsichtlich des Nebenkeulenpegels und der Halbwertsbreite des Strahls hat. Darüber hinaus liegen die SPL-Abweichungen der Wellenleiter innerhalb der Fertigungstoleranzen der Wandler.

Der letzte in dieser Arbeit untersuchte Aspekt ist die Wasserbeständigkeit des Wellenleiters. Da er für luftgekoppelten Ultraschall ausgelegt ist, kann er durch Schmutz, Staub oder Flüssigkeit verstopft werden. Zwei allgemein bekannte Lösungen für dieses Problem sind die Verwendung von hydrophoben Geweben oder dünnen Filmen. Daher wurden beide Lösungen miteinander verglichen. Zunächst zeigte sich, dass diese beiden Ansätze keinen signifikanten Einfluss auf die Strahlformungsfähigkeiten des Phased Array haben. Darüber hinaus erreichte die IP-Klasse des Gewebes IPX7 und der Dünnfilm sogar IPX8. Außerdem hat das Gewebe eine geringe Einfügedämpfung von nur $-1{,}8$ dB. Im Gegensatz dazu reduziert die Folie den Schalldruckpegel um $-7{,}5$ dB. Dieser Verlust kann mit besonderem Aufwand auf $+0{,}4$ dB reduziert werden, indem die Geometrie des Wellenleiters geändert und das System auf die richtige Resonanzfrequenz abgestimmt wird. Dies zeigt jedoch, dass die Folie im Vergleich zum Gewebe eine hohe Temperaturabhängigkeit aufweist.

Zusammenfassend lässt sich sagen, dass akustische Wellenleiter die akustischen Eigenschaften von Ultraschallsensoren verbessern. Die Richtwirkung kann vom Wandler entkoppelt und für eine bestimmte Anwendung angepasst werden.

List of publications

2022

- G. Allevato, **M. Rutsch**, J. Hinrichs, C. Haugwitz, R. Müller, M. Pesavento, M. Kupnik, "Air-coupled Ultrasonic Spiral Phased Array for High-Precision Beamforming and Imaging", *IEEE Open Journal of Ultrasonics, Ferroelectrics, and Frequency Control*, vol. 2, pp. 40-54, 2022, doi: 10.1109/OJUFFC.2022.3142710.
- C. Haugwitz, C. Hartmann, G. Allevato, **M. Rutsch**, J. Hinrichs, J. Brötz, D. Bothe, P. Pelz, M. Kupnik, "Multipath Flow Metering of High-Velocity Gas using Ultrasonic Phased-Arrays", *IEEE Open Journal of Ultrasonics, Ferroelectrics, and Frequency Control*, vol. 2, pp. 30-39, 2022, doi: 10.1109/OJUFFC.2022.3141333.

2021

- **M. Rutsch**, A. Unger, G. Allevato, J. Hinrichs, A. Jäger, T. Kaindl, M. Kupnik, "Waveguide for air-coupled ultrasonic phased-arrays with propagation time compensation and plug-in assembly", *The Journal of the Acoustical Society of America 150*, 3228-3237, 2021, https://doi.org/10.1121/10.0006969.
- T. Maier, G. Allevato, **M. Rutsch**, M. Kupnik, "Single Microcontroller Air-coupled Waveguided Ultrasonic Sonar System", *2021 IEEE Sensors*, 2021, pp. 1-4, doi: 10.1109/SENSORS47087.2021.9639849.
- J. Hinrichs, M. Sachsenweger, **M. Rutsch**, G. Allevato, W. MD. Wright, M. Kupnik, "Lamb waves excited by an air-coupled ultrasonic phased array for non-contact, non-destructive detection of discontinuities in sheet materials", *2021 IEEE International Ultrasonic Symposium*, 2021, pp. 1-4, doi: 10.1109/IUS52206.2021.9593363.
- **M. Rutsch**, F. Krauß, G. Allevato, J. Hinrichs, C. Hartmann, M. Kupnik, "Simulation of protection layers for air-coupled waveguided ultrasonic phased-arrays", *2021 IEEE International Ultrasonic Symposium*, 2021, pp. 1-4, doi: 10.1109/IUS52206.2021.9593561.
- O. B. Dali, S. Zhukov, **M. Rutsch**, C. Hartmann, H. Von Seggern, G. M. Sessler, M. Kupnik, "Biodegradable 3D-printed ferroelectret ultrasonic transducer with large output pressure", *2021 IEEE International Ultrasonic Symposium*, 2021, pp. 1-4, doi: 10.1109/IUS52206.2021.9593738.
- C. Hartmann, C. Haugwitz, G. Allevato, **M. Rutsch**, J. Hinrichs, J. Brötz, D. Bothe, P. Pelz, M. Kupnik, "Ray-tracing simulation of sound drift effect for multi-path ultrasonic high-velocity gas flow metering", *2021 IEEE International Ultrasonic Symposium*, 2021, pp. 1-4, doi: 10.1109/IUS52206.2021.9593898.
- A. Rahimzadeh, **M. Rutsch**, M. Kupnik, R. von Klitzing, "Visualization of Acoustic Energy Absorption in Confined Aqueous Solutions by PNIPAM Microgels: Effects of Bulk Viscosity", *Langmuir*, 2021, 37 (19), 5854-5863 doi: 10.1021/acs.langmuir.1c00235

2020

- G. Allevato, **M. Rutsch**, J. Hinrichs, E. Sarradj, M. Pesavento, M. Kupnik, ”Spiral Air-Coupled Ultrasonic Phased Array for High Resolution 3D Imaging”, *2020 IEEE International Ultrasonic Symposium*, 2020, pp. 1-4, doi: 10.1109/IUS46767.2020.9251675.

- J. Hinrichs, Y. Bendel, **M. Rutsch**, G. Allevato, M. Sachsenweger, A. Jäger, M. Kupnik, ”Schlieren photography of 40 kHz leaky Lamb waves in air”, *2020 IEEE International Ultrasonic Symposium*, 2020, pp. 1-4, doi: 10.1109/IUS46767.2020.9251532.

- R. Müller, D. Schenck, G. Allevato, **M. Rutsch**, J. Hinrichs, M. Kupnik, M. Pesavento, ”Dictionary-Based Learning for 3D-Imaging with Air-Coupled Ultrasonic Phased Arrays”, *2020 IEEE International Ultrasonic Symposium*, 2020, pp. 1-4, doi: 10.1109/IUS46767.2020.9251726.

- **M. Rutsch**, G. Allevato, J. Hinrichs, M. Kupnik, ”Protection layer for air-coupled waveguide ultrasonic phased arrays”, *2020 IEEE International Ultrasonic Symposium*, 2020, pp. 1-4, doi: 10.1109/IUS46767.2020.9251728.

- G. Allevato, **M. Rutsch**, J. Hinrichs, M. Pesavento, M. Kupnik, ”Embedded Air-Coupled Ultrasonic 3D Sonar System with GPU Acceleration”, *2020 IEEE Sensors*, 2020, pp. 1-4, doi: 10.1109/SENSORS47125.2020.9278601.

- G. Allevato, J. Hinrichs, **M. Rutsch**, J. Adler, A. Jäger, M. Pesavento, M. Kupnik,”Real-time 3D imaging using an air-coupled ultrasonic phased-array”, *IEEE Transactions On Ultrasonics, Ferroelectrics, And Frequency Control*, vol. 68, no. 3, pp. 796-806, March 2021, doi: 10.1109/TUFFC.2020.3005292.

2019

- **M. Rutsch**, O. Dali, A. Jäger, G. Allevato, K. Beerstecher, J. Cardoletti, A. Radetinac, L. Alff, M. Kupnik, ”Air-coupled ultrasonic bending plate transducer with piezoelectric and electrostatic transduction element combination”, *2019 IEEE International Ultrasonic Symposium*, 2019, pp. 147-150, doi: 10.1109/ULTSYM.2019.8925701

- **M. Rutsch**, A. Jäger, A. Unger, T. Kaindl, M. Kupnik, ”Wave propagation in an acoustic waveguide for ultrasonic phased-arrays”, *2019 IEEE International Ultrasonic Symposium*, 2019, pp. 796-799, doi: 10.1109/ULTSYM.2019.8926307.

- G. Allevato, J. Hinrichs, D. Großkurth, **M. Rutsch**, J. Adler, A. Jäger, M. Pesavento, M. Kupnik, ”3D imaging method for an air-coupled 40 kHz ultrasound phased-array”, *ICA*, pp. 4775-4782, 2019.

2017

- A. Jäger, D. Großkurth, **M. Rutsch**, A. Unger, R. Golinske, H. Wang, S. Dixon, K. Hofmann, M. Kupnik, ”Air-coupled 40-kHz ultrasonic 2D-phased array based on a 3D-printed waveguide structure”, *2017 IEEE International Ultrasonic Symposium*, 2017, pp. 1-4, doi: 10.1109/ULTSYM.2017.8091892.

2015

- E. Konetzke, **M. Rutsch**, M. Hoffmann, A. Unger, R. Golinske, D. Killat, S. Ramadas, S. Dixon, M. Kupnik, ”Phased array transducer for emitting 40-kHz air-coupled ultrasound without grating lobes”, *2015 IEEE International Ultrasonic Symposium*, 2015, pp. 1-4, doi: 10.1109/ULTSYM.2015.0019.

- **M. Rutsch**, E. Konetzke, A. Unger, M. Hoffmann, S. Ramadas, S. Dixon, M. Kupnik, ”Extending the receive performance of phased ultrasonic transducer arrays in air down to 40 kHz and below”, *2015 IEEE International Ultrasonic Symposium*, 2015, pp. 1-4, doi: 10.1109/ULTSYM.2015.0095.
- R. Golinske, M. Hoffmann, E. Konetzke, A. Unger, **M. Rutsch**, M. Kupnik, ”Diffraction loss calculation based on boundary element method for an air-coupled phased array”, *2015 IEEE International Ultrasonic Symposium*, 2015, pp. 1-4, doi: 10.1109/ULTSYM.2015.0375.
- A. Unger, E. Konetzke, **M. Rutsch**, M. Hoffmann, S. Ramadas, S. Dixon, M. Kupnik, ”Versatile air-coupled phased array transducer for sensor applications”, *2015 IEEE Sensors*, 2015, pp. 1-4, doi: 10.1109/ICSENS.2015.7370187.

Contents

1 State of the art and motivation for air-coupled duct acoustics

In general, an acoustic waveguide, as the name indicates, is a duct with rigid walls which directs a wave in a certain direction. These effects are called duct acoustics in physics and can be observed in nature and technical applications. This chapter will point out the significance of acoustic waveguides in different fields. As a result, the chapter is divided into duct acoustics for the audible range ($16\,\mathrm{Hz} - 20\,\mathrm{kHz}$) and duct acoustics for ultrasound ($> 20\,\mathrm{kHz}$). In both cases, the state of the art will be presented and the author will state the research questions of this thesis. Last, the original work in this thesis will be described.

1.1 Duct acoustics in the audible range

In science, many inventions are inspired by nature which is also known as bio-mimicry [1]. The same applies for acoustic waveguides. For instance, the human voice is a complex acoustic phenomenon which consists of different components of the human body. First, the sound is created by the vocal cords [Figure 1.1(a)]. Afterwards, the sound wave propagates through the vocal tract and last it is emitted into free-field [2]. The vocal tract provides a filter characteristic which can be used to change the acoustics of the human voice. This effect can be described with the vocal tract transfer function. The tract can be assumed as a linear time invariant system, which means that the principle of superposition is valid and time-delayed signals do not change the filter characteristics. As a result, the vocal tract can be modeled as an acoustic duct which consists of a closed end at the vocal cords and an opened end where the mouth is located. This creates a frequency dependent filtering, which is often used by professional singers. The resonance frequencies, in physiological acoustics also refereed to as formants, depend on the length of the vocal tract and its cross-section. A trained singer can modify both geometries by raising or lowering their larynx which decreases or increases the length of the acoustic duct. In addition, the cavities beneath the soft and hard palate influence the diameter of the vocal tract as well [3], [4].

Acoustic waveguides are important for human sound interaction not only in transmission but also in reception. The hearing mechanism of the ear can be divided into three parts: the external ear, the middle ear and the inner ear [Figure 1.1(b)]. The external ear includes an auditory canal which can be modeled as an acoustic duct [5], [6]. Apart from protecting the sensitive tympanic membrane (ear drum) it adds a frequency filter to the overall human hearing. In the ear canal, standing waves can occur creating resonances and these frequencies are optimized for speech and ease of communications. The ear-canal acoustics can be further investigated with duct acoustics. Again, the ear-canal can be modeled as a duct with an ear canal center line curve and the ear-canal area function defining the cross-section depending on the position in the canal. Since the eardrum moves due to sound waves, the ear-canal is not terminated with a sound hard wall but with an acoustic impedance. The sound propagation can be described with the Webster's Horn equations, because the change in diameter can be compared to an acoustic horn [7].

After the external ear, the middle ear is located which serves as an impedance matching between external ear and inner ear. In the inner air the cochlear is located which includes the basilar membrane. It consists of multiple small hairs which sit in a liquid. Again, sound waves travel through this fluid and excite the

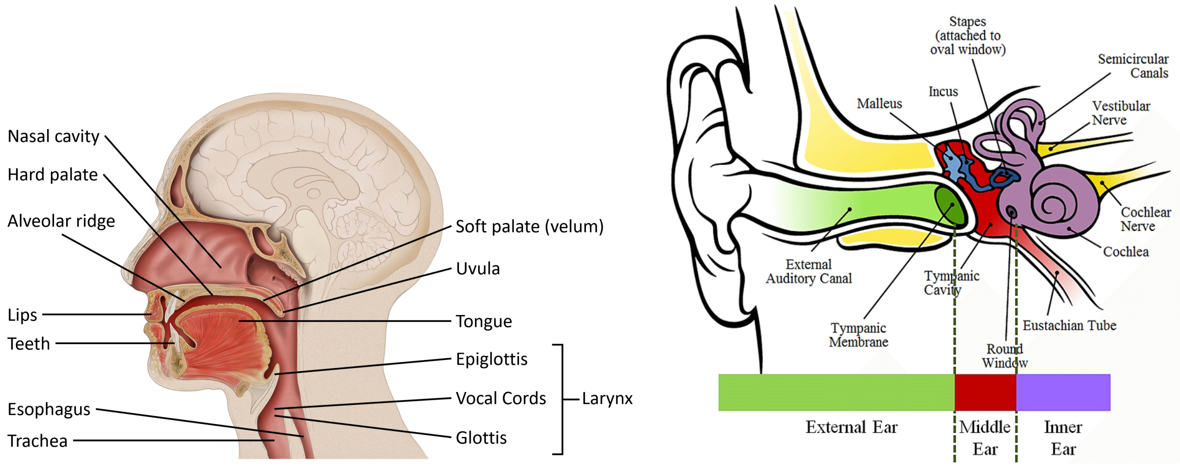

(a) (b)

Figure 1.1: The vocal cords of the human are connected to the mouth via an acoustic waveguide (vocal track) (a) [2]. In addition, the ear drum is connected to the external ear via an acoustic waveguide as well (b) [5].

hairs for an acoustic stimulation. Thus, the basilar membrane is a waveguide with a varying diameter providing a broadband frequency response. Near the middle ear, the diameter of the basilar membrane is the smallest. Consequently, in this section it is sensitive to the upper frequency range of the human hearing. In contrast, at the end of the basilar membrane the diameter is the biggest providing sensitivity for low end frequencies. Due to the attenuation of the sound waves in the liquid, which increases with higher frequencies, the basilar membrane increases its diameter along the center line [8]. The modeling of this structure including the small hairs is still under research [9].

The concept of separating a sound source from the radiating aperture is used in many different musical instruments. For instance, church organs consist of multiple pipes with different geometries, thus providing a wide tonal range (musical frequency range). The sound creation starts with a wind system creating a static air flow. When a key is pressed, a specific valve opens and air flows over a brass strip which is also refereed to as reed or tongue. This constant stream of air creates vibrations of the reed and thus creating the initial sound of the instrument. Afterwards, the acoustic wave propagates from the reed through the pipe. Last, the wave is reflected at the end of the pipe and superposed with the next incident wave, creating a standing wave. These standing waves are also called eigenmodes. As a result, the pipe can be seen as an acoustic resonator. The geometry of the pipe shapes the sound created by the reed by means of resonance frequency, overtones and attack-time. The wide pipes produce the fundamentals of the instrument with fast attack-times. For higher eigenmodes, irregularities occur. Higher frequencies produce transverse resonances inside the pipe leading to cross-sectional eigenmodes. In addition, the walls start vibrating. These irregularities cause a detuning of the instrument, which is quiet rare in practice. Since the geometry of the pipes influence the tone of the instrument, there are several design rules for church organs. The eigenfrequencies are tuned that they are the same as the overtones of a note. Thus, the excitation of these overtones is more efficient. The acoustic effects of pipe geometries are still under research [10].

Another musical instruments which uses duct acoustics are woodwind instruments. They consist of an air jet or pair of reeds as an acoustic source. These sources react with the acoustic duct, which serves as a resonator. The tone holes on the duct define its effective length and thus its resonance frequency. This interaction between source and resonator define the pitch, loudness and timbre (overtones and attack-time) of the instrument. For example, flutes with openings on both side create a standing wave. The wavelength λ of this wave is the double of the ducts length $\lambda = 2l_{\text{duct}}$. In addition, a harmonic series of overtones can be expressed with $f_{\text{n}} = \frac{nc_{\text{air}}}{2l_{\text{duct}}}$ where c_{air} is the speed of sound and n is the n-th overtone. In contrast, a clarinet is closed on one side leading to a different overtone dependency. This is created when $f_{\text{n}} = \frac{(2n-1)c_{\text{air}}}{4l_{\text{duct}}}$ is fulfilled. This creates a lower fundamental compared to the flute when both instruments have the same length [11].

The manipulation of audible sound for music is also used in the design of speakers. For instance, transmission line speakers consist of a speaker driver and a speaker cabinet. In consumer electronics, often a bass reflex cabinet is used as a speaker cover. These cabinets have a short open port and serve as a Helmholtz resonator amplifying the low end of the speaker [12]. However, since the resonator has a high quality factor, the acoustic energy retains for a longer time inside the cabinet introducing ringing in the lower end frequency range. As a result, the speakers sound more ”boomy” in the bass section. In order to reduce this decay time, acoustic transmission lines can be used inside the cabinet. In addition, these transmission lines are filled with absorbing materials (long fibre wool) which attenuate the wave propagation inside the cabinet. Furthermore, the port at the end of the line is opened leading to a reduction of diffraction and a flat bass response which sounds more natural [13].

Another technical application of duct acoustics are car mufflers in the automotive industry [14]. They are used for attenuating noise from the engine including its fundamentals and harmonics, which depend on the speed of the engine. In addition, the muffler needs to pass as much exhaust gases as possible. Otherwise, the engines power is decreased.

There are two types of mufflers on the marked. First, the reflective muffler uses destructive interference due to reflections inside resonating chambers. They consist of geometric discontinuities which lead to reflections and superposition of reflected and incident waves. When the phase shift of the reflected wave is $180°$, the wave for a certain frequency is attenuated. In order to increase this frequency range, a series of resonating chambers is used. In addition, the inlet and outlet of the muffler have offsets and are perforated. Thus, leading to the sound being scattered and producing additional destructive interferences. For crucial frequencies, additional side branches can be mounted to the muffler which serve as narrow band Helmholtz resonators. Thus, specific single frequencies that are problematic can be attenuated. However, reflective mufflers increase the back pressure which decreases the power output of the engine.

A second type of mufflers is the absorptive or dissipative muffler. In contrast to reflective mufflers, it does not use destructive interference but porous media which converts acoustic energy into heat. This way, a wider frequency range is attenuated.

Today, car mufflers are not only used to reduce environmental noise emission but also to give a car its specific sound. For example, sport cars are designed to emit a certain frequency range and shape the sound of the engine.

1.2 Duct acoustics in ultrasound

Low frequency ultrasound (25 kHz up to 250 kHz) is used in many technical applications. This frequency range provides a compromise between low atmospheric attenuation in air and a safety margin from the audible frequency range. As a result, high ranging systems can be built.

Air-coupled phased arrays especially benefit from this frequency range, which allows for applications such as 3D imaging, compensation of sound drift effects in acoustic flow meters [15], [16], generation of variable focus points for haptic displays [17] or steerable vortex beams [18]. These ultrasonic phased arrays consist of several independently excitable ultrasonic transducers. Each transducer signal is time-delayed in order to create a steerable main lobe[8], [19]. These delays can be generated acoustically with different sound propagation paths [20]–[22] or electrically e.g. using microcontrollers [17] or field programmable gate arrays (FPGAs) [23].

In order to avoid ambiguities, grating lobe free beamforming is needed for the aforementioned applications [24]. Otherwise, sound emission in unwanted directions occurs. These grating lobes can be suppressed with multiple approaches. For example, the inter element spacing between the transducers can be reduced to halve wavelength ($\lambda/2$)[8] or a non-regular arrangement (e.g. spiral arrays) can be used [23], [25].

In 1993 Langen showed the advantages of combining ultrasonic transducers with acoustic waveguides [26] for air-coupled ultrasound phased arrays. The author presents methods for modifying the directivity pattern of commercially available ultrasonic transducers for different air-coupled applications. The four resulting acoustic waveguides are:

- Wide angle ultrasound emission[Fig 1.2(a)],
- focused ultrasound for up to $20\,\mathrm{m}$ [Fig 1.2(b)],
- near-field scanning for increased resolution for up to $2\,\mathrm{m}$ [Fig 1.2(c)],
- line array for side lobe suppression and steering of the main lobe for up to $10\,\mathrm{m}$ [Fig 1.2(d)].

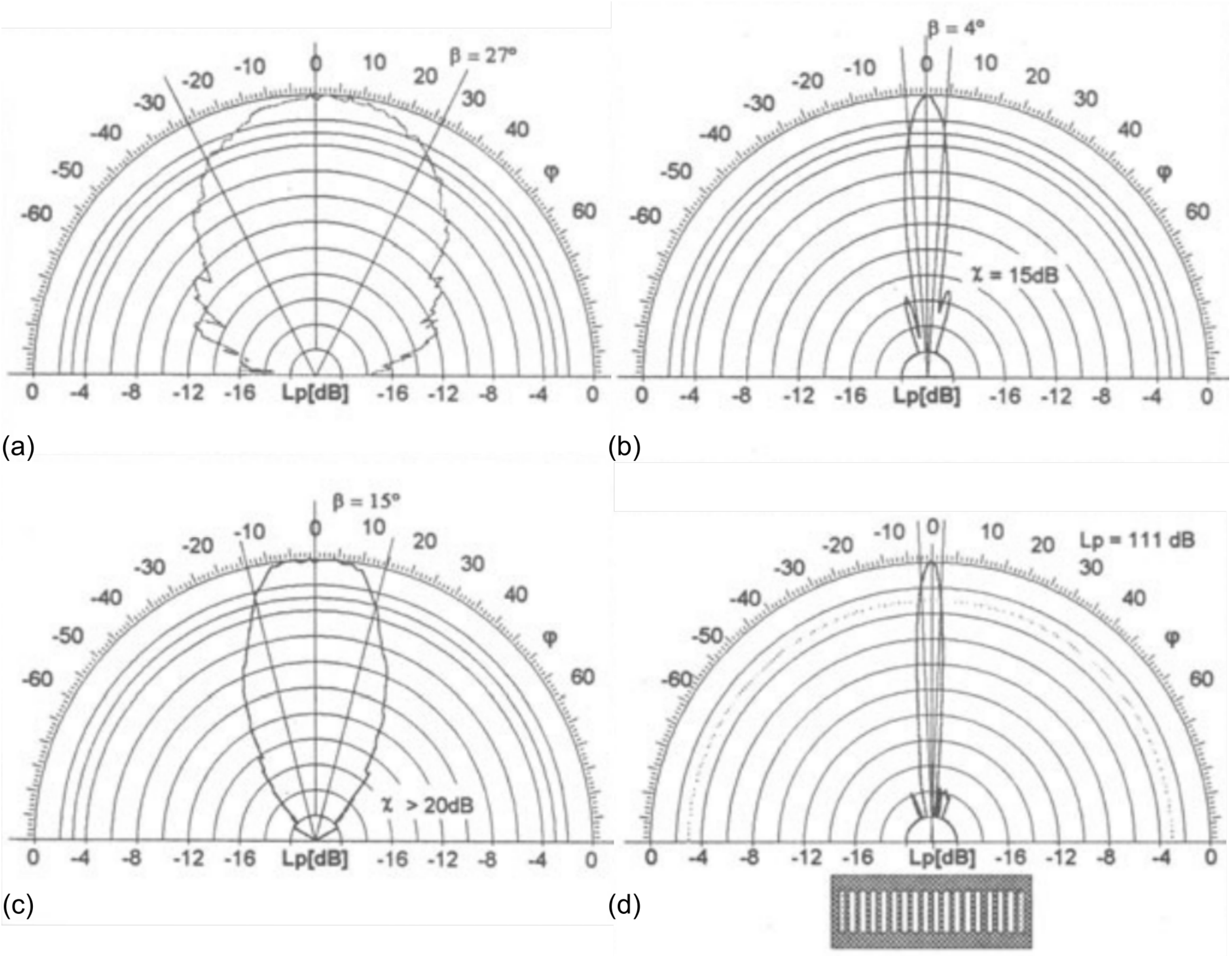

Figure 1.2: Langen showed in his work, that it is possible to change the directivity of an ultrasonic transducer with acoustic waveguides [26].

For all four waveguides, a horn structure was used which widens the acoustic aperture of the ultrasonic transducers used in the study (MASSA TR89 $\varnothing = 25.4$ mm and Nippon T40-12 $\varnothing = 12.6$ mm, both at 40 kHz). The entire waveguide is divided into four parts. First, the wave of the ultrasonic transdcuer is emitted into a Helmholtz resonator. Second, an inner aperture focuses the acoustic energy. Third, the wave propagates in an acoustic duct with varying diameter. Last, the wave is emitted into the free-field from the outer aperture (Figure 1.3).

In general, the Helmholtz resonator serves as an acoustic amplifier. In addition, it improves the impedance matching between the ultrasonic transducer and the free-field by increasing its acoustic impedance. Furthermore, the rise time of the ultrasound can be modified, since the superposition of reflected and incident waves needs time which depends on the propagation length of the waves. In summery, this resonator improves the overall acoustic efficiency of the system. The author states that the most important parameter of this Helmholtz resonator is the distance between the inner aperture and the transducer. The fabrication tolerances need to be at least 0.01λ. However, since the Helmholtz resonator is an acoustic energy storage, the decay time of the ultrasound is increased which is the same issue which bass reflex cabinets have [13]. This leads to an increased blind zone in a pulse-echo configuration, because the decaying wave and the reflected wave from obstacles superpose. This effect was not investigated in this work.

The Helmholtz resonator is terminated by an inner aperture. The diameter of this aperture needs to be small compared to the wavelength. This way, the author decoupled the resonator from the duct section. In addition, it increases the robustness against temperature and frequency deviation. However, the results show that the complex modes inside the Helmholtz resonator are highly temperature dependent. Last, the efficiency of the entire system is reduced when the diameter of the inner aperture is below half the wavelength.

After the inner aperture, an acoustic duct with varying diameter is located. This duct is used to adapt from the inner to the outer aperture with continuous geometries. Langen tested different geometries. The author found out, that concave forms lead to reflections at the outer aperture causing local maxima inside the duct. In contrast, convex structures provide a plane wave propagation inside the duct and spherical wave propagation in the free-field. In addition, these geometric parameters correlate with the wavelength, and, thus, are also temperature dependent.

At the end of the duct, the outer aperture is located which mainly defines the directivity of the entire system. In addition, the termination of the aperture also influences the directivity. For instance, whether the system is back baffled or not changes the sound emission. Furthermore, the author states, that waveguides with the same aperture and the same basic shape create the same directivity pattern. Last, the side lobe suppression depends on the phase deviation on the apertures plane.

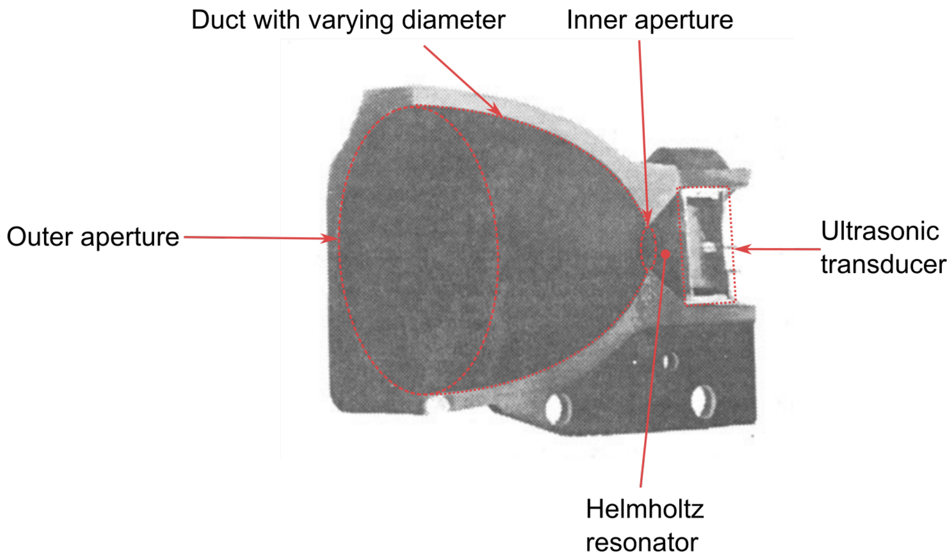

Figure 1.3: In the work of Langen, the acoustic waveguide is divided in a Helmholtz resonator, an inner aperture, a duct with varying diameter and an outer aperture [26].

In his research, Langen used numerical approaches in addition to measurements. The use of numerical models were selected, since the mode shapes differ from a plane wave propagation. Thus, analytic waveguide theories are not applicable anymore.

First, the finite element method (FEM) was used to analyze the acoustic modes inside the waveguide. As boundary conditions an ideal piston transducer, ideal sound hard walls and the acoustic impedance in free-field were used. For free-field calculations the boundary element method (BEM) was used. In general, the simulations in the free-field and the results of the boundary element method are in good agreement. However, the results were derived from an empiric methodology. General dependencies of acoustic properties and geometries in form of cartesian diagrams are not provided by the author.

In 2014, Shigeru et al. used acoustic waveguides to increase the sound pressure level (SPL), using piezoelectric transducers, while retaining the same aperture of the transducer system [27]. This way, there is no need for increasing the electrical voltage and thus damaging the transducer for higher SPL.

They simulated the wave propagation in water in two dimensions using the finite difference method of Wave2000 (Cyberlogic Inc.) [Figure 1.4(a, b)]. For excitation, a longitudinal wave of 1 MHz was used. The model consists of five piston transducers with individual tapered ducts. In addition, the four outer ducts are bent in order to form the identical aperture size as of a single piston transducer. This leads to different propagation lengths of each duct which needs to be compensated with additional delays. Each duct creates a point source at the output, thus the amplitude, frequency and phase needs to be controlled.

As a result, the bending of the ducts has just a minor impact on the pressure of about 8%. In contrast, the length of the duct changes the pressure by 33%. The overall pressure was increased by a factor of 1.57. Last, the half power beam width retained the same but the side lobe level was increased by 16%.

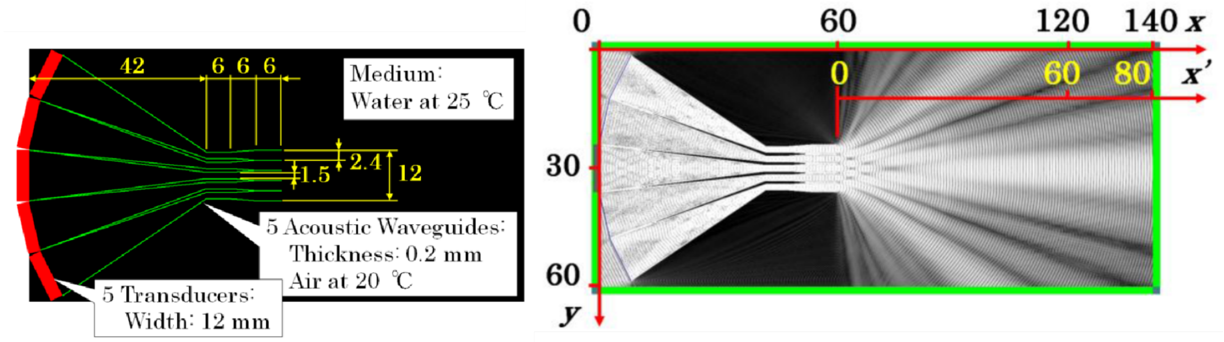

(a) (b)

Figure 1.4: Shigeru et al. simulated the wave propagation in acoustic waveguides in order to increase the sound pressure level of an ultrasonic transducer, while retaining the same driving voltage and aperture size [27].

In 2008 Takahashi et al. built an air-coupled ultrasonic phased array with acoustic waveguides [28]. It serves as a travel aid for visual impaired people. Using a phased array, the searching range and the detection of multiple obstacles was offered in comparison to single transducer approaches.

In general, phased arrays are a combination of multiple single sensors [8]. In addition, the phase between each individual sensor can be modified, in order to steer the main lobe in transmit and receive mode. However, the inter-element spacing is crucial when it comes to ambiguities. When the spacing is greater than half the wavelength, grating lobes occur in a fully populated structure leading to sound emission in undesired directions. Furthermore, sound can be received with high sensitivity in these unwanted directions. These grating lobes can be suppressed with an irregular distribution of the transducers resulting in an increased geometry of the device [23].

Takahashi et al. decided to use acoustic waveguides with tapered geometry. This way, they built a compact air-coupled phased array with an inter element-spacing of half the wavelength [Figure 1.5]. They used Muratas 40 kHz-transducers (MA40S4S) which have a diameter of 10 mm. At a frequency of 40 kHz the wavelength is 8.6 mm in air. By using the proposed waveguides the aperture of each transducer was reduced from 10 mm to 4 mm which fulfills the half wavelength criteria.

With this approach, a grating lobe free directivity pattern was created which allows for unambiguous pulse echo measurements. The resulting system is able to detect two separate aluminum square pillars ($30\,\mathrm{mm} \times 30\,\mathrm{mm}$) with an angular resolution of $10°$. The maximum steering angles are $\pm 60°$.

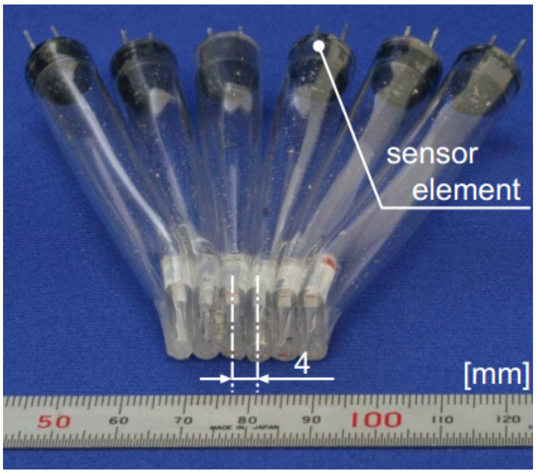

Figure 1.5: Takahashi et al. built an ultrasonic phased array by using shrinking tube as acoustic waveguides [28].

In 2015 Unger et al. modified commercially available ultrasonic transducers to try and achieve an inter-element spacing of halve the wavelength. The housing was removed from the transducers and the polymer base was sanded to reduce the diameter of the transducer. As a result, the achieved spacing was $7.8\,\mathrm{mm}$ which was not sufficient for an air-coupled phased array [29]. Afterwards, the authors used the same method of Takahashi to build a grating lobe free air-coupled ultrasonic phased array with acoustic waveguides. Again, Murata's MA40S4S transducers were used with an outer diameter of $10\,\mathrm{mm}$. By applying an acoustic waveguide with a tapered structure, the effective acoustic aperture was reduced from a circle with a diameter of $10\,\mathrm{mm}$ to a rectangle with $4.8\,\mathrm{mm} \times 3\,\mathrm{mm}$ [Figure 1.6(b)]. The length of each waveguide is $60\,\mathrm{mm}$. An aluminum mold was used in order to reproduce the right shape for the shrinking tubes [Figure 1.6(a)]. Please note that the shrinking tubes were hand-fabricated, and, thus, each shrinking tube varies in length and cross-sectional shape [30]–[32].

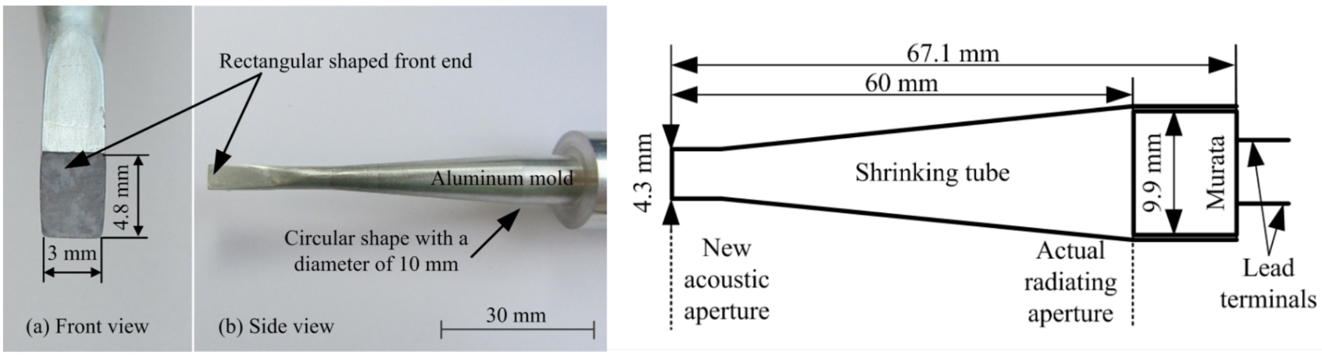

(a) (b)

Figure 1.6: Unger used an aluminum mold to define the shape of the shrinking tubes [32]. These are used as acoustic waveguides for an air-coupled phased array.

Afterwards, 96 transducers where soldered on a breadboard by hand and connected to its individual waveguide (Figure 1.2). Since each waveguide has the same length, the input plane of each waveguide is tilted. Consequently, each transducer needs to be tilted as well. The output port of each waveguide is mounted into a metal plate with individual sockets. This plate serves as a rigid baffle which defines the acoustic boundary condition of the phased array. In order to provide mechanical stability, four metal spacers where used which connect the breadboard with the rigid baffle. Last, eight BNC connectors are used for electrical connection.

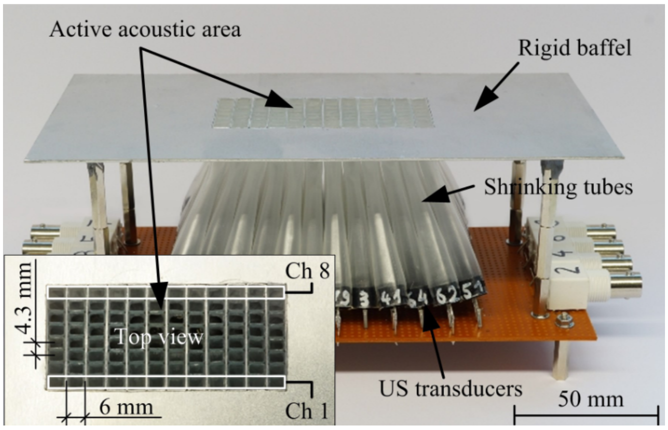

Figure 1.7: The phased arrays consists of 96 ultrasonic transducers. which are divided in 8 channels [32].

This proof-of-concept prototype array was characterized in transmit and receive mode. In transmit, all transducers where driven with $40\,$kHz, $10\,\mathrm{V_{pp}}$ and 80 cycles. By using burst signals, standing waves in the measurement room were avoided, and, thus, wall absorbers were not needed. The 96 transducers were divided in 8 channels, each with an electric impedance of $50\,\Omega$ for impedance matching with the function generator (33522B, Keysight). The driving system consisted of five double channel wave generators in a master-slave configuration with a $10\,$MHz time base.

As a result, the directivity pattern of this first prototype showed no grating lobes [Figure 1.8(a)]. It is able to steer the main lobe within a range of $\pm 55°$. In addition, the array achieved a sound pressure level of $130\,$dB $\pm\ 1\,$dB at a distance of $1\,$m without a focusing of the main lobe. Last, the acoustic losses due to the waveguide where $3\,$dB.

In receive mode, two 4-channel oscilloscopes (DSO-3024A) where used to capture the receiving signals. The sampling rate was $200\,$MSa/s which leads to a theoretical angle resolution of $0.023°$. Afterwards, a delay-and-sum algorithm was used for beamforming. Again, the directivity patterns showed no grating lobes, which proved the reciprocity of the waveguided ultrasonic phased array [Figure 1.8(b)]. In addition, the sensitivity achieved $-55.9\,$dB ($0\,$dB$\widehat{=}1\,$V/Pa). However, the losses in receive were higher compared to the transmission measurements with $6\,$dB.

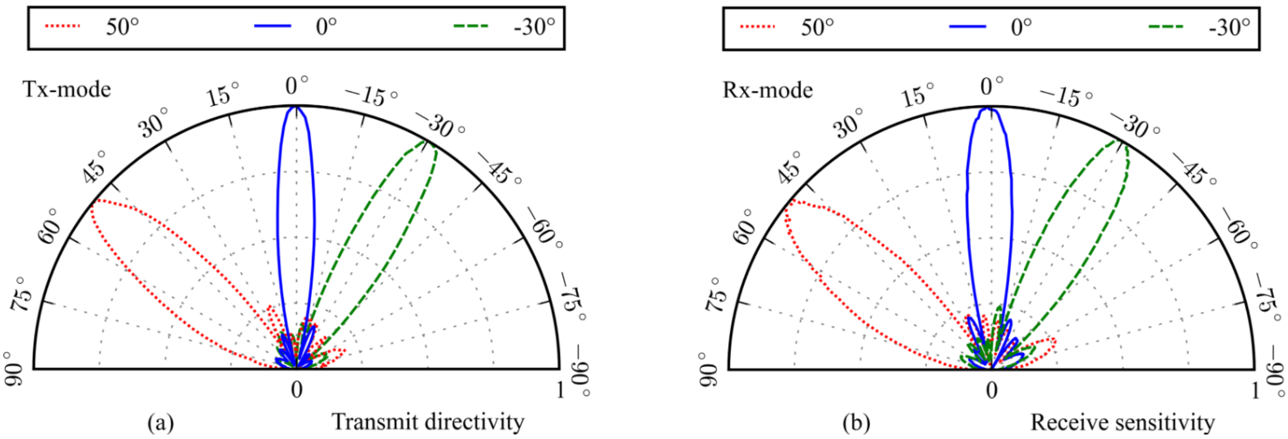

Figure 1.8: The phased arrays using shrinking tubes has no grating lobes in transmit and receive [32].

In 2017 Jäger et al. further improved the waveguide approach by using 3D printed components and custom built electronics [33], [34]. This way, a 2D array was built for multiple applications (Figure 1.9). First, the shrinking tubes were exchanged by 3D-printed waveguides. The center lines of the waveguide are based on arcs and all center points of these arcs are located on the output surface of the waveguide. Each waveguide has the same length of 80 mm. A length optimization was not conducted in this work. The length was selected to minimize the bending of the waveguides located at the edges. However, this introduces a time consuming assembly process. Since, each waveguide has the same length and the input surfaces need to be perpendicular to the centerline, each transducer must be tilted. As a result, the transducers can not be soldered onto a plane printed circuit board (PCB) but must be soldered with air wires. This time consuming process was performed by hand. On the other hand, the author states a solution for this issue by using Bézier-shaped waveguides. This approach allows for PCB compatibility, because the input and output surface of the waveguide can be in parallel. Therefore, the different waveguide lengths need to be compensated with additional time delays for the channels. The Bézier waveguide was not further investigated by the author. In this work, the waveguide was manufactured using an Ultimaker 2 (Ultimaker BV, Geldermasen, Netherlands) and polylactic acid (PLA) (Innofill PLA, Innofill 3D BV, Emmen, Netherlands).

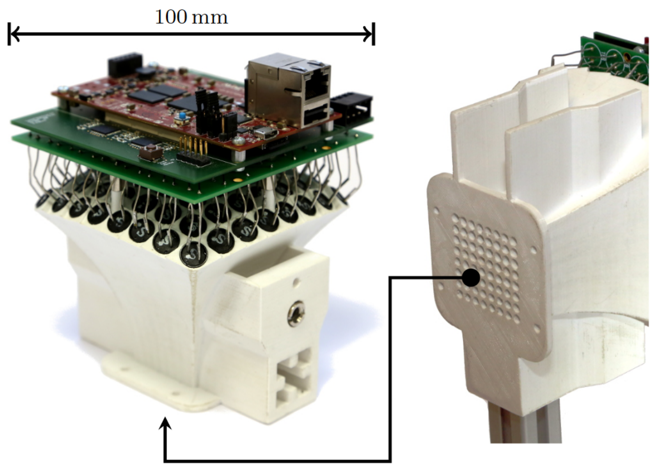

Figure 1.9: Jäger et al. built an air-coupled phased array using 3D-printing for the acoustic waveguide [34].

In order to reduce the complexity of the electronics, custom boards were built. For transmit mode, eight 8-channel pulser IC (HV7355, Microchip, Chandler AZ, USA) were used. They provide a rectangular driving signal for each individual transducer. In receive mode, a variable gain amplifier AD8335 (Analog Devices, Norwood, MA, USA) was used. This allows for an increased receive signal over time. The basic idea is that in pulse echo mode the ultrasound is attenuated over the propagation length in free-field. This effect can be compensated by increasing the gain of the amplifier over time. Afterwards, the signal is quantized using an analogue to digital converter AD7761 (also Analog Devices, Norwood, MA, USA). All time delays and communication to a personal computer is handled by a field programmable gated array (FPGA) Zynq 7010 (Xilinx, San Jose, CA, USA). Last, a switch (TX810, Texas Instruments, Dallas, TX, USA) is used to use the array in transmit or receive mode. In order to synchronize the electronics with additional hardware, a trigger-in and -out was implemented.

The signal processing for pulse-echo measurements is conducted in the time domain. Later, G. Allevato extended the algorithms into the frequency domain [35]. First, the signal is bandpass filtered for the desired $40\,\mathrm{kHz}$. Second, an upsampling is conducted using zero stuffing. This allows for a higher resolution of the delay-and-sum algorithm. Afterwards, the envelope of the signal is extracted by using the Hilbert transformation. Last, the delay-and-sum algorithm is used for receive beamforming. All calculations are performed on a graphics processing unit (GPU) which allows for parallel computing.

Alongside the work and improvements on the air-coupled phased array, R. Golinske worked on the simulation of the acoustic field of the array [36], [37]. His model is based on the linear wave equation. This way, the model is valid for SPLs under $140\,\mathrm{dB}$. This equation is transformed into the frequency domain yielding the Helmholtz equation. Afterwards, the Greens function is used to build a boundary problem. As a result the Rayleigh integral is derived. This approach uses the boundary element method (BEM) and is suitable to solve for the acoustic field of a piston transducer in an infinite-sized rigid baffle. All calculations were conducted by using the GPU due to its parallel processing power. In addition, the Kirchhoff Helmholtz integral was used. This allows for calculations of piston transducers located in a finite-sized rigid baffle, because it solves for an interior problem. The comparison between these two models showed that the acoustic boundary condition of an ultrasonic transducer affects its directivity pattern. This especially effected the side lobes at directions $> 50°$ and the zero crossings are influenced by the baffle. In addition, the aperture size of the receiving microphone is regarded in the model. By averaging the acoustic pressure over the surface of the microphone, the simulations had further similarities with the measurements. As a result, the accuracy of the numerical model is 0.53% compared to analytic models.

The results of the simulations showed, that the relative orientation of the microphone to the ultrasonic transmitter has a major influence on the measured directivity. The best way to measure acoustic directivities is, when the receiving microphone always directs towards the ultrasound source. This model was used to predict the directivity pattern of the phased array. However, only the radiating aperture was regarded without the wave propagation inside the waveguide. In general, there are several studies which investigate guided wave propagation in solids[38], [39], liquids[40] and gases[27], [41]–[44]. However, the authors did not combine their approaches with ultrasonic phased arrays [45]–[47] yet.

In conclusion, duct acoustics are used in different ways. In the audible range these ducts are used to shape the sound by amplifying certain frequencies or attenuating them. In contrast, in the ultrasonic range duct acoustics are used to guide the sound wave and shape the acoustic aperture engineering its radiation pattern. However, there is a lack of investigations regarding the wave propagation inside the waveguide for higher modes in combination with the ultrasonics range. In this work, new key properties such as the geometry of the waveguide, how the output ports can be made waterproof and further simulations including the waveguide are investigated.

1.3 Structure of this thesis

This thesis is structured as follows. First, different examples of duct acoustics are given in the introduction. The examples are divided into the audible and ultrasonic range. In addition, the state of the art of waveguided ultrasonic phased arrays in air are shown.

In chapter 2 the principles of acoustics and models for duct acoustic are described. First, the linear Helmholtz equation is derived. Afterwards, the thermoviscous effects in acoustic ducts are described in more detail. The derivations show for which case the equations are applicable. Last, the models are compared with each other and investigated, whether they are suitable for the given waveguide geometry at 40 kHz.

Chapter 3 investigates and validates the boundary element method for the waveguided phased array. First, the experimental setup for validation is described in detail. Facts such as mechanical structure, measurement routine and how to setup a measurement are provided. In addition, the noise floor and measurement uncertainties are investigated. Next, this model is compared with the numerical model which includes the acoustic waveguide, a finite-sized rigid baffle and the free-field acoustics including atmospheric attenuation.

Chapter 4 presents the results of the geometry optimization of the waveguide. The boundary element method is used to provide parameter studies for various geometries. This extends the results of Langen [26] and questions the design rules of Jäger [34]. In addition, the acoustic losses inside the waveguide are split into its origins. These methods are based on impedance tubes and include a numerical model in the time domain and validation measurements as well. Last, the derived results are used to build a new generation of waveguided line arrays.

Chapter 5 compares a waveguide with equal propagation lengths and a waveguide consisting of Bézier-shaped waveguides. The waveguide built by Jäger [34] is suitable for multiple applications. However, a waveguide with equal propagation paths results in a time consuming assembly process of the ultrasonic transducers. Each transducer needs to be tilted which makes this process not compatible with a plane PCB, since multiple air wires are needed. Jäger proposed the use of Bézier shaped to solve this issue. However, this approach was not investigated in his work. In this thesis, the Bézier waveguides are investigated in detail with simulations and measurements. The methodology of compensating the different propagation paths is described with analytic, numeric models and is validated with measurements.

Chapter 6 investigates the possibility of two commonly know solutions to waterproof acoustic waveguides. They are derived from consumer electronics. Since the waveguide is built for air-coupled applications, the outputs are opened which can lead to clogging due to liquids or dirt. In order to solve this issue, thin films were compared with hydrophobic fabrics and both approaches have been simulated and validated. As a result, the two solutions are compared regarding its watertightness and acoustical insertion loss.

The last chapter covers the conclusion of this thesis and future work packages for further investigations.

1.4 Original work

In the author's opinion the main contributions carried out through this thesis are:

1. Comparing and selecting the right waveguide model for the given geometry and frequency range.

   Acoustic ducts can be modeled with multiple approaches. However, each model has its specific limitations which needs to be compared with the given geometry and frequency range. In this work, multiple models which are commonly used for duct acoustics are presented and validated for the given waveguide structure.

2. Comparing numerical and analytic models for calculating duct acoustics in the ultrasound frequency range.

   In duct acoustics, there are multiple models both for analytic and numeric methods. This work compares these models and shows their individual advantages and limits. The differences are shown in the frequency response and deviations are explained.

3. Adding the waveguide to the boundary element method.

   R. Golinske showed the advantages of the boundary element method for simulating the directivity pattern of ultrasonic phased arrays. However, only the acoustic aperture at the output of the waveguide was considered in this model. This work adds the entire waveguide geometry to the simulations. All calculations are validated with calibrated measurements. These Results were published in [48].

4. Optimizing the waveguide geometry and validating the design rules.

   The first 3D-printed waveguided phased array postulated with its design rules. In this work, parametric studies were conducted for getting a better understanding of the wave propagation inside the waveguide. The results were published in [49].

5. Using the achieved knowledge to build compact 1D-line arrays.

   The results of the parameter studies are used to build new line arrays. These arrays are compact, have a reduced element number and are capable of detecting obstacles.

6. Build numerical models and perform suitable validation for propagation time compensation inside waveguides.

   For further simplification of the assembly of waveguided phased arrays, Bézier-shaped waveguides were used. These geometries introduce propagation delays, since each centerline of the waveguide differs. Methods for compensating these additional delays are presented in this work. The results were published in [50].

7. Adding water resistance to the acoustic waveguide while increasing its sound pressure level.

   For industrial applications, the waveguides must be water resistant. Therefore, hydrophobic fabrics are compared with thin films. The criterias are their IP-class and their insertion loss. The results were published in [51], [52]

2 Theory and modeling of duct acoustics

This work investigates wave propagation in acoustic ducts. The investigated round duct has a tapered geometry reducing its radius r_{duct} from $5\,\mathrm{mm}$ to $1.7\,\mathrm{mm}$ along a length l_{duct} of $80\,\mathrm{mm}$. The chapter describes analytic and numerical models for simulating duct acoustics. First, each model is derived from the acoustic fundamentals. This way, a deep understanding of the limits of the model is provided. Second, the models are validated, whether they are suitable for an aspect ratio between the wavelength λ and the radius of the duct of $\lambda/r_{\mathrm{duct}} = 8.575\,\mathrm{mm}/5\,\mathrm{mm} = 1.715$ and $8.575\,\mathrm{mm}/1.7\,\mathrm{mm} = 5.04$ for a frequency of $40\,\mathrm{kHz}$. All models discussed in this chapter are linear, include just one frequency and are used for air.

2.1 Wave equation

In the following sections the theory and derivations of the wave equation are taken and summarized from [8], [53]–[56], since for the subsequent chapters these equations are used in the models and calculations presented. In addition, the derivatives provide a deeper understanding when and how these models are applicable. For instance, all assumptions of the models can be easily explained with this methodology.

In general, the fundamentals of acoustics are based on the equations of state. These equations describe the relationship between the total pressure p_{t} and the total density ρ_{t}. This relation is assumed as lossless. The total pressure p_{t}, density ρ_{t} and velocity $\vec{v}_{\mathrm{t}}$ are split into a constant or often refereed to as atmospheric (0 as index), and variable part (no index) [8]

$$p_{\mathrm{t}} = p_0 + p, \tag{2.1}$$
$$\rho_{\mathrm{t}} = \rho_0 + \rho, \tag{2.2}$$
$$\vec{v}_{\mathrm{t}} = \vec{v}_0 + \vec{v}. \tag{2.3}$$

Since the atmospheric component is much higher compared to the variable component (factor 10^5) the following assumption is valid, i.e.

$$p \ll p_0, \tag{2.4}$$
$$\rho \ll \rho_0, \tag{2.5}$$
$$\vec{v} \ll \vec{v}_0. \tag{2.6}$$

First, the equation of motion, based on newtons second law, describes the relation between inertia, pressure gradients ∇p_{t} and external forces $\vec{F}$ [8]. These quantities are time dependent (t), i.e.

$$\rho \frac{D\vec{v}_{\mathrm{t}}}{Dt} + \nabla p_{\mathrm{t}} = \vec{F}. \tag{2.7}$$

The inertia depends on the time dependent deviation of the density ρ_{t} and the creation of convective accelerations of the velocity $(\vec{v}_{\mathrm{t}}\nabla)\vec{v}_{\mathrm{t}}$, i.e.

$$\frac{D\vec{v}_{\mathrm{t}}}{Dt} = \frac{\partial \vec{v}_{\mathrm{t}}}{\partial t} + (\vec{v}_{\mathrm{t}}\nabla)\vec{v}_{\mathrm{t}}. \tag{2.8}$$

This equation can be more generalized in the following form [8], i.e.

$$\frac{\partial \vec{v}_{\mathrm{t}}}{\partial t} + \text{grad } \frac{\vec{v}_{\mathrm{t}}^2}{2} - \vec{v}_{\mathrm{t}} \times \text{rot } \vec{v}_{\mathrm{t}} + \frac{1}{\rho_{\mathrm{t}}}\text{grad } p_{\mathrm{t}} = \frac{1}{\rho_{\mathrm{t}}}\vec{F}. \tag{2.9}$$

However, in acoustics only small deviations of the quantities are regarded leading to vertex free sound fields, i.e.

$$\text{rot}\vec{v}_{\mathrm{t}} = 0. \tag{2.10}$$

Since the sound field is vertex free, the velocity has a velocity potential Φ [8], i.e.

$$\vec{v}_{\mathrm{t}} = -\nabla\Phi, \tag{2.11}$$

$$\text{rot grad } \Phi = 0. \tag{2.12}$$

In addition, since the atmospheric quantities are much higher than the variable quantities (eq. 2.4) the following simplification is valid, i.e.

$$\frac{\partial \vec{v}}{\partial t} + \frac{1}{\rho_0}\text{grad } p = \frac{1}{\rho_0}\vec{F}. \tag{2.13}$$

Second, the continuity equation, which describes the conservation of the mass [8], is defined by, i.e.

$$\frac{\partial \rho_{\mathrm{t}}}{\partial t} + \text{div}(\rho_{\mathrm{t}}\vec{v}_{\mathrm{t}}) = 0. \tag{2.14}$$

Here again (eq. 2.4) is valid, justifying the following simplification, i.e.

$$\frac{\partial \rho}{\partial t} + \rho_0 \text{div } \vec{v} = 0. \tag{2.15}$$

Last, the change of state in gases can be assumed as adiabatic, since the state transitions have no energy exchange with the environment [8]. This involves the specific heat capacity at constant pressure and constant volume $\kappa = C_{\mathrm{p}}/C_{\mathrm{V}}$ i.e.

$$\left(\frac{p_{\mathrm{t}}}{p_0}\right) = \left(\frac{\rho_{\mathrm{t}}}{\rho_0}\right)^{\kappa}. \tag{2.16}$$

For gases a Taylor series can be developed, i.e.

$$\frac{p_0 + p}{p} = \left(\frac{\rho_0 + \rho}{\rho_0}\right)^{\kappa} = \left(1 + \frac{\rho}{\rho_0}\right)^{\kappa} \approx 1 + \kappa\left(\frac{\rho}{\rho_0}\right), \tag{2.17}$$

or in short,

$$p = \kappa\frac{p_0}{\rho_0}\rho. \tag{2.18}$$

With the speed of sound $c_{\text{air}} = \sqrt{\kappa p_0/\rho_0}$ the equation can be further simplified [8], i.e.

$$p = c_{\text{air}}^2 \rho. \tag{2.19}$$

In order to derive the wave equation, all three simplified versions of the acoustic fundamental equations are combined, i.e.

$$\frac{1}{c_{\text{air}}^2} \frac{\partial^2 p}{\partial t^2} - \nabla^2 p = 0. \tag{2.20}$$

This wave equations is the fundamental for calculations of wave propagation in the time domain. It includes the sound pressure p, the speed of sound c_{air} and is time dependent t. In addition, it includes spacial pressure distributions ∇ [8].

2.2 Thermoviscous acoustics

The previous section derived the well known wave equation which is assumed as lossless. However, in the field of duct acoustics a propagating wave is enclosed by a defined sound hard wall, which can introduce significant acoustic losses [56]. For a lossless model, the air molecules slip at the sound hard wall providing a lossless propagation. In order to introduce friction into the model the so called no slip boundary condition is used. This effect is well described by Swift [56]. In the following, the equations are derived in order to provide a deeper understanding of the physical reasons of this acoustical effect. Only the relevant derivations for this thesis are summarized and arranged in a convenient order.

Due to the boundary condition, the air molecules stick to the sound hard wall and can not move introducing friction [57]. This boundary effect is divided into thermal conductivity and viscous losses. They are described by the viscous δ_{v} and thermal δ_{t} penetration depth, which depend on the medias dynamic viscosity μ, the the circular number π, the frequency f, the ambient density ρ_0, the thermal conductivity k and the specific heat capacity at constant pressure c_{p} [56], i.e.

$$\delta_{\text{v}} = \sqrt{\frac{\mu}{\pi f \rho_0}}, \tag{2.21}$$

$$\delta_{\text{t}} = \sqrt{\frac{k}{\pi f \rho_0 C_{\text{p}}}}. \tag{2.22}$$

This boundary introduces a shear wave which is exponentially damped towards the center of the duct. This shear wave creates a viscous wave which oscillates perpendicular to the wall with a wavelength λ_{v} [57], i.e.

$$\lambda_{\text{v}} = 2\pi \sqrt{\frac{\mu}{\pi \rho_0 f}} = 2\pi \delta_{\text{v}}, \tag{2.23}$$

$$v(z) = v_0 e^{-\sqrt{\frac{\pi f \rho_0}{\mu}}(1+j)z}. \tag{2.24}$$

In addition, this creates a thermal wave with a wavelength λ_{t} of, i.e.

$$\lambda_{\text{t}} = 2\pi \sqrt{\frac{k}{\pi \rho_0 f C_{\text{p}}}} = 2\pi \delta_{\text{t}}, \tag{2.25}$$

$$T(z) = T_0 e^{-\sqrt{\frac{\pi f \rho_0 C_{\text{p}}}{k}}(1+j)z}. \tag{2.26}$$

The ratio between the viscous and thermal wavelength is called Prandlt number P_{r}. This value indicates which effect is dominant in a specific media [57], i.e.

$$\frac{\lambda_{\mathrm{v}}}{\lambda_{\mathrm{t}}} = \sqrt{\frac{\mu C_{\mathrm{p}}}{k}} = \sqrt{P_{\mathrm{r}}}. \tag{2.27}$$

In air this value is $P_{\mathrm{r}} = 0.8$ which indicates that both effects are important.

Next, Root's acoustic approximations are defined for thermoviscous acoustics. First the thermoviscous penetration depths are small compared to the wavelength [57], i.e.

$$\delta_{\mathrm{v}} \ll \lambda, \tag{2.28}$$
$$\delta_{\mathrm{t}} \ll \lambda. \tag{2.29}$$

Adding these effects to the equation of motion and neglecting the generation of vertexes yields an additional viscous contribution, i.e.

$$\rho \frac{\partial \vec{v}}{\partial t} = -\nabla p + \mu \nabla^2 \vec{v}. \tag{2.30}$$

Since the propagation of the wave is in z direction, the viscous wave oscillates perpendicular to the propagating wave (x and y direction) [57], the equation simplifies to

$$\rho \frac{\partial \vec{v}}{\partial t} = -\frac{dp}{dz} + \mu \left(\frac{\partial^2 v}{\partial x^2} + \frac{\partial^2 v}{\partial y^2} \right). \tag{2.31}$$

In the frequency domain, including the angular frequency ω and the imaginary number j, this equation yields

$$j\omega\rho\vec{v} = -\frac{dp}{dz} + \mu \left(\frac{\partial^2 v}{\partial x^2} + \frac{\partial^2 v}{\partial y^2} \right). \tag{2.32}$$

This is an ordinary differential equation which is zero at the center of the duct, since there is no friction with the inner walls of the duct. In contrast, at the walls the effect needs to be considered. As a result, the following boundary conditions are introduced [57], i.e.

$$\vec{v}(x = 0, y = 0) = 0, \tag{2.33}$$
$$\vec{v}(x \to \infty, y \to \infty) \neq 0. \tag{2.34}$$

Using these boundary condition yields

$$v = \frac{j}{\omega\rho} \left[1 - e^{-(1+j)y/\delta_{\mathrm{v}}} \right] \frac{dp}{dz}. \tag{2.35}$$

Now the viscosity influences the amplitude and the phase as well.

In order to express the no slip boundary condition, a function $\mathcal{F}(y)$ is needed. This function provides the property to go to zero outside of the boundary. This problem is solved using a spatial averaging over a cross-sectional area of the duct A_{duct}. Using the hydraulic radius $r_{\mathrm{h}} = A_{\mathrm{duct}}/\Pi_{\mathrm{duct}}$, which is the ratio between the ducts area and its perimeter Π_{duct}, this function can be written as [57],

$$\langle \mathcal{F} \rangle = \frac{1}{A_{\mathrm{duct}}} \int \mathcal{F} dA = \frac{1}{\Pi_{\mathrm{duct}} r_{\mathrm{h}}} \int_0^{r_{\mathrm{h}}} \mathcal{F}(y) \Pi_{\mathrm{duct}} dy, \tag{2.36}$$
$$\cong \frac{1}{r_{\mathrm{h}}} \int_0^{\infty} \mathcal{F}(y) dy. \tag{2.37}$$

In this case it yields

$$\frac{1}{r_{\mathrm{h}}}\int_0^\infty e^{-(1+j)\frac{y}{\delta_{\mathrm{v}}}}\,dy = (1-j)\,\frac{\delta_{\mathrm{v}}}{2r_{\mathrm{h}}}. \tag{2.38}$$

Applying this equation to the velocity yields

$$\langle v\rangle = \frac{j}{\rho\omega}\left[1-(1-j)\,\frac{\delta_{\mathrm{v}}}{2r_{\mathrm{h}}}\right]\frac{dp}{dz}. \tag{2.39}$$

Next, transforming the expression from a differential quotient into an difference quotient and solving for the pressure yields [57]

$$\Delta p = -\frac{j\omega\rho\Delta z/A}{1-(1-j)\,\delta_{\mathrm{v}}/2r_{\mathrm{h}}}v. \tag{2.40}$$

In the next step the thermal losses are added to the equation. Therefore, the temperature and the entropy is considered [57], i.e.

$$T_{\mathrm{t}} = T_0 + T, \tag{2.41}$$

$$s_{\mathrm{t}} = s_0 + s. \tag{2.42}$$

Expressing a thermal wave starts with the first law of thermodynamic [56]. This way, energy conservation can be applied to acoustics. The following quantities are taken into account for an open system, a small change in energy in the system $d\mathcal{E}$, heat Q, pressure-volume work $dW = pdV$, enthalpy $h_{\mathrm{ent}} = \epsilon + p/\rho$, energy per unit mass ϵ and the change in mass dM [57], i.e.

$$d\mathcal{E} = dQ - dW + \left(h_{\mathrm{ent}} + \frac{|\vec{v}|^2}{2}\right)dM. \tag{2.43}$$

The first law of thermodynamics can be applied for many mechanical applications such as the transformation of kinetic energy into potential energy and vice versa. However, as long as the energy conversion is reversible the equations are valid. When heat plays a role in the system, irreversible energy conversion occur. These effects can be mathematically described using entropy dS. In general, entropy describes the ratio between heat and the temperature. By adding $(ds)_{\mathrm{gen}}$ generated energy by irreversible processing can be described. This way heat and a flow of mass for an open system yields [57], i.e.

$$ds = \frac{dQ}{T} + s\cdot dM + (ds)_{\mathrm{gen}}. \tag{2.44}$$

Using this approach, a small fluid volume can be regarded when all molecules in this volume have the same temperature, pressure and velocity [57]. In these cases the first law of thermodynamics is

$$d\left(\epsilon + \frac{|\vec{v}|^2}{2}\right) = dq - dw. \tag{2.45}$$

This equation regards the internal energy per mass unit of the system ϵ, the kinetic energy per mass unit $|\vec{v}|^2/2$.

Next, the mass flow dM can be expressed using the mass-flux density $\rho\vec{v}$. In addition, all mechanical work only occur due to viscous shear forces which is indicated by the viscous-stress tensor σ [57]. The other mechanical work which is caused by pressure is taken into account by the term $h_{\mathrm{ent}}\rho$

$$\frac{\partial}{\partial t}\left(\rho\epsilon + \frac{1}{2}\rho|\vec{v}|\right) = -\nabla\left[-k\nabla T - \vec{v}\sigma + \left(\rho h_{\mathrm{ent}} + \frac{1}{2}\rho|\vec{v}|^2\right)\vec{v}\right]. \tag{2.46}$$

Combining the energy equation, the momentum equation and the continuity equation with thermodynamic quantities yields the general equation of heat transfer for fluids

$$\rho T\left(\frac{\partial s}{\partial t}+v\nabla s\right)=\nabla k\nabla T+(\sigma\nabla)\,\vec{v}. \tag{2.47}$$

In general, thermodynamic properties are divided in independent variables such as the pressure p and the temperature T and dependent variables such as ϵ, h_{ent}, s and ρ. However, for many applications it is useful to convert the dependencies to derive equations that show a relation between certain quantities [57]. In order to perform these conversions, the Maxwell relations are used. In this, case some of the derivations are assumed as zero which indicates that certain quantities are constant. First, $d\mathcal{E}=Tds-\rho dV$ can be expressed as

$$\left(\frac{\partial\mathcal{E}}{\partial s}\right)_V=T, \tag{2.48}$$

$$\left(\frac{\partial\mathcal{E}}{\partial V}\right)_S=-p. \tag{2.49}$$

Second, since the order of differentiating two independent variables is not important, the following expression can be derived

$$\frac{\partial}{\partial s}\left[\left(\frac{\partial\mathcal{E}}{\partial V}\right)_s\right]_V=\frac{\partial}{\partial V}\left[\left(\frac{\partial\mathcal{E}}{\partial s}\right)_V\right]_S. \tag{2.50}$$

Combining the two before mentioned equations (eq. 2.48) and (eq. 2.49) with (eq. 2.50) [57] yields

$$-\left(\frac{\partial p}{\partial s}\right)_V=\left(\frac{\partial T}{\partial V}\right)_S. \tag{2.51}$$

When divide the equation by the regarded volume V, the equation becomes

$$-\left(\frac{\partial p}{\partial s}\right)_V=\left(\frac{\partial T}{\partial(1/\rho)}\right)_s, \tag{2.52}$$

which can be further transformed into

$$\left(\frac{\partial p}{\partial s}\right)_\rho=\rho^2\left(\frac{\partial T}{\partial\rho}\right)_s. \tag{2.53}$$

The second Maxwell relation is derived [57] by using

$$d\epsilon=dq-dw=Tds-pd(1/\rho). \tag{2.54}$$

Using $h_{\text{ent}}=\epsilon+p/\rho$ results in

$$dh_{\text{ent}}=T\cdot ds+\frac{1}{\rho}dp. \tag{2.55}$$

In addition, enthalpy is derived with two different differentiating orders [57]

$$\frac{\partial}{\partial s}\left[\left(\frac{\partial h_{\text{ent}}}{\partial p}\right)_s\right]_p=\frac{\partial}{\partial p}\left[\left(\frac{\partial h_{\text{ent}}}{\partial s}\right)_p\right]_s. \tag{2.56}$$

Combining the two before mentioned equations (eq. 2.55) and (eq. 2.56) yields

$$\left(\frac{\partial T}{\partial p}\right)_s = -\frac{1}{\rho^2}\left(\frac{\partial \rho}{\partial s}\right)_p. \tag{2.57}$$

Last the two Maxwell relations are used allow a transformation from $h_{\text{ent}}(s,p)$ to $h_{\text{ent}}(T,p)$ [57]

$$ds = \left(\frac{\partial s}{\partial p}\right)_T dp + \left(\frac{\partial s}{\partial T}\right)_p dT = -\frac{1}{\rho^2}\left(\frac{\partial \rho}{\partial T}\right)_p dp + \left(\frac{\partial s}{\partial T}\right)_p dT. \tag{2.58}$$

By substituting for ds into the equation of general heat transfer for fluids, the following relation can be concluded

$$\frac{d}{dt}\rho C_{\text{p}} T + \rho C_{\text{p}} \frac{dT}{dz}\vec{v} = \frac{d}{dt}p + k\left(\frac{\partial^2 T}{\partial y^2} + \frac{\partial^2 T}{\partial x^2}\right). \tag{2.59}$$

Omitting the temperature wave in the direction of the acoustic wave propagation and transforming into the frequency domain yields [57]

$$j\omega\rho C_{\text{p}} T - j\omega p = k\frac{\partial^2 T}{\partial y^2}. \tag{2.60}$$

Adding the boundary conditions

$$T(y=0) = 0, \tag{2.61}$$

$$T(y\to\infty) \neq 0 \tag{2.62}$$

yields

$$T = \frac{1}{\rho C_{\text{p}}}\left[1 - e^{-(1+j)y/\delta_{\text{t}}}\right]p. \tag{2.63}$$

Using the spacial average $\langle \mathcal{F} \rangle$ this equation can be written as [57]

$$\langle T \rangle = \frac{1}{\rho C_{\text{p}}}\left[1 - (1-j)\frac{\delta_{\text{t}}}{2r_{\text{h}}}\right]p. \tag{2.64}$$

Similar to the viscosity, the thermal boundary influences the phase and the amplitude of the temperature wave. However, molecules which are further away from the boundary ($> \delta_{\text{t}}$) experiencing adiabatic temperature oscillations $T = \left(1/\rho C_{\text{p}}\right)p$. Here, the temperature and the pressure are in phase.

Next, a relation between the spatially averaged Temperature and the acoustic properties such as pressure is needed [57]. Therefore, the first order of state is used

$$\frac{p}{p_0} = \frac{T}{T_0} + \frac{\rho}{\rho_0}. \tag{2.65}$$

Since the density is affected by the boundary layer as well, the spatially average needs to be applied [57], i.e.

$$\langle \rho \rangle = -\frac{\rho_0}{T_0}\langle T \rangle + \frac{\rho_0}{p_0}p. \tag{2.66}$$

In addition, the spatial average is applied to the continuity equation in the frequency domain, i.e.

$$j\omega\langle \rho \rangle + \rho_0\frac{d\langle v \rangle}{dz} = 0. \tag{2.67}$$

Combining the equations and eliminating C_p yields [57]

$$j\omega \left[1 + (\gamma - 1)\,(1 - j)\,\frac{\delta_\mathrm{t}}{2r_\mathrm{h}}\right] \frac{p}{\gamma\rho_0} + \frac{d\langle v\rangle}{dz} = 0. \tag{2.68}$$

As a result, thermoviscous losses can be introduced to duct acoustics by adding the dynamic viscosity of the media μ, its thermal conductivity k and the hydraulic radius r_h. In addition, these effects are frequency dependent, which is indicated by the viscous penetration depth δ_v and the thermal penetration depth δ_t [57]. These lengths must be compared with the wavelength λ for estimating their effect on the losses inside the duct.

2.3 Analytic models

When it comes to simulating acoustic effects there are multiple methods. In general, all these models are suitable for certain problems. For instance the ratio between the wavelength and the regarded geometry is a crucial aspect in selecting the right model. In addition, these models have different computational costs.

2.3.1 Transmission lines

Duct acoustics is a special field in the acoustic section which is often used for car mufflers. In this case, the propagating wave is surrounded by a sound hard wall which guides the wave in one direction. At the end of the duct, there is a specific acoustic termination impedance. This impedance causes a reflection leading to a superposition of the incident wave and the reflected wave depending on the position inside the duct. This effect is called standing wave [58].

The one dimensional wave propagation can be described with the wave equation. The propagation direction is the z-axis [58]. In the time domain this yields

$$\frac{\partial^2 p}{\partial z^2} = \frac{1}{c_\mathrm{air}^2}\frac{\partial^2 p}{\partial t^2}, \tag{2.69}$$

or in the frequency domain the one-dimensional Helmholtz equation, which includes the wavenumber k_wave, i.e.

$$\frac{\partial^2 p}{\partial z^2} + k_\mathrm{wave}^2 p = 0. \tag{2.70}$$

At the end of the duct the wave is reflected with the reflection coefficient R [58]. This causes a superposition inside the duct at a specific position z, i.e.

$$p(z) = p_+\left(e^{-jk_\mathrm{wave}z} + R\cdot e^{jk_\mathrm{wave}z}\right) = p_+e^{-jk_\mathrm{wave}z} + p_-e^{jk_\mathrm{wave}z}. \tag{2.71}$$

The relation between the amplitude of the incident wave p_+ and the reflected wave p_- can be described as follows

$$p_+ \geq p_-, \tag{2.72}$$

$$R = \frac{p_-}{p_+}. \tag{2.73}$$

As a result, the reflected wave has the same or lower amplitude which depends on the acoustic termination impedance. In general, an acoustic impedance Z_{ac} can be described as a ratio between sound pressure and velocity [58]. This approach yields

$$Z_{\text{ac}} = \frac{p}{v} = \rho c_{\text{air}} \frac{e^{-jk_{\text{wave}}z} + Re^{jk_{\text{wave}}z}}{e^{-jk_{\text{wave}}z} - Re^{jk_{\text{wave}}z}}. \tag{2.74}$$

Applying two boundaries $z = 0$ and $z = l_{\text{duct}}$ results in the following acoustic termination impedance $Z_{\text{ac,t}}$

$$Z_{\text{ac,t}} = \frac{\rho c_{\text{air}}}{A_{\text{duct}}} \frac{1+R}{1-R}, \tag{2.75}$$

$$Z_{\text{ac,t}} = \rho c_{\text{air}} \frac{e^{-jk_{\text{wave}}l_{\text{duct}}} + Re^{jk_{\text{wave}}l_{\text{duct}}}}{e^{-jk_{\text{wave}}l_{\text{duct}}} - Re^{jk_{\text{wave}}l_{\text{duct}}}}. \tag{2.76}$$

This way the reflection coefficient can be described as follows [58], i.e.

$$R = \frac{Z_{\text{ac,t}} - \frac{\rho c_{\text{air}}}{A_{\text{duct}}}}{Z_{\text{ac,t}} + \frac{\rho c_{\text{air}}}{A_{\text{duct}}}}. \tag{2.77}$$

Combining the before mentioned equations (eq. 2.76) and (eq. 2.77) yields the acoustic impedance of the duct which depends on the acoustic termination impedance [58]

$$Z_{\text{ac}} = \frac{Z_{\text{ac,t}}\cos\left(k_{\text{wave}}l_{\text{duct}}\right) + j\left(\frac{\rho c_{\text{air}}}{A_{\text{duct}}}\right)\sin\left(k_{\text{wave}}l_{\text{duct}}\right)}{j\left(\frac{A_{\text{duct}}}{\rho c_{\text{air}}}\right)Z_{\text{ac,t}}\sin\left(k_{\text{wave}}l_{\text{duct}}\right) + \cos\left(k_{\text{wave}}l_{\text{duct}}\right)}. \tag{2.78}$$

Next, two cases can be derived from this point. First, a closed termination results in a total reflection. This causes a reflection coefficient of $R = 1$ and yields $Z_{\text{ac,t}} \ll \frac{\rho c_{\text{air}}}{A_{\text{duct}}}$. Second, the end of the duct can be open which leads to a termination impedance which equals to the duct impedance with $R = 0$ [58]. In addition, ρc can be defined as $Z_{\text{ac,0}}$, which is the acoustic characteristic impedance, i.e.

$$Z_{\text{open}} = \frac{jZ_{\text{ac,0}}\tan\left(k_{\text{wave}}l_{\text{duct}}\right)}{A_{\text{duct}}}, \tag{2.79}$$

$$Z_{\text{closed}} = \frac{-jZ_{\text{ac,0}}\cot\left(k_{\text{wave}}l_{\text{duct}}\right)}{A_{\text{duct}}}. \tag{2.80}$$

These two equations are sufficient when the diameter of the duct is small compared to the wavelength. In this case the wave propagation only occurs in one direction which is called plane wave propagation. However, when the diameter is increased, the resonance frequency of the duct is shifted. This effect can be added to the model by using an end correction [59]. The end correction extends the length of the duct depending on the radius of the duct. This way, the resonance frequency is adjusted according to the radius of the duct.

This effect can be explained by the pressure distribution at the end of an open duct [54]. The analytic model assumes an ideal reflection at the end of the duct, which reduces the pressure at the end to zero. However, not the entire acoustic wave is reflected into the duct. Parts are emitted into the free-field. Thus, the assumption of the impedance at the end of the duct needs to be adjusted. The last layer of the open duct can be compared with a piston which radiates sound. The pistons impedance introduces a different acoustic termination compared to the assumption of the transmission line model, which influences the wave propagation inside the duct. In general, the impedance of an acoustic piston Z_{piston} in the frequency domain is defined as [54]

$$Z_{\text{piston}} = \rho c_{\text{air}} \frac{1}{\pi r_{\text{duct}}^2} \left(R_{\text{piston}} 2 k_{\text{wave}} r_{\text{duct}} + j X_{\text{piston}} 2 k_{\text{wave}} r_{\text{duct}} \right). \tag{2.81}$$

This impedance considers the density ρ and speed of sound c_{air} of the fluid, the radius of the duct r_{duct} and the reactance X_{piston} and resistance R_{piston} of the piston [54]. When only the plane wave propagation is assumed, the lumped-element approximation ($k_{\text{wave}} r_{\text{duct}} \ll 1$) can be applied. This leads to the following reactance

$$X_{\text{piston}} = \frac{8 k_{\text{wave}} r_{\text{duct}}}{3\pi} \tag{2.82}$$

and resistance

$$R_{\text{piston}} = \frac{k_{\text{wave}}^2 r_{\text{duct}}^2}{2}. \tag{2.83}$$

This yields

$$Z_{\text{piston}} = \rho c_{\text{air}} \frac{k_{\text{wave}}^2}{2\pi} + \frac{j\omega\rho 8 r_{\text{duct}} / (3\pi)}{\pi r_{\text{duct}}^2}. \tag{2.84}$$

The right hand side of this equation defines an acoustic mass, and, thus, the acoustic load is not zero at the end of the duct. More precise, a small mass can be assumed as acoustic termination which extends the length of the duct [54]. For a flanged duct the follow additional length can be used

$$\Delta l_{\text{duct}} = \frac{8 r_{\text{duct}}}{3\pi} = 0.85 r_{\text{duct}}. \tag{2.85}$$

This leads to the following end correction for a flanged acoustic duct [54], i.e.

$$l_{\text{corrected}} = l_{\text{duct}} + 0.85 r_{\text{duct}}. \tag{2.86}$$

As a result, transmission lines can be used for duct acoustic, when the radius of the duct is small compared to the wavelength [54].

2.3.2 Lumped models

Lumped models are an efficient way to calculate harmonic physical effects. The principle is based on a physical system which is divided into integral elements, differential elements, which are often refereed to as energy storage systems and linear elements (dissipative elements). This way the frequency response including the phase information of a system can be easily derived in the frequency domain. In this case, the elements can be compared with electrical components such as an inductor, a capacitor or a resistor [8]. There are two analogies. The first analogy focuses on the same impedance of the electrical and acoustical circuit. This means that a mass can be mathematically compared to an inductor. For example an electrical current i_{el} is defined as a derivation of electrical charge Q_{el} and time t [8], i.e.

$$i_{\text{el}} = \frac{dQ_{\text{el}}}{dt}. \tag{2.87}$$

This can be compared with the velocity v and displacement x_{dis} in the mechanical domain [8], i.e.

$$v = \frac{dx_{\text{dis}}}{dt}. \tag{2.88}$$

Using Newtons law and the relation between current i_{el}, voltage u_{el} and the inductance L_{el} the following two equations show similarities in the electrical and mechanical domain [8], i.e.

$$F_{\text{mech}} = m_{\text{mech}} \frac{dv}{dt}, \tag{2.89}$$

$$u_{\text{el}} = L_{\text{el}} \frac{di_{\text{el}}}{dt}. \tag{2.90}$$

This thought can be extended for the other components leading to the follow analogy [8].

Table 2.1: First electromechanical analogy [8].

Mechanical domain	Electrical domain
Force	Voltage
Velocity	Current
Mass	Inductance
Compliance	Capacity
Friction	Ohmic resistor

In addition, there is a second analogy which focuses on the same circuit design of the electrical and mechanical system [8]. In this case, the relations between the mechanical and electrical domain are inverted compared to the first analogy. In order to reduce confusion between these two analogies, this work only uses the first one.
In acoustics this analogy can be used as well. However, this model is only valid when the geometry is small compared to the wavelength $< \lambda/10$ [8]. In this case, the thermoviscous relation between the velocity v and the pressure p for a linearized fluid in the frequency domain can be used [60], i.e.

$$\langle v \rangle = \frac{j}{\rho\omega} \left[1 - (1 - j) \frac{\delta_{\text{v}}}{2r_{\text{h}}} \right] \frac{dp}{dz}. \tag{2.91}$$

By exchanging the velocity v with the volume flow U and solving for the pressure Δp the following equation is valid

$$\Delta p = -\frac{j\omega\rho\Delta z / A_{\text{duct}}}{1 - (1 - j)\,\delta_{\text{v}}/2r_{\text{h}}} U. \tag{2.92}$$

This expression defines the change in pressure due to a small duct with the length Δz and the cross section A_{duct} [60]. By sorting the parameters the acoustic inductance L_{ac} and viscous resistance R_{v} can be extracted, i.e.

$$\Delta p = -\left(j\omega L_{\text{ac}} + R_{\text{v}} \right) U \tag{2.93}$$

and defined as

$$L_{\text{ac}} = \frac{\rho\Delta z}{A_{\text{duct}}}, \tag{2.94}$$

$$R_{\text{v}} = \frac{\mu\Pi_{\text{duct}}\Delta z}{A_{\text{duct}}^2 \delta_{\text{v}}}. \tag{2.95}$$

The inductance defines the acoustic mass which is defined by the geometry and the density of the media. In addition, the viscous resistance includes the viscous losses of the media. Not only the media properties are included but also the geometry of the diameter [60].
In addition, thermal losses can be added to the lumped model by using the continuity equation in combination with the thermal relaxation effect, i.e.

$$j\omega\left[1+(\gamma-1)(1-j)\frac{\delta_{\mathrm{t}}}{2r_{\mathrm{h}}}\right]\frac{p}{\gamma\rho_0}+\frac{d\langle v\rangle}{dz}=0. \tag{2.96}$$

This equation can be rewritten as a parallel circuit of a resistor and a capacitor [60], i.e.

$$\frac{1}{Z_{\mathrm{ac}}}=j\omega C_{\mathrm{ac}}+\frac{1}{R_{\mathrm{t}}}. \tag{2.97}$$

This includes the acoustic compliance C_{ac} and thermal resistance R_{t} [60], i.e.

$$C_{\mathrm{ac}}=\frac{V}{\gamma p_0}, \tag{2.98}$$

$$R_{\mathrm{t}}=\frac{2\gamma p_0}{\omega(\gamma-1)\Pi_{\mathrm{duct}}\delta_{\mathrm{t}}\Delta z}. \tag{2.99}$$

Combining all four components yields the following equivalent circuit for an acoustic duct (Figure 2.1).

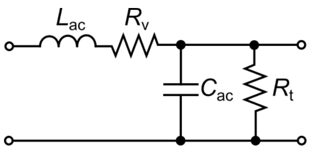

Figure 2.1: Equivalent circuit of an acoustic waveguide including thermoviscous losses [60].

As a result, lumped models can be used for modeling duct acoustic even including its thermal and viscous losses. However, this model is only valid, when the geometry of the duct in all dimensions is small compared to the wavelength [60].

2.4 Numerical models

2.4.1 Cascaded lumped models

Lumped models are suitable to solve duct acoustics when the geometry is smaller than the wavelength $< \lambda/10$. However, when the length of the waveguide is bigger than the wavelength, a single lumped element section is not valid anymore. In this case, the length of the waveguide needs to be considered in the model by cascading multiple sections of the duct (Figure 2.2). First, the duct is divided into small discs which represents the acoustic impedance $Z'_{\mathrm{ac}}(dz)$. This impedance includes the acoustic mass, compliance and the two resistances for thermal and viscous losses which are normalized on the length of the duct. Afterwards, multiple of these segments are cascaded which lead to a resulting impedance of the entire duct [60].

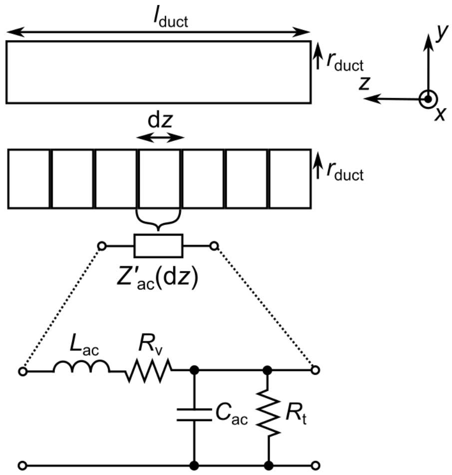

Figure 2.2: When the length l_{duct} of an acoustic duct is longer than the wavelength, the duct needs to be split into smaller sections with the length dz. Afterwards, the discretized impedances $Z'_{\text{ac}}(dz)$ are cascaded to calculate the entire impedance of the duct [60].

Since this semi analytic approach requires a discretization of the duct, a convergence analysis must be performed [61]. This analysis shows which discretization size, in numeric often refereed to as mesh size, is suitable for the given length to wavelength ratio. The objective is to reduce the mesh size until it has no effect on the resonance frequency f_{res} of the duct.
A duct with a constant radius of 5 mm, a length of 80 mm and a frequency around 40 kHz ± 1 kHz is used as an example. Since the length of the duct exceeds the wavelength of 8.575 mm, a discretization of the duct is needed. With a length of 80 mm and a minimal mesh size of $\lambda/10$ a minimal number of 94 is required.

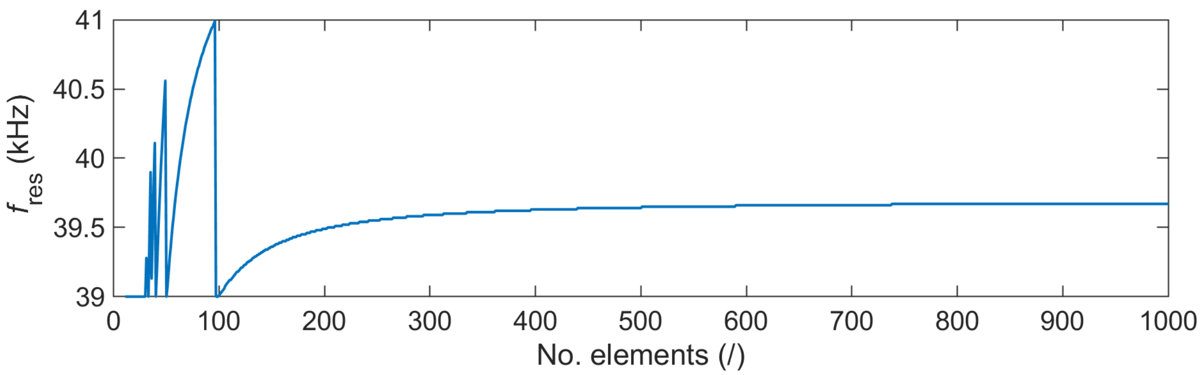

Figure 2.3: Convergence analysis of the cascaded lumped model with a length of 80 mm. The resonance frequency varies between 39 kHz and 41 kHz depending on the number of elements.

Between 11 and 97 elements the resonance frequency is not stable. This proofs the $< \lambda/10$ rule. After 97 elements the frequency stabilizes and after 592 elements the deviation is within 0.025%, and, thus, can be considered as being converged (Figure 2.3).
As a result, ducts with a length longer than the wavelength can be modeled with cascaded lumped models. However, the radius of the duct still must be smaller than the wavelength.

2.4.2 Finite element method

The finite element method (FEM) is a numerical model to solve differential equitations. This method is commonly used in the mechanics domain to solve for vibrations and displacements of mechanical problems. This way, arbitrary geometries can be simulated without analytic approximations of the geometry. In addition, this approach can be used in other domains such as the acoustic domain [53].
In general, the FEM in the acoustics domain can be split into two categories. First, time studies and second frequency studies. Time studies solve the wave equation in the time domain which is used to conduct transient analysis. On the other hand, frequency studies are used to conduct steady state analysis.

Time studies

The time studies analyze acoustic problems with a linear model in a compressible media. Only small acoustics pressure variation p are considered which are superposed with the atmospheric pressure p_0 [53]. In addition the model omits thermal and viscosity losses. The basic equations include the momentum equation, continuity equation and the energy equation [53], i.e.

$$\frac{\partial v}{\partial t} + (v \cdot \nabla) v = -\frac{1}{\rho} \nabla p + F, \tag{2.100}$$

$$\frac{\partial \rho}{\partial t} + \nabla \cdot (\rho v) = M, \tag{2.101}$$

$$\frac{\partial s}{\partial t} + \nabla \cdot (s v) = 0, \tag{2.102}$$

with M as a flow source and F as an external force [53].

This set of equations considers reversible and adiabatic processes, so no transport of heat or matter out of the system is performed. In addition, small signals are assumed leading to the following assumptions;

$$p \ll p_0, \tag{2.103}$$

$$\rho \ll \rho_0, \tag{2.104}$$

$$v \ll c_{\text{air}}. \tag{2.105}$$

In this work the Murata MA40S4S ultrasonic transducer is used. It has a maximum normal velocity of $1 \frac{m}{s}$ which validates the small signal assumption and linear acoustic.
From this equation set, the wave equation

$$\frac{1}{c_{\text{air}}^2} \frac{\partial^2 p}{\partial t^2} - \nabla \cdot (\nabla p) = 0 \tag{2.106}$$

can be derived.
In COMSOL Multiphysics [53] two source terms are added to the equation. These are monopole sources which represent mass sources Q_{m} and dipole sources representing force source q_{d} [53], i.e.

$$\frac{1}{\rho c_{\text{air}}^2} \frac{\partial^2 p}{\partial t^2} + \nabla \cdot \left[-\frac{1}{\rho} \left(\nabla p - q_{\text{d}} \right) \right] = Q_{\text{m}}. \tag{2.107}$$

When building an FE-model, boundary conditions are always necessary. There are two basic types. First, the Dirichlet boundary condition. This condition is in the applied science often refereed as the fixed boundary condition. It sets the boundary to a fixed value. In acoustics this can be a sound-soft boundary with the condition $p = p_0$. In contrast, a Neumann boundary condition sets the normal $\mathbf{n}$ of a quantity to a certain value. For instance, sound-hard walls can be modeled with this approach using $\mathbf{n} \cdot \nabla p = 0$ [62]. These two boundaries can be used for most interior acoustic problem. However, open acoustic problems need an additional boundary. Using just a Dirichlet boundary at the end of the calculation region would lead to reflections, and, thus, not representing an open acoustic field [8]. In this case a damping layer is needed. In COMSOL a perfectly matched layer is used to dampen all radiated sound [8], [53]. In order to introduce this damping layer, the local dependent part of the wave equation is multiplied by a damping component $\sigma(x)$, i.e.

$$\frac{\partial}{\partial x} \rightarrow \frac{1}{1 + j\frac{\sigma(x)}{\omega}} \frac{\partial}{\partial x}. \tag{2.108}$$

Since the damping coefficient is location dependent, the coordinate origin of the radiating wave and the coordinate origin of the PML needs to be the same.

COMSOL uses different solving methods for transient problems. However, a transient solver can be compared to a controller which can become instable when the controller parameters are not correct. In order to set up the solver the right way, it is important to calculate the Courant-Friedrichs-Lewy number (CFL). This number is defined as a quotient between time and location discretization, i.e.

$$\text{CFL} = \frac{c_{\text{air}} \Delta t}{\Delta x_{\text{mesh}}}. \tag{2.109}$$

COMSOL recommends for their transient solvers a CFL of 0.1 [53].

Frequency studies

For many studies, however, a transient analysis is time consuming and requires a lot random access memory (RAM). In many cases a frequency study offers multiple benefits compared to a transient analysis. For instance, the steady state for a given frequency can be calculated without the need of calculating multiple time steps. This way, the directivity pattern, and, thus, the halve power beam width and side lobe level can be easily calculated. As the name of the frequency study already indicates, it solves for the wave equation in the frequency domain also known as Helmholtz equation [53], i.e.

$$\nabla \cdot \left[-\frac{1}{\rho_{\text{c}}} \left(\nabla p - q_{\text{d}} \right) \right] - \frac{\omega^2 p}{\rho_c c_c^2} = Q_{\text{m}}. \tag{2.110}$$

In order to implement damping effects, the speed of sound c_{c} and the density ρ_{c} of the media is complex [53]. The real component has the material properties, whereas the imaginary part provides the damping of the propagating sound wave.
In order to further simplify a problem, it can be described in cylinder coordinates (r, z). This way, a three dimensional problem, which provides rotational symmetry, can be solved in the 2D space, i.e.

$$\frac{\partial}{\partial r} \left[-\frac{r}{\rho_{\text{c}}} \left(\frac{\partial p}{\partial r} - q_{\text{r}} \right) \right] + r \frac{\partial}{\partial z} \left[-\frac{1}{\rho_{\text{c}}} \left(\frac{\partial p}{\partial z} - q_{\text{z}} \right) \right] - \frac{k_{\text{eq}}^2}{\rho_c} rp = rQ_{\text{m}}. \tag{2.111}$$

including the equivalent wave number k_{eq}, which is calculated by using the order m of the wavenumber assumed for the rotational symmetry k_{m} [53], i.e.

$$k_{\text{eq}}^2 = \left(\frac{\omega}{c_{\text{c}}} \right)^2 - k_{\text{m}}^2, \tag{2.112}$$

$$k_{\text{m}} = \frac{m}{r}. \tag{2.113}$$

Thermoviscous acoustics

The before mentioned model provides a lossless analysis of acoustic phenomena. However, for the calculation of losses, thermoviscous effects need to be considered. For instance, the friction of the air molecules with other particles, a sound hard wall or losses in porous media introduce losses. The models which consider these effects can be divided in two categories. First, atmospheric damping and second losses in ducts [57].

COMSOL provides multiple models to account for these types of acoustic losses. In general, the small signal assumption is used in these models as well, including the total velocity v_t, total pressure p_t, total temperature T_t, total density ρ_t, total mechanical force $F_\text{mech,t}$ and total heat Q_t [53], i.e.

$$v_\mathrm{t} = v_0(x) + v(t,x), \tag{2.114}$$
$$p_\mathrm{t} = p_0(x) + p(t,x), \tag{2.115}$$
$$T_\mathrm{t} = T_0(x) + T(t,x), \tag{2.116}$$
$$\rho_\mathrm{t} = \rho_0(x) + \rho(t,x), \tag{2.117}$$
$$F_\text{mech,t} = F_\text{mech,0}(x) + F_\text{mech}(t,x), \tag{2.118}$$
$$Q_\mathrm{t} = Q_0(x) + Q(t,x). \tag{2.119}$$

The set of equations is based on the linearized Navier-Stokes equation, continuity equation and energy conversation. The quantities, which COMSOL solves the equations for, are the pressure variation p, the fluid velocity variation v and the acoustics temperature variation T. In order to stabilize the solver, the order of pressure should be one less than the order of the velocity [53]. As a result, the set of equations considers the viscous-stress tensor σ, external forces F, the specific heat capacity at constant pressure C_p, the isobaric coefficient of thermal expansion α_p, the velocity potential, the heat flux q_t and the velocity potential Φ, i.e.

$$\frac{\partial \rho}{\partial t} + \rho(\nabla v) = 0, \tag{2.120}$$
$$\rho\frac{\partial v}{\partial t} = \nabla \cdot \sigma + F, \tag{2.121}$$
$$\rho C_\mathrm{p}\frac{\partial T}{\partial t} - \alpha_\mathrm{p} T\frac{\partial p}{\partial t} = -\nabla \cdot q_\mathrm{t} + \Phi + Q. \tag{2.122}$$

When adding the energy equation to the motion of viscous compressible Newtonian fluid, the equations are extended with the unit matrix I, the bulk viscosity μ_B and the thermal conductivity k, i.e.

$$\sigma = -pI + \tau = -pI + \mu(\nabla v + (\nabla v)^T) - \left(\frac{2}{3}\mu - \mu_B\right)(\nabla \cdot v)I, \tag{2.123}$$
$$q = -k\nabla T, \tag{2.124}$$
$$\rho = \rho(p,T). \tag{2.125}$$

This way, the total stress tensor σ and the viscous stress tensor τ are defined [53]. In addition, the Fourier heat conduction law and the equation of state are implemented. The density is expressed in terms of pressure and temperature variations using Taylor expansion at steady state, i.e.

$$\rho = p\left[\frac{\partial \rho}{\partial p}\right]_{T_0} + T\left[\frac{\partial \rho}{\partial T}\right]_{p_0} = \rho_0(p\beta_\mathrm{T} - T\alpha_\mathrm{p}). \tag{2.126}$$

The two thermodynamic quantities are in square brackets defining the isobaric coefficient of thermal expansion α_{p} and isothermal compressibility β_{T}, i.e.

$$\beta_{\mathrm{T}} = \frac{1}{\rho_0}\left[\frac{\partial \rho_0}{\partial p}\right]_T = \frac{1}{K_{\mathrm{T}}} = \frac{\gamma}{\rho_0 c_{\mathrm{air}}^2} = \gamma\beta_s, \tag{2.127}$$

$$\gamma = \frac{C_{\mathrm{p}}}{C_{\mathrm{v}}} = \frac{K_{\mathrm{s}}}{K_{\mathrm{T}}}, \tag{2.128}$$

$$\alpha_{\mathrm{p}} = -\frac{1}{\rho_0}\left[\frac{\partial \rho_0}{\partial T}\right]. \tag{2.129}$$

With the isentropic bulk modulus K_{s}, the isothermal bulk modulus K_{T}, the heat capacity at constant volume C_{v}, the isentropic speed of sound c_{air}, the ratio of specific heats the adiabatic index γ, the isothermal compressibility β_{T}, the isentropic or adiabatic compressibility β_{s} and the thermal expansion α_{p} [53], i.e.

$$\beta_{\mathrm{s}} = \beta_{\mathrm{T}} - \frac{\alpha_p^2 T_0}{\rho_0 C_{\mathrm{p}}}, \tag{2.130}$$

$$\beta_{\mathrm{T}} = \gamma\beta_{\mathrm{s}}. \tag{2.131}$$

These quantities are derived using Maxwell relations. The isothermal compressibility and isobaric coefficient of thermal expansion can be expressed in terms of the speed of sound, i.e.

$$\beta_{\mathrm{T}} = \frac{\gamma}{\rho_0 c_{\mathrm{air}}^2}, \tag{2.132}$$

$$\alpha_{\mathrm{p}} = \frac{1}{c_{\mathrm{air}}}\sqrt{\frac{C_{\mathrm{p}}(\gamma-1)}{T_0}}. \tag{2.133}$$

Next, the thermal components are inserted into the governing equations and a linearization is performed [53], which yields to

$$j\omega v = \nabla\cdot\left[-pI + \mu(\nabla v + (\nabla v)^T) - (\frac{2}{3}\mu - \mu_B)(\nabla\cdot v)I\right], \tag{2.134}$$

$$j\omega\left(\frac{p}{p_0} - \frac{T}{T_0}\right) + \nabla\cdot v = 0, \tag{2.135}$$

$$j\omega(\rho_0 C_{\mathrm{p}} T - p) + v\cdot\nabla p_0 + \rho_0 C_{\mathrm{p}}(v\cdot\nabla T_0) = -\nabla\cdot(-k\nabla T) + Q. \tag{2.136}$$

This way, thermoviscous losses can be implemented in the frequency domain.

Losses in acoustic ducts

In duct acoustics, thermoviscous losses may occur due to the interaction between the media and the sound hard walls. In order to estimate whether this effect can be omitted, the Wormsley number Wo needs to be calculated [57]. This number is a ratio between the inertia force and the shear force. It is derived from the linearized Navier-Stokes equations for an oscillating flow. When this number is small (< 1) the velocity distribution has enough time to fully develop during each oscillation. This way, the velocity profile is parabolic and thermoviscous effects can be omitted. On the other hand, when the Wormsley number is big (> 10) thermoviscous effect will occur. One effect can be observed in the velocity profile showing overshoots near the sound hard walls. The Wormsley number depends on the frequency ω, the density of the media ρ, the radius of the duct r_{duct} and the viscosity μ. It can also be defined with the viscous penetration depth [57], i.e.

$$\text{Wo} = \sqrt{\frac{\omega \rho r_{\text{duct}}^2}{\mu}} = \sqrt{\frac{2 \cdot \pi \cdot 40\,\text{kHz} \cdot (5\,\text{mm})^2}{18.24 \cdot 10^{-6}\,\text{kg/m/s}}} = 587. \tag{2.137}$$

For this work frequencies around $40\,\text{kHz}$ are regarded. Thus, the Wormsley number indicates, that thermoviscous losses in the duct are significant. In order to implement these losses in a numerical model, the mesh must be refined near the rigid walls [57]. The two important quantities defining this additional mesh size are the viscous penetration depth δ_v and the thermal penetration depth δ_t. Therefore, the dynamic viscosity μ, the frequency f, the atmospheric density ρ_0, the thermal conductivity and the specific heat capacity at constant pressure C_p are needed, i.e.

$$\delta_\text{v} = \sqrt{\frac{\mu}{\pi f \rho_0}} = \sqrt{\frac{18.24 \cdot 10^{-6}\,\text{kg/m/s}}{\pi \cdot 40\,\text{kHz} \cdot 1.188\,\text{kg/m}^3}} = 11\,\mu\text{m}, \tag{2.138}$$

$$\delta_\text{t} = \sqrt{\frac{k}{\pi f \rho_0 C_\text{p}}} = \sqrt{\frac{0.026\,\text{W/K}}{\pi \cdot 40\,\text{kHz} \cdot 1.188\,\text{kg/m}^3 \cdot 1000\,\text{J/kg/K}}} = 13\,\mu\text{m}. \tag{2.139}$$

These quantities depend on the frequency and the density of the media. They differ in viscosity and thermal conductivity and specific heat capacity. In addition, the Prendtl number defines whether both or just one of the losses are significant. This number is defined as a ration between the viscous penetration depth and the thermal penetration depth [57]. Since $P_\text{r} = 0.7$, both effects need to be implemented, i.e.

$$P_\text{r} = \frac{\mu C_\text{p}}{k} = \frac{18.24 \cdot 10^{-6}\,\text{kg/m/s} \cdot 1000\,\text{J/kg/K}}{0.026\,\text{W/K}} = 0.7. \tag{2.140}$$

Meshing thermoviscous acoustics increases the computational load. In addition to the mesh size of at least 10 elements per wavelength, the thermal and viscous penetration depth must be meshed with the same discretization ratio [53]. This leads to a refined boundary mesh, and, thus, an increased element number. At a frequency of $40\,\text{kHz}$ this penetration depth is $13\,\mu\text{m}$ [Figure 2.4(a, b)].

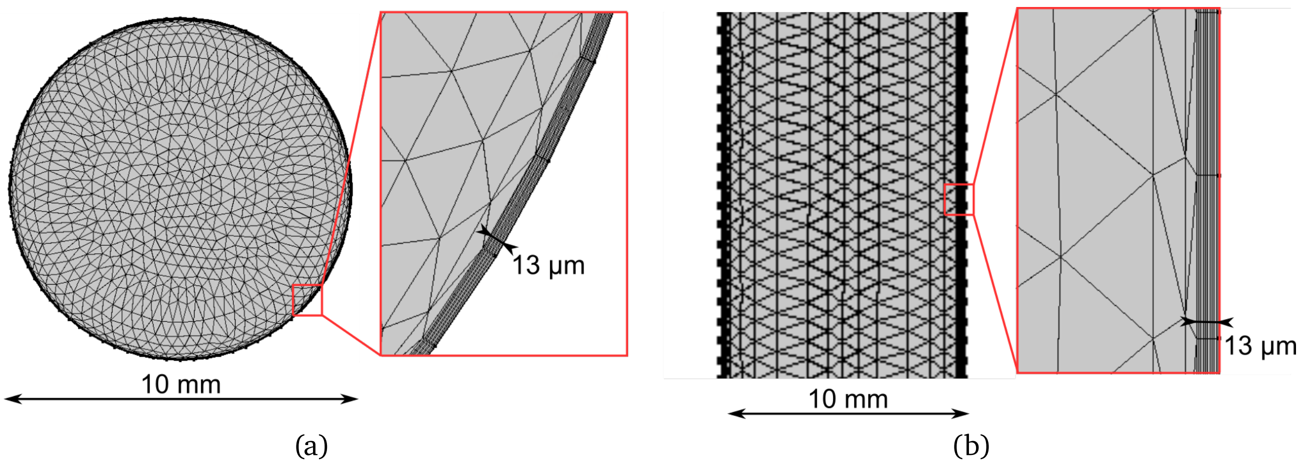

Figure 2.4: Mesh refinement at the boundary of the cross-section of a round duct (a) and along the wave propagation (b) [53].

Since thermoviscous losses increase the calculation time, COMSOL provides additional analytic approximations of these losses [53]. This way, a mesh refinement near the boundary can be avoided. In these models the losses at the boundary are applied to the entire bulk. This way, the losses are homogenized in the entire duct. Thus, the geometry of the duct influences which narrow region model is suitable.

The first model provided by COMSOL is used for very narrow circular ducts. Here, the diameter of the duct is smaller compared to the viscous penetration depth. Thus, this model is not applicable for this work [53].

The second model is used for slits, circular ducts, rectangular ducts and equilateral triangular ducts. However, this model is only applicable when the frequency of the duct is below the cut-off frequency, which is not the case for this work [53].

The last model is called wide duct approximation. It is used when the diameter of the duct is bigger compared to the thermoviscous penetration depth. In addition, the duct needs a constant diameter or a small variation in diameter. The losses are implemented in the duct using complex values for the speed of sound and the density of the media [53].

This model assumes shear forces at the walls which where defined by Blackstock [54]. First, a drag force F_{drag} is defined which occurs due to the viscous effect at the walls of the duct, i.e.

$$F_{\mathrm{drag}} = -\mu v_{\mathrm{y}}|_{\mathrm{y}=0}. \tag{2.141}$$

In order to implement this boundary condition as a general approach, the Laplace transformation is used for the velocity [54]. This way, an arbitrary force function F_{arb} is implemented, i.e.

$$v(y, s_{\mathcal{L}}) = \int_0^{\infty} v(y,t) e^{-s_{\mathcal{L}} t} dt. \tag{2.142}$$

In the same way, the force function can be defined as a Laplace transformation. In addition the boundary needs to vanish at $y = 0$. This way, the force variation donates to the mainstream yielding

$$v(y, s_{\mathcal{L}}) = -\frac{F_{\mathrm{arb}}(s_{\mathcal{L}})}{\rho s_{\mathcal{L}}} \left(1 - e^{-\sqrt{s_{\mathcal{L}}/\mu y}}\right). \tag{2.143}$$

Substituting the velocity in the drag force yields [54]

$$F_{\mathrm{drag}} = \sqrt{\frac{\mu}{s_{\mathcal{L}}}}. \tag{2.144}$$

Next, using a convolution the transformation can be inverted, i.e.

$$F_{\mathrm{drag}} = \sqrt{\frac{\mu}{\pi}} \int_0^t \frac{F_{\mathrm{arb}}(x, t-\tau)}{\sqrt{\tau}} d\tau. \tag{2.145}$$

The derived drag force is implemented in the forces of the momentum equation yielding [54]

$$\rho \frac{Dv}{Dt} + F = \frac{4}{2r_{\mathrm{h}}} \sqrt{\frac{\mu}{\pi}} \int_0^t \frac{F_{\mathrm{arb}}(x, t-\tau)}{\sqrt{\tau}} d\tau. \tag{2.146}$$

Afterwards, the formulation is linearized and the dynamic viscosity is exchanged by taking the Prendtl number into account. This leads to an implementation of thermal effects for the model, i.e.

$$\sqrt{\mu} \to \sqrt{\mu}\left(1 + \frac{\gamma - 1}{\sqrt{P_{\mathrm{r}}}}\right). \tag{2.147}$$

This leads to [54]

$$v_{\mathrm{x}} - \frac{1}{c_{\mathrm{air}}^2} v_{\mathrm{t}} = B \int_0^{\infty} v_{\mathrm{x}}(x, t-\tau) \frac{d\tau}{\sqrt{\tau}}, \tag{2.148}$$

with

$$B = \frac{4}{2r_\mathrm{h}}\sqrt{\frac{\mu}{\pi\rho}}\left(1+\frac{\gamma-1}{\sqrt{P_\mathrm{r}}}\right). \tag{2.149}$$

This way, a formulation is derived which includes the geometry of the duct defined by the hydraulic radius r_h, the media properties speed of sound c, the dynamic viscosity μ, the density ρ the ratio of specific heat γ and the Prendtl number of the fluid P_r [54]. As a result, a complex wave number k_c can be expressed which includes the losses in its imaginary part

$$k_\mathrm{c} = \frac{\omega}{c_\mathrm{air}}\frac{1}{\sqrt{1-B\sqrt{\frac{\pi}{j\omega}}}} \cong \frac{\omega}{c_\mathrm{air}}\left(1+\frac{B}{2}\sqrt{\frac{\pi}{j\omega}}\right). \tag{2.150}$$

As already mentioned, this model is valid when the diameter of the duct is bigger then the viscous penetration depth and small enough that thermoviscous losses occur inside the duct. For a duct with a diameter of $10\,\mathrm{mm}$ at a frequency of $40\,\mathrm{kHz}$ the needed quantities can be compared with the penetration depth, i.e.

$$\delta_\mathrm{v} \ll r_\mathrm{h} \ll \frac{c^2}{\omega^2\delta_\mathrm{v}}, \tag{2.151}$$

$$0.011\,\mathrm{mm} \ll 5\,\mathrm{mm} \ll 169.5\,\mathrm{mm}. \tag{2.152}$$

Since both assumptions are valid, this analytic model for thermoviscous effects can be used in this work.

Atmospheric losses

Beside acoustic losses inside the waveguide, atmospheric damping can be implemented in COMSOL Multiphysics as well. The model used in this case is based on the ansi standard S1.26-2014 [63], [64]. This model is a quasi-empirical approach, and, thus, is valid under specific circumstances. For instance, the altitude is defined between $0\,\mathrm{km}$ and $20\,\mathrm{km}$, the frequency range is from $40\,\mathrm{Hz}$ to $100\,\mathrm{kHz}$ and the molar concentration of water needs to be between 0.05% and 5%. In addition, this model is based on empirical algorithms for single frequency acoustics, also refereed to as pure-tone acoustics. Last, it is suitable for attenuations less then $50\,\mathrm{dB}$.

In general, this model uses a complex wavenumber k_c to implement acoustic losses. The atmospheric attenuation coefficient is defined as α_atm [63], i.e.

$$k_\mathrm{c} = \frac{\omega}{c_\mathrm{air}} - j\alpha_\mathrm{atm}. \tag{2.153}$$

Next, the frequency dependency of this attenuation factor is defined. This attenuation considers atmospheric absorption which is induced due to molecular interaction. This interaction can be split into classical absorption α_cl, rotational relaxation α_rot and vibrational relaxation $\alpha_\mathrm{vib,i}$ for the gas components [63], i.e.

$$\alpha_\mathrm{atm} = \alpha_\mathrm{cl} + \alpha_\mathrm{rot} + \sum_\mathrm{i}\alpha_\mathrm{vib,i}. \tag{2.154}$$

The classical absorption includes losses due to viscosity, thermal conductance and diffusion. The relaxation is the process of heat induced motion of air molecules. When a wave propagates through air, the molecules adopt to their new state of equilibrium. This way, acoustic energy of the wave is transformed into inner energy of the molecules. This process is called relaxation. The time needed for achieving the new equilibrium is called relaxation time and the reciprocal is called relaxation frequency [63]. It depends on the properties of the fluid. For instance, humidity does not effect dissipation of acoustic energy but increases the relaxation frequency.

The classical and rotational attenuations are combined to the first quasi-empirical formulation, i.e.

$$\alpha_{\mathrm{cl}} + \alpha_{\mathrm{rot}} = 1.6 \cdot 10^{-10} \sqrt{\frac{T}{T_{\mathrm{r}}}} f^2 \frac{p_{0\mathrm{r}}}{p_0}. \tag{2.155}$$

Here, the frequency f and the atmospheric pressure p_0 and temperature T are implemented. In addition, a reference temperature T_{r} of 293.15 K and a reference pressure $p_{0\mathrm{r}}$ of 1 atm is added to the equation [63].

The losses due to relaxation are defined the following way:

$$\alpha_{\mathrm{vib,i}} = [(\alpha_{\mathrm{i}}\lambda)_{\mathrm{max}}] \frac{f}{c} \frac{2 f_{\mathrm{r,i}} f}{f_{\mathrm{r,i}}^2 + f^2}. \tag{2.156}$$

The vibrational relaxation contributes from the different gas components of the fluid. Thus, the maximal absorption per wavelength of all components donates to the equation. In addition, the two dominant relaxation frequencies are from oxygen f_{rO} and nitrogen f_{rN} [63]. The speed of sound is derived from the atmospheric temperature with

$$c_{\mathrm{air}} = 343.2\mathrm{m/s} \sqrt{\frac{T}{T_{\mathrm{r}}}}. \tag{2.157}$$

As a result the entire attenuation in decibel per meter is

$$\begin{aligned} \alpha_{\mathrm{atm}}(f) = 8.686 f^2 \left(1.84 \cdot 10^{-11} \frac{p_{0\mathrm{r}}}{p_0} \sqrt{\frac{T}{T_{\mathrm{r}}}} \right) \\ + \left(\sqrt{\frac{T_{\mathrm{r}}}{T}} \right)^5 \left[0.01275 \cdot e^{-2239.1/T} \left(\frac{f_{\mathrm{rO}}}{f_{\mathrm{rO}}^2 + f^2} \right) + 0.1068 \cdot e^{-3352/T} \left(\frac{f_{\mathrm{rN}}}{f_{\mathrm{rN}}^2 + f^2} \right) \right]. \end{aligned} \tag{2.158}$$

Both, the relaxation frequency of oxygen and nitrogen are based on empirical models as well, i.e.

$$f_{\mathrm{rO}} = \frac{p_0}{p_{0\mathrm{r}}} \left\{ 24 + \left[\frac{4.04 \cdot 10^4 h_{\mathrm{water}} (0.02 + h_{\mathrm{water}})}{0.391 + h_{\mathrm{water}}} \right] \right\}, \tag{2.159}$$

$$f_{\mathrm{rN}} = \frac{p_0}{p_{0\mathrm{r}}} \sqrt{\frac{T_{\mathrm{r}}}{T}} (9 + 280 h_{\mathrm{water}})\, e^{-4.17\left(\sqrt[3]{\frac{T_{\mathrm{r}}}{T}} - 1\right)}. \tag{2.160}$$

Next, the influence of the molar concentration of water h_{water} is implemented using [63]

$$h_{\mathrm{water}} = h_{\mathrm{rel}} \frac{p_{0\mathrm{r}} 10^V}{p_0}. \tag{2.161}$$

This way, the relative humidity h_{rel} is included to the equation. Last, the exponent V is defined which mainly depends on the temperature T and the triple-point isotherm temperature $T_{\mathrm{triple}} = 273.16$ K [63], i.e.

$$
\begin{aligned}
V = {} & 10.79586\left(1-\frac{T_{\text{triple}}}{T}\right) - 5.02808\cdot\log_{10}\left(\frac{T}{T_{\text{triple}}}\right) \\
& +1.50474\cdot 10^{-4}\left[1-10^{-8.29692\left(\frac{T}{T_{\text{triple}}}-1\right)}\right] \\
& +0.42873\cdot 10^{-3}\left[-1+10^{4.76955\left(1-\frac{T_{\text{triple}}}{T}\right)}\right] \\
& -2.2195983.
\end{aligned}
\tag{2.162}
$$

2.4.3 Boundary element method

The FEM is a useful tool for multiphysical simulations. For instance, the electro mechanical transduction of a loudspeaker can be combined with the acoustics domain, which allows for convenient simulations. However, free-field calculations are often not efficient especially for ultrasound. These problems need a fine mesh compared to the air volume, since the aspect ratio between the air volume and the ultrasound wavelength is large. Additionally, in 3D simulations these problems scale with $\mathcal{O}^3$. These free-field calculations can be solved much faster with the boundary element method (BEM) [53]. In contrast to the FEM, only the surface of a 3D problem is meshed instead of the entire volume leading to increased calculation speeds compared to the FEM. On the other hand, the BEM always has a fully populated system matrix instead of a sparse matrix. As a result, the selection of the right simulation tool always needs to be validated for the specific problem.

The BEM is based on the Helmholtz equation, and, thus, just considers the frequency domain, i.e.

$$
-\frac{1}{\rho_{\mathrm{c}}}\nabla^2 p_{\mathrm{t}} - \frac{k_{\mathrm{eq}}^2}{\rho_{\mathrm{c}}} p_{\mathrm{t}} = 0, \tag{2.163}
$$

$$
k_{\mathrm{eq}}^2 = \left(\frac{\omega}{c_{\mathrm{c}}}\right)^2. \tag{2.164}
$$

The speed of sound c_{c} and the density ρ_{c} can be defined as complex values. This way atmospheric attenuation can be implemented. Last, the BEM needs to solve singular integrals near the boundaries leading to the usage of iterative solvers [53].

2.5 Comparison of models

In the prior chapter multiple methods of modeling acoustic problems where explained. However, all models are suitable for different cases. In this chapter theses models are compared and their applicability for duct acoustics at 40 kHz is discussed.

First, a general comparison between analytic and numerical models is conducted. Afterwards, the FEM and BEM are compared. In all cases deviations and model limits are calculated and discussed.

2.5.1 Comparison between analytic and numeric models

In general, analytic models for acoustic problems assume concentrated components such as point masses [8]. This leads to models with no geometrical dimensions since all dimensions are small compared to the

wavelength. When the propagation of the wave in one direction can not be omitted, these models can be extended to a one dimensional model. For example lumped models can be cascaded or a transmission line model can be used. In both cases, plane wave propagation in one direction is assumed [60].
However, the other two dimensions need to be small compared to the wavelength. In the context of duct acoustics, the diameter d_{duct} of the duct is used as a criteria. When $d_{\text{duct}} < 0.586\lambda$, a plane wave propagation inside the duct can be assumed [65]. Since the investigated waveguide geometry consists of tapered ducts there are two cases which need to be considered.
First, the input section of the waveguide has a diameter of $10\,\text{mm}$. With a frequency of $40\,\text{kHz}$ an analytic model would not be sufficient because the plane wave propagation is not valid (Figure 2.5). On the other hand, the output section of the waveguide has a diameter of 3.4 mm where a plane wave propagation is valid again.

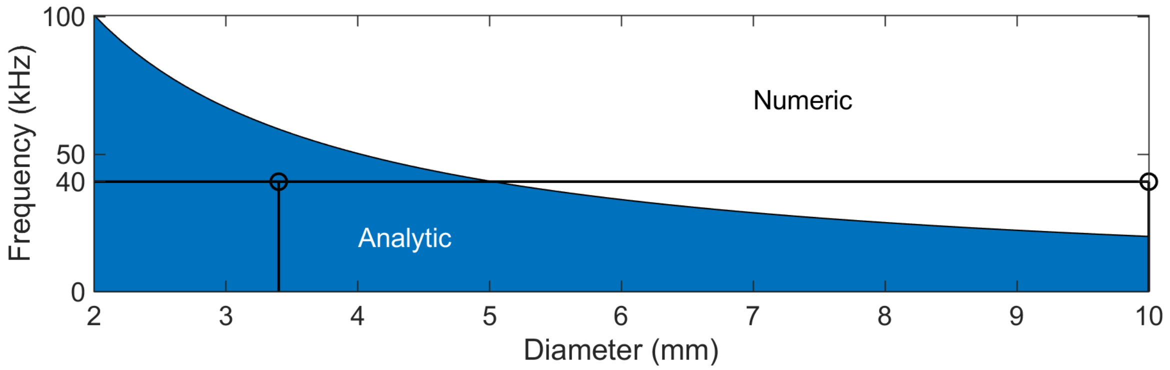

Figure 2.5: Analytic models assume a plane wave propagation which is valid when the diameter of the duct is small compared to the wavelength $d_{\text{duct}} < 0.586\lambda$. Otherwise, a numerical models must be used.

The validity of a duct acoustics model depends on the ratio between the wavelength and the diameter of the duct. This relation is now further analyzed in detail on a 80-mm-long duct. First, a numerical model is set up using the FEM with a closed end of the duct. Second, the same model is used with an open end structure. In the end, both results are compared with the theory of transmission lines to see when the wavelength diameter ratio is sufficient for an analytic model. End correction is implemented as well.
The FE-analysis consists of a 2D rotational model of the duct with a PML used as a damping layer for the open field calculations. The acoustics are based on the Helmholtz equation leading to a lossless model. A normal velocity is used as an acoustic excitation. In addition, all walls are assumed as ideal sound hard walls. In order to compare the models, the acoustic impedance is normalized and plotted on a logarithmic scale. This way, the resonance frequencies can be clearly compared.
The duct with a closed end has in the frequency range of $35\,\text{kHz}$ to $45\,\text{kHz}$ four resonance maxima. Both the analytical and numerical model show the same resonances. In addition, the resonances are independent of the diameter of the duct between $0.2\,\text{mm}$ and $2\,\text{mm}$ (Figure 2.6). Both models have singularities at the resonances, since both models are lossless. The non-existing influence of the radius on the impedance can be explained with the wavefront inside the waveguide. Independent of the radius of the waveguide, the wave is a plane wave simulated for each case [Figure 2.7(a)]. This shows, that the analytic model is valid as long the wave is a plane wave.

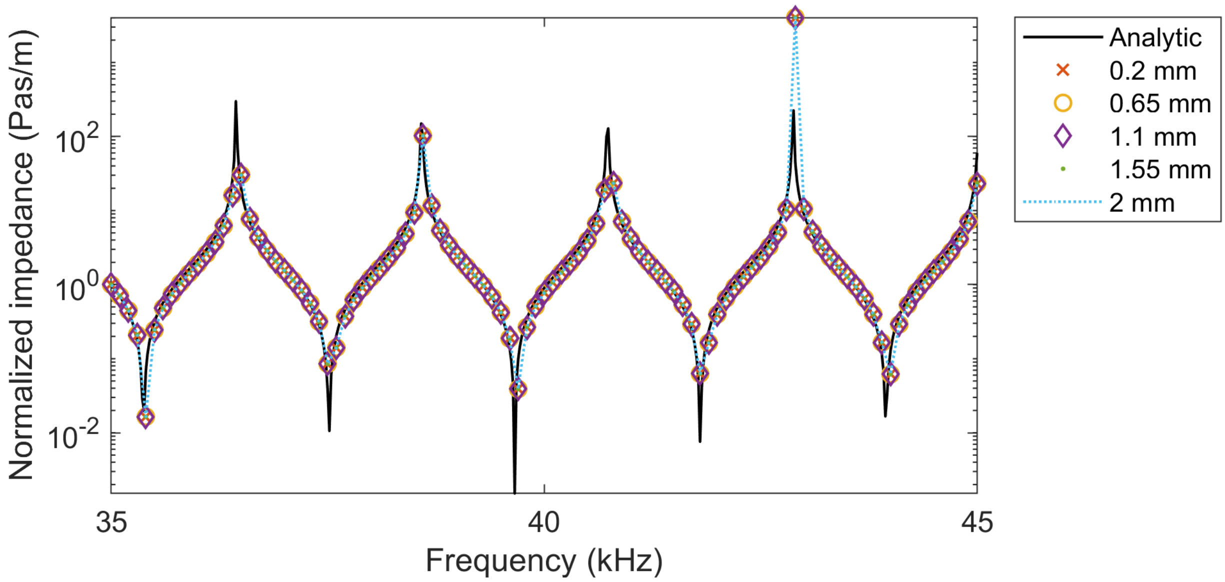

Figure 2.6: Comparison between an analytic model and FE-model of a 80 mm duct with a closed end with varying diameter of the duct d_{duct}.

In contrast to the closed duct, the open duct has a clear diameter dependency (Figure 2.8). The wave inside the duct is still a plane wave comparable to the wave propagation inside the closed duct. On the other hand, the pressure distribution at the end of the opened duct is not plane anymore, which causes a frequency shift [Figure 2.7(b)]. This effect already occurs with a diameter of 0.65 mm which represents a ratio of $\lambda/13.2$ at a frequency of 40 kHz. In order to take this effect into account, an end correction is conducted. This model extends the length of the duct by a small amount which depends on the redius of the duct $\Delta l_{\text{duct}} = 0.85 r_{\text{duct}}$.

In addition to the frequency shift, the Q-factor changes with the diameter of the duct as well. Resonances in an acoustic duct are based on the superposition of an emitted sound wave and a reflected sound wave at the end of the duct. This causes high Q-factors since this superposition leads to ideal destructive or positive interference in a lossless model, which alters the standing wave ratio $s_{\text{ratio}} = \frac{1+|R|}{1-|R|}$. However, since the wavefront is not an ideal plane anymore, the interference is blurred due to the bended wavefront. Thus, the superposition is spatially filtered which can be compared to a low pass filter in imaging processing.

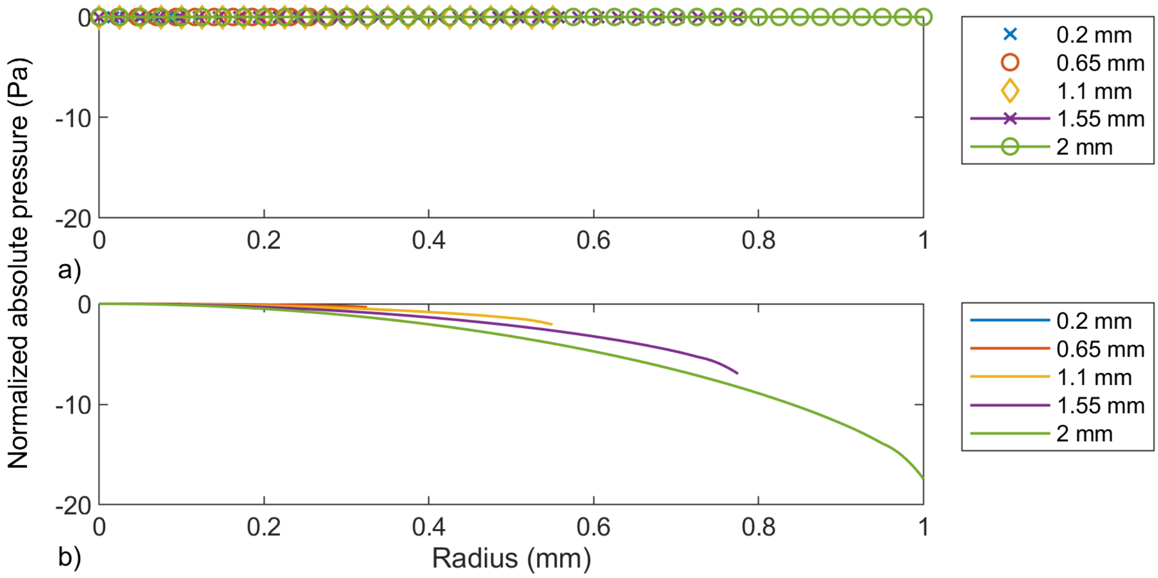

Figure 2.7: The wavefront at the output of a duct with closed end (a) is independent of the diameter of the duct. In contrast, a duct with an open end (b) has a clear diameter dependency.

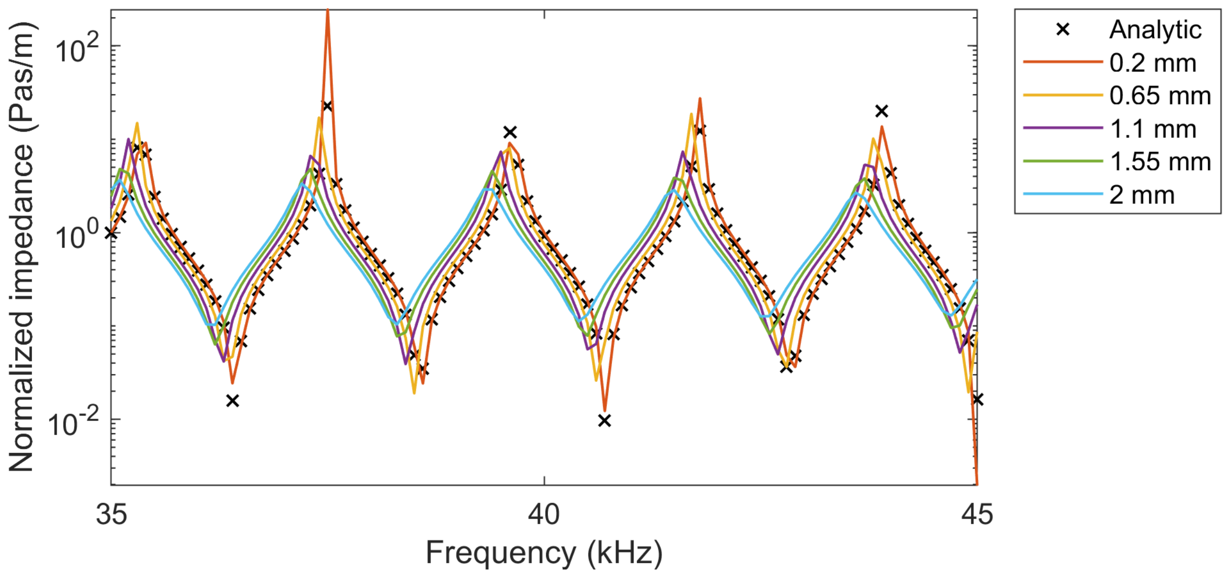

Figure 2.8: Comparison between an analytic model and FE-model of a 80 mm duct with an opened end with varying diameter.

Last, the analytic and numerical models are compared with the correct diameters which are investigated in this work. This consists of an analysis with a diameter of the duct of 3.4 mm, which is the output diameter of the tapered duct in the waveguide. In addition, the input diameter of 10 mm is also analyzed. The analytic model also considers the end-correction of the duct and losses which are implemented in the complex value of the speed of sound.

When the duct has a diameter of 3.4 mm, there is a significant difference between the numeric and analytic method. The resonance frequencies differ by 400 Hz (Figure 2.9). Whether the end correction nor the added imaginary part of $j2.3$ m/s to the speed of sound compensate for this effect.
The same results can be observed for a duct with a diameter of 10 mm and an added imaginary part of $j8$ m/s. In addition, at a frequency above 41.4 kHz higher modes occur in the duct. This effect can only be solved by a two dimensional model such as the FEM. The analytic model only considers one direction, and, thus, omits wave propagation in other directions besides the length of the duct.

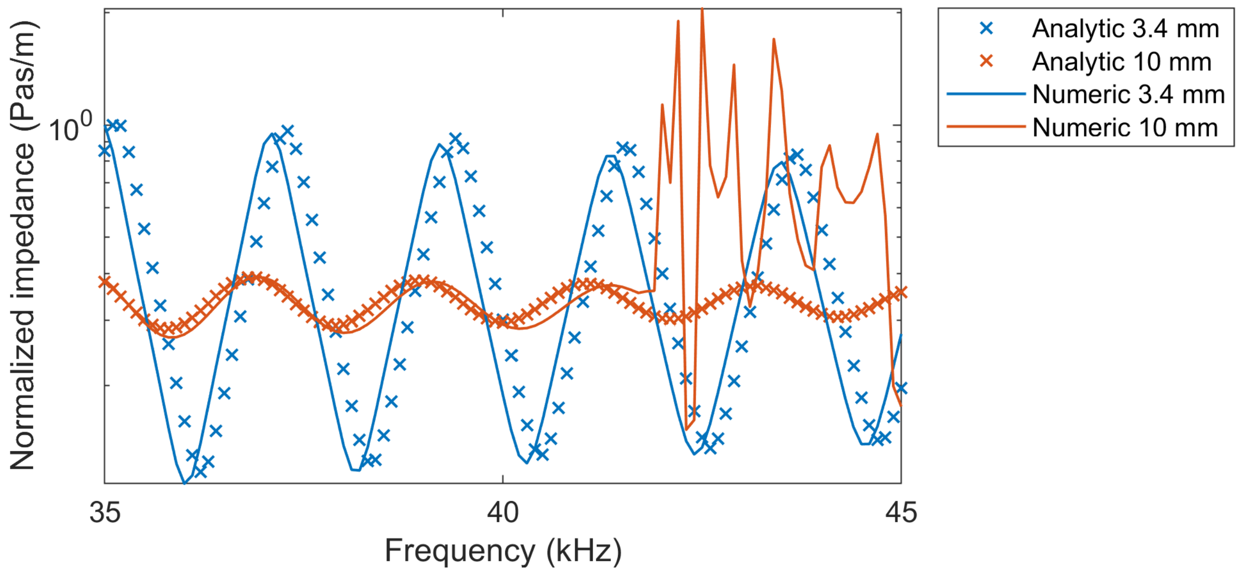

Figure 2.9: The FEM and an analytic model are compared for a open duct with a diameter of 3.4 mm and 10 mm.

2.5.2 Comparison between FEM and BEM

COMSOL provides two methods for simulating acoustic fields with numerical approaches. First, the FEM and second the BEM. In this chapter, these two methods are compared regarding the directivity of an acoustic duct. The duct is 80 mm long and has a diameter of 8 mm. In both cases the acoustic excitation is conducted using a normal velocity of 1 m/s. The FEM uses the rotational symmetry of this system including an PML for free-field calculations [Figure 2.10(a)]. The BEM uses two symmetry planes (yz and xz) [Figure 2.10(b)]. This way, only a quarter of the model needs to be calculated saving computational resources. Both models are based on the Helmholtz equation omitting thermoviscous losses.

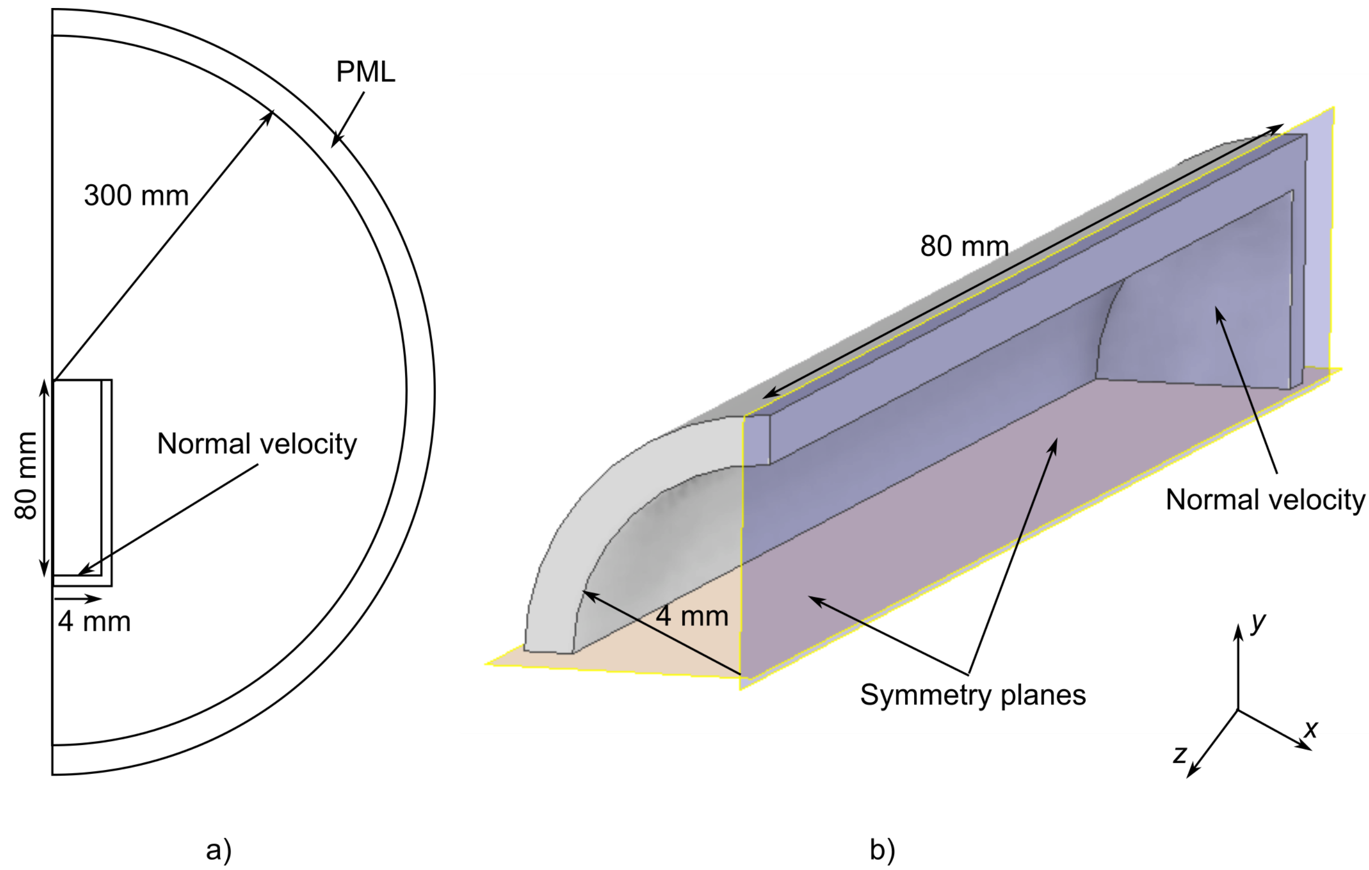

Figure 2.10: The comparison between the FEM (a) and the BEM (b) is conducted on a 80 mm-long duct with a diameter of 8 mm. Both simulations are used to calculate the directivity pattern in the free-field.

First, the dependency of the mesh size on the SPL at a distance of 300 mm is investigated. Both models start with a mesh size of 10 mm and end with 0.4 mm. As a convergence criteria a deviation of ± 0.1 dB was defined. This convergence criteria was used because it is a good compromise between the calculation time and since a deviation of ± 0.1 dB is irrelevant for most ultrasonic applications.
The FEM starts converging with a mesh size of 2.4 mm which is $\lambda/3.5$. In this range, the SPL deviation is only ± 0.1 dB (Figure 2.11). In contrast, the BEM already converges with a mesh size of 4 mm which is $\lambda/2.1$. COMSOL recommends a mesh size for the FEM of at least $\lambda/10$ and for the BEM $\lambda/4$ [53]. Both recommendations can be confirmed for the given duct geometry.

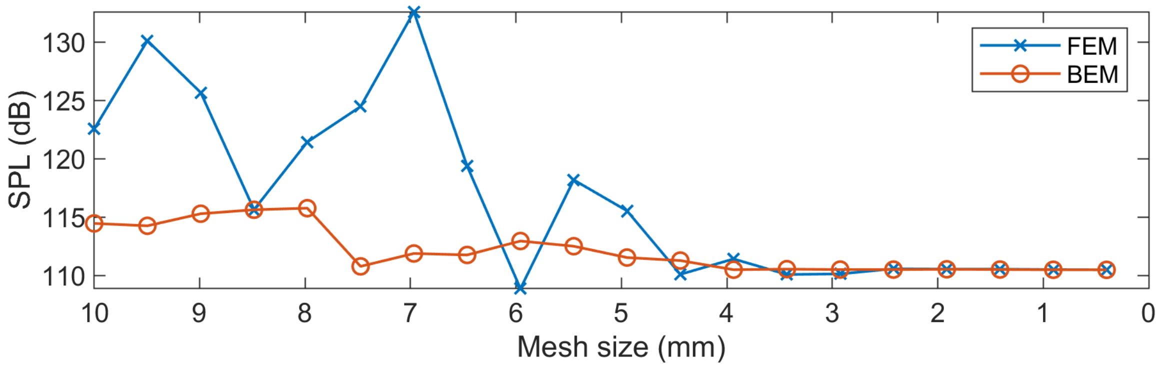

Figure 2.11: The directivity of the FEM and the BEM are compared at a distance of $300\,\mathrm{mm}$ (a). They only differ by $0.05\,\mathrm{dB}$ (b).

Next, the calculated directivity of both methods are compared at a distance of $300\,\mathrm{mm}$. In general, both simulations are in good agreement [Figure 2.12(a)]. In addition, the two directivities were subtracted for a better comparison. The maximal deviation of the two models is $\pm 0.05\,\mathrm{dB}$ [Figure 2.12(b)]. These simulations were conducted on an intel i7-5820K with $3.3\,\mathrm{GHz}$, with no over-clocking and $32\,\mathrm{GB}$ RAM. The FEM finished the calculations within $87\,\mathrm{s}$. In contrast, the BEM already finished the calculations in $7\,\mathrm{s}$. The main difference in performance can be explained with degrees of freedom (DoF) solved in both cases. Since the FEM solved for the entire air volume, it needs 1342264 DoF for this calculation. On the other hand, the BEM only needed 471 DoF for the same problem. In addition, the BEM needed less RAM with $4.8\,\mathrm{GB}$ compared to the FEM with $6.5\,\mathrm{GB}$.

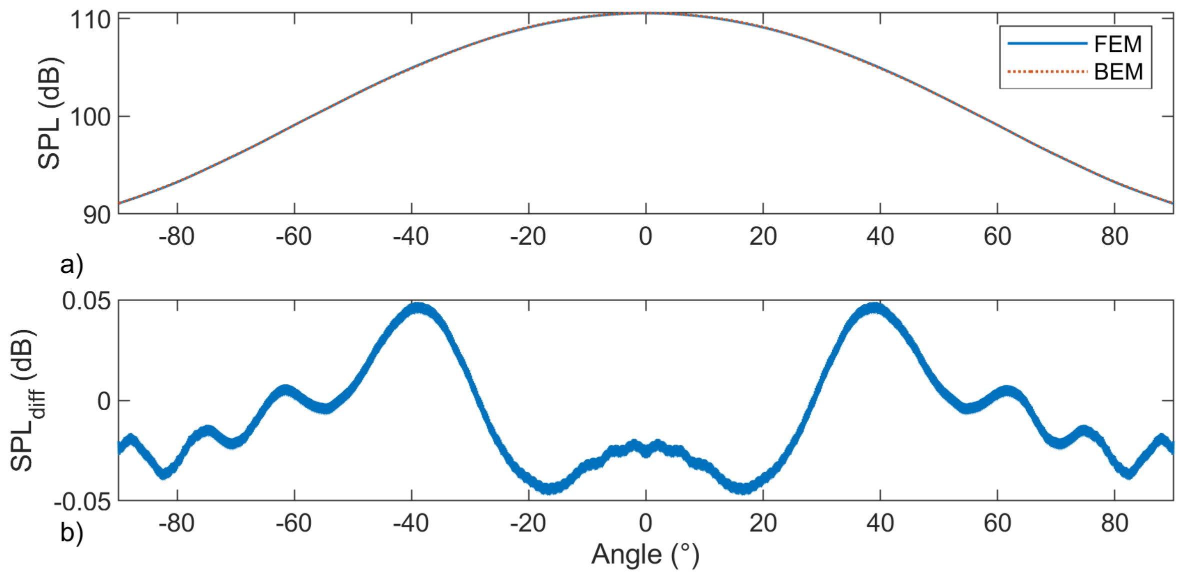

Figure 2.12: Comparison of the directivity of the FEM and the BEM at a distance of $300\,\mathrm{mm}$ (a). Both results are in excellent agreement with a maximal deviation of $\pm 0.05\,\mathrm{dB}$ (b).

Next, two different methods to implement thermoviscous losses in an acoustic duct are compared. As

reference, a lossless model is used which is based on the Helmholtz equation. The simulations where conducted using the FEM in COMSOL, since the BEM in COMSOL provides atmospheric damping but no thermoviscous losses inside a duct.
The thermoviscous losses are implemented in two ways. First, an analytic model is used which derives the losses on the hydraulic diameter. Second, a fully thermoviscous model is used which regards the no slip boundary condition. The simulations were conducted with an 80-mm long duct and a diameter of 8 mm. As discretization of the elements for the pressure quadratic Lagrange elements were used in all three cases. In order to investigate the effect of the no slip boundary condition a cut line at 20 mm inside the duct is defined. This way, the velocity distribution perpendicular to the wave propagation can be investigated. The lossless model shows a constant velocity across the diameter of the duct. Its value is 0.6571 m/s. The analytic loss has also no diameter dependency. Its value is slightly below the lossless model of 0.6549 m/s. In contrast, the fully thermoviscous model shows a clear dependency of the diameter (Figure 2.13). In the center the velocity reaches a value of 0.6585 m/s which is slightly above the other two models.

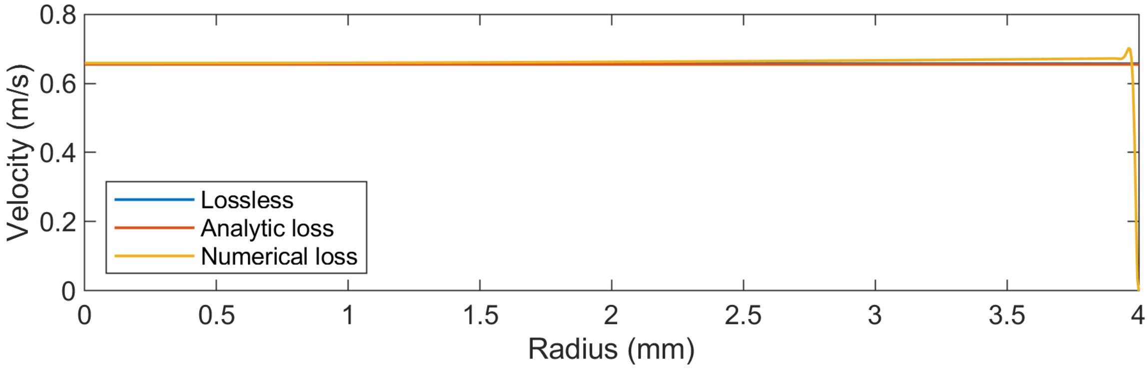

Figure 2.13: The velocity distribution inside a 80 mm-long duct at 20 mm. The numerical losses show a clear radius dependency due to the no slip boundary condition.

Next, the influence of the loss models on the SPL at a distance of 100 mm is investigated. This effect is analyzed in dependency of the length of the duct, since a longer duct provides a bigger friction area between the sound hard wall and the air molecules. This way the total loss and the length dependent loss can be extracted.
The lossless model has a maximal SPL of 119.6 dB. A length dependency can not be observed with this model because the maxima are periodic. The analytic losses decrease the SPL to a value of 118.8 dB (Figure 2.14). In addition, these losses depend on the length of the duct with 0.0078 dB/mm. This result is in good agreement with the fully thermoviscous model. The numerical losses calculated a maximum SPL of 118.8 dB and a length dependency of 0.0077 dB/mm as well. All three models are space efficient with 3.28 GB for the lossless and analytic loss models and 3.58 GB for the fully thermoviscous model. However, since the thermoviscous model need a finer boundary mesh inside the duct in order to account for the no slip boundary condition, this model needs 172351 DoF. In contrast, the lossless and analytic loss model only need 143246 DoF. Due to the increased DoF, the fully thermoviscous model needs 885 s whereas the lossles and analytic loss model only need 517 s.

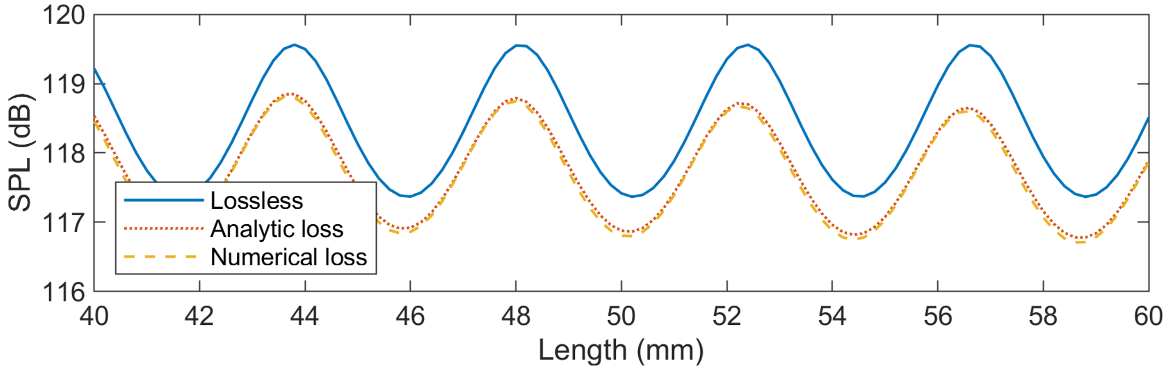

Figure 2.14: The length of an acoustic duct is varied. The lossless model shows multiple maxima and minima. Both loss models are in good agreement and have a lower out SPL compared to the lossless model.

Last, the stiffness matrices of the BEM, the lossless FEM and the fully thermoviscous FEM are compared. This way the prior results can be understand in further detail.
In general, the main difference between the BEM and the FEM is the arrangement of the stiffness matrices. The BEM has a dense matrix, since all knots interact with each other. This effect is needed because the wave propagation of the point sources superpose even at the boundary conditions. Thus, all boundaries are connected with each other.
In contrast, an FEM has a sparse stiffness matrix. In the FEM only the neighbored knots are interacting with each other. This is implemented by using elements such as Lagrange polynomials with a certain order. The matrix always has a main diagonal because these are the entries of the knots themselves.
When adding thermoviscous acoustics to the FE-analysis, additional entries occur in the stiffness matrix due to energy conservation. These terms solve for the velocity and the temperature of the wave in addition to the pressure.

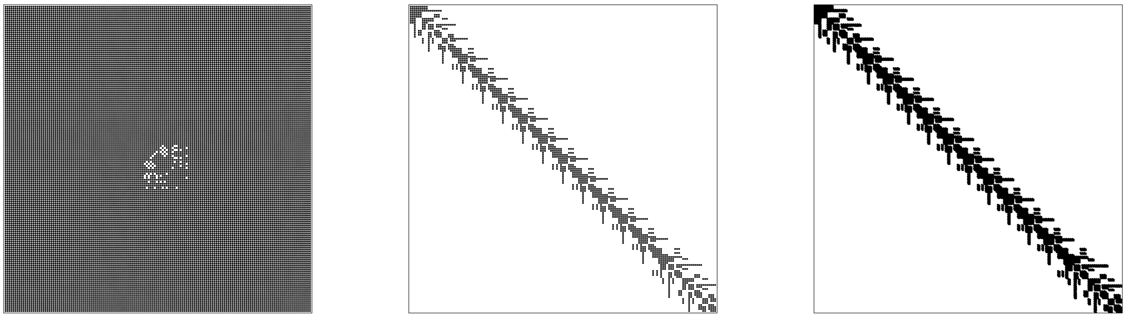

(a) (b) (c)

Figure 2.15: Stiffness matrices of BEM (a), FEM Pressure acoustics (b) and FEM thermoviscous acoustics (c).

In conclusion, the comparison between the different duct acoustics models yield the following results. Analytic models are not applicable for this work, since the diameter is in the range of the wavelength. Thus, higher modes can occur, which can not be solved with an analytic model. Not even a straight duct can be described with this model in this work. Thats why, the focus of this work will be the use of numeric models which are the FEM and the BEM. Both methods provide versatile methods for analyzing the wave propagation inside and outside the duct. In addition, thermoviscous effects can be implemented using analytic approximations, since the deviation between the fully numeric losses and the analytic losses for the given geometry are minor.

3 Methods for validating the numerical model

Every numerical model needs to be validated with an experimental setup. This way, it is possible to ensure the right assumptions were made, especially the boundary conditions are a crucial aspect of each simulation. Therefore, an acoustic goniometer setup was built to offer convenient and versatile acoustic characterizations for air-coupled ultrasonic phased arrays.

This work was done in cooperation with Dr. Axel Jäger. He conducted the selection of the components and the design of the mechanics. In this work, the software was implemented in Labview (Austin, Texas) and it was characterized regarding the noise floor and its measurement accuracy. Additionally, the work flow of the measurements were optimized for versatile measurements including transmit, receive and pulse-echo characterization. In addition, the complexity of the software was reduced to allow for a convenient handling of the setup. Furthermore, the setup provides communication with the software PAIUS for controlling the prototype phased arrays, which was developed in cooperation with Gianni Allevato.

3.1 Previous setup

One of the first volumetric setups to characterize air-coupled ultrasonic transducers was built by Hoffmann et al. [66]. This way, it is possible to quantify an acoustic pressure field in three dimensions. The research group used a calibrated measurement microphone (Type 4138, Brüel & Kjaer, Denmark) which can be freely positioned within a volume of $1\,\mathrm{m}^3$ [Figure 3.1(a)].

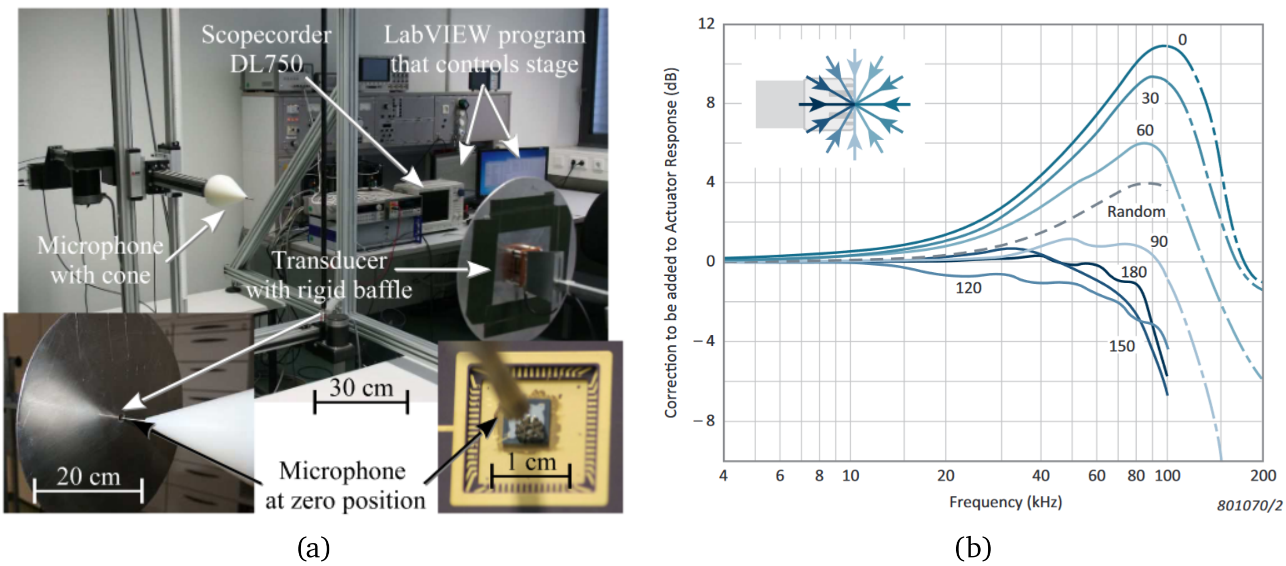

Figure 3.1: Volumetric acoustic characterization setup from BTU Cottbus [66] (a). The sensitivity of the calibrated measurement microphone depends on the angle of the incident wave (b) [67].

In addition, the microphone is equipped with a pre-amplifier (Type 2670, Brüel & Kjaer, Denmark). All axis are from (BAHR Modultechnik, Luhden, Germany and Phytron-Elektronik GmbH, Grobenzell, Germany) and provide a positioning accuracy of $50\,\mu\text{m}$. These axes move the microphone in cartesian coordinates. This way, the front of the microphone and the transducers front are in parallel, thus the angular orientation to the transmitter needs to be corrected [Figure 3.1(b)].

Since the walls of the measurement environment were not treated with acoustic absorbers, time windows were defined. Within this time, the sound wave propagates towards the microphone. Afterwards, the wave is scattered in the measurement environment. After the decay time, no superpositions occur between a second wave, emitted by the device under test, and the reflected wave. However, this only allows for characterization of transducers in burst mode.

The signals of the microphone were captured with an oscilloscope (Scopecorder DL750 with module 701251, Yokogawa Electric Corporation, Tokyo, Japan). The overall noise floor of this system is $73\,\text{dB}$. Furthermore, the measurement uncertainty is $\pm 2\,\text{dB}$ and the setup needs $1\,\text{s}$ per measurement point. This setup was used to test different boundary conditions of ultrasonic transmitters [68].

3.2 Updated measurement setup

In general, closed rooms influence every type of sound and vibration. The so called room modes produce significant resonances due to reflections at walls. However, these effects need to be treated when it comes to acoustic transducer characterization. Since the characteristics of the transducer must not superpose with the room characteristics, reference rooms are used for measurements. For this reason, an anechoic chamber was the perfect choice for this purpose. As the name indicates, the walls, ceiling and the floor are covered in acoustic absorbers which reduce acoustic reflections. This allows for free wave propagation in this room which can be compared with free-field measurements. Consequently, these rooms are used for transmit and receive characterization of acoustic transducers and directivity measurements.

The key feature of anechoic chambers are the cones on the walls which have high absorption coefficients that are realized in three steps. First, the material of the cones is dense mineral wool. This way, the poro-acoustic effect can be used to attenuate sound waves. When a sound wave penetrates the wool, the acoustic energy is transformed into vertexes which reduce the sound pressure of the reflected wave. Second, multiple cones are used to benefit from multi reflections between the cones. This introduces interference absorption at the walls. Third, multiple Helmholtz resonators are located between the cones and the wall. These cavities can be compared to a voltage divider in electrical circuits. The acoustic energy retains in these resonators, which further reduces the pressure of the reflected wave. In addition, anechoic chambers are mechanical decoupled from the foundation of a building with mechanical dampers. This reduces low frequency vibrations such as traffics [8].

The university of technology Darmstadt also provides an anechoic chamber. It was built in 1976. The anechoic chamber has a size of $7.7\,\text{m} \times 5.22\,\text{m} \times 5.8\,\text{m}$ (Figure 3.2).

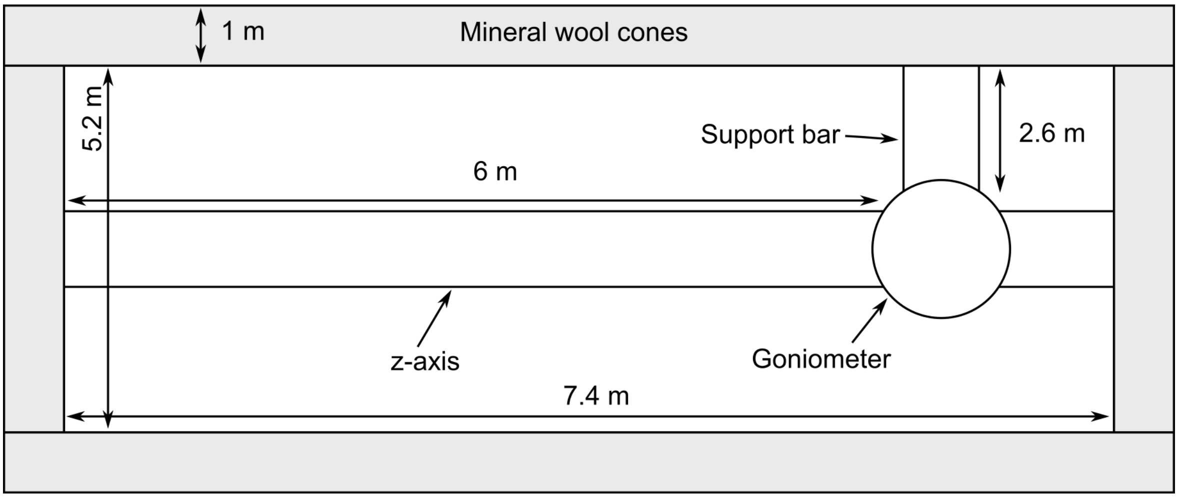

Figure 3.2: Anechoic chamber from top view.

The walls are covered with mineral wool cones (Grünzweig + Hartmann AG, Germany) covered in synthetic resin. These cones have a length of 1000 mm and a base area of 240 mm $\times$ 240 mm. They have a cut off frequency of 70 Hz. Above 100 Hz, the reflection coefficient is below 0.01. The room is decoupled from the foundation with steel springs. By using this room, the device under test can be characterized in burst mode and with continuous signals.

In the updated measurement setup the same measurement microphone is used. The advantage of this capacitive microphone is the linearity of its frequency response. In general, capacitive transducers have two significant resonances. The lower resonance frequency mainly depends on the main capacity of the transducer and its termination resistor. The second frequency is the upper resonance frequency, which is defined by the mass and compliance of the entire system. However, the sensitivity is independent of the frequency between the two resonances [8].

In contrast to the prior measurement system, the orientation of the microphone is tilted by $90°$. This way, the angular correction of the microphones sensitivity is not longer needed [Figure 3.1(b)]. In addition, the sensitivity has a flatter linearity around the 40 kHz range in comparison with $0°$. The comparison between these two measurement setups was conducted by Golinske. As a result, the $90°$ tilting of the microphone improves the measurements of the directivity and increases the resemblance with ideal simulations [36].

The previous measurement system is based on a cartesian coordinate system [Figure 3.3(a)]. The updated setup uses a polar system [Figure 3.3(b)] which is based on a goniometer setup [69]. This system reduces the size of the components, otherwise the components introduce vibrations due to its movements. On the other hand, the coordinates need to be transformed for post processing, i.e.

$$\begin{pmatrix} x \\ y \\ z \end{pmatrix} = R_{\text{gon}} \begin{pmatrix} -\cos(\alpha_{\text{gon}})\sin(\beta_{\text{gon}}) \\ \sin(\alpha_{\text{gon}})\sin(\beta_{\text{gon}}) \\ \cos(\beta_{\text{gon}}) \end{pmatrix}. \tag{3.1}$$

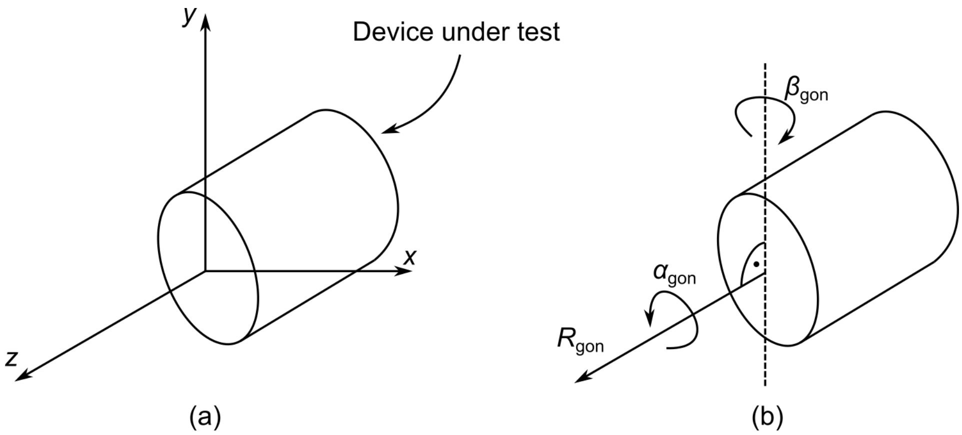

Figure 3.3: The first volumetric measurement system was based on cartesian coordinates (a). The updated setup is based on a polar system (b).

The assembly of the goniometer is divided into four steps. First, the β_{gon}-axis is mounted onto an item profile [Figure 3.4(a)]. This builds the base for the entire system. An adapter plate is used for a 285 mm-long item profile. This extension serves as a mount for the device under test. Second, an aluminum fork is mounted onto the back of the item profile [Figure 3.4(b)]. This fork has a hole at the top which allows for a better cable management. Third, the α_{gon}-axis is mounted to the top of the fork [Figure 3.4(c)]. This axis has a hole in the center as well supporting better cable management. A cage, made of aluminum profiles, is mounted onto the top axis. This cage offers possibilities for additional cable management and mounting holes for a rigid baffle. Last, the baffle is screwed onto the cage [Figure 3.4(d)]. Besides defining the boundary condition of the ultrasonic transducer, it serves as a mechanical connection between the transducer and the cage.

This measurement setup consists of moving parts. For this reason, caution is advised to protect the components. First, the rotation of the β_{gon}-axis is limited to $\pm 55°$. As a result, a collision between the rigid baffle and the microphone can be avoided. This protection is implemented in the software at two points. The first is right after the reading of the desired coordinates and the second is before sending the coordinates to the axis.

Second, special effort was done regarding the cable management. This protects the electric motors of the axis from mechanical damage and the loss of steps. The cables leading to the device under test direct along the α_{gon}-axis. In addition, the cables are fixed with velcro tape. Last, stationary cables are hidden in the slits of the item profiles of the entire structure.

The specifications of the axis are summarized in the following table:

Table 3.1: Specifications of the axis

Axis	Name	Accuracy	Range
α_{gon}	PI M-061.2S	$\pm 0.00051°$	$0°$ - $360°$
β_{gon}	PI M-062.2S	$\pm 0.001°$	$\pm 55°$
R_{gon}	Isel MS135HT2	± 0.2 mm	0 m - 6 m

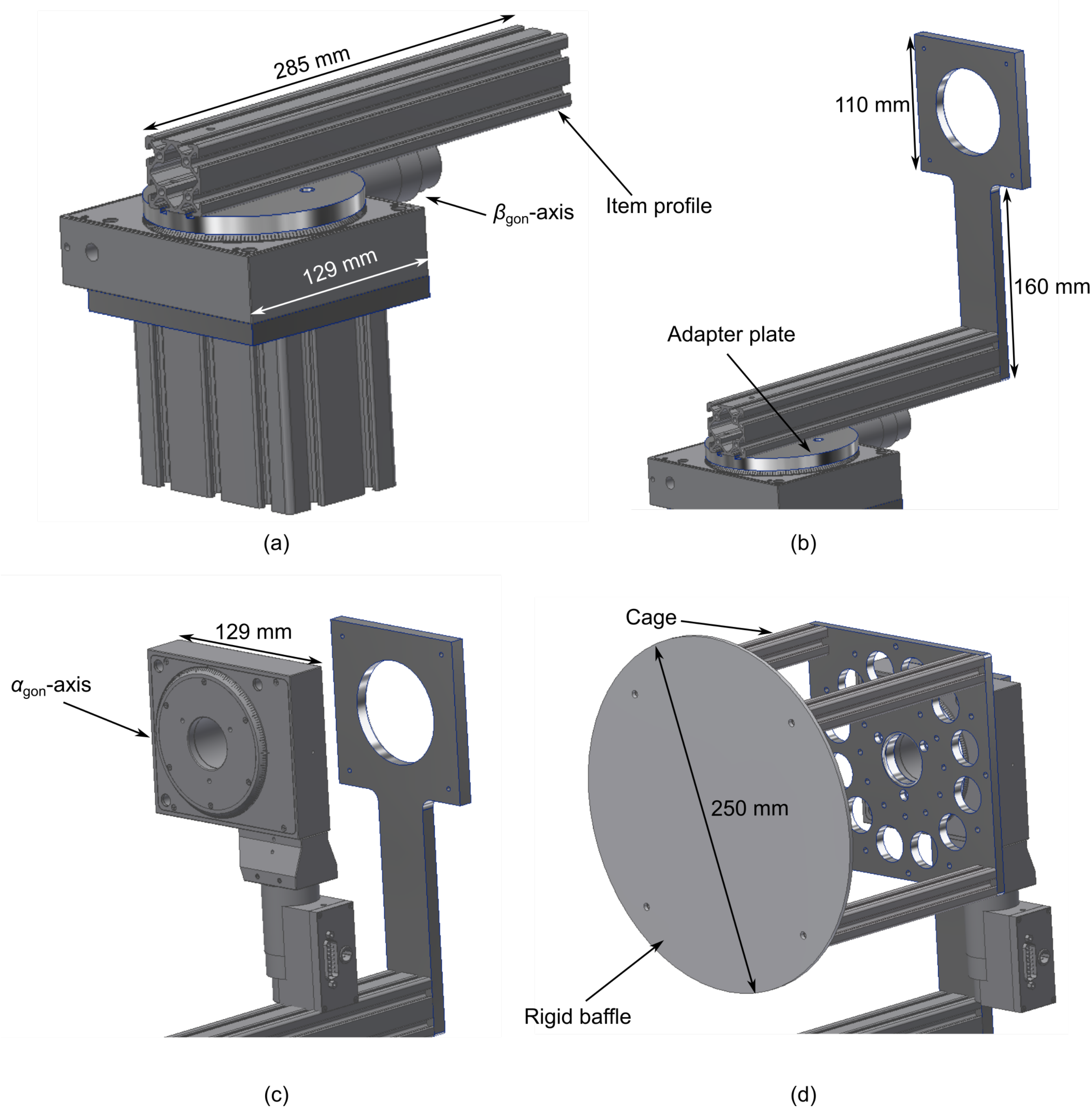

Figure 3.4: Assembly of the axis of the goniometer.

This measurement setup is versatile and suitable for numerous transducers differing in size, resonance frequency and characterization method. Thus, accurate positioning of the measurement microphone is crucial prior to each characterization. This alignment process is divided into two steps. First, the transducer is rotated to $90°$ [Figure 3.5(a)]. Then, the horizontal and vertical alignment of the microphone is conducted. The objective of this process is to position the top end of the microphone in the center of the device under test. The microphone is mounted with a 3D-printed clip onto an item profile. In addition, between the microphone and the clip is a silicone layer located. This allows for manual positioning and insulates the housing of the microphone from the rest of the measurement setup.

Second, the device under test is rotated to $0°$ [Figure 3.5(b)]. While this rotation, the user can make sure that there are no collisions between the components and the cable management can be checked as well. Afterwards, the item profile can be adjusted. After this alignment, the setup is ready for the measurement.

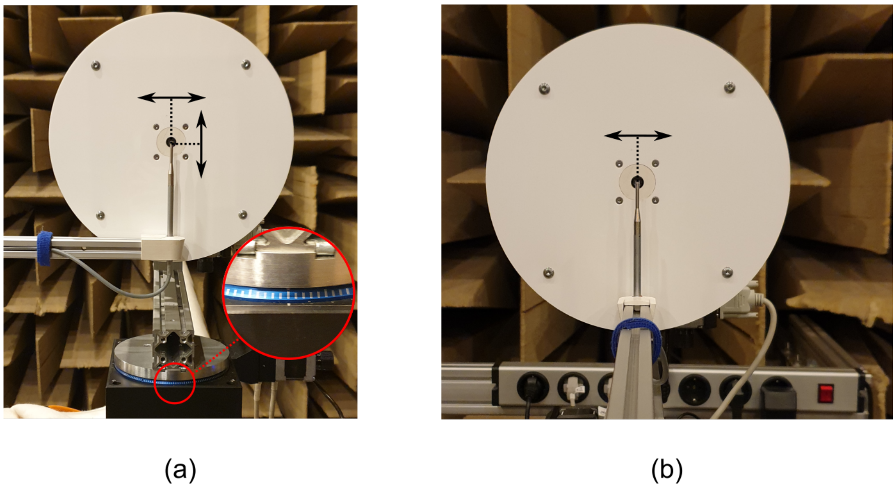

Figure 3.5: Prior to the measurements, the position of the microphone needs to be adjusted.

First tests of the measurement setup showed issues with the linear axis. Since the aluminum profile is a sound hard wall, reflections occurred, and, thus, corrupted the measurements. When a sound wave is emitted by the transmitter, one part of the wave directly propagates towards the receiver which is the direct sound path s_{direct}. In addition, the transmitter emits sound to the linear axis which is reflected. This forms a second indirect sound path s_{indirect} (Figure 3.6). These two waves superpose at the receiver, which can be compared to a Helmholtz resonator with constructive and destructive interference.

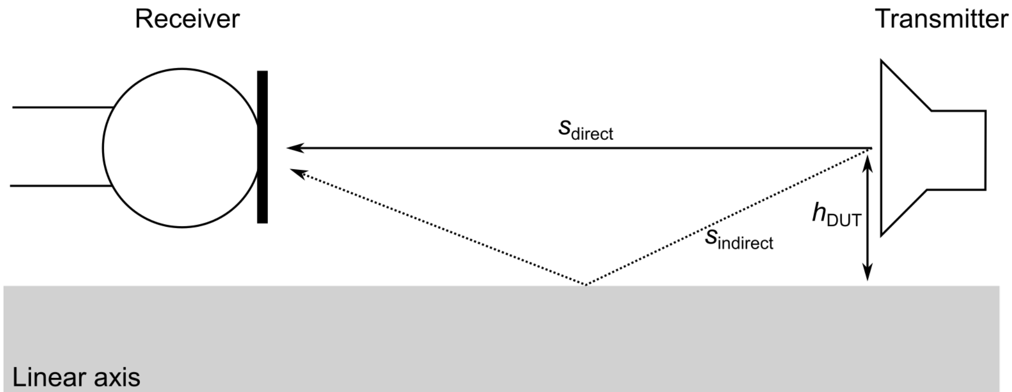

Figure 3.6: The sound wave not only propagates directly from the transmitter to the receiver but also has indirect paths. These indirect paths needs to be attenuated.

This effect can be described with the theorem of Pythagoras. The distance between the tip of the receiver and the linear axis h_{DUT} is $0.33\,\text{m}$. When the transmitter is exited with 80 cycles the first effects were observed at a distance s_{direct} of $0.1\,\text{m}$.

At this point, the difference between the direct and indirect path is $567.6\,\mathrm{mm}$

$$s_{\text{indirect}} = 2 \cdot \sqrt{h_{\text{DUT}}^2 + \left(\frac{s_{\text{direct}}}{2}\right)^2} = 2 \cdot \sqrt{(0.33\,\mathrm{m})^2 + \left(\frac{0.1}{2}\,\mathrm{m}\right)^2} = 0.6676\,\mathrm{m}, \tag{3.2}$$

$$\Delta s = s_{\text{indirect}} - s_{\text{direct}} = 0.6676\,\mathrm{m} - 0.1\,\mathrm{m} = 0.5676\,\mathrm{m}. \tag{3.3}$$

Dividing this distance by the wavelength of $8.575\,\mathrm{mm}$ yields 66 cycles. Assuming the transmitter needs additional 14 cycles for reaching a significant amplitude leads to the 80 cycles use in the experiment

$$n_{\text{cycles}} = \frac{\Delta s}{\lambda} = \frac{567.6\,\mathrm{mm}}{8.575\,\mathrm{mm}} = 66\,\text{cycles}. \tag{3.4}$$

Reducing the cycles in the experiment moved the effect to higher distances.

This issue was fixed by adding a $3\,\mathrm{mm}$-thick felt (Feltico, Filzfabrik Fulda GmbH & Co KG) to the linear axis (Figure 3.7). This felt has a mass of $900\,\frac{\mathrm{g}}{\mathrm{m}^2}$ and is made of wool. This wool attenuates the reflected waves. Before the application of the wool, clear resonances can be observed in the measurements. After applying the wool these effects are gone.

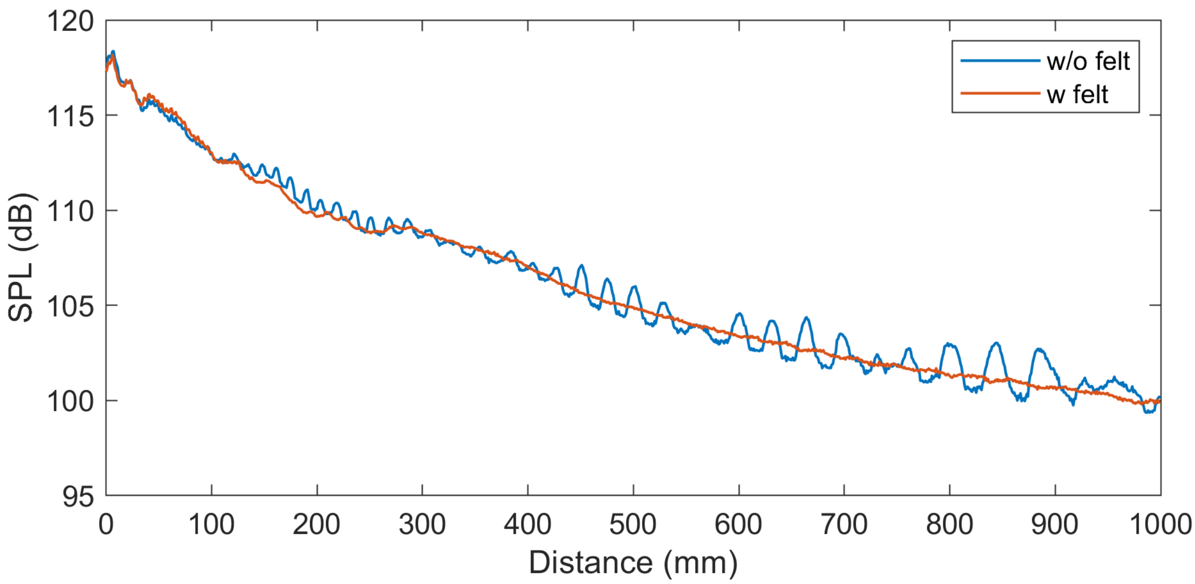

Figure 3.7: By applying a felt to the linear axis, the acoustic reflections can be reduced.

This measurement setup is suitable to characterize acoustic quality criteria. The most important is the sound pressure level L_{p}. This defines the acoustic pressure on a logarithmic scale, which simplifies the comparison between transducers. The measured pressure is compared to a reference value p_{ref}. This value is the audible threshold in air with $20\,\mu\mathrm{Pa}$, i.e.

$$L_{\mathrm{p}} = 20 \cdot \log_{10}\left(\frac{p}{p_{\text{ref}}}\right), \tag{3.5}$$

$$p_{\text{ref}} = 20\,\mu\mathrm{Pa}. \tag{3.6}$$

In addition to the SPL, the shape of the directivity is important for different applications. For this reason, the half power beam width (HPBW) is used to specify the width of the main lobe. It compares the -3 dB of the main lobe compared to its maximum level. This value shows, whether a transducer has a wide or narrow characteristic. The result is expressed as an angular information. In addition, the side lobe level (SLL) compares the difference between main lobe and the side lobe. This value is crucial to estimate whether an ultrasonic transducer can produce sound emissions in undesired directions. This causes ambiguities for applications such as ultrasonic sonar.

The measurement setup offers versatile acoustic characterization of acoustic systems. Thus, the calibrated microphone can be exchanged with a pre-characterized transmitter. This allows for characterization of receive performance of acoustic transducers. As a result, the sensitivity can be measured.

In addition, the microphone can be even exchanged with an acoustic reflector. This allows for automated pulse-echo measurements for ultrasonic sonar systems. The reflector can be freely positioned relative to the sonar system. The system offers software solutions to connect with the software PAIUS which was developed by Gianni Allevato. Thus, the connection was implemented in cooperation with him.

Besides providing reliable results, the objective of this setup is to provide versatile and convenient work flows. This was achieved by importing a file with coordinates for the axis and not hard-coding the positions. This approach was inspired by the g-code of 3D-printers. First, the user defines the coordinates and saves them into an HDF5 file [70]. The benefit of HDF5 is the open standard which can be read by multiple programs. In addition, it saves its data in a folder structure using the binary format. This allows for space efficient data saving.

Next, the user specifies whether the measurement is in transmit, receive or pulse-echo mode in the Labview software. Afterwards, the coordinates are used for the automatic measurements. For each position, a raw file is stored in the HDF5 file. After the entire measurement, the axis move into an assembly position. This way, all components can be easily excessed. Additionally, environmental properties are measured in the anechoic chamber. A BMP180 (Bosch) is used to measure the temperature (± 0.5°C) and ambient pressure (± 1 hPa). Furthermore, a DHT22 (Aosong Electronics Co.,Ltd) measures the relative humidity (± 2%) in the room. The sensors are located beneath the goniometer. These values are needed for simulations.

In conclusion, the measurement setup saves the following parameters in the HDF5 file:

- Sensitivity of the microphone;
- the desired coordinates by the user;
- the measured coordinates by the axis;
- the ambient temperature during the measurement;
- the relative humidity during the measurement;
- the ambient pressure during the measurement;
- the raw data of the A-scans of the microphone (only in transmit mode);
- personal notes by the user.

3.3 Characterization of the measurement setup

After the first tests of the measurement setup, the noise floor and the accuracy of the microphone was analyzed. First, the influence of the metal mesh in the anechoic chamber was investigated. This mesh serves as a protection for the user inside the room. In addition, it is electrically grounded. This introduces additional noise, since it behaves as an antenna and captures broadband noise. Furthermore, the metal housing of the microphone cable is connected to the signal ground. As a result, when the metal parts of the microphone are electrically connected to the metal mesh, the noise floor of the microphone is increased (Figure 3.8). This was tested in the anechoic chamber. The microphone is connected to the pre-amplifier and the oscilloscope. The root mean square of the noise is calculated for every time sample and converted in an equivalent SPL. Each time the cable is in direct contact with the mesh the noise floor is increased by 8 dB. In order to solve this issue, a 3D-printed clip was made. This clip holds the cable in position and insulates the metal case of the cable from the rest of the measurement setup.

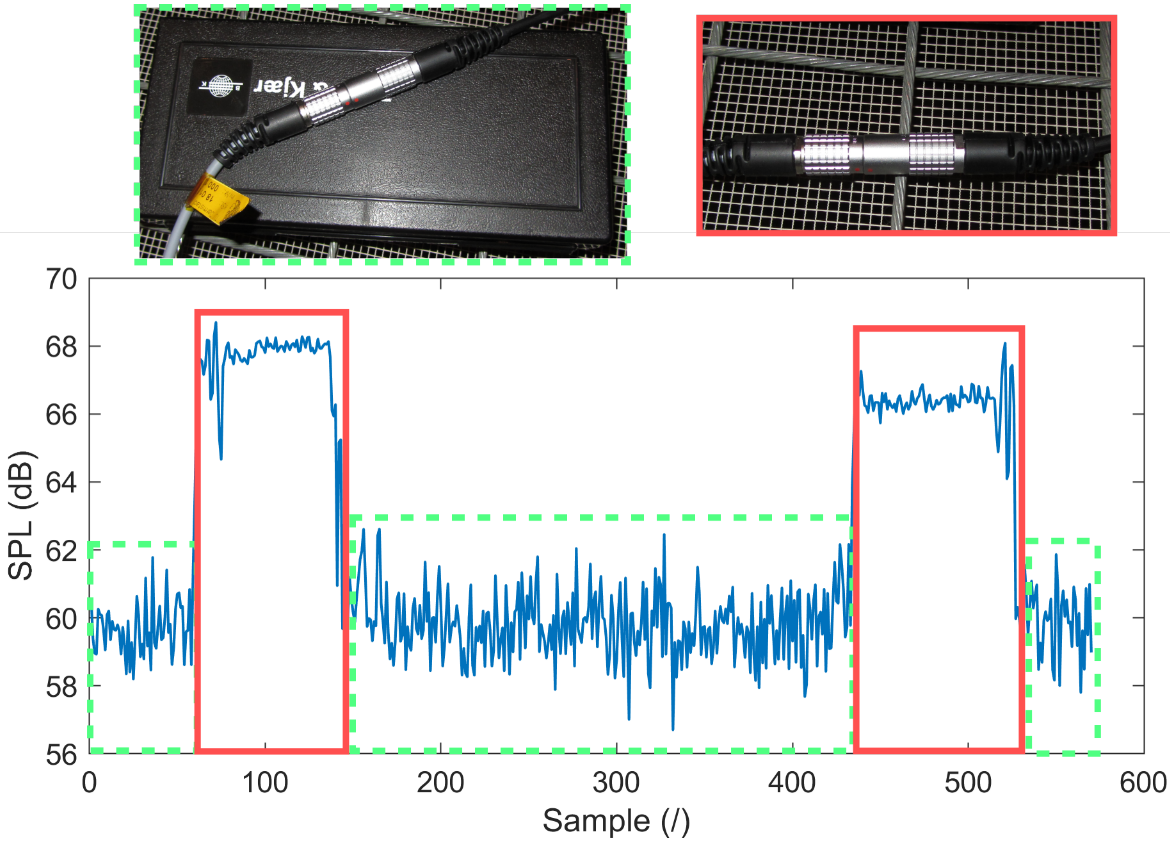

Figure 3.8: The metallic mesh serves as protection. However, when it is in contact with the measurement cable it increases the noise floor by 8 dB.

In general, the noise floor of the measurement setup can be estimated with the manufacturer information. The oscilloscope has a noise floor of $4.2\,\mu V_{RMS}$ with 1 MSa/s, DC-coupling and a $50\,\Omega$ termination. In addition, the microphone including the pre-amplifier contributes a noise floor of $3.6\,\mu V_{RMS}$. In combination the total theoretical noise floor is $7.8\,\mu V_{RMS}$ or in SPL 58.8 dB.

In order to achieve such low noise floors, multiple tests were conducted. First, the dependency between the sampling rate and the noise floor is investigated. The sampling rate defines the maximum frequency that can be captured of a signal. However, this not only influences the measured signal but also the noise floor. The higher the sampling rate the higher the noise floor since, a higher band width increases the frequency components of the noise. In this work the investigated ultrasound is located around 40 kHz. Thus, the minimal sampling rate of the oscilloscope of 500 kSa/s can be used, since it is more than sufficient with $> 10 \cdot f$. As a result, this sampling rate provides a noise floor of 59.2 dB±1.2 dB.

Table 3.2: Noise floor in comparison of the sampling rate with DC-coupling and 2000 samples.

Sampling rate (kSa/s)	Noise SPL $\pm\sigma$ (dB)	Voltage (μV_{RMS})
500	59.2 ± 1.2	8.1
1000	60.7 ± 0.6	9.7
5000	69.7 ± 0.2	27.3
10000	71.2 ± 0.2	32.4
15000	78.4 ± 0.1	74.2

Second, the influence of the number of samples is compared with the noise floor. The more samples are captured the lower the minimal noise frequency that can be captured is presence with constant sampling rate. The table shows, that a reduced sample count also reduces the noise floor. With 2000 samples the minimal noise floor is 59 dB $\pm$ 1.2 dB.

Table 3.3: The noise floor is compared with the number of samples with DC-coupling and 500 kSa/s.

Number of samples	Noise SPL $\pm\sigma$ (dB)	Voltage (μV_{RMS})
20000	66.1 ± 2.8	18.0
18000	66.1 ± 3.0	18.0
16000	66.3 ± 3.2	18.4
14000	65.4 ± 4.7	16.6
12000	64.8 ± 3.2	15.5
10000	64.5 ± 3.4	15.0
8000	63.5 ± 2.9	13.3
6000	62.2 ± 2.6	11.5
4000	60.9 ± 2.1	9.9
2000	59.0 ± 1.2	8.0

Third, the noise floor can be further reduced by introducing averaging. The theory defines, that doubling the averaging number reduces the noise floor each time by 3 dB. However, this increases the measurement time for each measurement position. As a result, averaging is always a compromise between minimal noise floor and minimal measurement time.

Table 3.4: The noise floor is compared with the averaging numbers with 2000 samples, DC-coupling and 500 kSa/s.

Averaging	Noise SPL $\pm\sigma$ (dB)	Voltage (μV_{RMS})	Measurement time (ms)
1	59.7 ± 1.2	8.6	10
2	56.3 ± 1.3	5.8	20
4	53.2 ± 1.3	4.1	40
8	50.4 ± 1.4	2.9	80
16	47.3 ± 1.3	21	160
32	44.1 ± 1.3	1.4	320
64	40.9 ± 1.2	0.99	640
128	38.0 ± 1.2	0.71	1280
256	35.0 ± 1.1	0.50	2560
512	31.7 ± 1.0	0.34	5120
1024	28.9 ± 1.2	0.25	10240

Last, the measurement uncertainty of the microphone also depends on the measured SPL. For this reason, this dependency is analyzed by connecting the microphone with the pre-amp and oscilloscope and using an ultrasonic transducer (Murata, MA40S4S) with varied driving voltage with 80 cycles at a distance of 30 cm. The dependency between the two quantities can be clearly observed (Figure 3.9). The lower the SPL by the transducer, the higher the standard error is. The lowest SPL of 73 dB causes an error of ± 0.64 dB. However, the most commonly SPL rating in this work is around 100 dB which causes an error of the microphone of ± 0.22 dB. Additional, the assembly tolerances by the user contributes to the overall uncertainty. As a result, the entire uncertainty of the measurement setup is ± 1 dB.

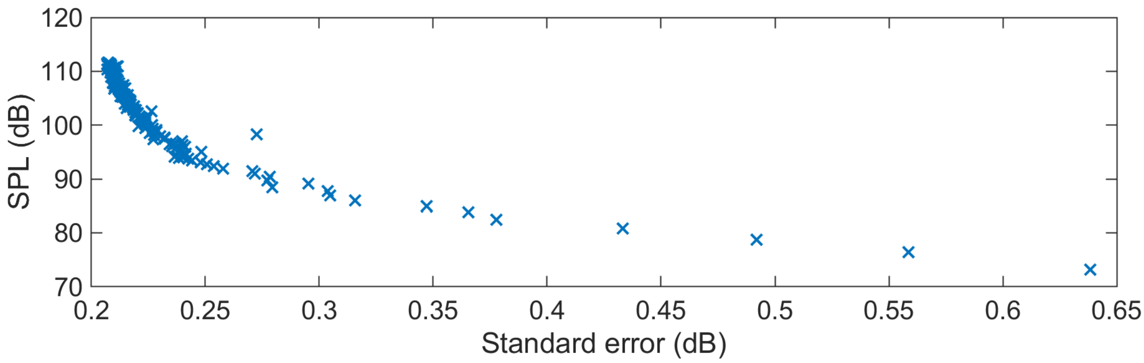

Figure 3.9: The standard error of the microphone measurement is increased with decreased SPL of the ultrasonic transducer.

As a result the measured noise floor of 59.7 dB $\pm$ 1.2 dB is in good agreement with the estimated noise floor of the manufacturer information of 58.8 dB.

3.4 Boundary element model for waveguided phased arrays

The following chapter was published in [48].

Next, the numerical model for an entire ultrasonic phased array including the waveguide is described. Numerical methods such as FEM or BEM provide the calculation of complex geometries which can not be analytically modeled using a reduction of the dimensional systems [27]. In particular, duct acoustics analytic models have geometrical restrictions such as a minor geometric expansion in comparison to the wavelength, plane wave propagation inside the duct and a straight direction of the waveguide. The BEM is used in this work for the ultrasonic phased array instead of the FEM, because of the small wavelength which results in numerous elements for far-field calculations [71]. In general, the discretization of acoustic systems are typically done with a mesh size of at least $\lambda/10$. For example, an acoustic hemisphere with a radius of $1\,\mathrm{m}$ at a wavelength of $\approx 8.6\,\mathrm{mm}$ results in $4.1 \cdot 10^9$ elements. A model with this element count is not conveniently solvable without a computing cluster or a significant reduction of the degrees of freedom. Especially, the random access memory (RAM) of a computer can be filled up quick, such as in three dimensional ultrasonic far-field calculations using FEM. One convenient way to avoid this high computational load is the BEM. This numerical approach uses the surface area of a geometry instead of the volume. In comparison to an FEM, the BEM creates a dense system matrix instead of a sparse matrix. So, there is a compromise where the complexity of an FEM exceeds a BEM. This is the case for the model of the waveguided ultrasonic phased array.

In previous work, the BEM was used for simulating air-coupled ultrasonic phased arrays [36]. However, only the output ports were considered in this model. Now, this model is extended with the waveguide and the finite-sized rigid baffle which is used in the measurements. A validated model of the waveguide geometry offers the optimization of the waveguide structure towards maximum SPL, beam steering capability and also reduction of higher modes. Therefore, the commercial software COMSOL is used. In addition, the environmental properties of the measurement were implemented in the simulation such as temperature, ambient pressure and humidity. Thus, the correct atmospheric attenuation caused by thermal conductivity, viscous and relaxation effects is used in the model. This attenuation is based on the ANSI standard S1.26-2014 [53].

The model is based on the Helmholtz equation in the frequency domain, i.e.

$$\nabla \cdot \left(-\frac{1}{\rho} \nabla p_\mathrm{t} \right) - \frac{\omega^2}{c_\mathrm{air}^2 \rho} p_\mathrm{t} = 0, \tag{3.7}$$

including the density ρ of the media, the speed of sound c_air of the media, the angular frequency ω and the total pressure p_t. In COMSOL the total pressure is split into two components, i.e.

$$p_\mathrm{t} = p + p_\mathrm{b}, \tag{3.8}$$

which are the pressure from the transducer p and additional harmonic background pressure p_b [53]. This model contains no background sound field which reduces equation 3.8. Thermoviscous acoustics or nonlinearities are neglected in the model as well in order to further reduce the computational costs.

The waveguide consists of 64 independent ducts with tapered diameter $10,$ mm to $3.2\,\mathrm{mm}$. Each duct has a length of $80\,\mathrm{mm}$ (Figure 3.10). The input and output surface of the duct is perpendicular to its center line. The simulation uses a frequency of $40\,\mathrm{kHz}$ leading to a wavelength of $8.575\,\mathrm{mm}$. As a result, the Helmholtz number at the output of the duct is 1.25 and at the input 3.66. Due to this high Helmholtz number at the input of the duct, higher modes occur requiring a fully 3D model [65]. A reduction of the dimension can not be applied for this geometry in this frequency range.

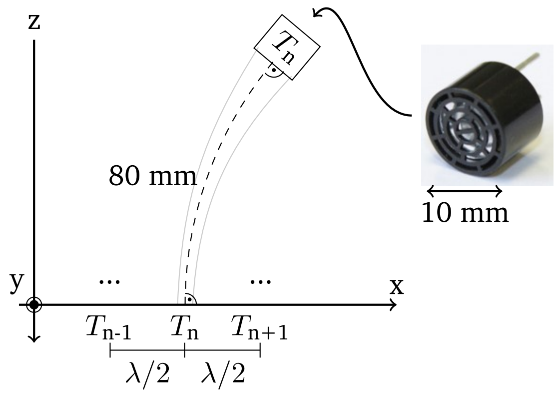

Figure 3.10: The 8×8 consists of multiple tapered ducts. The geometry of the duct is an arc leading to perpendicular connection between the input surface of the transducer and the output surface of the waveguide. As a result, the inter element spacing is reduced to $\lambda/2$.

The transducer surface is modeled as an ideal piston transducer, i.e.

$$-\mathbf{n} \cdot \left(\frac{1}{\rho \nabla p_{\mathrm{t}}} \right) = j\omega v_{\mathrm{n}}, \tag{3.9}$$

with a normal velocity v_{n}, applied on the inner surface at the input of each duct. The rigid baffle is a finite-sized sound hard wall with a thickness of $3\,\mathrm{mm}$ and a diameter of $250\,\mathrm{mm}$. It has the same geometry as in the measurements. All walls are assumed as ideal sound hard [Figure 3.11(a)], i.e.

$$-\mathbf{n} \cdot \left(\frac{1}{\rho \nabla p_{\mathrm{t}}} \right) = 0. \tag{3.10}$$

In order to reduce calculation time, only a quarter of the geometry is simulated using the symmetric xz-plane and yz-plane [Figure 3.11(b)].

All calculations where conducted on a Dell server with an Intel (Santa Clara, Silicon Valley, United States of America) Xeon CPU E5-2660 v3 and 256 GB RAM.

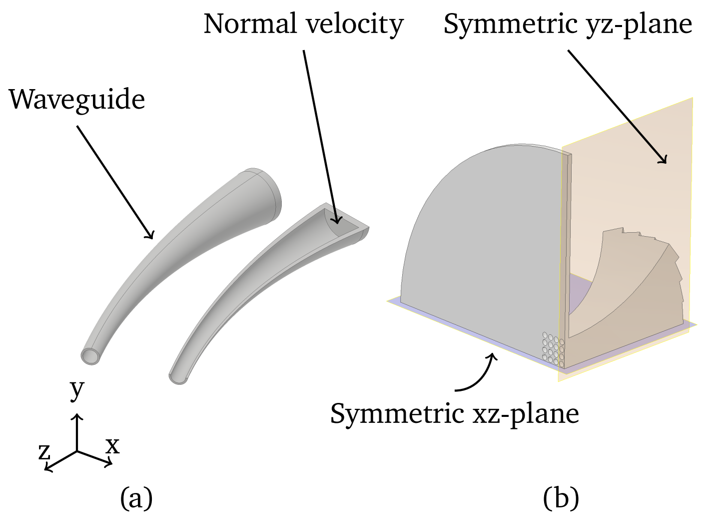

Figure 3.11: A duct of the waveguide reduces its diameter from $10\,\mathrm{mm}$ to $3.4\,\mathrm{mm}$ (a). The input and output surfaces are perpendicular to the center line of the waveguide. The complete model uses two symmetry planes (xz,yz), in order to reduce calculation time (b).

An ultrasonic phased array prototype of the research group is used, to validate the numerical model [34]. The transducers are driven with burst signals of $40\,\mathrm{kHz}$ with a cycle number of 30. This way, parasitic heating effects are reduced, and, thus, reducing drift of resonance frequencies as well. Furthermore, the driving voltage is reduced to $6\,\mathrm{V_{pp}}$ to avoid nonlinear effects in air. All measurements were conducted in an anechoic chamber (Figure 3.12). In order to validate the correct speed of sound and atmospheric attenuation used in the simulation, digital pressure and temperature sensors are used to measure environmental properties in the anechoic chamber. The temperature during measurements was $26^\circ\mathrm{C} \pm 0.5^\circ\mathrm{C}$ which caused a speed of sound of $347.1\,\mathrm{m/s}$ [8]. The atmospheric pressure was $100314\,\mathrm{hPa} \pm 1\,\mathrm{hPa}$. In addition, atmospheric damping effects were estimated by measuring the humidity in the room. This value reached $39\% \pm 2\%\,\mathrm{RH}$ during the experiments.

The phased array is designed as an far-field array. In the far-field, the signals amplitude is reduced with $\frac{1}{r}$ dependency where r is the distance between the arrays and an arbitrary point in the far-field (Figure 3.12). Following the far-field criteria

$$N = \frac{d^2_{\text{aperture}} - \lambda^2}{4\lambda} \tag{3.11}$$

the transition between near and far-field of the characterized phased arrays is around $30\,\mathrm{mm}$ [8]. As a result, the microphone is positioned at a distance of $1\,\mathrm{m}$, which is a sufficient range in the far-field. The same distance is used in the evaluations points of the BEM.

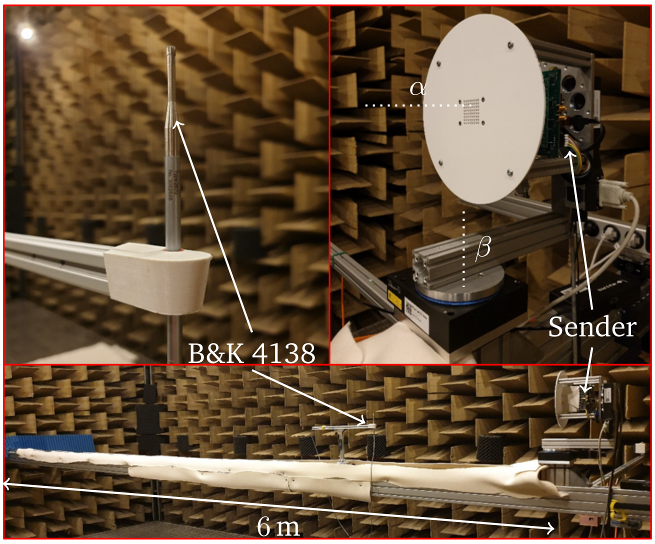

Figure 3.12: A calibrated measurement microphone is located on a linear axis. The sender is mounted onto two rotational axis. The maximal measurement range is 6 m resulting in an maximum measurement volume of $905\,\mathrm{m}^3$.

Next, the simulation results are analyzed. This part is split into two steps. First, the wave propagation inside the waveguide is observed. Afterwards, the far-field characteristics are derived and compared with the measurements. In general, most ducts inside the waveguide have a plane wave propagation [Figure 3.13(a)]. However, the corner duct has a wave propagation which differs from a plane wave [Figure 3.13(b)]. Since this duct has the highest bending angle, the wave propagates in a curve which leads to this mode. In addition, the input of the duct has a diameter which is bigger than the wavelength resulting in higher mode excitation. As a result, the propagation direction of the wave has an influence on the mode shape.

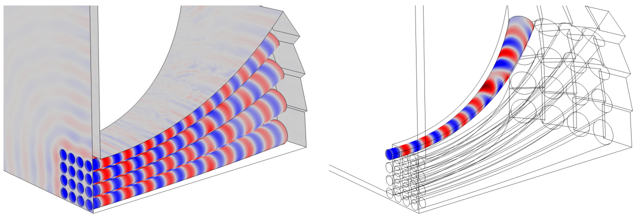

(a) (b)

Figure 3.13: Inside the waveguide most ducts provide a plane wave propagation(a). Only the corner duct deviates from plane wave propagation (b).

The directivities of the measured and simulated waveguides are compared by normalizing there respective SPLs. In general, the simulations and the measurements are in good agreement (Figure 3.14). The HPBW just differs by $4°$ and the SLL deviates by 3 dB. The side lobes show slightly different behavior caused by the manufactures tolerances of the transducers. This causes varying amplitudes at the output of the waveguide. This deviation is not implemented in the model. The side lobes between $\pm 60°$ and $\pm 90°$ show in both measurement and simulation a rippled distribution. This effect is caused by the finite-sized rigid baffle. The finite-sized sound-hard wall results in an sudden change in acoustic impedance. Thus, the waves are reflected at the end of the rigid baffle and superpose with the incident waves. This effect does not occur when the transducer is located in an infinite rigid baffle [36].

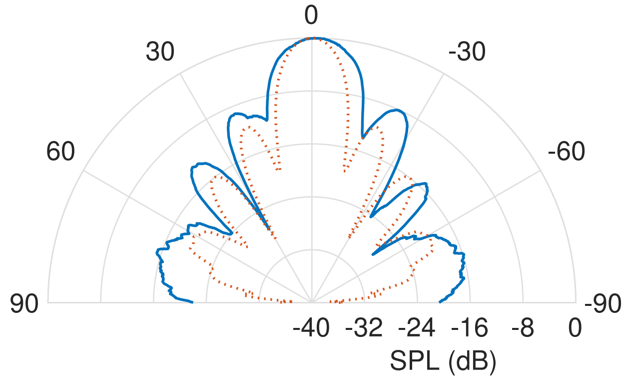

Figure 3.14: The simulations (:) are in good agreement with the measurements (-). The HPBW differs only by $4°$. Due to the amplitude deviation of the used transducers, the side lobes differ from the simulation.

The two-dimensional pressure field of the measurements and the simulations are in good agreement as well.

However, the influence of the transducer manufacturer tolerances, which introduce an uneven pressure distribution at the output of the waveguide, can be observed. The main lobe has the same direction and there is a small difference between the HPBW of $4°$. The first side lobe highlights a sharp borderline from the main lobe. In the measurements, this transition is not as sharp due to the different amplitudes of the transducers at $\pm 15°$ [Figure 3.15(a)]. The destructive interferences of the sound field are not ideal causing a much higher resulting pressure at this point, when each transducer emits sound waves with a different amplitude. In contrast, the second side lobe is in a good agreement with the measurement. The last side lobe contains ripples [Figure 3.15(b)] as well. This is caused by the finite-sized rigid baffle. At the edge of the baffle a sudden change in impedance occurs, which leads to reflections on the surface of the rigid baffle. The incident and reflected waves superpose leading to this pressure distribution.

Furthermore, in the measurements the acoustic pressure is averaged over the diameter $3\,\mathrm{mm}$ of the microphone. This causes a spatial averaging effect of the sound pressure in the measurements. This effect is not considered in the simulations. Instead, the pressure field is evaluated with an infinite small microphone. As a results, the separation of the side lobes in the measurements is not as sharp as in the simulations.

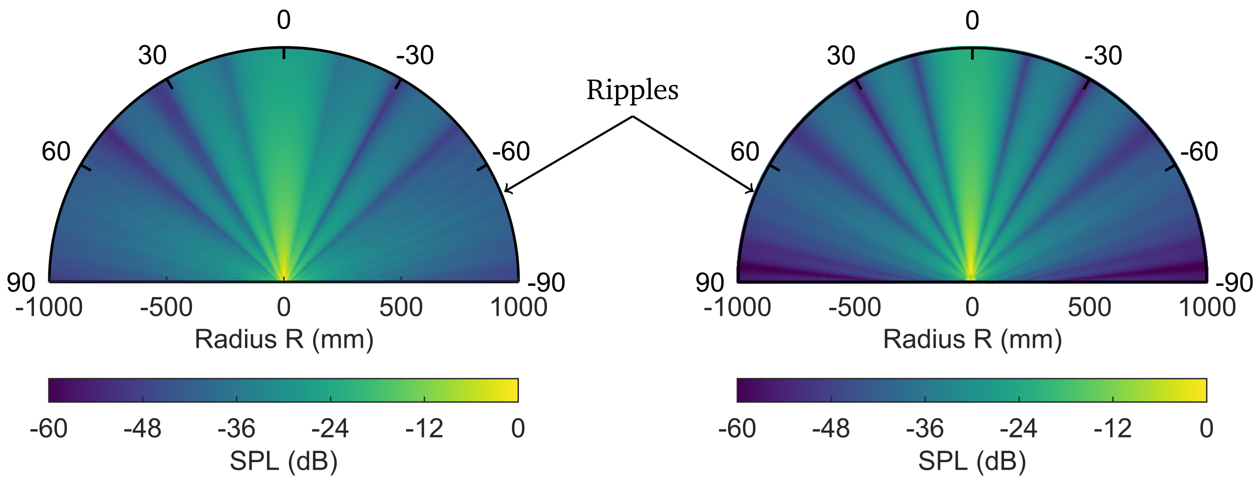

(a) (b)

Figure 3.15: The measurements and the simulations have a similar two-dimensional pressure field (a,b). The transition between the lobes, e.g. at $\pm 15^\circ$ in the measurement, are not as sharp as in the simulation due to the manufacturer tolerances of the transducers used in the experiment. Additionally, in both graphs the influence of the finite-sized rigid baffle is noticeable in the third side lobe (ripples).

In conclusion, the proposed measurement setup offers versatile and convenient acoustic characterizations of air-coupled ultrasonic phased arrays. Properties such as maximum SPL, HPBW and SLL can be easily derived from the measurements. In addition, the pressure field can be measured in one, two or even three dimensions. Last, the measurement microphone can be exchanged offering further characterization possibilities in receive and pulse echo mode.

This setup is used to validate the BEM model of the waveguided phased array. This model is suitable for predicting the acoustic pressure field of the phased array. The differences regarding the HPBW is only 4° and for the SLL $3\,\mathrm{dB}$. The influence of the finite-sized rigid baffle can be observed, since additional ripples occur at the position of the side lobes. Last, the influence of the manufactures tolerances of the transducers cause a pressure distribution at the output of the waveguide. This explains the differences between the side lobes of the measurement and the simulation. Furthermore, this model can be calculated on a consumer PC. Thus, a cluster is not needed.

4 Optimization of acoustic waveguide geometries

Jäger showed in his work [33] one of the first 3D-printed waveguides for air-coupled phased arrays. However, the geometry of these waveguides was not analyzed. In this work numerical simulations are conducted to improve the understanding of the wave propagation inside the waveguide. This allows for improved SPL, size reduction of the waveguide and simplified geometries. Especially, industrial applications benefit from these results, since waveguides can be optimized for different demands.

In addition, often a 1D line array is sufficient for multiple applications. For this reason, a set of line arrays is developed, simulated and measured for pulse-echo systems.

4.1 Perpendicular input and output surface

The first geometric parameter which is investigated is the orthogonality of the input and output ports. This parameter influences the direction of the wave coupling between the transducer and the waveguide at the input port and between the waveguide and the free-field at the output port. For this case, four geometries are investigated. First, the ducts geometry is defined as a straight line between the input and output without any orthogonality [Figure 4.1(a)]. Second, only the input port is orthogonal to the center line of the waveguide [Figure 4.1(b)] and third only the output port is orthogonal [Figure 4.1(c)]. Last, both ports are orthogonal [Figure 4.1(d)]. All geometries have a distance between the input and output port of 80 mm. In addition, all input diameters are 10 mm and all output diameters are 3.4 mm. Last, the offset between the center of the input and output is varied. This parameter is crucial for building phased arrays, since the input and output port have different diameters. As a result, the maximal investigated offset is 26.8 mm, because this is the maximal value which is needed for an 1×8 line array. All designs were constructed in Inventor (Autodesk, United States of America).

The simulations are conducted in COMSOL combining the finite element method (FEM) and the boundary element method (BEM). The FEM always needs to mesh an entire volume but has a sparse matrix. In contrast, the BEM only meshes the surfaces of a three-dimensional system but always produces a dense system matrix. As a result, the FEM is faster for small systems and the BEM has faster calculations times for bigger systems. Therefore, the BEM is used to calculate the free-field and the FEM is used to calculate the wave propagation inside the duct. At the output port, the simulation methods are coupled via the acoustic pressure. In addition, all walls of the duct are assumed as sound hard walls. The excitation at the input port is a normal velocity with 1 m/s. Calculations are done in the frequency domain at 40 kHz in a three dimensional system. In order to derive information from the simulation results, the directivity at a distance of 1 m is analyzed and the SPL at the same distance over the offset is observed. The SPL values of the directivities are normalized to there individual maximum values for better comparison.

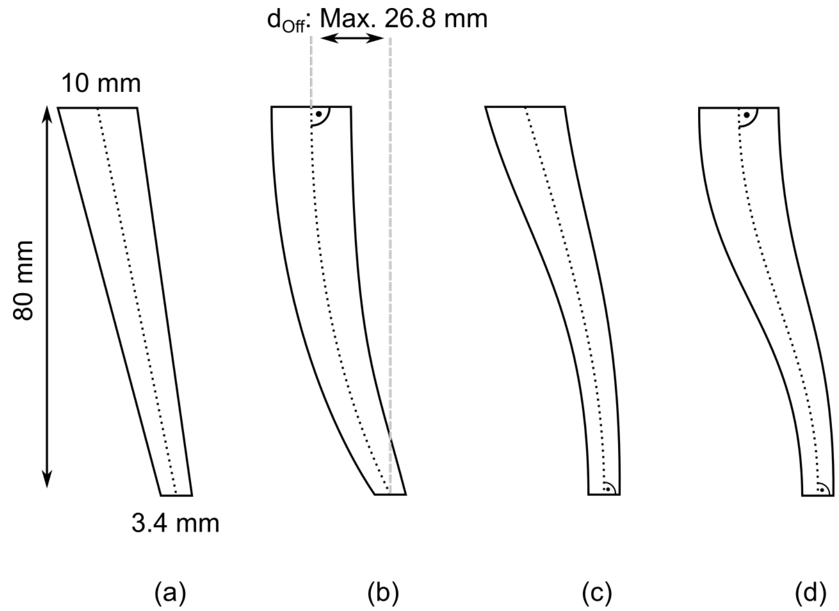

Figure 4.1: Four different geometries are compared, in order to test the orthogonality of the waveguide. First, there is no orthogonality (a). Second, only the input is orthogonal (b). Third, only the output is orthogonal (c). Fourth, both input and output are orthogonal. The offset d_{Off} between the input and output ports is limited to 26.8 mm.

The first duct geometry has no orthogonality. However, the directivity is not effected by the variation of the offset [Figure 4.2(a)]. Only a minor asymmetry is noticeable, since the simulation dos not include a rigid baffle for convenient simulation times. On the other hand, the influence of the offset variation is significant [Figure 4.2(b)]. At an offset of 18.3 mm the SPL is reduced by 17.4 dB. This loss in SPL is caused by the inefficient acoustic mode inside the waveguide. The pressure distribution has the shape of a checkerboard with neighboring pressure maxima and minima. This reduces the SPL that is emitted from the output port of the waveguide. Apart from that, there are higher modes at an offset of 15.5 mm and 22.5 mm as well. These higher modes only occurs in the first $3/4$ of the waveguide, because of the tapering. After this length, the fundamental mode is visible.

In order to further investigate the pressure distribution along the inside of the waveguide, the pressure distribution on the top and bottom side is analyzed. Since the input and output port differ in diameter, the propagation length at the top and bottom of the waveguide differ as well. The length deviation can be expressed with a geometric calculation. Fundamental modes propagate only in direct paths. For this reason, fundamentals will propagate from P_4 to P_1 and from P_3 to P_2. On the other hand, the higher modes will also propagate along the diagonals. These propagation paths are from P_3 to P_1 and from P_4 to P_2 (Figure 4.3).

In the numerical result the fundamental mode can be observed in the section below 22 mm. Afterwards, the mode is converted into a higher order. The fundamental mode has a path difference of 1.03 mm. The geometric calculations lead to a difference of 1.25 mm. Thus, there is a significant deviation between the these two approaches. On the other hand, the geometric estimation of the two diagonal paths yields a difference of 2.76 mm. This is in good agreement with the difference for higher modes of the simulation with 2.87 mm at positions bigger then 70 mm (Figure 4.3). As a result, the input section of the waveguide is sensitive to higher modes for the given geometry at 40 kHz.

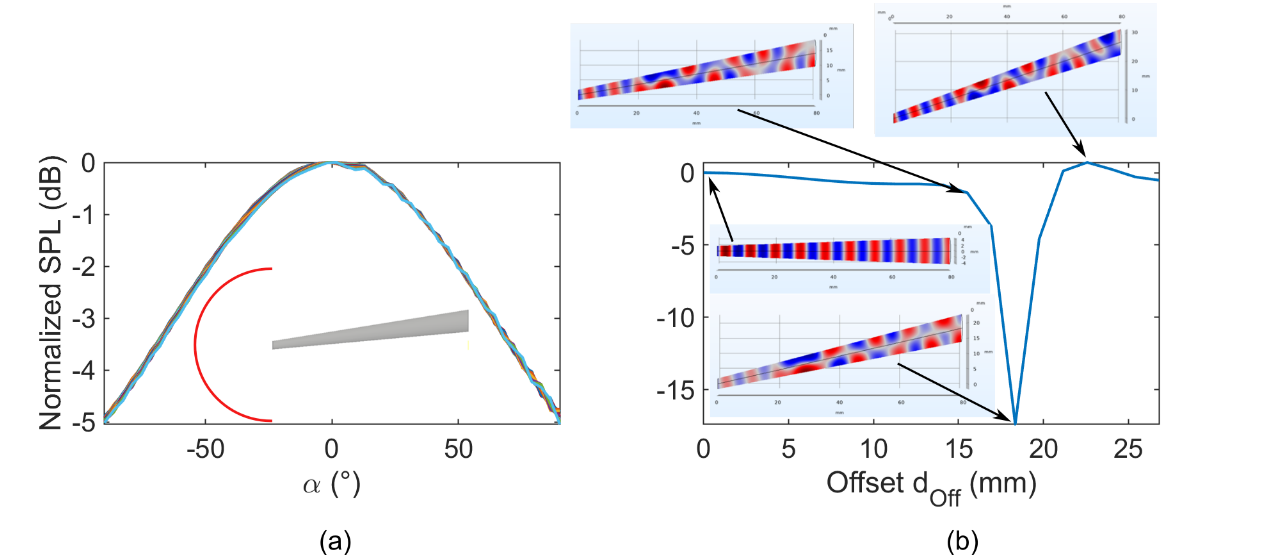

Figure 4.2: The directivity of the waveguide without any orthogonality does not change with varying offset d_{Off} between input and output (a). However, the offset has a significant influence on the SPL (b), since the acoustic mode inside the waveguide varies.

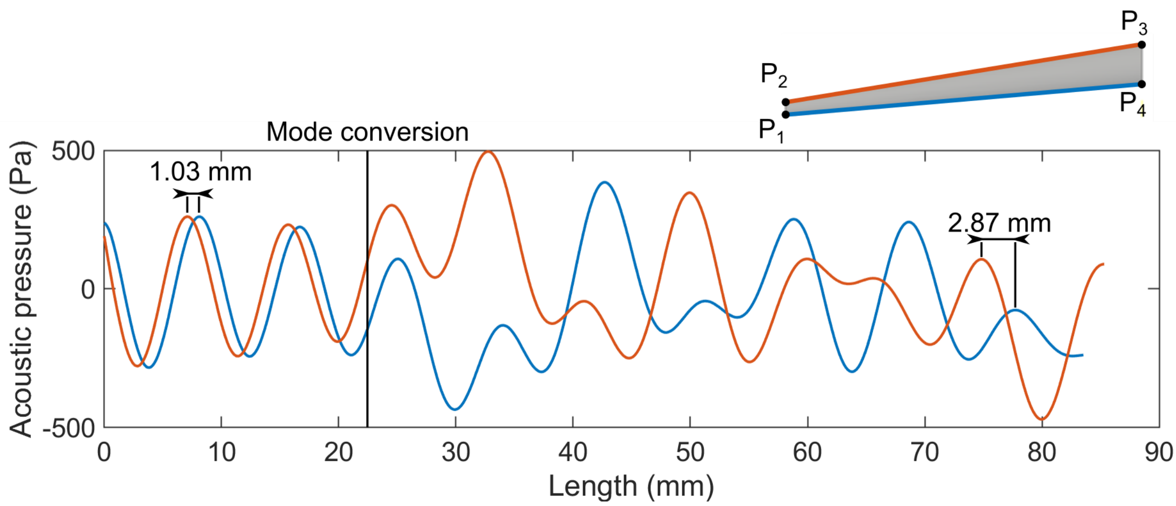

Figure 4.3: Acoustic pressure along the top (P_2 to P_3) and bottom (P_1 to P_4) side of the duct. Due to the offset of the input and output port, the length of the top and bottom side differ. In addition, the diameter of the duct varies which leads to different acoustic modes along the length. At a length of 22 mm the mode conversion can be observed from the fundamental mode to a higher order.

Next, only one port of the waveguide is orthogonal. Therefore, the two directivities of the orthogonal input [Figure 4.4(a)] and output [Figure 4.4(b)] are compared. Here, the same result can be observed. In both cases, the orthogonality does not affect the directivity. In addition, the same asymmetries can be observed.

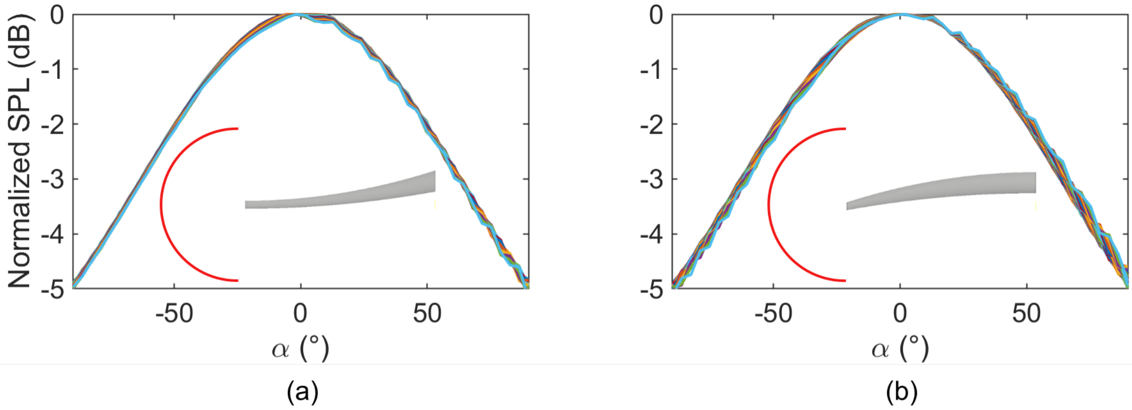

Figure 4.4: The directivity of a waveguide with orthogonal output port (a) and orthogonal input port are compared (b). In both cases, there is no significant influence on the directivity.

However, the offset dependancy of the SPL differs in the two geometries [Figure 4.5(a, b)]. Using only orthogonal output ports results in minima at 7 mm and 22.5 mm. Here, higher modes are created causing losses of up to 8.8 dB. In contrast, using an orthogonal input port suppresses these higher modes. Throughout the entire parameter range, only fundamental modes occur. The maximal loss in SPL is 1 dB. In addition, there is a resonance which increases the SPL by 10 dB.

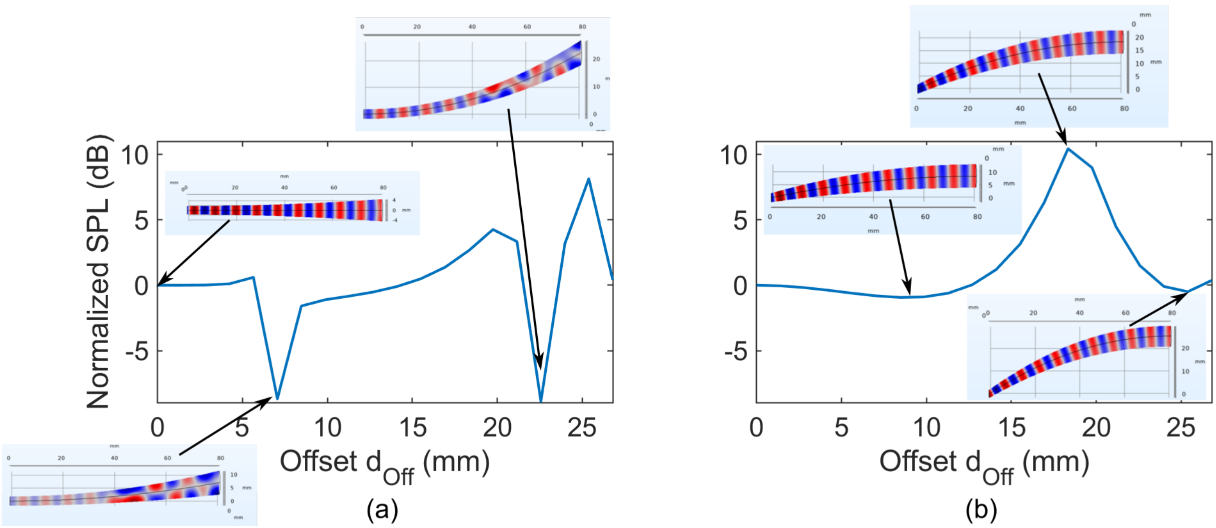

Figure 4.5: The offset has a significant influence on the SPL of the waveguide with orthogonal output port (a). In addition, higher modes occur. In contrast, using an orthogonal input port suppresses higher modes and only allows for fundamental modes (b).

The last investigated geometry provides on both sides, input and output, orthogonal sections. Again, the directivity is no affected by the geometric variation [Figure 4.6(a)]. As already observed for the waveguide with orthogonal input, only fundamental modes occur in this study. The minimal observed SPL loss is 1 dB at an offset of 8.5 mm. This result shows that the input port of an acoustic waveguide needs to be orthogonal. Otherwise, higher modes occur in the input section leading to reduced SPLs. These modes occur, since the diameter at the input is bigger compared to the wavelength. In addition, the output port has not such a drastic influence on the acoustic performance. Since the diameter of the output is small compared to the wavelength, it behaves as a point source at 40 kHz.

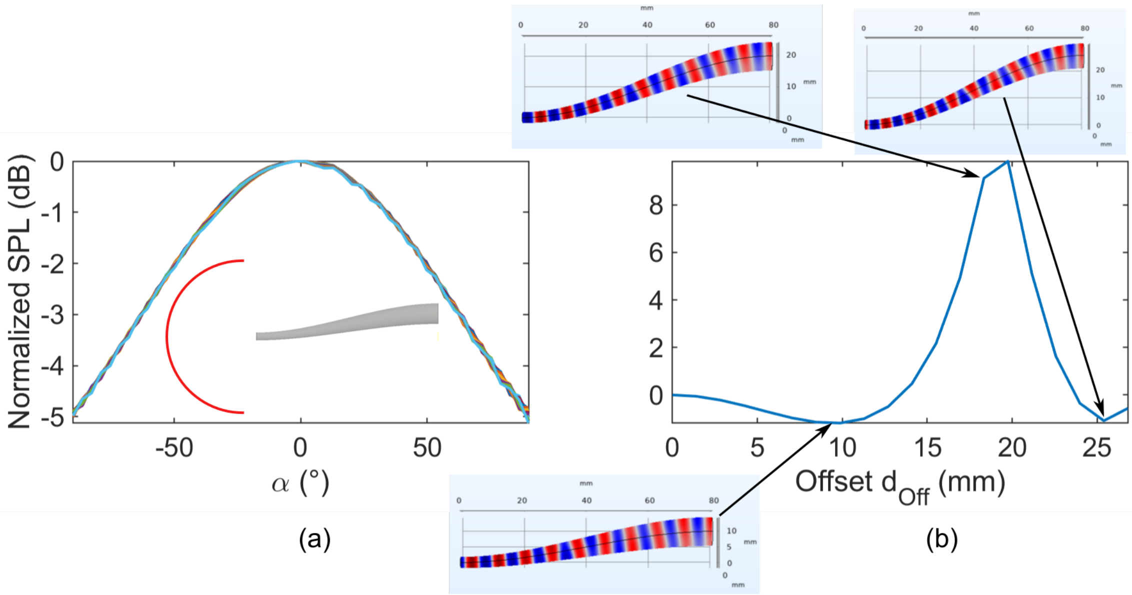

Figure 4.6: Using orthogonal geometries at both sides of the waveguide does not affect the directivity as well (a). Throughout the entire offset study, only fundamental modes are observed (b).

The results of the orthogonality study show, that the direction of the input wave is crucial for the acoustic performance of the waveguide. However, Golinske showed in his work, that the Murata transducer used in the phased arrays have tilted cones due to manufacturers tolerances [36]. This even causes a tilted directivity of up to 10°. Thus, the simulation is extended with an air-filled disk. It has the same diameter as the input port of the waveguide and a height of 1.7 mm. This value is the average distance between the cone and the output surface of Muratas transducers. The simulation varies two parameters. First, the angle of the cone α_{trans} is varied (Figure 4.7). This value changes from 0° up to 10°. In addition, the rotation along the main axis of the transducer β_{trans} is conducted, because during the assembly process of the transducer with the waveguide, the position between cone and transducer base is unknown. Again, the SPL is evaluated at a distance of 1 m.

Figure 4.7: Since the cone of the transducer used in the experiment is tilted, the simulation is extended with a 1.7 mm-cylinder. The angles α_{trans} and β_{trans} adjust the orientation of the imperfection of the cone position.

The resulting SPL for all α_{trans} and β_{trans} combinations are plotted and normalized to the SPL of $\alpha_{\text{trans}} = 0°$ and $\beta_{\text{trans}} = 0°$ [Fig 4.8(a)]. This plot shows a periodicity along both axis. In addition, along the α_{trans}-axis there is a symmetry. This leads to the conclusion, that multiple combinations of the two mentioned angles result in the same SPL. Therefore, all calculated points were plotted in a histogram showing the normalized probability over the normalized SPL. Of all combinations, 83.3% provide a deviation of the SPL of ± 3 dB [Fig 4.8(b)]. This shows that, binning the transducers is crucial for maximizing the output SPL of an entire waveguided array. As a result, using orthogonal input sections for the waveguides provides fundamental modes when the wave is coupled orthogonal. In reality, the transducers manufacturer tolerances cause a deviation of the SPL of ± 3 dB, since the cone of the transducers is tilted.

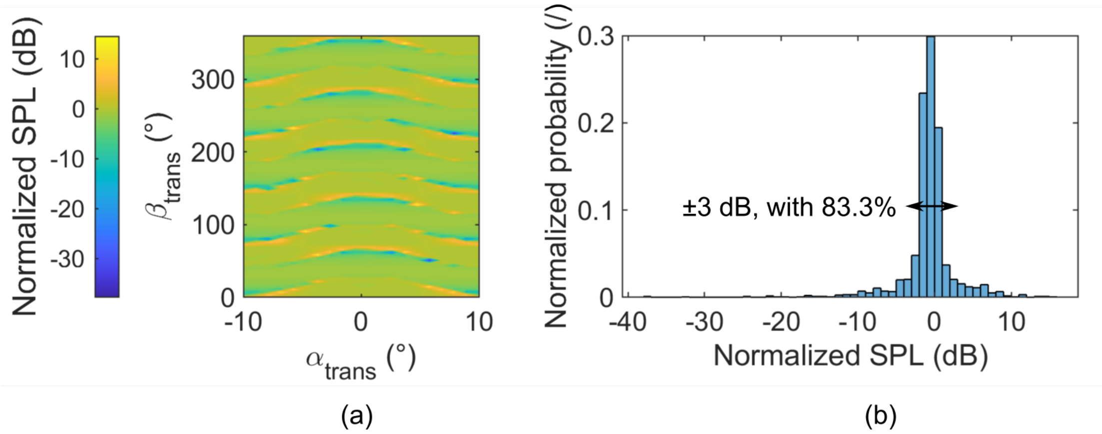

Figure 4.8: The normalized SPL has a periodic pattern when varying the position of the simulated transducers cone (a). Using all results and transforming them into a normalized probability yields an SPL deviation of ± 3 dB with 83.3% (b).

4.2 Acoustic aperture optimization

Using acoustic waveguides for line arrays increases the design freedom of the output aperture by one degree. Thus, not only round shapes [Figure 4.9(a)] can be used but also elliptic [Figure 4.9(c)] and rectangular shapes [Figure 4.9(c)]. Therefore, the length of a rectangular and elliptic output are varied and compared with each other. This way, the main lobe can be narrowed in one dimension and the overall SPL is increased. The simulation of the round output is conducted as a reference for the normalization of the SPL. For the simulations, the height of the shapes is fixed with 3.4 mm and the width w_{aperture} is increased. Again, SPLs are evaluated at a distance of 1 m with a frequency of 40 kHz.

The width increase of the ellipsis can be divided in multiple sections. First, a wide directivity occurs [Figure 4.10(a)]. Here, the width variation is smaller compared to the wavelength causing no additional side lobes. At a width of 11.2 mm the first minima occur showing the beginning of the first side lobes.

Next, the main lobe starts to narrow [Figure 4.10(b)]. At a width of 51.4 mm the main lobe defocuses, which decreases the SPL in its center [Figure 4.10(c)]. With further increase of the width the main lobe starts focusing again [Figure 4.10(d)]. For bigger widths, the main lobe switches between focusing and defocusing [Figure 4.10(e, f)].

This effect occurs due to different propagation lengths inside the waveguide. The center line and the length at the edge create a pressure distribution at the output surface. This distribution determines whether the main lobe is focused or defocused.

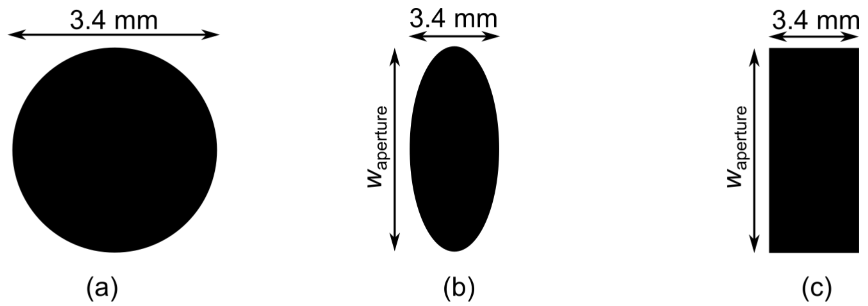

Figure 4.9: In order to optimize the output aperture, a variation of the width of an ellipsis (b) is compared with the width variation of a rectangle (c). The round shape is used as a reference SPL (c).

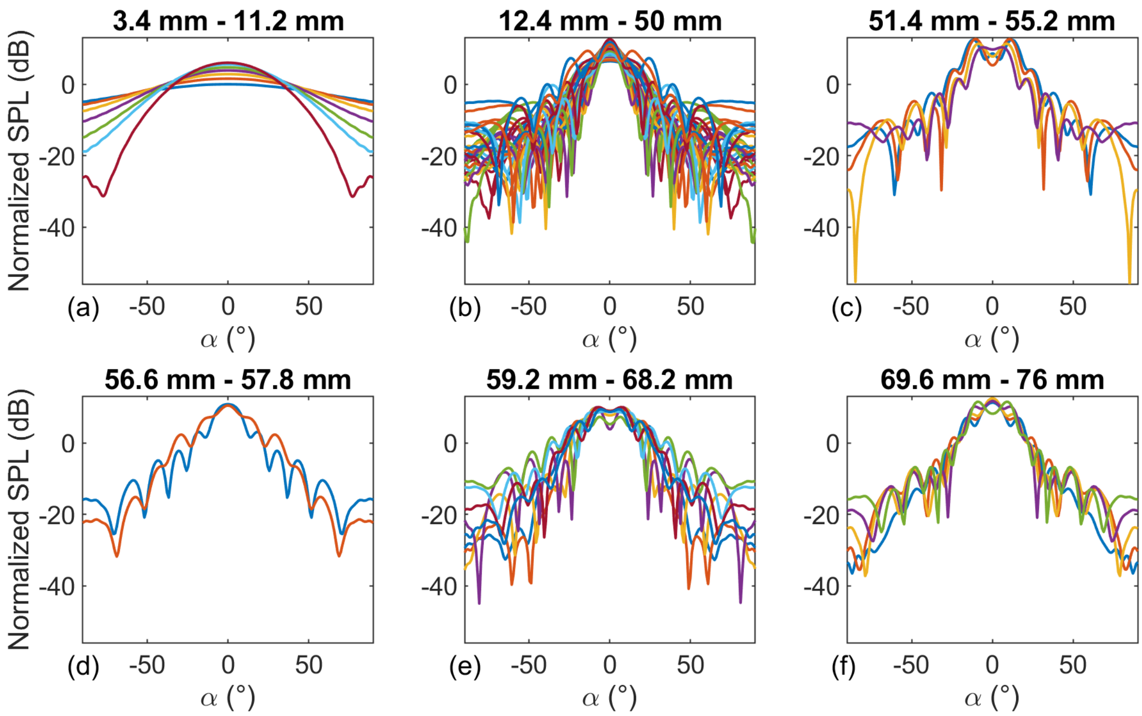

Figure 4.10: Varying the width of the elliptic output aperture results in a narrowing of the main lobe (a). With further increase of the width, a focused main lobe can be achieved (b). However, at a certain width, the main lobe defocuses (c). Afterwards, the directivity pattern alternates between focusing and defocusing (d-f).

This effect can be observed when comparing the SPL and the HPBW. First, the SPL is increased with increased width because the HPBW is decreased (Figure 4.11). However, after 32 mm multiple minima occur due to the defocused main lobe. In these ranges, the HPBW is increased. Each time the main lobe is defocused, the SPL in the center is decreased because the pressure distribution widens which increases the HPBW.

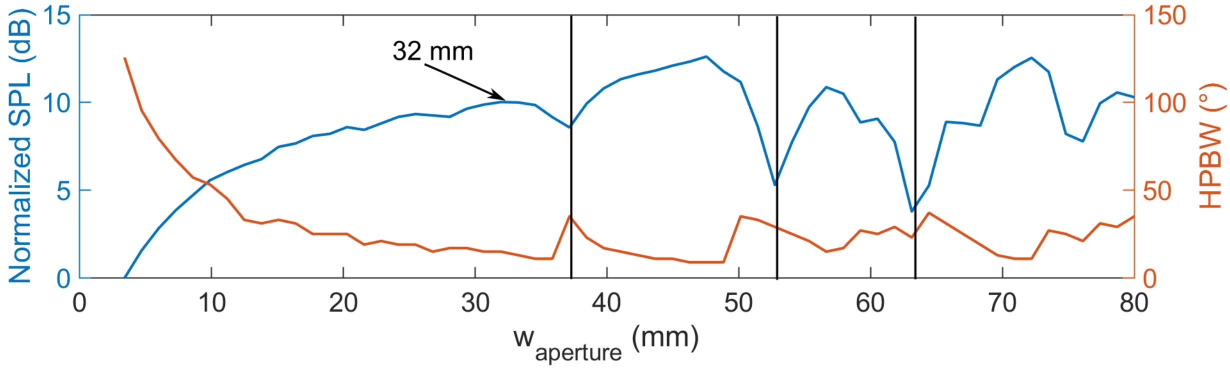

Figure 4.11: Increasing the width of the elliptic aperture increases the SPL and decreases the HPBW. In addition, the SPL and HPBW have opposing tendencies.

Next, the simulation is repeated but with a rectangular aperture. In addition, the receive performance is simulated for both geometries. Therefore, a 0.1 mm thick disk with a diameter of 10 mm is located at a distance of 1 m. The disk is excited with a normal velocity of 1 m/s at a frequency of 40 kHz.

In transmit, the overall SPL of the rectangle is 1 dB higher compared to the ellipsis with the same width [Figure 4.12(a)]. This result can be explained with the effective area of both geometries. When comparing the area of a rectangle and an ellipsis, the rectangle has always a higher area by a factor of $4/\pi$, due to the filled corners, i.e.

$$\frac{A_{\text{Rectangle}}}{A_{\text{Ellipsis}}} = \frac{h_{\text{aperture}} \cdot w_{\text{aperture}}}{\frac{h_{\text{aperture}}}{2} \cdot \frac{w_{\text{aperture}}}{2} \pi} = 4/\pi. \tag{4.1}$$

Due to the higher acoustic aperture the radiated SPL of the rectangle is increased. For this reason, the SPL of both geometries is compared by using the respective areas. Here, both shapes have the same SPL until an area of $100\,\text{mm}^2$ [Figure 4.12(b)]. Afterwards, the SPL values differ since the two geometries produce different modes inside the duct.

In receive mode, the same result can be observed. In general, the rectangle receives a higher SPL with 1 dB compared to the ellipsis [Figure 4.12(c)]. When normalized to the area, both geometries receive the same SPL until an area of $100\,\text{mm}^2$ [Figure 4.12(d)]. Afterwards, they differ due to different modes. As a result, the rectangle has a higher transmitted and received SPL ($+1$ dB) compared to the ellipsis. The maximum width that can be used is 32 mm for a frequency of 40 mm. Using the widened rectangle, the SPL can be increased by 11.6 dB compared to the round aperture. The same result applies for the receive mode.

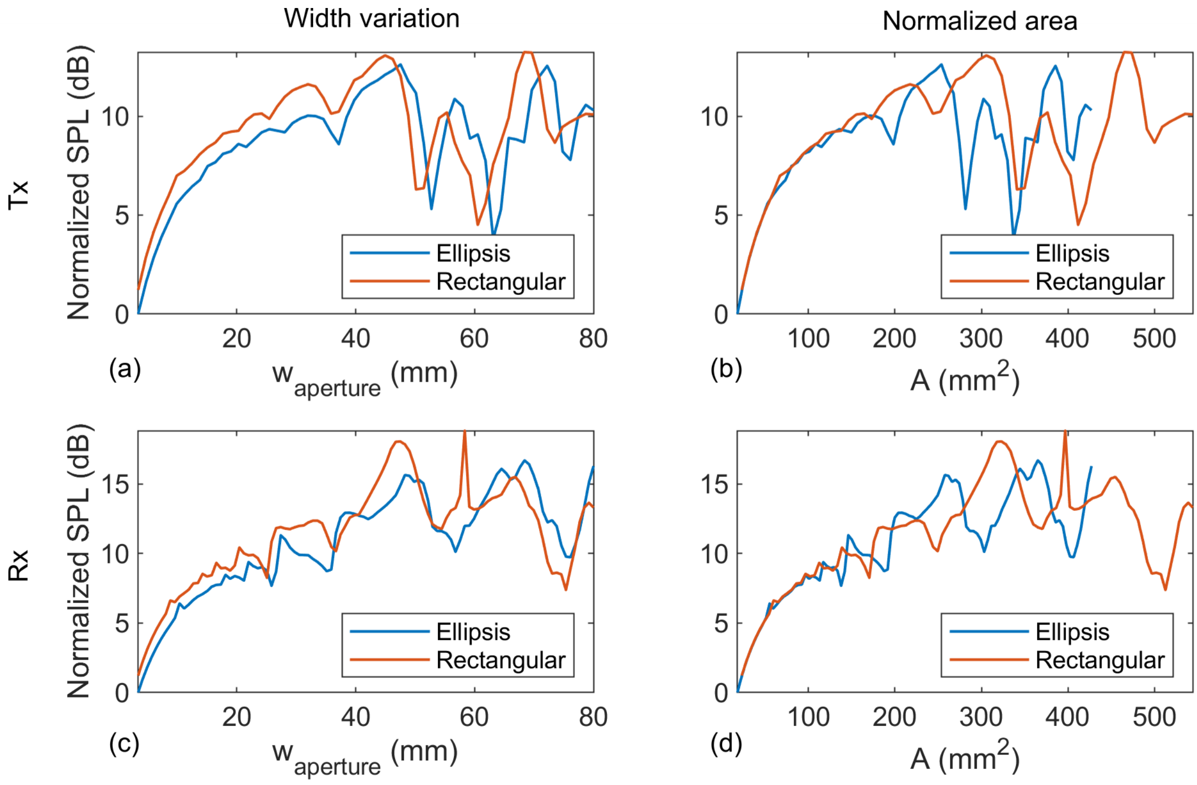

Figure 4.12: In general, the rectangle aperture has a higher SPL of 1 dB compared to the elliptic shape(a). For better comparison, the area of both geometries is used, which shows similar SPL values (b). The same results from the transmit simulations can be observed in receive mode (c), (d).

4.3 Length optimization and temperature influence

Acoustic waveguides can be compared to Helmholtz resonators. Since the length of the waveguide determines its resonance frequency, the SPL can be optimized for a frequency of 40 kHz. Im more detail, the resonance depends on the ratio between the length of the waveguide and the wavelength. Thus, the temperature needs to be considered, since it changes the wavelength. Therefor, two simulations were conducted. First, the length of the duct is increased from 10 mm up to 80 mm. The SPL is evaluated at a distance of 1 m. Afterwards, the same geometry is used but the temperature is increased from $-25°$C up to $75°$C.

The length variation shows multiple maxima and minima [Figure 4.13(a)]. The minima occur at a length of $(0.5n + 0.887) \cdot \lambda, n \in \mathbb{N}$ and the maxima occur at $(0.5n + 1.134) \cdot \lambda, n \in \mathbb{N}$. In both cases correction factors appear. These are needed due to the end correction of the duct [59]. Since the diameter in the input section is bigger compared to the wavelength, the model of a plane wave propagation is not applicable anymore. This can be compensated with the method of end correction. In addition, the SPL variations are ± 4.3 dB over the simulated range. In theory, the SPL can be optimized to one of the maxima.

However, the simulation of the temperature variation shows a similar influence [Figure 4.13(b)]. Over the entire temperature range the SPL variation is nearly in the same range with ± 4.8 dB as the length variation. In addition, there is a decreasing tendency of the SPL. This is caused by the temperature induced increase of the wavelength. This leads to a wider directivity which decreases the SPL in the center of the main lobe. As a result, the increased SPL due to length variation can only be maintained under controlled environmental influences and is not applicable for a product with high temperature ranges.

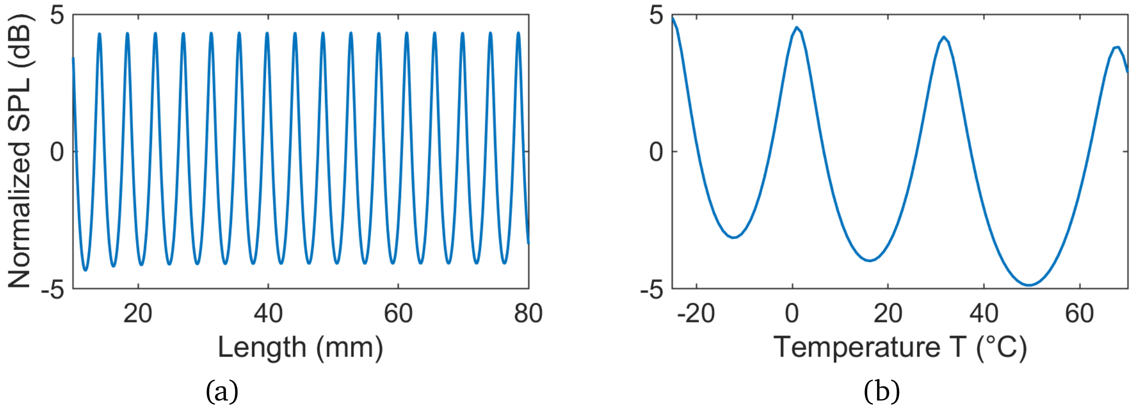

Figure 4.13: The variation of the waveguide length varies the SPL between ± 4.3 dB (a). A varying temperature has nearly the same influence of ± 4.8 dB (b).

4.4 Position of tapering

The last geometric parameter which is investigated is the positioning of the tapering. Therefor, a straight duct was simulated and the support points of the Bézier shapes are varied. This tapering factor ranges from 0 to 2. The tapering factor of 1 resembles the value which is used in previous work. Thus, this parameter 1 serves as a reference for SPL normalization. As a result the normalized SPL ranges from -0.22 dB to $+0.34$ dB (Figure 4.14). In conclusion, the positioning of the tapering has just a minor influence on the SPL and is not further investigated.

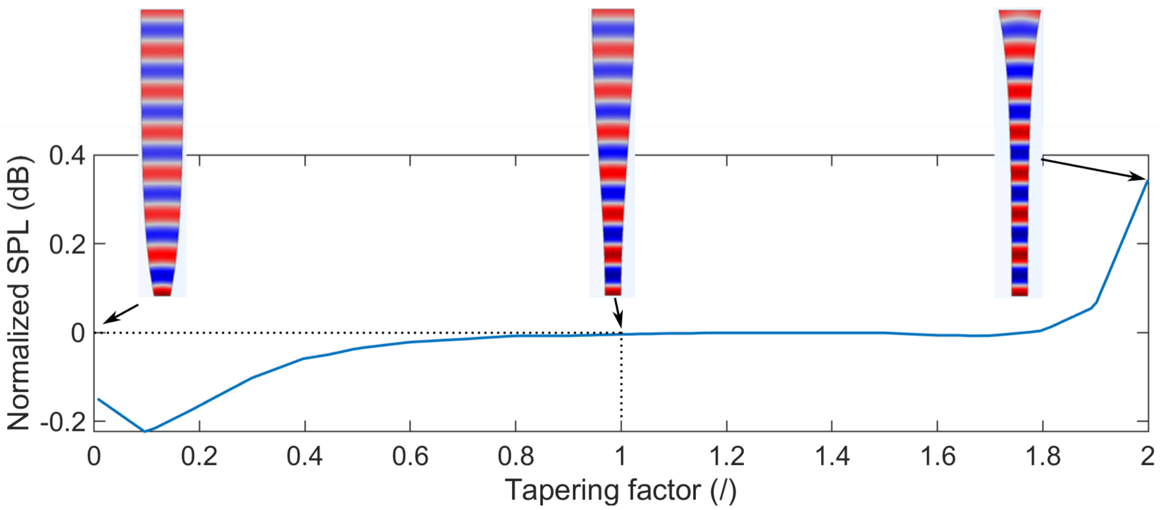

Figure 4.14: The positioning of the tapering has no significant influence on the SPL.

4.5 Losses in acoustic waveguides

In previous work, the acoustic losses of the waveguide compared with a bare transducer were measured [35]. As a result, the measured losses were 7.1 dB. However, the acoustic mechanics inside the waveguide are far more complex to analyze the losses with one microphone measurement in the far-field.

When an acoustic wave is emitted by the transducer, first the wave losses energy due to friction with the inner walls of the waveguide. These are the well known thermoviscous losses in duct acoustics. Afterwards, the pressure is increased due to the reduction of the cross sectional area. At the end of the waveguide, an abrupt geometry change of the air volume occurs into the free-field. This causes an impedance discontinuity leading to wave reflections at the output of the waveguide. Part of the acoustic energy is reflected back into the waveguide. Last, the tapered duct increases the directivity width. Thus, the SPL in one single point in the free-field is reduced, since the pressure distribution widens introducing diffraction loss. In this chapter, all these four mentioned effects are analyzed in more detail using numerical simulations.

4.5.1 Numerical model

The simulations are conducted in the time domain. Since the different effect superpose in the steady state, using the frequency domain increase the difficulty to distinguish the different effects. For instance, the reflection of the wave at the end of the waveguide superposes with the effect of pressure increase due to the decreasing diameter of the duct. In addition, it is not possible to conduct first a simulation without thermoviscous losses and afterwards with these effects to show there isolated influences. The thermoviscous losses change the acoustic impedance of the duct, and, thus, change the reflection coefficient as well. Thus, the simulations are divided into three steps.

First, only the surface of the transducer is used in the model as a reference. The model is two dimensional with a rotational symmetry [Figure 4.15(a)]. In order to reduce the model size, a perfectly matched layer (PML) is used to attenuate all emitted sound waves. This allows for time efficient simulations. The PML has a thickness of 10 mm and the radius of the air volume is 40 mm. The transducer is excited with a pressure of 1 Pa and two sinusoidal cycles with 40 kHz. Additionally, the sound pressure received by the microphone is averaged over the area (diameter 3.175 mm) of the receiver. All calculations were conducted using COMSOLs thermoviscous transient package.

Second, a straight waveguide is added to the model with a closed end. This simulation provides ideal reflections at the end of the waveguide allow for investigating just the thermoviscous losses and the pressure increase due to the tapering. The waveguide has a length of 80 mm [Figure 4.15(b)].

Last, the same waveguide is used in an open simulation including the free-field [Figure 4.15(c)]. Here, the reflection of the wave at the output can be evaluated. In addition, the same microphone model is used as in the first simulation. This way, the entire losses can be calculated.

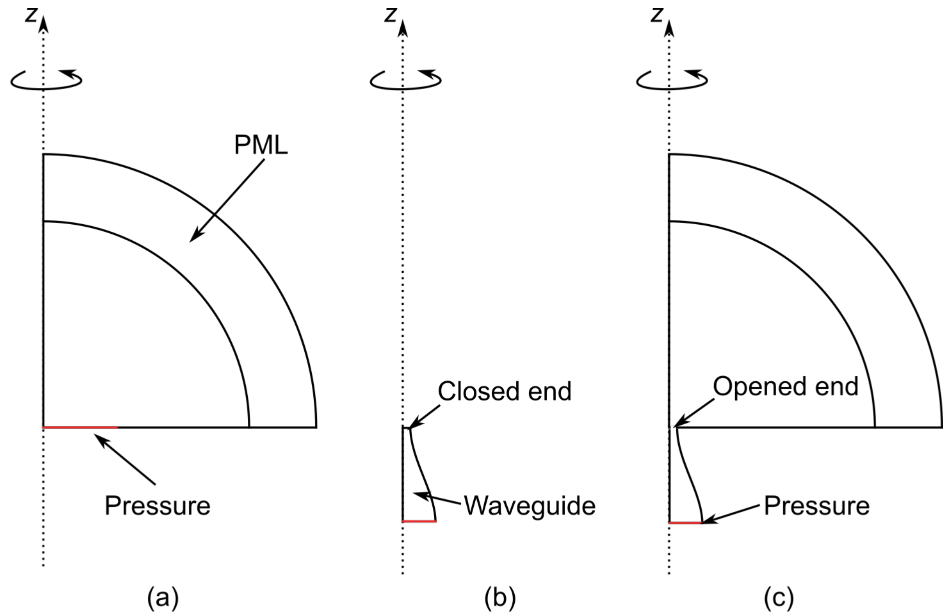

Figure 4.15: The simulations of the acoustic losses are divided into three steps to isolate the acoustic effects. First, the single transducer without the waveguide is simulated (a). Afterwards, the waveguide with closed end is simulated, in order to evaluate the thermoviscous losses and the effect of the tapering. Last, the waveguide is opened to the free-field, to simulate the reflection losses and the diffraction loss.

In order to analyze the different losses, the absolute pressure is evaluated at different positions in the pressure field. Please note, all absolute pressure have a different scaling, since the three different scenarios produce different pressures.

First, the absolute pressure for the bare transducer compared with the waveguided transducer is compared at the microphone position [Figure 4.16(a)]. In the simulation the microphone is located at a distance of 34 mm. This position can be validated in the time signal. This curve yields a distance of 34.3 mm between the transducer and the microphone. The waveguided transducer signal has a bigger time delay due to the length of the waveguide. It adds additional 80 mm yielding a distance of 114.3 mm. In addition, the total loss between these two pressures is 10.07 dB. This value serves as a reference loss for the entire acoustic system.

Second, the losses due to thermoviscous effects and the tapering is analyzed with a closed waveguide. The evaluation points are directly on the surface of the transducer (Input) and at the end of the waveguide (Output) [Figure 4.16(b)]. The thermoviscous losses can be calculated by comparing the first cycle of the incident wave with the reflected wave. The other cycles are not useful for this comparison, since the wave cycles superpose at 0.49 ms. These thermoviscous losses need to be divided by two, because the wave undergoes the friction two times in this simulation. As a result, The thermoviscous losses are 1.72 dB. In addition, there is a pressure increase when comparing the sound wave at the input with the output. Due to the tapering, the cross-sectional area is decreased, which increases the pressure by 14.37 dB. Furthermore, the time delay is plausible, since the length of the waveguide with 80 mm can be observed as well.

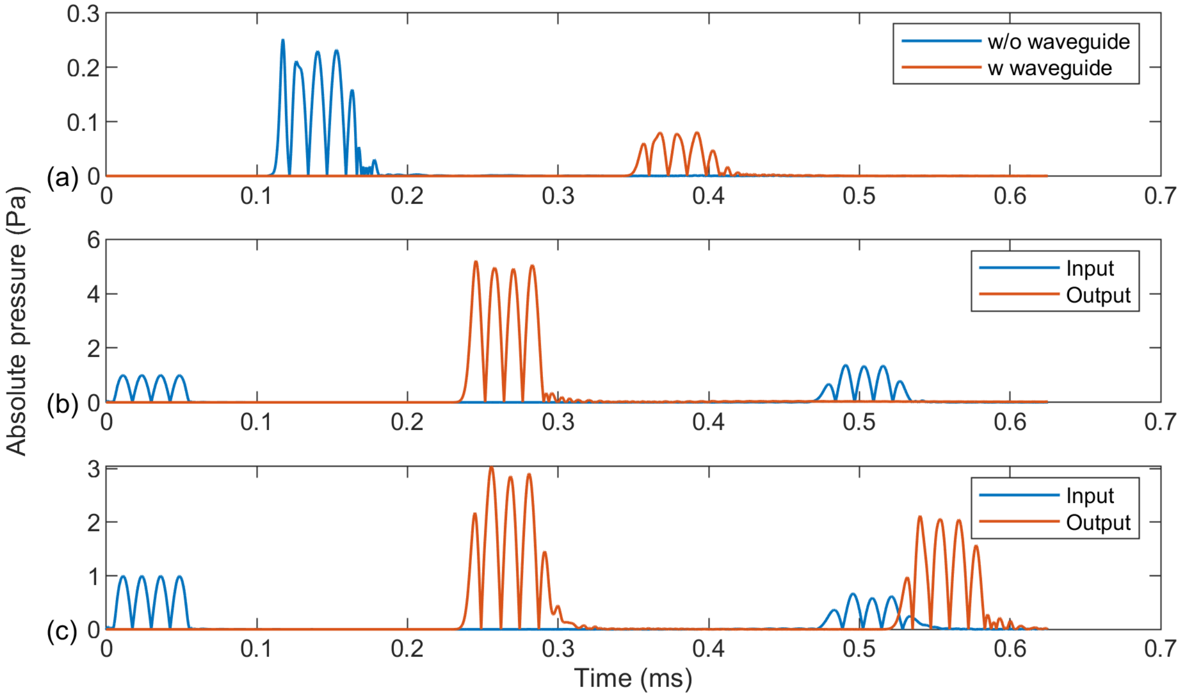

Figure 4.16: The total loss due to the waveguide is 10.07 dB (a). Due to the tapered duct the pressure is increased by 14.37 dB and the thermoviscous losses are 1.72 dB (b). Last, the evaluated pressures for the open model yields reflection losses of 5.31 dB and diffraction losses of 17.4 dB (c).

Last, the waveguide is connected to free-field [Figure 4.16(c)]. The reflection losses are determined by evaluating the pressure at the input of the waveguide. Therefore, the first cycle of the incident and reflected wave are compared and the thermoviscous losses from previous simulations are subtracted. These losses are 5.31 dB. Afterwards, the diffraction loss is calculated by comparing the pressure and normalize it to the respective aperture size of the microphone, transducer and output of the waveguide. This approach yields a diffraction loss of 17.4 dB.

When combining all these losses, a total loss of 10.05 dB can be observed. This value differs only in 0.02 dB from the reference losses of the simulations. In comparison with the measurements in previous work, the losses are 3 dB higher. This difference can be explained with the influence of the cone position of the transducer. As in previous chapter explained 4.1, the angle of the transducer cone influences which acoustic mode is excited inside the waveguide. This can create SPL variations of up to ± 3 dB. Regarding this effect, the simulations are plausible compared to the measurements.

Table 4.1: Comparison of the different losses inside the waveguide of the numerical simulations.

Name of the effect	Affect on the SPL (dB)
Tapering of the duct	$+14.37\,\text{dB}$
Thermoviscous losses	$-1.72\,\text{dB}$
Reflection	$-5.31\,\text{dB}$
Diffraction loss	$-17.4\,\text{dB}$
$\sum$	$-10.05\,\text{dB}$
Reference loss	$-10.07\,\text{dB}$

4.5.2 Experimental validation

In order to validate the simulations, at least two microphones need to be inserted into the waveguide. The first is located at the input port of the waveguide next to the transducer and the second is located at the output of the waveguide. These microphones must not disturb the sound field. Otherwise, measurement feedback is created which corrupts the measurements. Thus, small mems microphones (Knowles, SPU0410LR5H-QB) were used in the experiment. They have an aperture of just $0.25\,\text{mm}$ and are soldered onto a custom PCB. The size of the top end of the PCB is $22\,\text{mm} \times 3.65\,\text{mm}$ with a height, including the soldered components, of $3\,\text{mm}$ [Figure 4.17(a)]. The microphone can be directly connected to an oscilloscope. For adequate measurements, the microphone needs to be implemented into the waveguide with a tight fit. Otherwise, acoustic cavities will occur which provide additional acoustic filters. Therefore, microphone sockets were designed into the waveguide [Figure 4.17(b)]. This way, the microphone is directly connected to the inner surface of the waveguide. Again, this waveguide has a length of $80\,\text{mm}$ with a transducer socket of $7\,\text{mm}$. The input diameter is $10\,\text{mm}$ and the tapered output diameter is $3.4\,\text{mm}$. The end of the waveguide is opened.

During the experiments, the transducer is driven with only two cycles and a voltage of $1.5\,\text{V}_{\text{RMS}}$ at $40\,\text{kHz}$. The reduced cycle number was used because, inside the duct the incident wave and the reflected wave must nor superpose. Otherwise, the different acoustic effects can not be separated. In addition, the driving voltage was reduced to avoid clipping of the microphones. Prior to each measurement, the two microphones were calibrated with a reference transducer at $40\,\text{kHz}$. Last, the transducer is rotated in $90°$ steps in its socket. Therefore, the influence of the modes can be observed. The microphone PCB was designed by David Dahlim in his masters thesis and the experiment was set up and conducted by Leon Schultz-Fademrecht in his bachelor thesis.

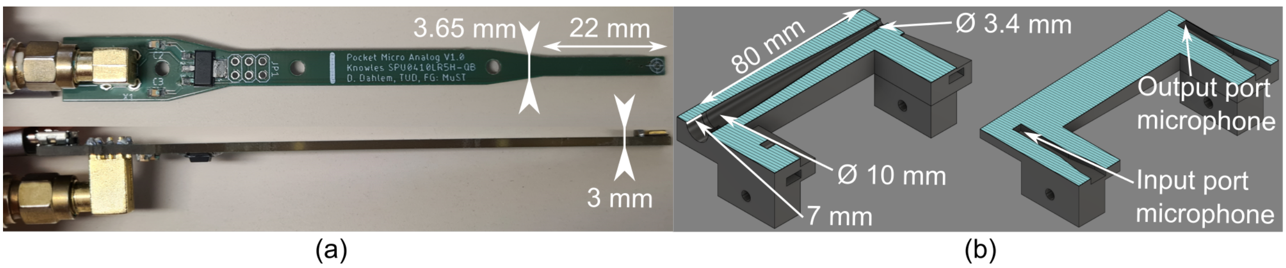

Figure 4.17: The mems microphone is soldered onto a custom PCB (a). In order to implement the microphones into the waveguide, two sockets were designed at the input port and the output port of the waveguide (b).

First, the signal of the microphone at the input port of the waveguide is analyzed. In general, the rotation of the transducer has an influence on the overall ultrasound [Figure 4.18(a-d)]. The envelope changes depending on the orientation. In addition, the signal amplitude and the time delay differs. The maximum value of the amplitude has a deviation of ± 1.7 dB. This influence is on the same level as the simulated thermosviscous losses of ± 1.72 dB. Additionally, the time delay differs by 9.4%. The first reflection occurs at 0.21 ms. However, this value varies by 6.6% depending on the rotation of the transducer. Last, the sound pressure of the incident wave and the reflected wave can be compared. Due to the before mentioned effects, the reflected sound wave has a loss of 5.5 dB $\pm$ 0.35 dB. All these results proof the simulations of the transducers cone influence. As a result of manufacturing tolerances, the cone can be tilted and rotated. This leads to a tilted sound wave coupling between the transducer and the waveguide. Consequently, the simulation results of this influence can be shown with this measurement.

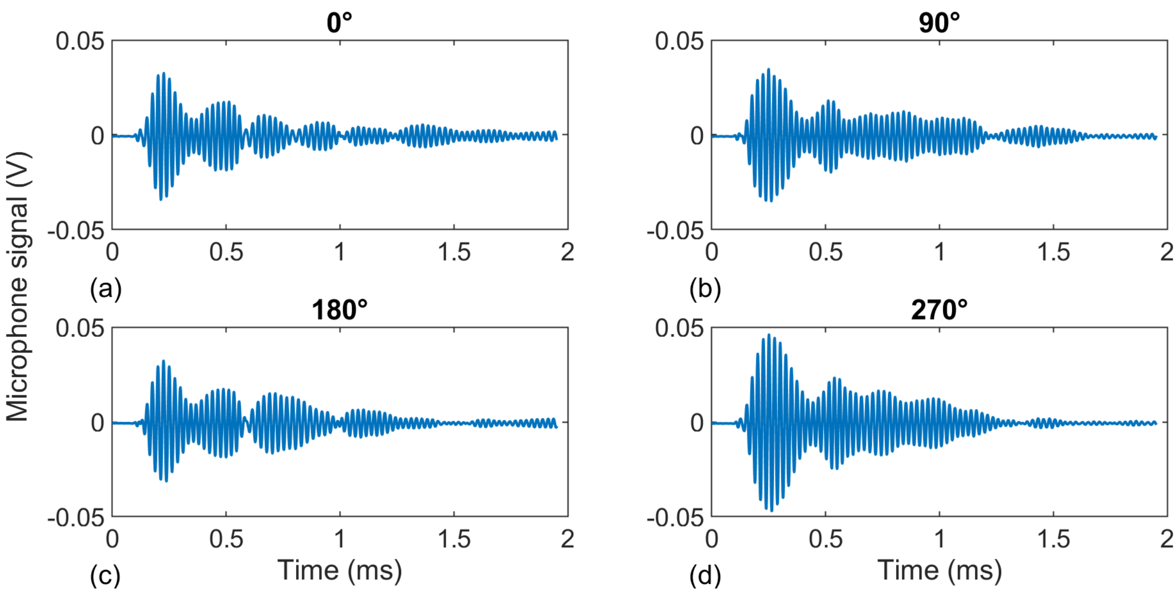

Figure 4.18: The ultrasound at the input port of the waveguide is analyzed by placing a microphone directly next to the transducer. Afterwards, the transducers rotation is varied in the socket resulting in different microphone signals (a-d).

Second, the signal at the output port is analyzed. Here the influence of the transducers rotation is less significant [Figure 4.19(a-d)]. The maximum signal varies by ± 0.1 dB. In addition, the time delay of this peak varies by 5.5%. The first reflection varies by ± 1 dB in amplitude and the time delay varies by 2.9%. As a result, the tapering of the diameter force a plane wave propagation inside the waveguide. Thus, the rotation of the transducer is less influential, since the mode shape does not depend on the inclination angle of the sound wave. However, when comparing the acoustic losses between the input and output microphone of all four angles, the signal varies 1.1 dB $\pm$ 1.8 dB. Since the uncertainty is larger than the averaged value, this experiment is not usable to separate all acoustic losses and therefore is not used to validate the simulations.

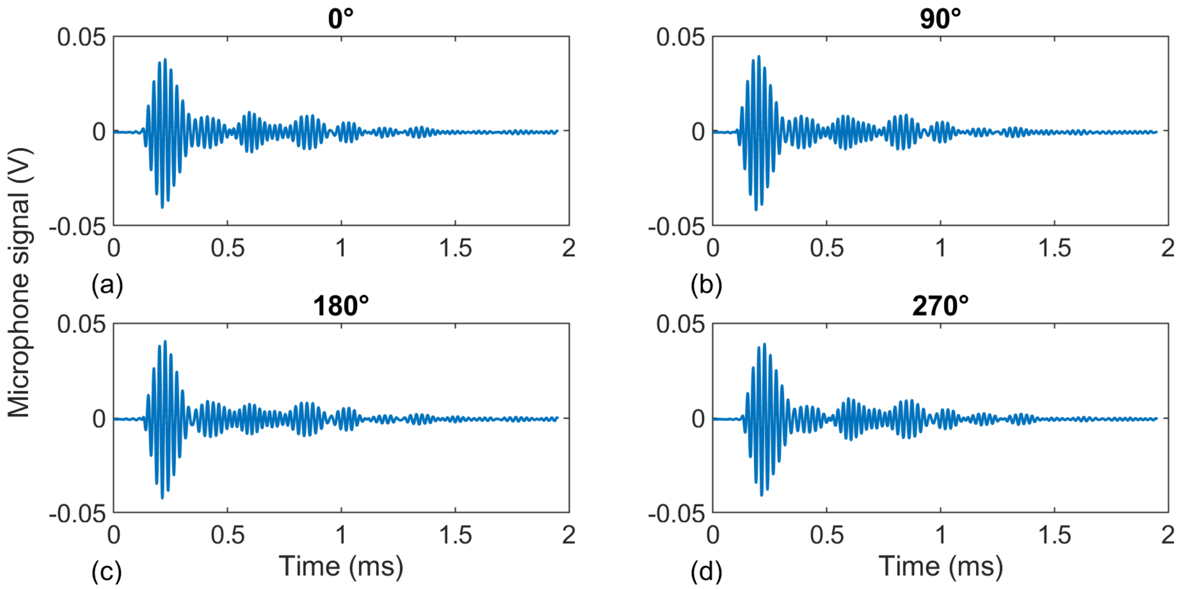

Figure 4.19: The output signal of the waveguide is not influenced by the transducers orientation (a-d).

In order to improve the setup, there are multiple aspects that need to be considered. First, the transducer needs to be exchanged. A small broadband capacitive ultrasonic transducer will solve most of the issues. Due to a higher bandwidth, the rise and decay time of the signal is reduced. This allows for an easier distinction between the incident wave by the transducer and the reflected wave by the output port. In addition, a plane output surface of the transducer offers orthogonal acoustic coupling between the transducer and the waveguide. This will drastically reduce the influence of the transducers rotation in the socket. However, to this date there is no transducer on the market with these properties and a diameter of 10 mm. Furthermore, there is still a disadvantage of this method. In the first phased arrays Muratas transducers are used. Since the transducer and the waveguide build a coupled system, changing the transducer will result in different array specifications. Thus, a new array must be build, characterized and compared with previous work.

4.6 1D line arrays with optimized geometry

The previous analysis of the waveguide geometry showed multiple ways to improve the geometry regarding increased SPL and reduction of size. Therefore, four waveguides for a 1D line array are designed, simulated and characterized. This way, the complexity of this waveguide is reduced in four steps. First, only eight transducers are used in a 1D line array reducing the number of transducers compared to the 8×8 array in previous work. Second, Bézier curves were used for the construction of the ducts in the waveguide. Consequently, all transducers are located on the same plane, which allows for easy PCB plug-in. Third, instead of using round output ports, rectangular shaped output ports were used, thus increasing the SPL in transmission and allowing more sensitivity in reception. Fourth, the length of the waveguide is reduced creating a more compact design.

All waveguides are designed for eight of Muratas MA40S4S transducers. Thus, the input diameter again is 10 mm. All waveguides consist of eight independent ducts each with tapering diameter. This way, the output port is reduced to 3.4 mm allowing for an inter element spacing of half the wavelength.

The first waveguide consists of ducts with the same length of 80 mm hereafter referred to as *equal length* *waveguide* [Figure 4.20(a)]. Since each of the eight ducts has a perpendicular connection to the transducers, each transducer socket is tilted. This leads to a time consuming assembly process of each of the transducer, because air wires are needed for an electrical connection between the transducers and the electronics.

The second waveguide reduces this assembly time by using Bézier shaped ducts hereafter referred to as *Bézier waveguide* [Figure 4.20(b)]. This way, all transducers are in the same plane and can be soldered onto a plane PCB. However, this introduces different propagation times of the sound waves inside the ducts since each Bézier curve has a different length. These lengths are calculated using Bernstein polynomials which are used to apply additional time delays as compensation.

The third waveguide consists again of Bézier shaped ducts but with rectangular output ports instead of round output ports hereafter referred to as *rectangular Bézier waveguide* [Figure 4.20(c)]. This way the SPL can be increased since the directivity is narrowed. In addition, the sensitivity increases due to the increased receive area. The optimal size of 16 mm for this output was determined using a BEM in COMSOL Multiphysics.

The fourth waveguide is again a rectangular Bézier waveguide but with a reduced length of 28 mm hereafter referred to as *short Bézier waveguide* [Figure 4.20(d)]. The reduced size of the waveguide is important for possible applications in order to save space. The length of 28 mm is limited by the minimal thickness between the ducts which is in this case 0.6 mm. Since the waveguides are 3D printed, the limitations of the fabrication needs to be considered.

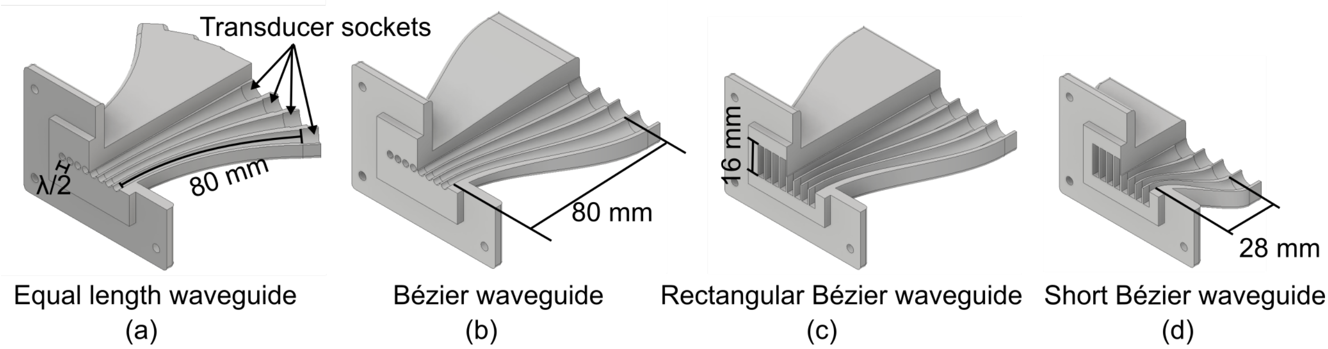

Figure 4.20: The acoustic waveguide reduces the inter-element spacing to half wavelength by using tapered ducts. The first waveguide consists of ducts of equal length (a). By using Bézier shaped ducts the waveguide provides PCB compatibility (b). The switch from round output ports to rectangular output ports allows for an increased acoustic surface improving transmission and reception (c). The fourth waveguide consists of Bézier shaped ducts, rectangular output ports and a reduced length of 28 mm (d).

All simulations were conducted using the BEM of COMSOL multiphysics. Calculations were conducted in the Frequency domain using the Helmholtz equation. In order to reduce the calculation time, only a half of the waveguide geometry is used in the model and a symmetry plane is applied to the cut. Ideal piston transducers were used as excitation at 40 kHz. In addition, the ambient temperature, humidity and pressure from the measurements were added to the model. The SPL is evaluated at a distance of 1 m. In order to investigate the influence of the waveguide geometry on the SPL, the SPL values are normalized to the maximal SPL of the *equal length waveguide*.

The *equal length waveguide* has a HPBW of 13°. In addition, the SLL is 12.5 dB. The *Bézier waveguide* has a decreased SPL of 1.7 dB. Since each duct of the waveguide has a different length, this causes an uneven amplification of the acoustic waves. Thats the reason why the SPL is reduced. In addition, the

HPBW retains nearly unchanged with $12°$. In contrast to the *equal length waveguide*, there is an uneven distribution of the side lobes. The first side lobe has a lower amplitude compared to the second one. This is another result of the uneven pressure distribution at the output ports due to the different duct lengths. The maximum SLL is -11.4 dB. In contrast, the *rectangular Bézier waveguide* has an even distribution of the side lobe amplitudes. The SLL is 14.3 dB. Again, the HPBW is nearly the same with $12.6°$. The SPL is 4.6 dB higher compared to the *equal length waveguide*. This is caused by the widen of the output port in one direction. This way, the main lobe is narrowed in one direction leading to a higher SPL in the center of the main lobe. The *short Bézier waveguide* has higher SPL compared to the *equal length waveguide* of 1.4 dB. However, the HPBW is increased by $2.5°$ compared to the *equal length waveguide*. The first side lobe and the main lobe have no clear separation. This is the effect of the reduction of the waveguide length. Due to the higher length deviations of the ducts, the pressure distribution between the output ports deviates. The maximum SLL is 16.8 dB.

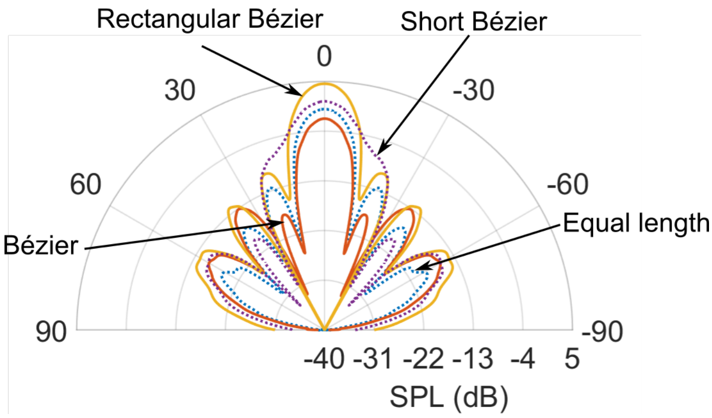

Figure 4.21: The SPL of the simulations were normalized to the maximum of the *equal length waveguide*. By using Bézier shape waveguide the SPL reduced by 1.7 dB. In contrast, the rectangular output ports increase the SPL by 4.6 dB. Last, even the 28 mm-short waveguide has a higher SPL of 1.4 dB in comparison to the *equal length waveguide*.

Table 4.2: Comparison of the influence of the waveguide geometry on the SPL the half power beam width (HPBW) and the side lobe level (SLL).

Waveguide	relative SPL	HPBW	SLL
Equal	0 dB	$13°$	12.5 dB
Bézier	-1.7 dB	$12°$	16.2 dB
Rect	$+4.6$ dB	$12.5°$	14.3 dB
Short	$+1.4$ dB	$15.4°$	16.8 dB

In order to validate the simulations, calibrated measurements were conducted in the anechoic chamber. The environmental properties during the measurements were $18.5°C \pm 0.5°C$, the ambient pressure was 101035 hPa± 1 hPa and the relative humidity was $27.8\% \pm 2\%$. All waveguides were 3D printed using a Prusa i3 MK3S (Prusa Research) and polylactide (PLA, RedlineFilament GmbH). The eight Murata MA40S4S ultrasonic transducers are driven with custom electronics from previous work [34]. In addition, a break out board was used to connect the ultrasonic transducers from the waveguide to the custom electronics. This ensured that the same transducers in the same orientations were used for each waveguide. The transducers are driven with $20\,\mathrm{V_{pp}}$ at $40\,\mathrm{kHz}$ with 30 cycles. The directivity of the waveguides was measured at a range of $1\,\mathrm{m}$.

The *equal length waveguide* creates an SPL of $104\,\mathrm{dB} \pm 1\,\mathrm{dB}$ at a range of $1\,\mathrm{m}$ [Figure 4.22(a)]. The same results can be observed for the *Bézier waveguide* [Figure 4.22(b)]. In addition, the difference of HPBW and the SLL of these two waveguides are within the measurement uncertainty. The *rectangular Bézier waveguide* has an increased SPL of $+7\,\mathrm{dB}$ compared to the waveguides with round output ports. The HPBW is the same as well but the SLL is decreased by $1\,\mathrm{dB}$. As the theory predicts, the increased acoustic aperture of the rectangular apertures increases the SPL since the directivity is narrowed in one direction. The *short Bézier waveguide* has a decreased SPL of $-2\,\mathrm{dB}$ compared to the longer *rectangular Bézier waveguide*. Nevertheless, its SPL is higher compared to the waveguides with round openings of $+5\,\mathrm{dB}$. Compared to the *rectangular Bézier waveguide*, the *short Bésier waveguide* has the same SLL but an increased HPBW by $3°$.

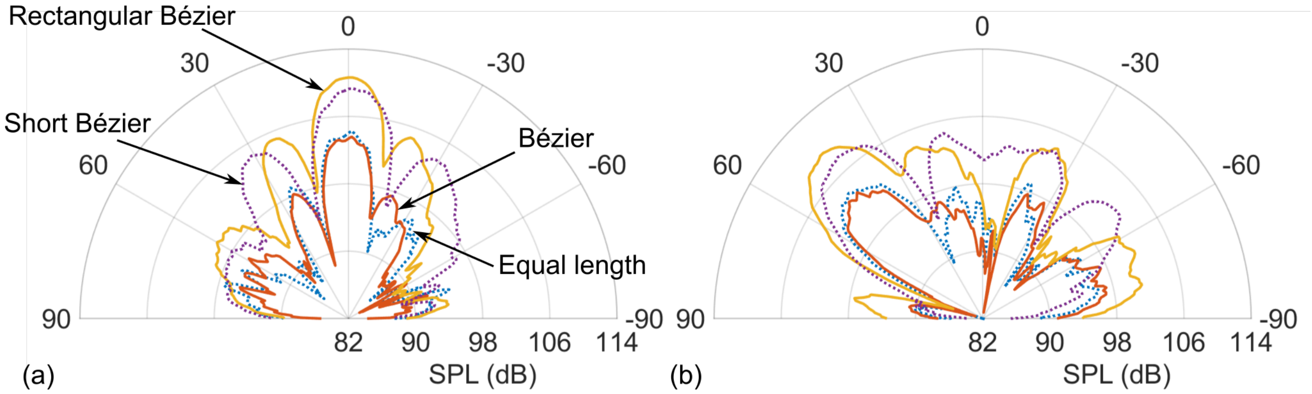

Figure 4.22: Directivity patterns of the equal length waveguide [Figure 4.20(a)], the Bézier waveguide [Figure 4.20(b)], the rectangular Bézier waveguide [Figure 4.20(c)] and the short Bézier waveguide [Figure 4.20(d)] at a steering angle of $0°$ (a) and $45°$ (b).

Next, pulse echo measurements were conducted with a hollow steel sphere with a diameter of $100\,\mathrm{mm}$ located at a distance of $1\,\mathrm{m}$. In receive mode conventional beam forming was used [35].

The results of the directivity measurements are reflected in the pulse echo measurements as well [Figure 4.23(a-d)]. The *equal length waveguide* and the *Bézier waveguide* barely detect the $100\,\mathrm{mm}-$steel sphere at a range of $1\,\mathrm{m}$. The benefits of the rectangular output ports can be observed since both waveguides with rectangular ports have high signal to noise ratio (SNR) compared to the round openings. In addition, the *short Bézier waveguide* has a reduced blind zone compared to the other three longer waveguides by 57%. Since the acoustic wave reflects more often in a shorter duct, the energy dissipation inside the duct is faster compared to a longer duct.

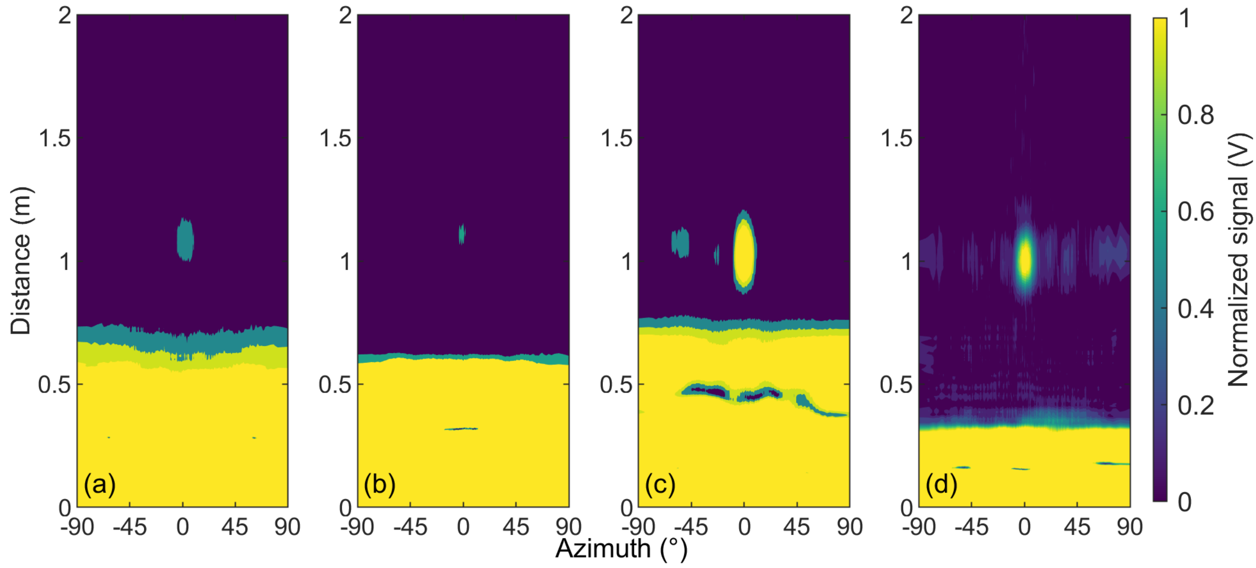

Figure 4.23: In pulse-echo mode the equal length waveguide (a) and the Bézier waveguide (b) can barely detect the 100 mm-steel sphere at a range of 1 m. On the other hand the rectangular Bézier waveguide (c) and the short Bézier waveguide (d) show a clear image of the sphere.

Table 4.3: Comparison of the four measured waveguides regarding its sound pressure level (SPL) at 1 m, its half power beam width (HPBW), its side lobe level (SLL), its length, the blind zone in pulse echo mode and its SNR in pulse-echo mode.

Waveguide	SPL	HPBW	SLL	Length	Blind zone	SNR
Equal	104 dB	15.5°	5.3 dB	80 mm	0.75 m	17.2 dB
Bézier	104 dB	16°	5.4 dB	80 mm	0.63 m	13.5 dB
Rect	111 dB	16.5°	4.4 dB	80 mm	0.76 m	29.8 dB
Short	109 dB	19°	4.8 dB	28 mm	0.32 m	19.9 dB

This work shows that it is possible to improve the overall performance of acoustic waveguides for air-coupled ultrasonic sonar. The 28 mm-short waveguide with the rectangular output ports provides multiple benefits. For example, it has improved transmission and reception performance, a plane transducer orientation providing PCB compatibility, a reduced blind zone in pulse echo mode and no measurable impact on the beam forming capability.

5 Comparison of waveguides with equal length ducts and Bézier ducts

The following chapter was published in [50].

In previous work, the 2D air-coupled phased array with 3D printed waveguide was used in many applications [16], [35], [72]. All these applications benefit from the selected $40\,\mathrm{kHz}$ range, due to its low atmospheric attenuation [73]. However, using an acoustic waveguide with ducts of equal length, the assembly process of the transducers, electronics and waveguide is time consuming. This effort can be reduced by having a plane input surface of the transducers. On the other hand, this results in different duct lengths, which must be compensated for. In this chapter the waveguide with equal length ducts is compared with a Bézier shaped waveguide which reduces the time for the assembly process.

5.1 Geometry of the equal length waveguide and the Bézier waveguide

In this work, the possibility to simplify the geometry of the acoustic waveguide, which leads to an decreased assembly time, is investigated. Therefore, two different waveguide geometries are simulated, characterized and compared. The first geometry is called *arc waveguide*. Its geometry is based on arcs which consists of ducts with equal length. However, this leads to a time consuming assembly of the ultrasonic transducers with the waveguide [Figure 5.1(a)]. In contrast, using Bézier curves as a waveguide geometry reduces the assembly time, since a PCB with transducers can be easily mounted at the input. On the other hand, this approach introduces ducts of varying lengths which must be compensated with additional time delays. In the following, this waveguide is called *Bézier waveguide* [Figure 5.1(b)].

When building acoustic waveguides, there are multiple design rules to avoid acoustic losses. Therefore, the following rules are used for both waveguides. Both waveguides are designed for two-dimensional phased arrays consisting of 64 independent ducts resulting in 8×8 elements. Each duct must be connected to a single transducer. Otherwise, acoustic cross talk between the ducts occurs, when two ducts intersect with each other. Since the ultrasonic transducer MA40S4S [74] is used, the input diameter is $10\,\mathrm{mm}$. Since the resonance frequency of the transducers is $40\,\mathrm{kHz}$, which results in a wavelength of $8.575\,\mathrm{mm}$, the inter-element spacing between the outputs of both waveguides is $4.3\,\mathrm{mm} = \lambda/2$. Therefore, tapered ducts are used for both waveguides. Last, the ducts must be perpendicular to the input and output surface as already investigated in previous chapters.

The arc waveguide consists of 64 independent arcs which have the same length l_{duct} of $80\,\mathrm{mm}$ [Figure 5.1(c)]. All transducers T_{n} have their individual input port with their specific angle leading to perpendicularity. Thus, the assembly between the transducers and the PCB is time consuming.

Next, a second waveguide geometry is investigated, in order to reduce the assembly time. This waveguide consists of 64 Bézier-shaped ducts. This way, all input ports of the waveguide are located on the same plane. As a result, all transducers T_{n} can be assembled with the waveguide using a single PCB [Figure 5.1(b)]. In order to fulfill perpendicularity for the input and output directions, cubic Bézier curves which consist of four Bézier points (B_0, B_1, B_2, B_3) were used [75]. These coordinates are the following,

$$
\begin{aligned}
B_0 &:= (x_{\text{in}}, y_{\text{in}}, z_{\text{in}})\,; && (5.1)\\
B_1 &:= (x_{\text{in}}, y_{\text{in}}, l_{\text{duct}}/3)\,; && (5.2)\\
B_2 &:= (x_{\text{out}}, y_{\text{out}}, 2l_{\text{duct}}/3)\,; && (5.3)\\
B_3 &:= (x_{\text{out}}, y_{\text{out}}, z_{\text{out}})\,. && (5.4)
\end{aligned}
$$

However, since this design leads to ducts with varying lengths, there are varying sound propagation times as well [Figure 5.1(d)].

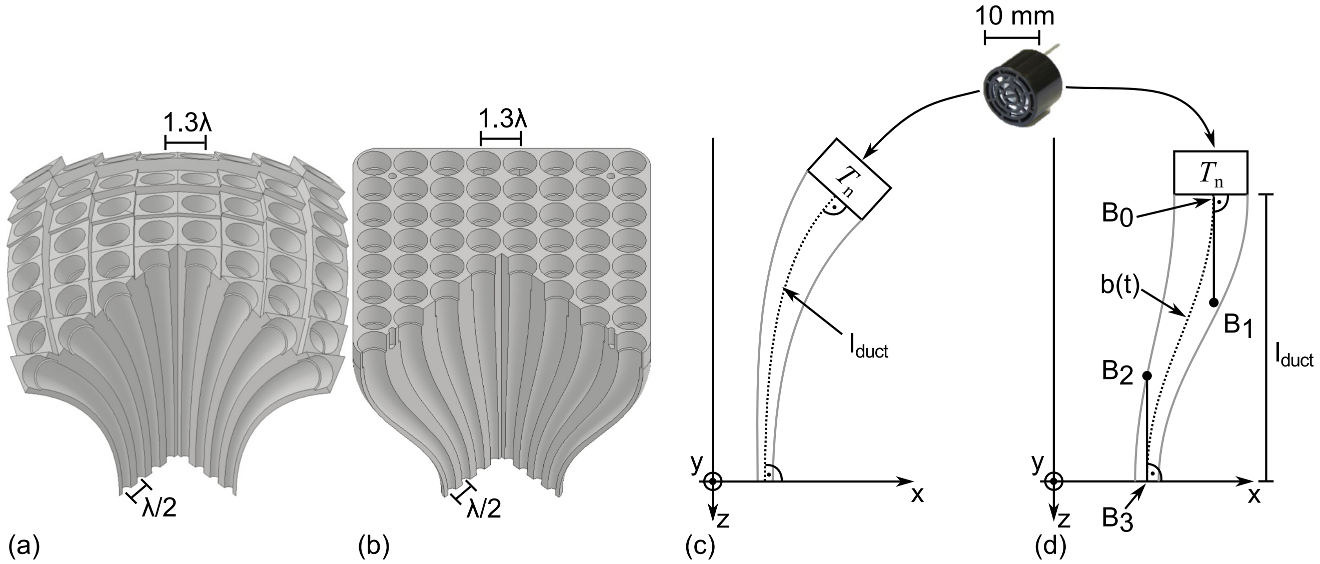

Figure 5.1: The two waveguide geometries consist of arcs with equal length (a) and Bézier curves (b) of non-equal lengths. In both cases each duct has a tapered output diameter of 3.4 mm and provides perpendicularity to the input and output surface of the waveguide. The transducers of the arc waveguide are not mountable on the same plane, since every input port requires a specific mounting angle (c). The Bézier waveguide consists of ducts with varying lengths, but the transducers are mounted on a PCB since they are on the same plane (d).

5.2 Numerical models and validation

Next, the propagation times in the Bézier waveguide are analyze by using analytical, numeric and experimental approaches. These results are used to compensate for the delays with additional electronic delays. First, the Bézier parameters are required for the analytic and numerical calculations. Afterwards, the numerical directivity of the phased arrays is calculated using previous results. Last, all models are validated with calibrated measurements. Please note, that there is a significant difference between the distance of the transducer output to the waveguide output ($l80$ mm) and the actual propagation path $b(t)$ of the wave inside of the Bézier-shaped duct. In order to calculate the propagation path, Bernstein basis polynomials of third order were used, i.e.

$$
b(t) = \sum_{i=0}^{3} \binom{3}{i} t^i (1-t)^{3-i} B_i, \tag{5.5}
$$

with $t \in [0, 1]$ [76]. Additionally, the length of the path is calculated iteratively.

The input section of the ducts has a Helmholtz number He of 3.66, since the input radius r_{duct} of the Bézier-duct is $5\,\mathrm{mm}$ and the wavelength λ is $8.575\,\mathrm{mm}$ [65], i.e.

$$He = 2\pi \frac{r_{\mathrm{duct}}}{\lambda}. \tag{5.6}$$

This geometry supports higher mode wave propagation. Therefore, direct and indirect sound path inside the duct are considered leading to plausibility ranges of the propagation time. There are three possible propagation paths based on Bézier curves for the analytic model. First, the path is along the center line of the Bézier duct. Second,the path follows the shortest possible Bézier line inside the duct. Third, the path leads along the longest possible Bézier line inside the duct [Figure 5.2].

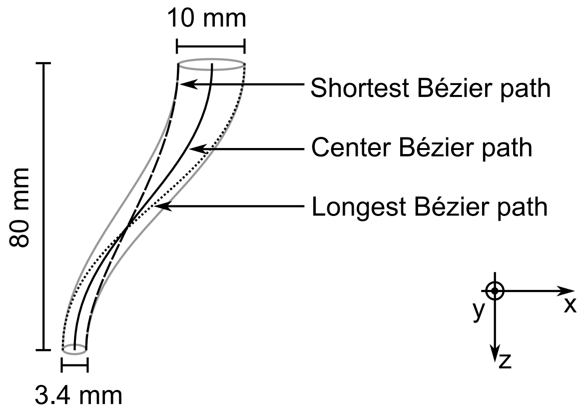

Figure 5.2: Since the duct geometry supports higher mode wave propagation at $40\,\mathrm{kHz}$, three possible propagation paths are considered. The first path is in the center (-). Due to the larger input diameter of $10\,\mathrm{mm}$ there are longer paths (:) from the inner input diameter to the outer output diameter or a shorter path (- -) from the outer input diameter to the inner output diameter.

The numerical models of the waveguided phased arrays are performed in two steps. First, a single Bézier duct is used for transient simulations. Therefore, a 3D FEA is used. This way, the propagation time of the ultrasound inside the duct is calculated. The software COMSOL Multiphysics is used for these calculations using the acoustic transient module for 3D models [53]. It is based on the wave equation

$$\frac{1}{\rho c_{\mathrm{air}}^2} \frac{\partial^2 p}{\partial t^2} + \nabla \left(-\frac{1}{\rho} (\nabla p - q_{\mathrm{d}}) \right) = Q_{\mathrm{m}}, \tag{5.7}$$

in the time domain. This model considers the density ρ of the media, the speed of sound c_{air} and the pressure p. Additionally, monopole Q_{m} and dipole q_{d} sources are included.

Only one duct with varying geometric properties is simulated, instead of the entire waveguide (Figure 5.3). The duct is filled with air and all surrounding walls are assumed as ideal sound hard, which omits vibrations on the inner surface, i.e.

$$\mathbf{n} \left(-\frac{1}{\rho} (\nabla p - q_{\mathrm{d}}) \right) = 0, \tag{5.8}$$

where n is the normal vector. The transducer is modeled as an ideal piston transducer with a defined normal velocity v_{n} (Figure 5.3)

$$\mathbf{n}\left(-\frac{1}{\rho}(\nabla p - q_{\mathrm{d}})\right) = \frac{\partial v_{\mathrm{n}}(t)}{\partial t}. \tag{5.9}$$

Free-field characteristics were modeled, by using a PML at the output of the duct [53].

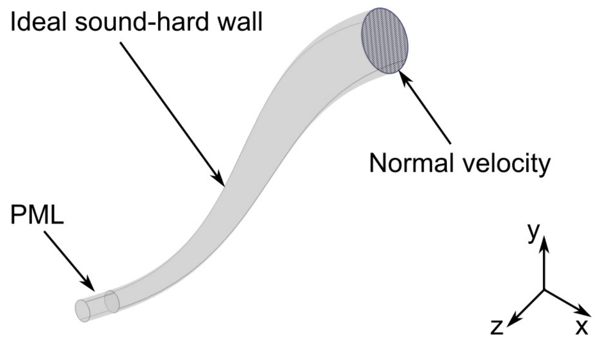

Figure 5.3: A 3D FEA transient simulation for calculating the propagation time between the input and output of a Bézier-shaped duct. Each transducer is modeled as an ideal piston transducer with a defined normal velocity. Additionally, a cylindrical PML is used at the output of the duct, thus no open field is required for this simulation. All walls are assumed as ideal sound-hard walls.

Afterwards, a 3D numerical model is designed using COMSOL Multiphysics to predict the directivity pattern of the two waveguides. In general, acoustic problems in the ultrasonic domain are numerically expensive due to the small wavelength [71]. Especially, this applies to free-field calculations due to the high number of elements required, i.e. with at least 10 nodes per wavelength in comparison to the volume of the media. For this reason, the BEM instead of an FEA is used. This avoids the need of meshing an entire volume. Instead, only the relevant surfaces are meshed. In COMSOL, the BEM is implemented using the Helmholtz equation in the frequency domain, i.e.

$$\nabla\left(-\frac{1}{\rho}\nabla p\right) - \frac{\omega^2}{\rho c_{\mathrm{air}}^2} p = 0, \tag{5.10}$$

with a defined angular frequency ω. The excitation consists of an ideal piston transducer with a defined normal velocity v_{n}, i.e.

$$-\mathbf{n}\cdot\left(\frac{1}{\rho\nabla p}\right) = j\omega v_{\mathrm{n}}. \tag{5.11}$$

All walls of the duct are assumed as ideal sound-hard walls as well [Figure 5.4(a)], i.e.

$$-\mathbf{n}\cdot\left(\frac{1}{\rho\nabla p}\right) = 0. \tag{5.12}$$

In order to further reduce the computational demands, only half of the geometry is solved by using one symmetry plane [Figure 5.4(b)]. In addition, the same finite-sized rigid baffle as in the measurements is used, in order to have better resemblance to the measurement setup. Furthermore, temperature, ambient pressure and humidity are implemented in the model. This results in a correct atmospheric attenuation caused by thermal conductivity, viscous and relaxation effects is considered in the model. This attenuation model is based on the ANSI standard S1.26-2014 [53].

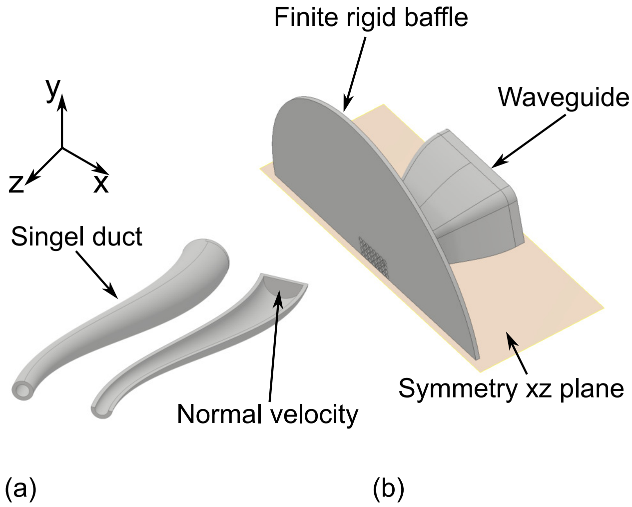

Figure 5.4: The BEM is used to simulate the directivity of the phased arrays. This way, only the surfaces need to be meshed. All walls are assumed as ideal sound hard walls. Additionally, the excitation is implemented using a normal velocity (a). A symmetry in the xz plane (b) is used, to reduce the calculation time.

The simulations were validated in two measurement steps. First, the propagation times in the Bézier waveguide were measured. These results were normalized. As a result, the normalized time delays were used to compensate for the different duct lengths of the Bézier waveguide.

Second, the directivity patterns of the arc waveguide and the Bézier waveguide were measured. Parameters such as HPBW, MSL and steering angle were obtained allowing for a comparison of the two waveguides. Both waveguides were fabricated using an Ultimaker 2 (Ultimaker, Netherlands) with polylactic acid (Innofill, Netherlands).

In addition, environmental important properties were measured in the anechoic chamber. This way, the correct speed of sound and atmospheric attenuation is determined. This values are used in the simulations. The temperature during measurements was $26°\mathrm{C} \pm 0.5°\mathrm{C}$ causing a speed of sound of $347.1\,\mathrm{m/s}$ [8]. The ambient pressure was $100314\,\mathrm{hPa} \pm 1\mathrm{hPa}$. In addition, the humidity was measured with $39\% \pm 2\%\mathrm{RH}$ estimating additional atmospheric attenuation effects [77].

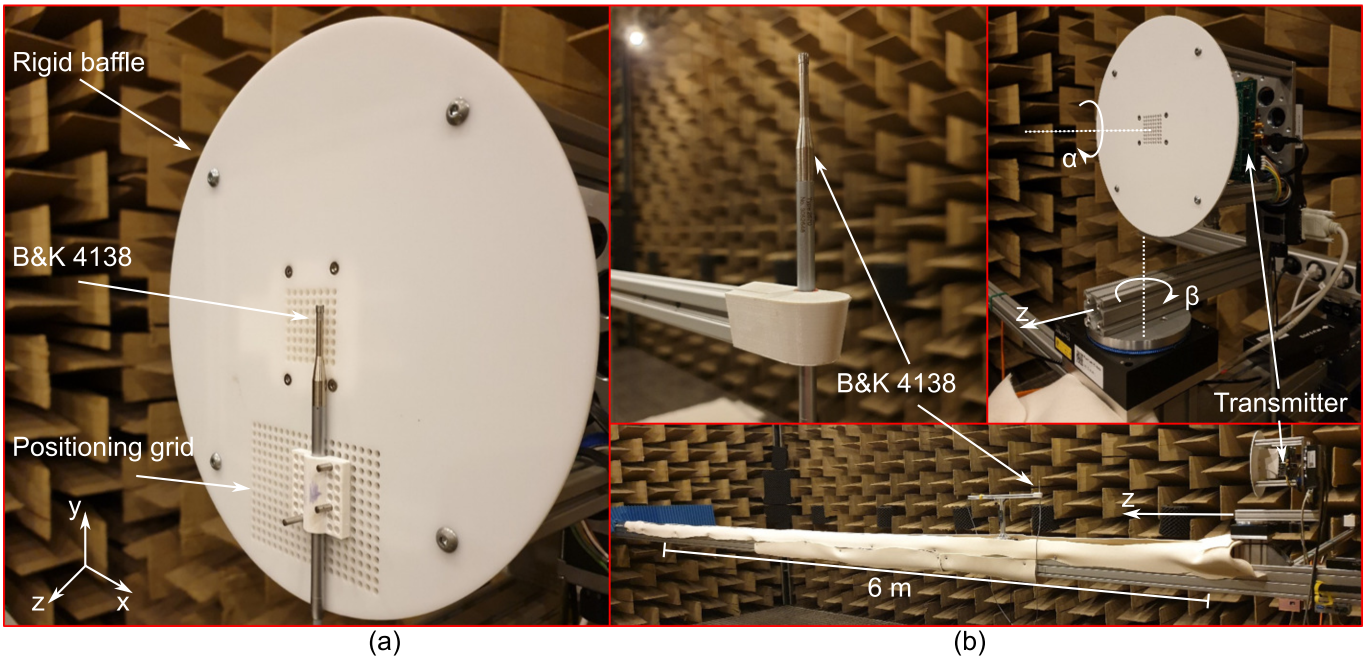

Figure 5.5: By using a calibrated measurement microphone, the propagation times in the Bézier-shaped ducts were measured. A positioning matrix on the rigid baffle allows for equidistant measurements (a). Free-field measurements were conducted as well (b). This way, the directivity of the two waveguides can be compared).

Each propagation time inside the Bézier waveguide is measured by positioning a calibrated microphone at a single output port [Figure 5.5(a)]. At the same time, a single transducer is positioned in the corresponding duct as well. Equidistant positioning of the microphone is ensured by using a positioning grid on the rigid baffle [Figure 5.5(a)]. The microphone is mounted to the baffle with a 3D-printed socket an multiple metal bolts. The ultrasonic transducer was excited with a function generator with $40\,\mathrm{kHz}$ and 30 cycles. Instead of the manufacturers specified driving voltage of $20\,\mathrm{V_{pp}}$, the transducers were driven with $6\,\mathrm{V_{pp}}$. This reduces the SPL of the array which avoids nonlinearities in air.

In the phased array, the transducers are driven with custom electronics. This allows for far-field characterization of the phased array. The signals consist of a rectangular burst signals with a frequency of $40\,\mathrm{kHz}$, 30 cycles. A burst period of $15\,\mathrm{ms}$ was selected to reduce the heating effect, and, thus, the resonance frequency drift.

5.3 Results of the duct length compensation

First, the results of the propagation times in the Bézier waveguide are compared, which were obtained via analytical calculations, numerical calculations and experiments. Second, the simulated and measured directivity properties in the far-field of the two waveguides are compared using the HPBW, MSL and steering angle.

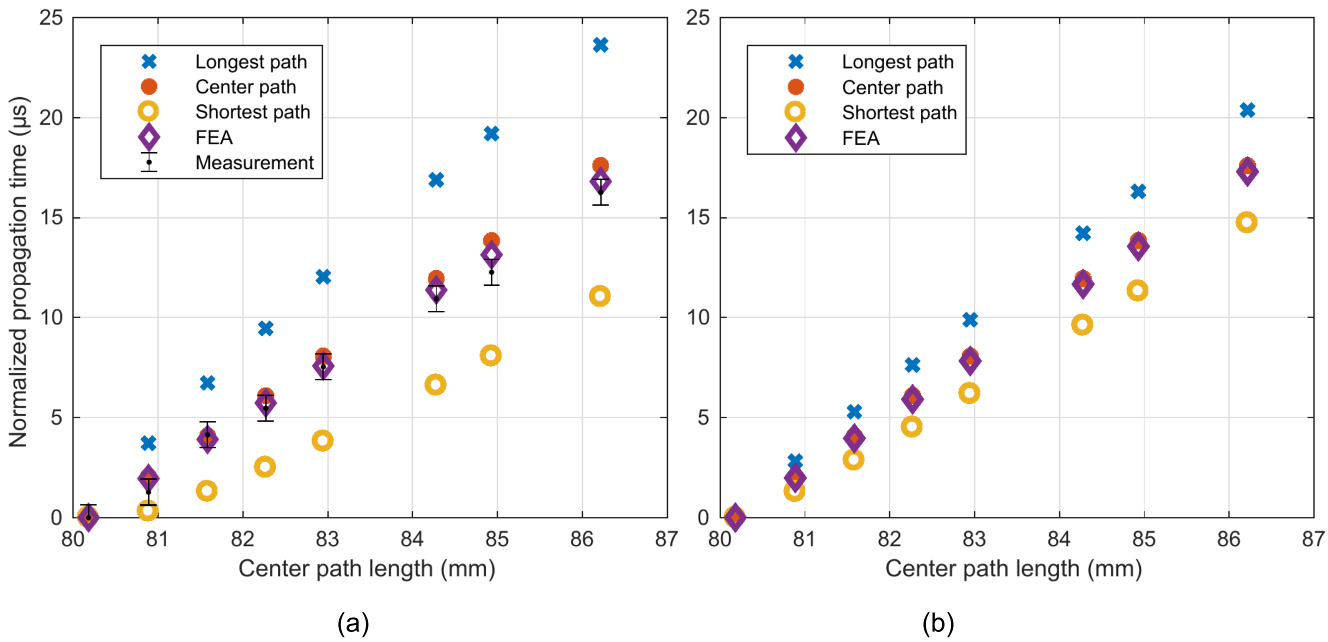

Figure 5.6: The analytic model has higher propagation times compared to the measurements and the transient FEM simulation (a). The resemblance of the FEM and the analytic model can be improved by reducing the diameter of the duct (b).

The results of the measured propagation times are within the results of the analytic model [Figure 5.6(a)]. Additionally, the center path of the analytic model and the measurements are in good agreement. However, longer propagation paths ($> 84\,\mathrm{mm}$) deviate with a maximum value of 7.6%.

Next, the numerical model has the same agreement with the analytic model as the measurements [Figure 5.6(a)]. For longer paths there is a maximum deviation of the propagation time of 4.7% as well. The measurements and the numerical model have a better similarity with a maximum deviation of 3.2%. As a result, the numerical calculations and the measurements smaller propagation times in comparison to the analytic model, which results in shorter propagation times.

Next, the influence of the duct diameter on the propagation time is analyzed with the numerical model. This way, the diameter of the duct can be reduced from $10\,\mathrm{mm}$ to $3.4\,\mathrm{mm}$. The tapering is removed as well. This geometrical change results in a better agreement between the analytic model and the numerical model [Figure 5.6(b)]. The maximum deviation between the two approaches is reduced to 1.7%.

In order to understand the influence of the ducts diameter on the propagation time, the Helmholtz number, which is the ratio between the wavelength and the diameter, is calculated. This number shows whether plane wave propagation can be assumed or not. When the diameter is small compared to the wavelength, $d_{\mathrm{duct}} < \lambda$ a plane wave propagates inside th duct [Figure 5.7(a)]. As a result, the propagation path is determined by the geometry of the duct. On the other hand, the input of the duct has a Helmholtz number of 3.66 leading to higher modes in this section of the duct. Thus, a plane wave propagation can not be assumed anymore [65]. In this case, direct and indirect propagation paths need to be considered. From point P_1 to point P_2 the wave can propagate directly or via reflections of the walls [Figure 5.7(b)]. As a result, the propagation length is not defined by the geometry of the duct.

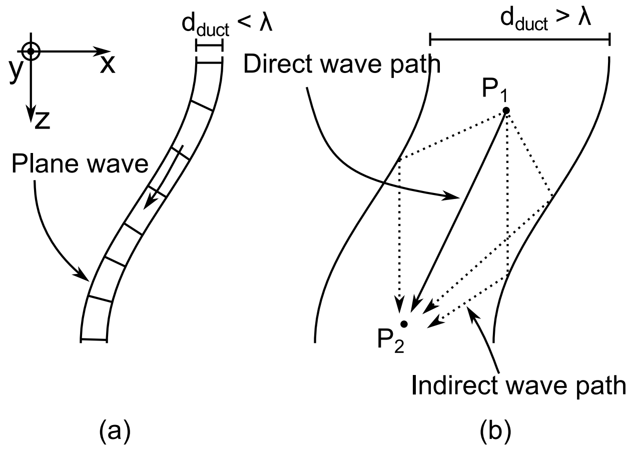

Figure 5.7: The model of a wave propagation inside a duct depends on the ratio between the diameter of the duct and the wavelength. An assumed plane wave propagation is suitable (a) for small diameter in comparison to the wavelength. The waves maxima and minima are equidistant and their positions are defined by the geometry. When the diameter is larger than the wavelength, there is no plane wave propagation anymore. A Huygens model is a more suitable model in this case (b). As a result, the propagation path is nit defined by the length of the geometry, i.e. it follows the shortest direct path (:) between two points e.g.: (P_1 and P_2), resulting in a lower propagation time than the estimated path of the Bézier curve.

The results of the BEM calculations show mainly fundamental modes inside the ducts [Figure 5.8(a)]. The only ducts which deviates from this result is the corner duct [Figure 5.8(b)]. Since, the input diameter of the ducts are larger in comparison to the wavelength, omni directional wave propagation or in this case higher modes can occur. Due to the reduced diameter at the end of the duct, the order of the mode is reduced to plane wave propagation. As a result of the varying propagation modes inside the ducts, a pressure distribution at the output ports occurs with a maximum deviation of 2 dB. Since, the waveguide consists of ducts with equal length, all waves are in phase at the output of the waveguide.

In contrast, the Bézier waveguide without phase correction has waves at the outputs which are out of phase [Figure 5.8(c)]. In addition, the pressures deviate as well. On the other hand, all ducts even the corner duct have a plane wave propagation [Figure 5.8(d)].

When the varying duct lengths are compensated with additional time delays, all output waves are in phase again [Figure 5.8(e)]. In contrast to the arc waveguide, the output pressures of the different path lengths deviate up to 9.5 dB. In addition, the averaged SPL at all outputs of the Bézier waveguide is 2.5 dB lower compared to the waveguide with equal lengths. These deviations can be explained with the length of the ducts. The reduced SPL are observed in ducts of the length of $\approx 9.6\lambda$. This result is counterintuitive compared to the analytic model of an open end pipe. Here, the maximum SPL occurs at a length of $0.5\lambda \cdot n$ with $n \in \mathbb{N}$. This analytic model of a one sided open duct is suitable for straight ducts with a small diameter compared to the wavelength, which results in plane wave propagation. However, this model is not applicable to the given problem, since the diameter of the duct is larger than the wavelength leading to higher mode wave propagation. Last, the corner duct shows plane wave propagation in contrast to the corner duct of the arc waveguide [Figure 5.8(f)].

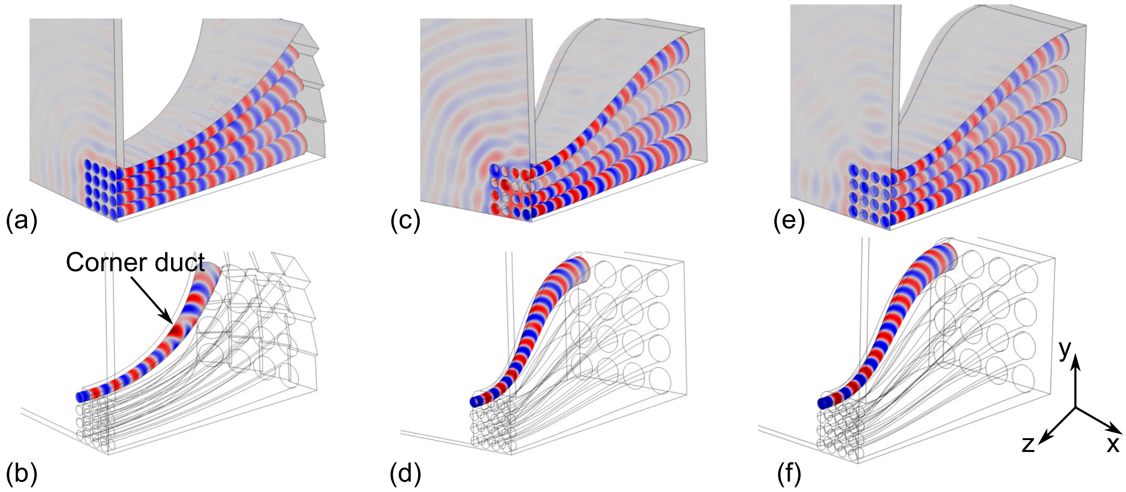

Figure 5.8: The results of the BEM have a fundamental mode of the wave propagation in most ducts of the arc waveguide (a). The corner duct is the only element that deviates from this result (b). The Bézier waveguides without phase correction has waves at the outputs, which are all out of phase (c). Compensating the varying propagation lengths results in equal output phases of the ducts (e). The corner duct of both Bézier waveguide simulations has a plane wave (d,f).

Next, the two-dimensional pressure distributions of the simulations are compared with the measurements. The arc waveguides pressure distribution is in good agreement in the simulations [Figure 5.9(a)] the measurements [Figure 5.9(b)]. In both cases, the direction of the main lobe is identical. The difference between the measured and simulated HPBW is $1.75°$ and the MSL is 4 dB [Figure 5.9(c)].

On the other hand, the manufactures tolerances of the transducers can be observed in the measurements. The SPL of the transducers varies by up to ± 3 dB [74]. First, the transition between the main lobe and the first side lobe has a clear differentiation in the simulations. However, this differentiation is not as clear in the measurements at $\pm 15°$. Since the pressure of the transducers varies, the destructive interference is reduced, which causes in increased SPL in this particular region. The pressure deviation of the transducers is not implemented in the simulations.

The next side lobe is in good agreement between simulations and measurements. In both cases, the last side lobe has minor ripples. These ripples occur due to the finite sized rigid baffle. When the sound wave propagates along the baffle, it is reflected at the end, due to the abrupt change of acoustic impedance. The reflected waves interfere with the incident waves, which results in a rippled directivity.

As expected, the simulation if the Bézier waveguide without time delay compensation results in undesired directivity. This pressure distribution can be observed in the results of the measurements as well [Figure 5.9(d), (e), (f)].

When the different duct lengths are compensated, the directivity consists of again of a main lobe and several side lobes [Figure 5.9(g), (h), (i)], which can be compared to the directivity of the arc waveguide. The simulated and measured HPBW differs by $1.75°$. Additionally, the MSL differs by 5.4 dB. Last, the unsharp transitions between the side lobes and the same ripple effects are observed in the measurement as with the arc waveguide.

Next, the steering of the main lobe of the Bézier waveguide is tested by adding additional time delays to the compensation delays. Steering the waveguide in the numerical model yields a correct angle at $45°$. In contrast, the measured steering has a minor deviation of $2°$ [Figure 5.9(m), (n), (o)]. At a steering angle of $45°$ the HPBW of the simulation results in $11.6°$ and of the measurements $14.4°$. The MSL remain the same within ± 1 dB, compared to a steering angle of $0°$.

When steering, both the arc waveguide and the Bézier waveguide perform similar regarding HPBW and MSL [Figure 5.9(j), (k), (l), (m), (n), (o)]. The simulated HPBW is within the uncertainty and the MSL has a minor difference of 1.7 dB. These simulation results can be confirmed with the measurements. The directivities of both waveguides are in good agreement as well. The parameters of both waveguides are summarized in Table 5.1.

However, the arc waveguide with equal length ducts has an overall higher SPL compared to the Bézier waveguide of 2 dB. This result of the simulation can not be validated, since the SPL deviation of the used ultrasonic transducers is ± 3 dB [74]. The HPBW of the two waveguides differs by $3°$. The MSL has a minor deviation of 0.3 dB, which is within the measurement uncertainty of ± 1 dB. The steered angle differs by $3°$, which is predicted by the numerical model.

Table 5.1: Simulation (sim.) and measurement (meas.) results of directivity patterns of the arc waveguide and the Bézier waveguide. The half power beam width (HPBW), the maximum side lobe level (MSL) and the steering angle of the main lobe are compared. All information are obtained from the 1D polar plots [Figure 5.9(c), (i), (l), (o)].

Arrangement	HPBW	MSL	Steering angle
Arc meas.	$8.25°$	-8 dB	$0°$
Arc sim.	$6.5°$	-12 dB	$0°$
Arc steered $45°$ meas.	$25.75°$	-7.7 dB	$44°$
Arc steered $45°$ sim.	$18.1°$	-11.4 dB	$45°$
Bézier corrected meas.	$8.25°$	-8.3 dB	$0°$
Bézier corrected sim.	$6.5°$	-13.7 dB	$0°$
Bézier steered $45°$ meas.	$22.75°$	-8 dB	$47°$
Bézier steered $45°$ sim.	$18.1°$	-12 dB	$45°$

This method shows the possibility of reducing the geometric complexity of the 2D arc waveguide for air-coupled ultrasonic phased arrays. This Bézier waveguide provides easy access to the ultrasonic transducers and fast exchange of the transducer printed circuit board. The SPL of the arc waveguide and the Bézier waveguide differs just by 2 dB, which is within the tolerances of the used ultrasonic transducers of 3 dB. In addition, the time compensation method showed no negative impact on the beam forming capabilities regarding HPBW, MSL or steering capability.

As a result, differing duct lengths inside an acoustic waveguides can be electrical compensated without significant drawbacks. Therefore, a more assembly friendly waveguide can be built for air-coupled ultrasonic phased arrays. In addition, the approach of length compensation offers additional design freedom for arbitrary waveguides. The resulting geometry of the waveguide can be adapted for different applications such as a restricted volume in the automotive industry.

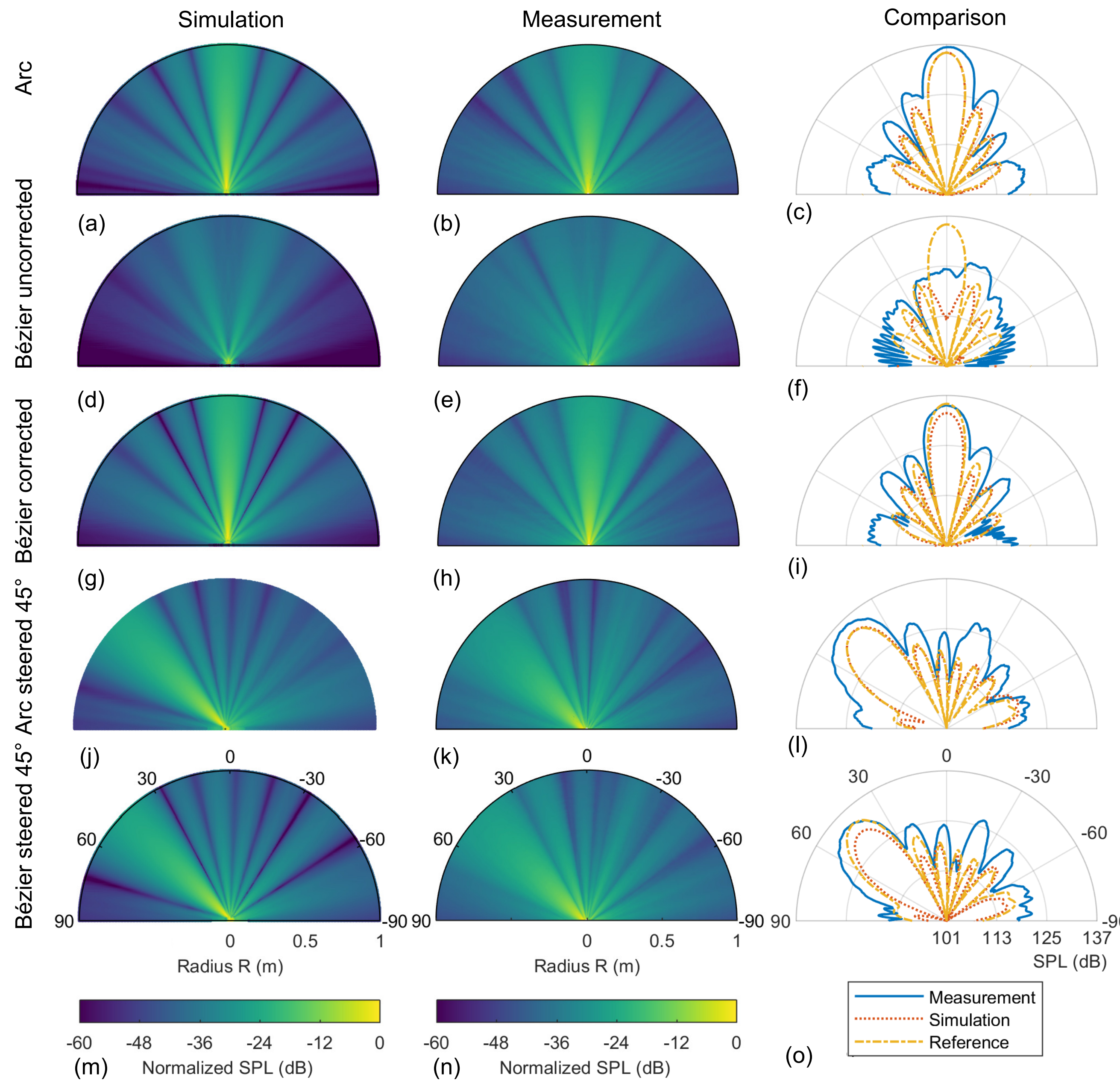

Figure 5.9: The simulation of the arc waveguide (a) is in good agreement with the measurements (b), (c). As expected, the Bézier waveguide without propagation time correction results in an undesirable pressure sound field (d), (e), (f). By compensating these different propagation paths with an electrical delay for each ultrasonic transducer, the sound field is corrected (g), (h), (i). After the propagation time correction the arc waveguide (j), (k), (l) and the Bézier waveguide have similar steering capabilities (m), (n), (o).

5.4 1D line waveguide combining equal length with plug-in assembly

Parts of this chapter were published in [49].

The previous chapter compared a waveguide with equal length ducts and Bézier shaped ducts. Both waveguides have individual benefits. The equal length waveguide has no need for a phase shift compensation due to the same duct lengths, but a time consuming assembly of the transducers. On the other hand, the Bézier waveguide has a simplified assembly process, but the lengths of the ducts must be compensated with additional time delays. Both benefits can not be combined for a 2D 8×8 phased array due to the limited space. However, a 1D line array has one additional design freedom allowing for a more flexible positioning of the transducers sockets. Again, Bézier shapes with orthogonal input and output surfaces were used for the new waveguide. In contrast to the before mentioned waveguides, this geometry uses the same duct geometry for each transducer [Figure 5.10(a)]. In addition, the transducers were split into two rows with alternating direction of the ducts. Further individual rotations were applied to ensure no intersections between the ducts. This allows for an easy assembly of the transducer PCB with the waveguide and provides equal length ducts without any phase correction. This entire waveguide has a compact size of $50\,\text{mm} \times 40\,\text{mm} \times 10\,\text{mm}$ [Figure 5.10(b)].

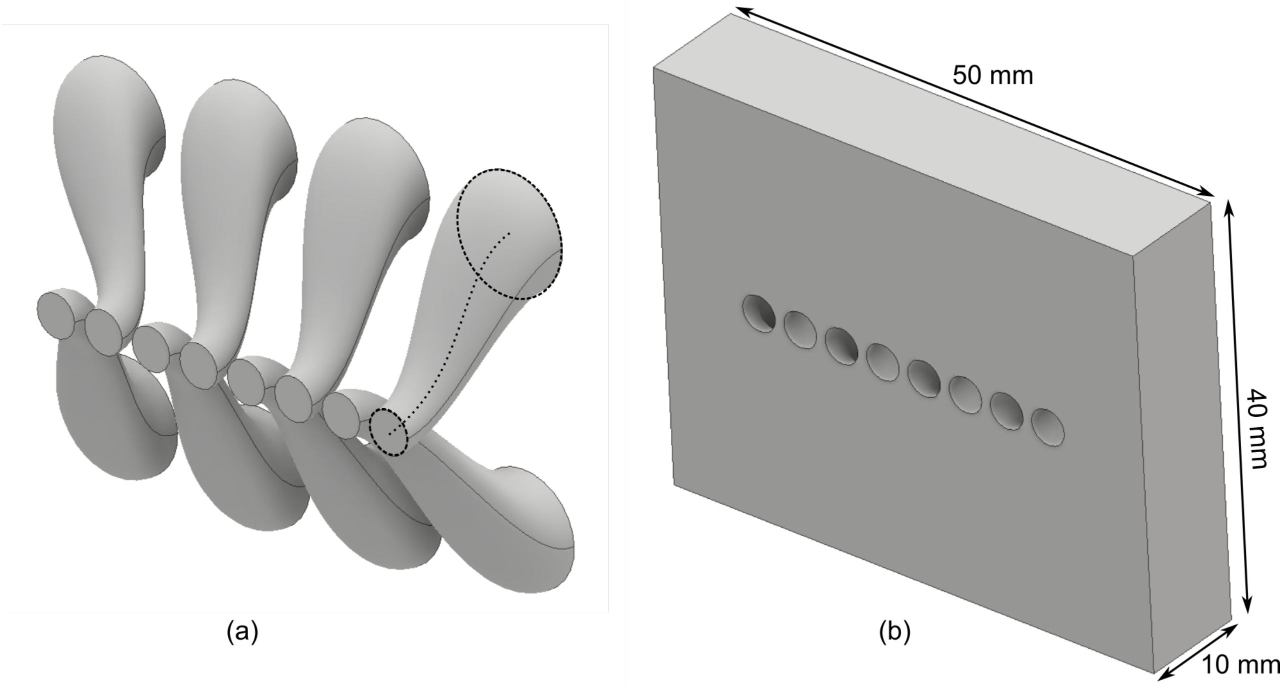

Figure 5.10: The waveguide consists of eight Bézier-shaped ducts, which have an alternating direction (a). This way, the transducers can be arranged in two rows resulting in a compact design of $50\,\text{mm} \times 40\,\text{mm} \times 10\,\text{mm}$ (b).

Next, the length of the waveguide is analyzed by using COMSOL Multiphysics BEM. This length is varied from $80\,\text{mm}$ to $10\,\text{mm}$. The SPL is evaluated at a range of $1\,\text{m}$ and normalized to the SPL of the $80\,\text{mm}$-long waveguide. In addition, the uncertainty of the transducers cone orientation is represented in the plot with a red bar of $\pm 3\,\text{dB}$ (Figure 5.11).

In general, the SPL variation has multiple sections where it varies within the uncertainty of the transducer. Thus, the length reduction of this waveguide shape is possible without a significant loss in SPL. For this reason, the waveguide was reduced to a length of $10\,\mathrm{mm}$.

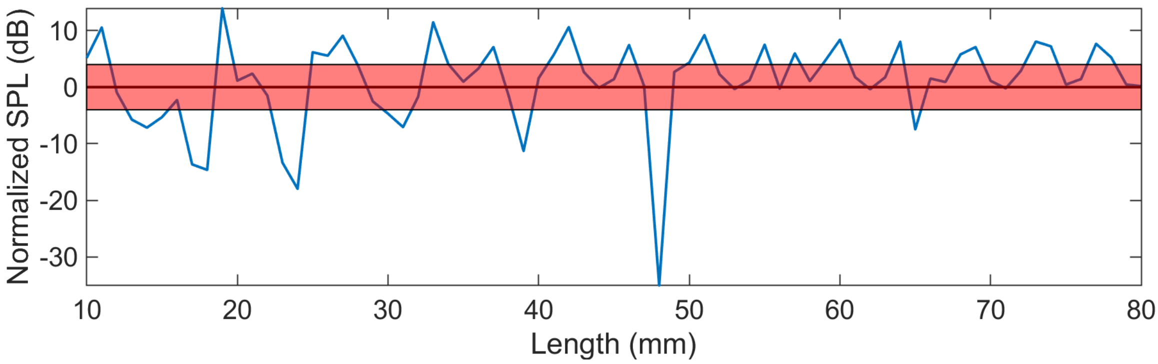

Figure 5.11: In order to reduce the size of the waveguide, its length is reduced from $80\,\mathrm{mm}$ to $10\,\mathrm{mm}$ using the BEM. Furthermore, the transducers uncertainty of $\pm 3\,\mathrm{dB}$ (red bar) is added to the plot. The SPL is normalized to a length of $80\,\mathrm{mm}$.

Next, the normalized directivities of the $80\,\mathrm{mm}$-long waveguide and the $10\,\mathrm{mm}$-long waveguide are compared. Both directivites have an SLL of $13\,\mathrm{dB}$ (Figure 5.12). Thus, the pressure distribution at the output ports of both waveguides is the same, since each duct of the individual waveguides has the same length. Consequently, the resonance frequency of the ducts is for one waveguide always the same. In addition, the HPBW of both waveguides is the same with $12°$. Due to these promising results, this waveguide was successfully used in the following publication for an ultrasonic array phased array [49].

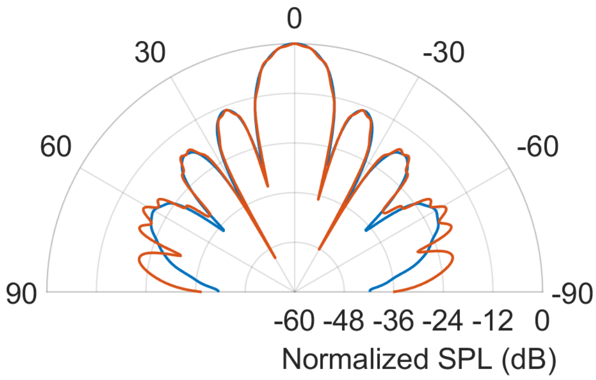

Figure 5.12: The directivity patterns of the $80\,\mathrm{mm}$-long waveguide is compared with the $10\,\mathrm{mm}$-long waveguide. Both SPLs were normalized to their maximums respectively.

In conclusion, acoustic waveguides for air-coupled phased arrays can consists of ducts with varying length. The length can be compensated by delaying the transducers signal electrically. This leads to more design flexibility of the waveguide such as reduced size, simplified assembly or arbitrary geometries for specific applications with limited construction volume.

6 Protection layers for acoustic waveguides

Combining air-coupled ultrasonic phased arrays with acoustic waveguides provides the benefit of grating-lobe-free beamforming. The waveguide separates the transducers aperture from the effective aperture by using tapered ducts. This allows for a free aperture design and an inter element-spacing of half the wavelength. This approach can be used for pulse-echo measurements [34], [35], obstacle detection [78], non-destructive testing [72], [79], [80], flow metering [16] or even for tactile feedback [81].

However, since this waveguide is designed for air-coupled applications, the output ports are opened. This can lead to clogging due to environmental hazards such as liquids, dirt or dust. A clogged duct results in a significant acoustic loss. Exchanging the transducers with more robust ones would not solve this issue, since it only protects the transducer itself and not the waveguide.

Therefore, the waveguide needs a proper sealing which allows for a sufficient protection and acoustic transparency as well. One commonly known solutions for waterproofing acoustic systems is the use of hydrophobic fabrics [82], [83], which is often used in consumer products such as smartphones, notebooks or smartwatches. The pores of the fabric cause minor thermoviscous losses, and, thus, they have just a minor impact on the acoustics [84]. Furthermore, a nano coat is applied to the fabric to provide a lotus effect. With this approach, IP classes of up to 68 can be achieved [85].

In addition, thin films with low density materials are used as a protection. In contrast to the fabric, thin films are based on a vibro acoustic effect. The propagating sound wave excites the thin film leading to an oscillation of the film itself. As a result, sound is emitted by the film [86] and losses occur due to reflections at the film. In this case, the losses are mainly determined by the thickness of the film and its density [87].

In this work, the influence of hydrophobic fabrics and thin films on the insertion loss (IL), side lobe level (SLL), half power beam width (HPBW), beamforming capability, blind zone in pulse-echo mode on an air-coupled ultrasonic phased arrays are compared. Additionally, the watertightness for both approaches are evaluated with an experiment.

6.1 Protection classes and industrial demands

Ultrasonic transducers are used in different environments. From car parking assistance which need to be waterproof over dusty environments in grain stores, transducers need to endure different environmental hazards and still provide reliable measurement. However, quantifying the waterproofness of electrical devices is not easily achieved. For most tests, the device is submerged in water under defined circumstances and tested afterwards. In order to define these circumstances, the international protection classes (IP classes) were defined by the ISO 20653 [88]. This norm defines the protection of enclosures for electrical devices such as smartphones, watches or cars. The norm defines three protections:

- Protection against foreign objects,
- protection against access,
- protection against water.

The degree of protection is defined by the IP-codes. They consist of two digits. The first digit defines the protection against objects whereas the second digit defines the protection against water. When just one of these properties were tested, the other digit can be exchanged with an ”X”. In addition, the letter ”k” can be used to indicate that the tests were conducted with increased pressure. Furthermore, the letters (A-D) indicate the protection against access. There are also supplementary letters for test in water under movement (M) or standstill (S).

In this work, the water resistance will be investigated. Therefore, only IP-classes between IPX7 and IPX8 are investigated. The definition of IPX0-IPX6 only defines the protection against waterdroplets of different sizes, velocities and inclination angles. The investigated IP classes define the experiments for submersion under water which is the scope of this work.

6.2 Experimental evaluation of the protection layers

The following chapter was published in [51].

First, the two approaches for waterproofing the waveguide are evaluated with experiments. These experiments consist of an acoustic evaluation in the anechoic chamber and an immersion experiment. Both tests were conducted with the hydrophobic fabric and the thin film. The fabric [Figure 6.1(a)] consists of $20\,\mu\mathrm{m}$-thick polyester fiber with a mesh size between $200\,\mu\mathrm{m}$ and $600\,\mu\mathrm{m}$. Thus, it is used for outdoor audible speaker applications (Akustikstoff, Mörlenbach, Germany). Its thickness is $1\,\mathrm{mm}$ leading to ”minimal acoustic losses”, as specified by the manufacturer. In addition, the polyester is nano-coated to provide water, oil and dirt resistivity.

The second approach which is investigated is the use of thin films. Since low density of the material result in low reflection coefficients, low density polyethylene (LDPE) was used in first tests. The LDPE film has a thickness of $13\,\mu\mathrm{m}$ and a density of $0.97\,\mathrm{g/cm}^3$. This leads to small acoustic attenuation, since these properties lead to low acoustic impedance [Figure 6.1(b)]. This film is often used as a plastic wrap (Priva Netto, Maxhütte-Haidhof, Bayern, Germany). The acoustic experiments use the phased array prototype [Figure 6.1(a)]. The transducers are driven with bursts of 30 cycles, $20\,\mathrm{V}_{\mathrm{pp}}$ at $40\,\mathrm{kHz}$.

The acoustic experiments are conducted to determine the insertions loss (IL) of the protection layer, and their influence on the beamforming capability and blind zone in pulse echo mode. Thus, measurements in an anechoic chamber were conducted [Figure 6.2(a)]. During the experiments, the temperature was $16.4°\mathrm{C} \pm 0.5°\mathrm{C}$, the ambient pressure was $101529\,\mathrm{hPa} \pm 1\,\mathrm{hPa}$ and the humidity was $36.6\% \pm 2\%$.

In order to measure the IL, three experiments are conducted. First, the directivity pattern in transmit mode is measured using a calibrated microphone [Figure 6.1(b)]. The distance between the array and the microphone is $1\,\mathrm{m}$. The array is located on a rotational axis allowing for variable positioning. The signals of the microphone ar captured with a sampling rate of $500\,\mathrm{kSa}$ and a resolution of $24\,\mathrm{Bit}$. A PC with LabVIEW controls the measurement system.

Second, a pre-characterized ultrasonic transmitter (MA40S4S) is used to conduct the receive measurements [Figure 6.1(c)]. The signal processing includes matched filtering, conventional receive beamforming and envelope extraction[35].

Third, the pulse-echo measurements are conducted using a hollow steel sphere with a diameter of $10\,\mathrm{cm}$ [Figure 6.1(d)]. This experiment combines the losses of the transmit and receive characteristics. The between the array and the characterization objects is the same with $1\,\mathrm{m}$.

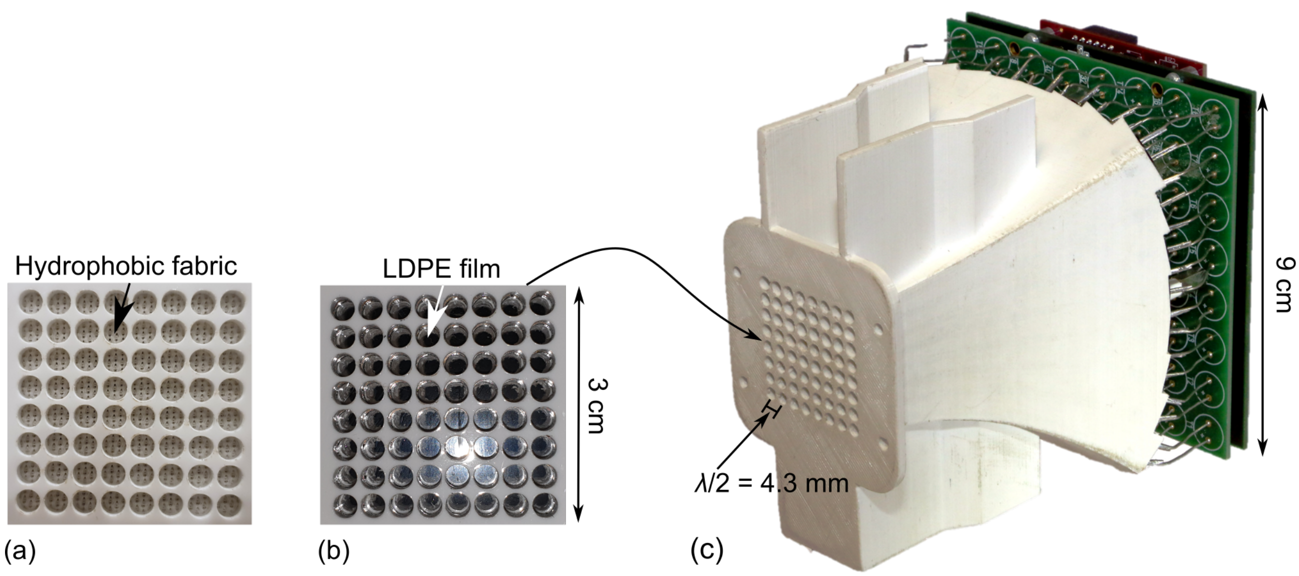

Figure 6.1: Hydrophobic fabric (a) and an LDPE film (b) are mounted directly on the output of the waveguide of the phased arrays. The air-coupled ultrasonic phased array consists of an acoustic waveguide, 64 ultrasonic transducers and custom electronics (c).

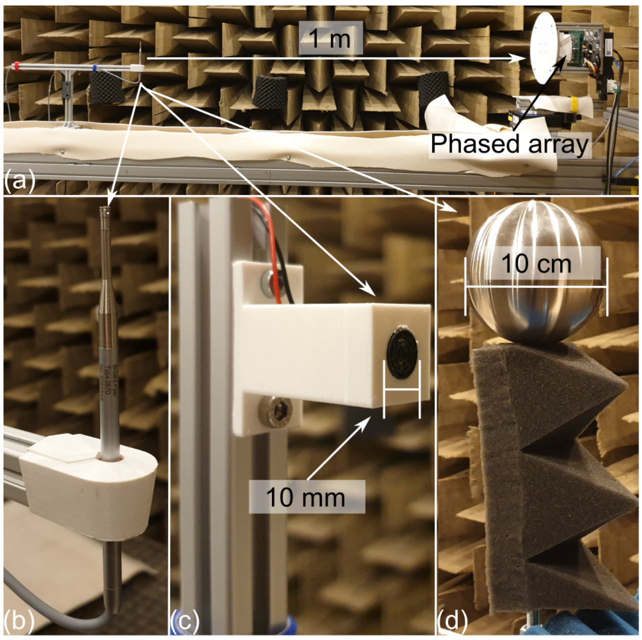

Figure 6.2: The acoustic measurements are conducted in three steps (a). First, the transmit directivity is measured using a calibrated microphone (b). Second, a pre-characterized transducer is used for the receive pattern (c). Last, a hollow steel sphere with a diameter of 10 cm is used for the pulse-echo measurements (d).

Next, the results of the transmit measurements are analyzed. At a steering angle of $0°$, the hydrophobic fabric has an IL of $1.8\,\mathrm{dB} \pm 1\,\mathrm{dB}$. At $45°$, the IL is $2.3\,\mathrm{dB} \pm 1\,\mathrm{dB}$ [Figure 6.3(a, b)]. On the other hand, the LDPE film has an IL of $7.5\,\mathrm{dB} \pm 1\,\mathrm{dB}$ at $0°$, which is higher compared to the fabric. At a steering angle of $45°$, the LDPE has an IL of $6.4\,\mathrm{dB} \pm 1\,\mathrm{dB}$. In receive the same results can be observed as in the transmit experiments [Figure 6.3(c, d)]. First, the fabric has an IL of $2.5\,\mathrm{dB} \pm 1.5\,\mathrm{dB}$ at $0°$ and $3\,\mathrm{dB} \pm 1.5\,\mathrm{dB}$ at $45°$. Second, the LDPE film has an IL of $7.3\,\mathrm{dB} \pm 1.5\,\mathrm{dB}$ at $0°$ and $9.5\,\mathrm{dB} \pm 1.5\,\mathrm{dB}$ at $45°$. Overall, the fabric increases the SLL by up to $3.1\,\mathrm{dB} \pm 1.5\,\mathrm{dB}$. In contrast, it reduces the HPBW by up to $4° \pm 2°$. The LDPE film increases the SLL as well by up to $3.6\,\mathrm{dB} \pm 1.5\,\mathrm{dB}$ and decreases the HPBW by up to $9° \pm 2°$ (Table 6.1).

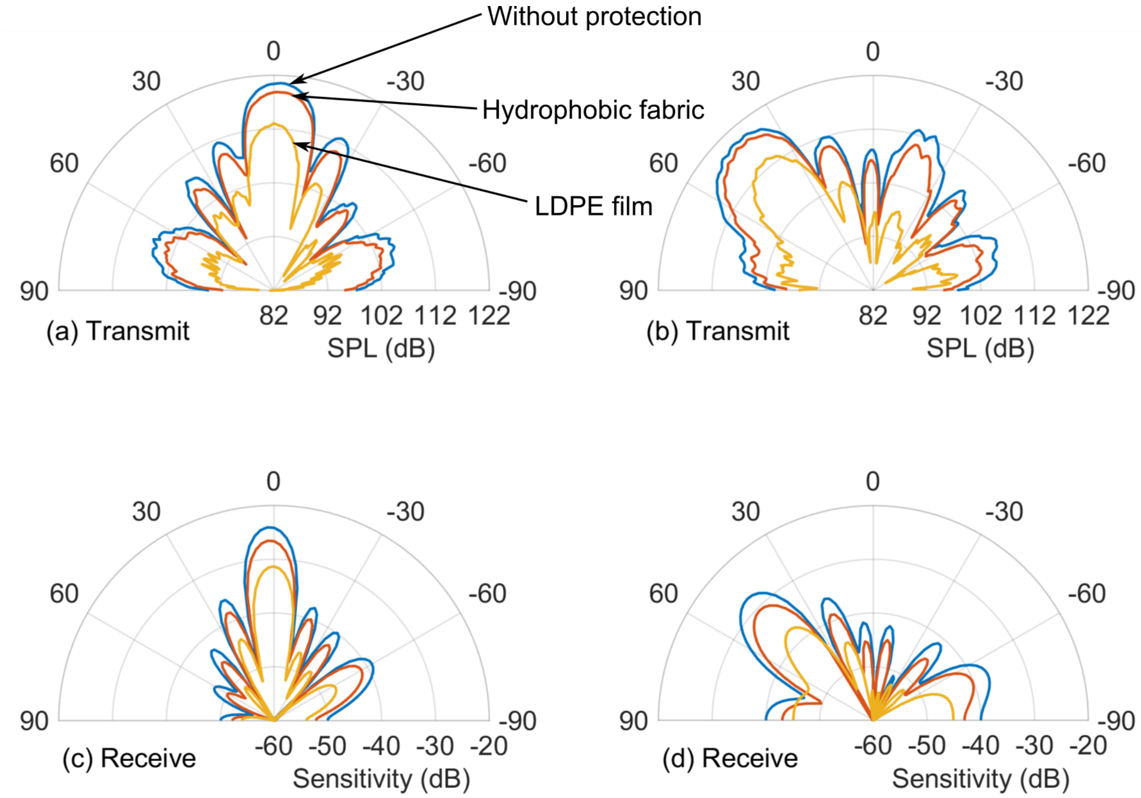

Figure 6.3: The directivity patterns of the phased array with and without protection layer in transmit mode at $0°$ (a) and $45°$ (b) and in receive mode at $0°$ (c) and $45°$ (d).

Table 6.1: SLL and HPBW of the directivity pattern without protection layer, with hydrophobic fabric and with LDPE at a steering angle of $0°$ and $45°$ in transmit and receive.

	Transmit		Receive	
SLL	$0°$	$45°$	$0°$	$45°$
Reference	7.7 dB	7.6 dB	8.7 dB	8.2 dB
Hydrophobic fabric	8.5 dB	8.6 dB	11.8 dB	8.3 dB
LDPE film	9.8 dB	10.5 dB	12.3 dB	7.7 dB
HPBW				
Reference	$19°$	$27°$	$13°$	$18°$
Hydrophobic fabric	$19°$	$23°$	$13°$	$20°$
LDPE film	$15°$	$18°$	$14°$	$18°$

Next, the results of the pulse-echo measurements are compared. This experiments combines the IL in transmit and receive. The hydrophobic fabric has an IL of $3.2\,\mathrm{dB} \pm 1.5\,\mathrm{dB}$. In contrast, the LDPE film has an increased IL of $11.9\,\mathrm{dB} \pm 1.5\,\mathrm{dB}$ [Figure 6.4(a, b, c)]. The fabric does not affect the blind zone of the phased array. On the other hand, the LDPE film increases the blind zone by 22% due to longer decay times [Figure 6.4(c)].

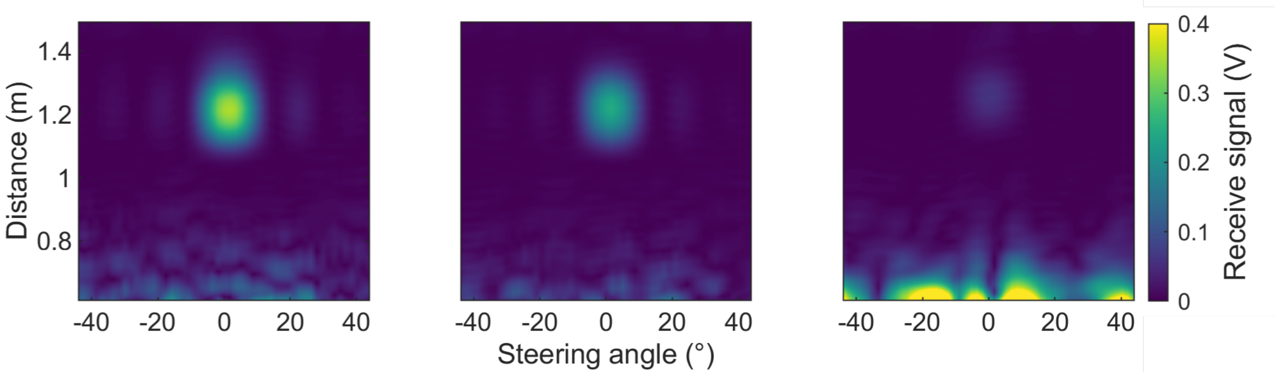

(a) (b) (c)

Figure 6.4: A hollow steel sphere with a diameter of $10\,\mathrm{cm}$ can be detected without any protection layer (a). The hydrophobic fabric attenuates the signal by $3.2\,\mathrm{dB} \pm 1.5\,\mathrm{dB}$ (b). The LDPE film attenuates the signal by $11.9\,\mathrm{dB} \pm 1.5\,\mathrm{dB}$ (c) and increases the blind zone by 22%.

After the determination of the IL of the hydrophobic fabric and the LDPE film, the measurements to investigate the watertightness of these two protection layers were conducted. The experiment is set up in accordance with norm EN60529 [85] with the following parameters. First, the protection layer is flanged between an air cavity ($35\,\mathrm{mm} \times 35\,\mathrm{mm} \times 14\,\mathrm{mm}$) covered with blotting paper and a perforated 8×8 grid, aligned with the output openings of the acoustic waveguide of half wavelength (Figure. 6.5). The parts are 3D printed (Prusa MK3s, Prusa Research, Prag, Czechia) using PLA (Geeetech, Shenzhen, People's Republic of China). Second, the test sample is submersed to a depth of $2\,\mathrm{m}$ for $30\,\mathrm{min}$. Third, the sample carrier is taken from the water and opened in order to check whether water has penetrated the hydrophobic fabric.

Before conducting the experiment with the protection layers, a reference test was conducted. Therefore, a round plate without the 8×8 grid was conducted. This serves as a validation, whether the 3D printed parts and the o-ring joint provide sufficient sealing. As a result, this test achieved proper sealing at a submersion depth of $2\,\mathrm{m}$ and $30\,\mathrm{min}$. Thus, this method is valid for testing the water resistances of the protection layers.

The fabric showed a proper water sealing up to a depth of $1\,\mathrm{m}$ for $30\,\mathrm{min}$. When this depth is increased, the water sealing is broken at the front due to the increased water pressure, which was immediately indicated by rising water bubbles. This pressure exceeds the surface tension, and, thus, the water can penetrate the fabric. As a result, the hydrophobic fabric achieved a protection class of IPX7. Since only the resistance against water was tested, the first digit is specified as ”X”.

In contrast, the LDPE film provided a proper sealing at a depth of $2\,\mathrm{m}$ and $30\,\mathrm{min}$. As long as the film is not mechanically damaged, this approach provides a proper sealing even for longer times or a higher depth.

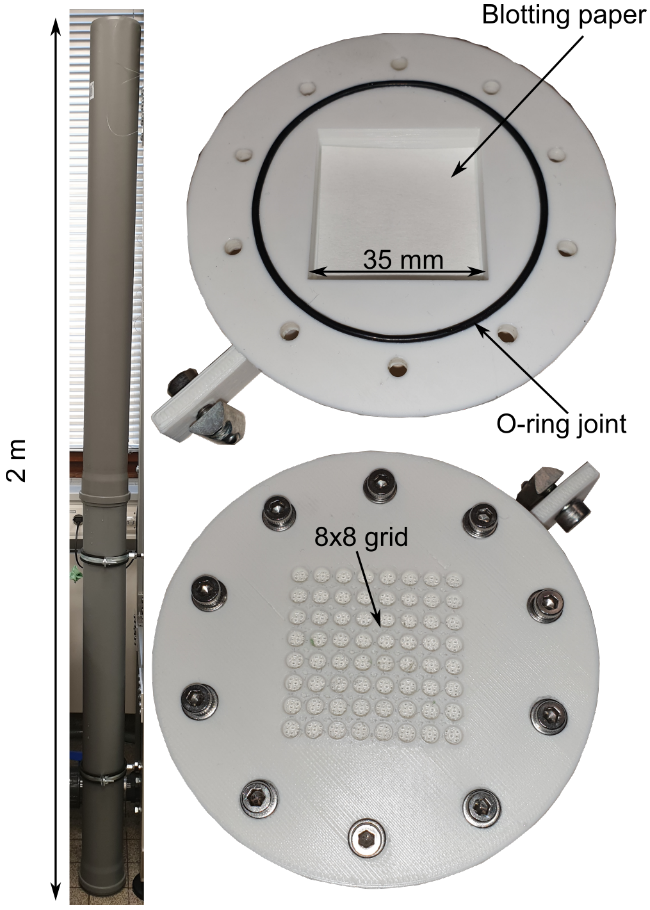

Figure 6.5: In order to classify the resistance of the protection layers against water the samples are flanged between an air cavity ($35\,\text{mm} \times 35\,\text{mm} \times 14\,\text{mm}$) and a plate with a 8x8 grid, aligned to the output openings of the acoustic waveguide. After the assembly, the sample is submersed in water up to $2\,\text{m}$.

Next, the influence of the position of the protection layer inside the waveguide is analyzed. Since both the hydrophobic fabric and the thin film introduces an acoustic impedance, reflections occur at the position of the protection layer. Thus, the reflected wave and the incident wave from the transducer superpose leading to increased and decreased SPL. In order to conduct these experiments, waveguide extensions were printed which increase the length of the waveguide by $9\,\text{mm}$. These extensions consist of two parts with varying depth. The protection layer is located between the two parts, and, thus, the position of the layers can be changed. The relative position is varied from $0\,\text{mm}$ to $8\,\text{mm}$ in $0.5\,\text{mm}$ steps. This range is derived from the wavelength of $8.575\,\text{mm}$. The SPL is evaluated at a distance of $1\,\text{m}$. First, the hydrophobic fabric was tested. In general, the measured SPL varies periodic over the tested range (Figure 6.6). The periodicity can be explained with the resonances of Helmholtz resonators. Due to superposition of reflected wave and incident wave maxima and minima occur. This effect depends on the ratio between the length of the waveguide and the wavelength.

In the case of the fabric, the distance between to maxima is $3.5\,\text{mm} \pm 0.25\,\text{mm}$ (Figure 6.6). This value can be compared with half the wavelength of $4.3\,\text{mm}$. However, there is a difference of $0.8\,\text{mm}$. This can be caused by higher modes in the input section of the waveguide, which lead to a different mode propagation. In addition, the maximal SPL variation due to this effect is $\pm 0.55\,\text{dB}$. This low position dependency can be explained with the thermoviscous effects. These losses occur due to friction between the air and the fibers of the fabric. This dissipative effect does not depend on the position of the fabric in an air volume. Thus, as long as the geometry of the waveguide does not change, the position of the hydrophobic fabric inside of the waveguide has no significant effect on the acoustic losses.

In contrast, the film has a much higher influence on the SPL with ± 2.1 dB (Figure 6.6). Again, the influence is periodic with a periodicity of 3.5 mm $\pm$ 0.25 mm. The film and the duct build a resonant system. Its resonance frequency depends on the length of this resonator, which is varied, with the position of the film inside of the waveguide. The results of this experiment show, that there is a significant SPL variation due to the position of the protection layer inside the waveguide. This leads to the conclusion, that the IL of both protection layers will be temperature dependent as well. Since the wavelength varies with the ambient temperature and the interferences depend on the ratio between the length of the waveguide and the wavelength, the losses due to the protection layer will be depend on the temperature.

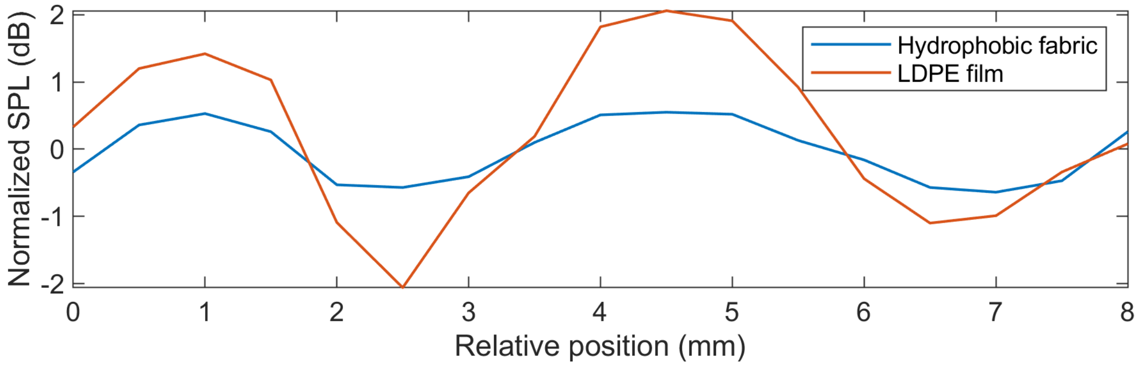

Figure 6.6: The position of the hydrophobic fabric and the thin film is varied inside the waveguide. In both cases the SPL depends on this positioning.

In conclusion, both the hydrophobic fabric and the LDPE film have no influence on the steering capability. Consequently, there is no significant additional pressure distribution at the output openings of the waveguide caused by the hydrophobic fabric or the LDPE film. In addition, reciprocity is still valid with both approaches.

However, for a real world application a compromise between IL and watertightness must be reached. On one hand, the hydrophobic fabric has a very low acoustic attenuation (1.8 dB $\pm$ 1 dB), but it is only waterproof up to a depth of 1 m corresponding to IPX7. On the other, hand the LDPE film has higher losses (7.5 dB $\pm$ 1 dB) but is waterproof up to a depth of 2 m, corresponding to IPX8. Even higher protection classes can be achieved with the LDPE film because the watertightness of the film depends on a proper sealing and an undamaged film. However, a 10 cm-hollow steel sphere is detectable with both protection layers at a distance of 1 m [Figure 6.4(c)].

6.3 Numerical model of the hydrophobic fabric

The following chapter was published in [52].

Next, the hydrophobic fabric was implemented into the before mentioned BEM model. Again, the commercial software COMSOL was used for the numerical model, including the acoustic waveguide and the hydrophobic fabric, allowing for the prediction of acoustic losses (Figure 6.7). This way it is possible to optimize the protection for a certain application. This time, the BEM is combined with the FEM for modeling acoustic losses due to the fabric. All wave propagation in air is simulated using the BEM. This way, the ultrasound propagation can be efficiently simulated in regions of interest that are bigger than the wavelength. On the other hand, the propagation of the ultrasound wave in the fabric is calculated using the FEM. This allows for an efficient approach of simulating poroacoustics. In order to model the hydrophobic fabric, the Delany-Bazley-Miki model was used. This model provides complex terms for the speed of sound and the density of the media for general fabrics [53]. The two important quantities of this set of equations are the thickness and the specific flow resistivity of the fabric. Since the resistivity of the hydrophobic fabric (Akustikstoff 2.0, akustikstoff.com) is not provided by the manufacturer, a 3D-printed flow pipe for measuring the specific flow resistivity was built. The results are used in a corner analysis in the numerical model. The model is validated with calibrated measurements in an anechoic chamber. In addition, the influence of the fabric on the beamforming capabilities can be observed.

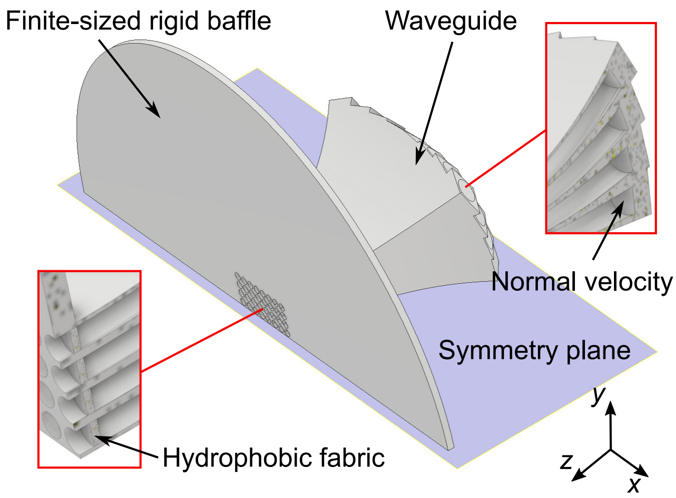

Figure 6.7: The numerical model includes the waveguide, the finite-sized rigid baffle from the measurement, a normal velocity as excitation and the hydrophobic fabric. In addition, only half of the model is simulated reducing calculation time.

The numerical model consists of the waveguide, a finite-sized rigid baffle, ideal piston transducers and the hydrophobic fabric. In order to reduce the calculation time, the geometry is halved by using a symmetry plane in xy-direction (Figure 6.7). The wave propagation in the waveguide and in the free-field is calculated using the Helmhotz equation with the boundary element method [53], i.e.

$$\nabla \cdot \left(-\frac{1}{\rho_0}\nabla p\right) - \frac{(2\pi f)^2}{c_{\text{air}}^2 \cdot \rho_0} p = 0. \tag{6.1}$$

The considered quantities are the density of air ρ_0, the pressure p, the frequency f and the speed of sound c_{duct}. Ideal piston transducers were used with a normal velocity v_{n} for the excitation [53], i.e.

$$-\mathbf{n} \cdot \left(-\frac{1}{\rho_0}\nabla p\right) = j2\pi f v_{\text{n}}. \tag{6.2}$$

The hydrophobic fabric is implemented using the poroacoustics module of COMSOL which is solved with a FEM. This way, the acoustic attenuation in the fabric is simulated using a complex density of the air ρ_{c} and a complex speed of sound c_{c}. COMSOL provides a variety of different material models for different geometries and frequency ranges. In this work, the Delany-Bazley-Miki model is used, since it is suitable for general fabrics [53], i.e.

$$c_{\mathrm{c}} = \frac{c_{\mathrm{air}}}{1 + C_1\left(\rho_0 \frac{f}{R_{\mathrm{f}}}\right)^{-C_2} - iC_3\left(\rho_0 \frac{f}{R_{\mathrm{f}}}\right)^{-C_4}}, \tag{6.3}$$

$$\rho_{\mathrm{c}} = \frac{\rho_0}{c_{\mathrm{c}}}\left(1 + C_5\left(\rho_0 \frac{f}{R_{\mathrm{f}}}\right)^{-C_6} - iC_7\left(\rho_0 \frac{f}{R_{\mathrm{f}}}\right)^{-C_8}\right). \tag{6.4}$$

This model considers the specific flow resistance R_{f} of the fabric and eight Delany-Bazley constants [53], i.e.

$$\begin{pmatrix} c_1 \\ c_2 \\ c_3 \\ c_4 \\ c_5 \\ c_6 \\ c_7 \\ c_8 \end{pmatrix} = \begin{pmatrix} 0.0978 \\ 0.7 \\ 0.189 \\ 0.595 \\ 0.0571 \\ 0.754 \\ 0.087 \\ 0.732 \end{pmatrix}. \tag{6.5}$$

The BEM and FEM are coupled via the pressure p [53], i.e.

$$p_{\mathrm{BEM}} = p_{\mathrm{FEM}}. \tag{6.6}$$

This numerical model is used to calculate the steering capabilities of the array, the IL, HPBW and SLL. The results were normalized and compared with the measurements.

However, prior to the simulations, the hydrophobic fabrics specific flow resistance R_{f} must be characterized in order to simulate its influence. Therefore, a flow pipe was created according to DIN 9053 [89]. Afterwards, the setup was calibrated with well-defined reference fabrics but with lower water resistance. This setup was built by Fabian Krauß in his bachelor thesis.

In general, the specific flow resistivity R_{f} is defined by the differential pressure Δp induced by the specific flow resistivity and the volume flow rate through the medium [89], i.e.

$$R_{\mathrm{f}} = \frac{\Delta p}{q_{\mathrm{v}}}. \tag{6.7}$$

In order to measure these two quantities, a 3D-printed flow pipe was built including a mass flow rate sensor (SFM3000-200-C, Sensirion) and a differential pressure sensor (SDP810-500, Sensirion) (Figv 6.8). A fan (Noctua NF-A4x10) was used as a flow source. All parts are 3D-printed with polylactide (PLA) using a Prusa i3 MK3S (Prusa Research). In addition, the flanges of the 3D-printed parts are sealed with o-ring joints, sealing compound and insulating tape. The total measurement uncertainty of the setup is $\pm 35\,\mathrm{kPas/mm^2}$. Since the fabric varies in thickness ($700.6\,\mu\mathrm{m} \pm 3.25\,\mu\mathrm{m}$, MarCator 1086Ri, Mahr GmbH) and porosity, ten samples were characterized. This led to a maximum, a minimum and averaged flow rates which can be derived. These values are used in the numerical model to perform a corner analysis. In addition, the fabrics flow resistivity is measured at different flow rates because nonlinearities may occur due to the creation of vortexes [90].

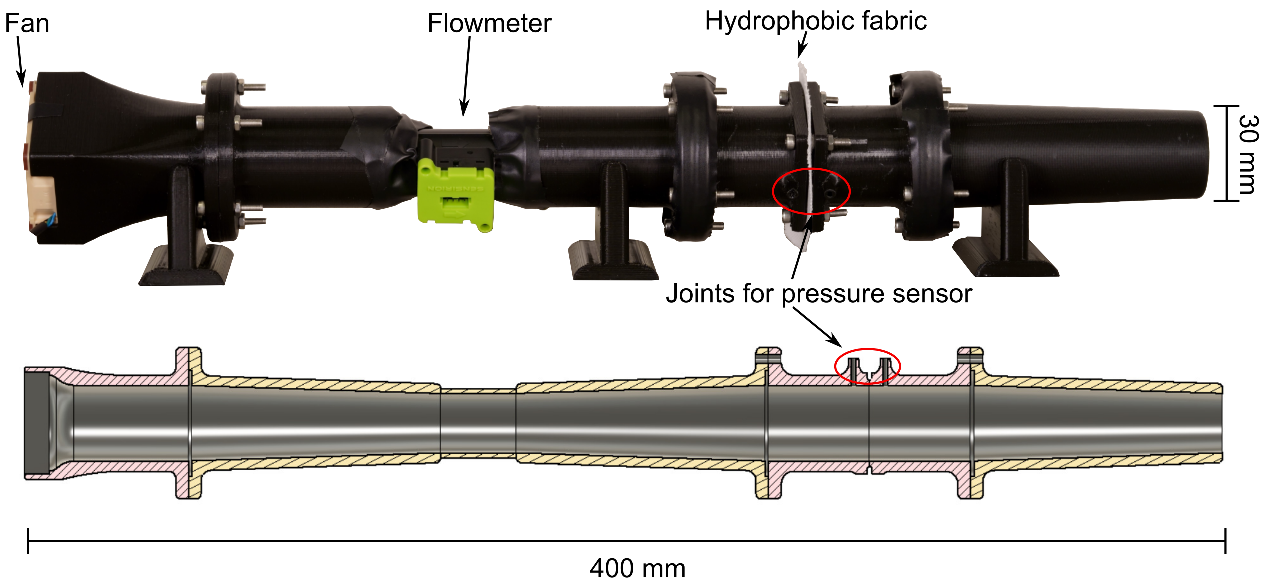

Figure 6.8: The flowpipe consists of a fan, a flowmeter, joints for the pressure sensor and the hydrophobic fabric.

In general, the specific flow resistivity for the ten samples ranges from $13.15\,\mathrm{kPas/mm^2} \pm 0.06\,\mathrm{kPas/mm^2}$ to $19.91\,\mathrm{kPas/mm^2} \pm 0.03\,\mathrm{kPas/mm^2}$ (Figure 6.9). In addition, the specific flow resistivity depends on the flow rate. The maximum variation due to nonlinearities is $\pm 1.83\,\mathrm{kPas/mm^2}$. This nonlinearity can be explained with the creation of vortexes [90]. When the flow penetrates the fabric, vortexes occur due to the geometry of the fabric. As a result, a part of the flow energy is transformed into the vortexes velocity which depends on the flow rate. Furthermore, between the ten samples there is a maximum flow resistivity variation of $\pm 1.965\,\mathrm{kPas/mm^2}$.

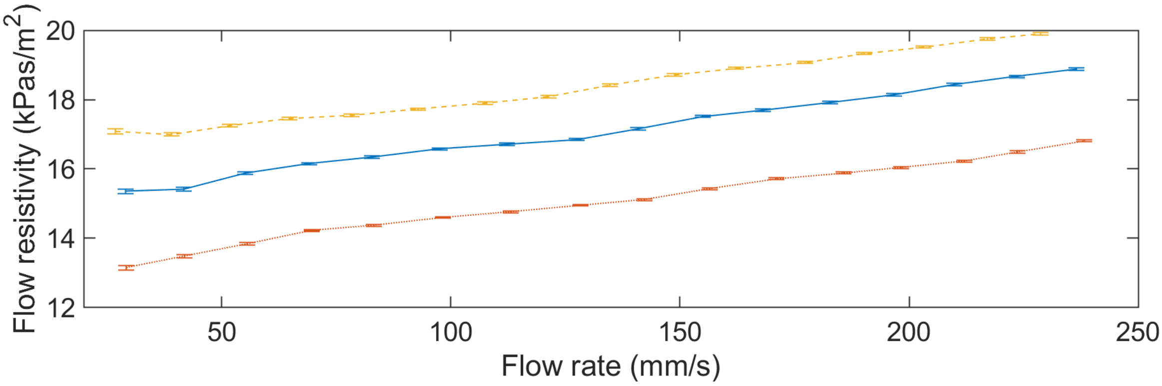

Figure 6.9: The maximum (- -), averaged (-) and minimum (:) flow resistivity of ten hydrophobic fabrics is nonlinear and varies between $13.15\,\mathrm{kPas/mm^2} \pm 0.06\,\mathrm{kPas/mm^2}$ and $19.91\,\mathrm{kPas/mm^2} \pm 0.03\,\mathrm{kPas/mm^2}$.

In this section, the influence of the hydrophobic fabric on the IL, the change of the half power beam width (ΔHPBW) and the change of the side lobe level (ΔSLL) are compared for the measurements and the simulations. The validation of the simulations regarding steering capability, HPBW, SLL and IL, were conducted in an anechoic chamber. In addition, the environmental properties such as temperature, humidity and ambient pressure were measured with a digital pressure sensor and a humidity sensor and also used in the simulations. During the measurements the temperature was $16.4°\mathrm{C} \pm 0.5°\mathrm{C}$ the ambient pressure was $101529\,\mathrm{hPa} \pm 1\,\mathrm{hPa}$ and the humidity was $36.6\% \pm 2\%$. In the numerical model, the complete range of the measurement results were used for the corner analysis, since it is challenging to assume which equivalent flow rates occur at the output ports when ultrasound is propagating in the waveguide. In order to derive the quantities, the SPL is normalized to the maximum value without the fabric in the simulations and the measurements.

In general, the simulation and the measurements are in good agreement. The IL of the simulated fabric is $1.2\,\mathrm{dB} \pm 0.2\,\mathrm{dB}$ which intersects with the result of the measurements, including the uncertainties, of $1.8\,\mathrm{dB} \pm 1\,\mathrm{dB}$ at a steering angle of $0°$ [Figure 6.10(a, b)]. The same agreement is observed at a steering angle of $45°$ [Figure 6.10(c, d)]. In addition, the ΔHPBW of the simulations is $0°$ which is the same result as in the measurements with $1° \pm 2°$. This result can be observed for a steering angle of $0°$ and $45°$ as well. Last, the hydrophobic fabric has no significant influence on the ΔSLL. Both the simulation and the measurements provide results which are within there respective uncertainties. Since the hydrophobic fabric introduces mainly thermoviscous losses, there are no significant time delay variations between the ducts of the waveguide.

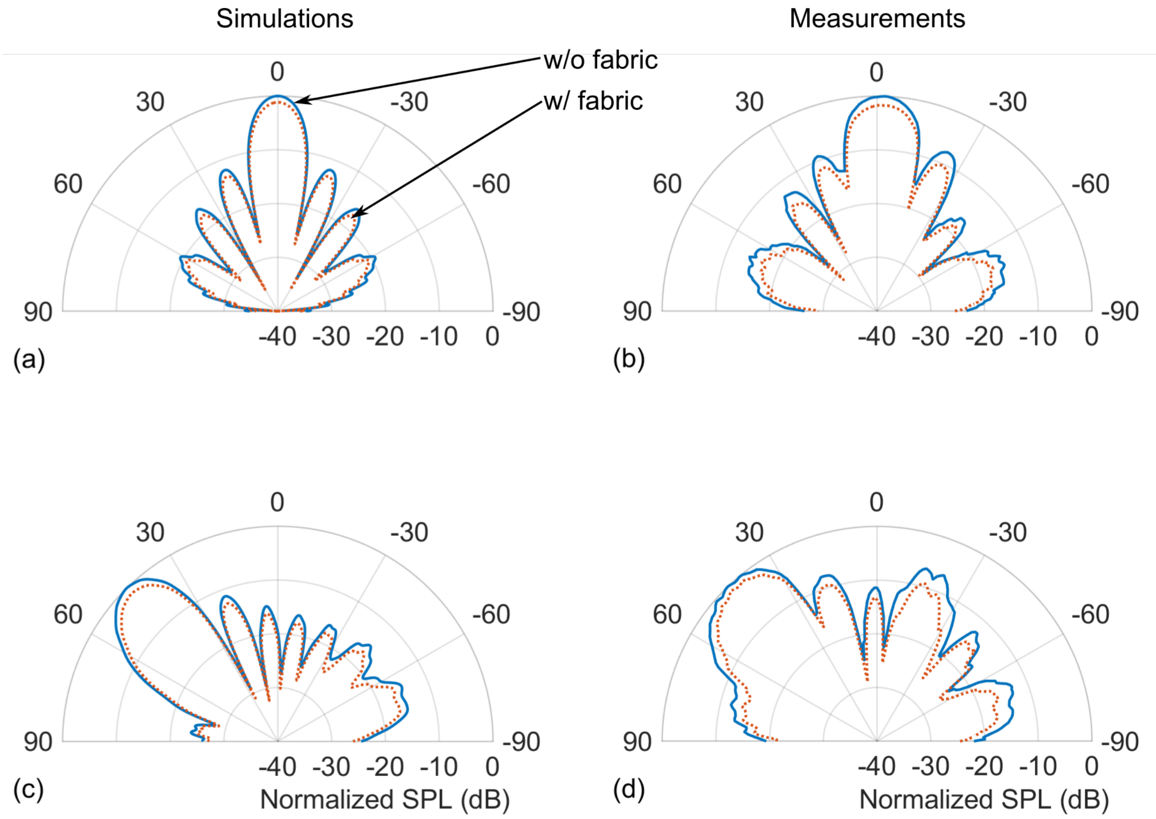

Figure 6.10: The hydrophobic fabric has just a minor IL in the numerical simulations (a) and the measurements (b). In addition, the fabric does not influence the beam-forming capabilities in the simulations (c) and the measurements (d).

Table 6.2: IL, influence on SLL and influence on HPBW of the directivity pattern with hydrophobic fabric at a steering angle of $0°$ and $45°$ for simulations and measurements.

Steering angle	Influence on	Simulation	Measurement
$0°$	IL	$1.2\,\mathrm{dB} \pm 0.2\,\mathrm{dB}$	$1.8\,\mathrm{dB} \pm 1\,\mathrm{dB}$
	ΔHPBW	$0°$	$1° \pm 2°$
	ΔSLL	$0.1\,\mathrm{dB}$	$0.8\,\mathrm{dB} \pm 1\,\mathrm{dB}$
$45°$	IL	$1.4\,\mathrm{dB} \pm 0.2\,\mathrm{dB}$	$2.3\,\mathrm{dB} \pm 1\,\mathrm{dB}$
	ΔHPBW	$0°$	$1° \pm 2°$
	ΔSLL	$0\,\mathrm{dB}$	$0.5\,\mathrm{dB} \pm 1\,\mathrm{dB}$

6.4 Optimization of the thin films

The first test of using thin LDPE films for waterproofing the waveguide showed a significant loss in SPL of $7.5\,\mathrm{dB}$ in transmit. On the other hand, the thin film provides a high protection class of IPX8. Next, methods are analyzed to further reduce the losses induced by the film while retaining the high IP class. Therefore, a different material of the film is used and the geometry of the waveguide is altered. All analysis is conducted on a single duct instead of the entire 8×8 phased arrays.

In general, the pre-stress of a membrane influences its mechanical behavior such as its resonance frequency or its resetting force. Thus, the bonding of the film onto a carrier structure is crucial. In order to ensure a proper bonding, a PLA carrier was directly printed onto the film. Since the acoustic waveguide is made of PLA, it is a convenient approach to combine the two parts.

In addition, the PLA film provides a much more linear strain-stress relation compared to LDPE, which was used in previous work. The PLA film used in the experiments has a thickness of $20\,\mu\mathrm{m}$. Since this film is a polymer, it provides a low density of $1.25\,\mathrm{g/cm^3}$ and thus low acoustic reflections.

The integration of the film into the 3D-printing process is divided in four steps. First, a droplet of deionized water ($0.3\,\mathrm{ml}$) is positioned onto the heating bed of the 3D printer. This droplet serves as an adhesive for the film. Tap water was not suitable for this purpose, since it introduced calcification on the film. Additionally, isopropanol leads to higher adhesive forces between the film and the heating bed of the printer resulting in a damaged film. Second, the film is laid on top of the droplet. Third, a doctor blade is used to even the surface of the film. Last, the print is started. The recommended settings of Prusa for PLA were used without additional considerations regarding bed temperature or bed leveling. This way, a sufficient bonding between the carrier and the film is achieved. No layer shifts or shrinking processes occurred during the printing.

The measurement setup consists of multiple parts to ensure a flexible positioning and pre-strain of the film inside the waveguide [Figure 6.11(a)]. The assembly of the film with the waveguide is divided in multiple steps. First, a base is positioned on top of the output port of the waveguide. This base has an embossment for the positioning of a bottom cylinder with the height h_{prot}. This cylinder defines the pre-strain of the thin film. Varies heights were tested and a height of $2\,\mathrm{mm}$ was the best compromise between a sufficient tensioning of the film without damaging it. Second, the carrier ring, which is directly printed onto the film, is put on top of the base. The carrier and the base are screwed together with a battery-powered screwdriver (Bosch GSR 12V), which applies the pre-strain onto the thin film. Third, a second hollow cylinder is placed on top of the film. By applying the top of the structure onto the second cylinder, the film is clamped at is periphery which provides an additional stress. The position of the film inside the waveguide d_{prot} can be changed by varying the height of the top and base. The top provides a flange which allows to conduct measurements with the goniometer system in the anechoic chamber. The optimal height of 4.5 mm was selected from previous measurements. All screws are applied with the same torque. By applying this structure onto the waveguide, the length of the waveguide is increased by 19 mm.

The film uses the vibroacoustic effect. By analyzing the vibration of the film the mechanical coupling between the waveguide and the free-field can be observed. For instance, the vibrational mode provides inside whether acoustic shortcuts can appear. In this work, Laser Doppler Vibrometer Measurements (LDVM) are used in two ways to ensure minimal measurement feedback. First, the thin film is coated with a 100 nm-thick layer of aluminum. This way, the mechanical velocity of the film can be directly measured. Second, the thin film is untreated retaining its optical transparency. Thus, the LDVM can directly measure the velocity of the transducer inside the waveguide. This information is used to derive the influence of the foil and the thin film on the transducer.

The LDVM consists of a laser unit (OFV 534, Polytec GmbH, Germany) and a controller unit (OFV 3001, Polytec GmbH, Germany) [Figure6.11(b)]. The setup includes three linear stages (Physik Instrumente, Karlsruhe, Germany). The first stage moves the laser head in z-direction. This way the focal point of the LDVM can be adjusted. The other two stages move the ultrasonic transducer in the x- and y-direction to scan the vibrational surface (Fig 3). The transducer is excited with $20\,V_{pp}$ at 40 kHz continuous sinusoidal signal (GW Instek, AFG-2225, Taiwan). All signals are captured by an oscilloscope (Keysight, DSO-X 3021A, USA). In addition, the entire setup is mounted on a passive damped optical table (Newport, USA) to reduce environmental vibrations. The measurements were conducted in a temperature controlled room at 22°C. This setup was built by Dr.-Ing. Alexander Unger in his Thesis [30].

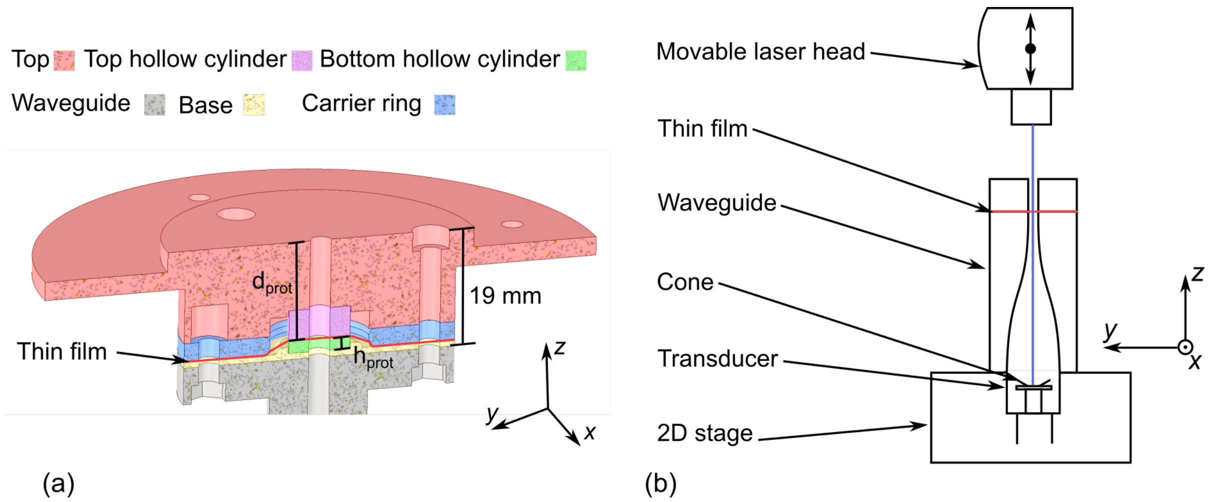

Figure 6.11: The pre-strain mechanism of the thin film consists of multiple components to ensure a versatile experiment (a). The measurements of the surface velocity is automated using two stages and a movable laser head (b).

The first LDVM experiment compares the mode shapes of the LDPE film from previous experiments with the mode shape of the PLA film at 40 kHz. The velocities are normalized to their respective maximum values for a better comparison.

The LDPE film has a [0,2] mode, which creates a 180° phase shift between the inner and outer section of the film [Figure 6.12(a)]. This leads to minimal SPL since the phase shift results in acoustic shortcuts. In addition, the maximal velocity is unevenly distributed. In the outer ring, three dominating maxima occur. Since not all parts of the film osculate with maximal amplitude, this further reduces the resulting SPL. There are two possibilities to decrease the order of the film. First, the frequency can be reduced, since the fundamental mode of the LDPE film is much lower. This leads to a switch of transducers and new phased arrays must be built. Second, the diameter of the output port can be decreased. A decreased diameter results in a smaller acoustic aperture which reduces the SPL further.

In contrast, the PLA film has a [0,1] mode [Figure 6.12(b)]. This even velocity distribution increases the emitted SPL, since no acoustic shortcuts occur. In addition, the maximal velocity is distributed on a bigger surface in comparison to the LDPE film. The larger the active sound emitting part of a surface is, the higher the resulting SPL will be. Thus, the 3D-printed connection between the film and the carrier provides a sufficient bonding. Additionally, the Young's moduli of the two materials differ. The LDPE film has a value of $200\,\mathrm{MPa} - 300\,\mathrm{MPa}$. However, the PLA film has a value of $4\,\mathrm{GPa} - 5\,\mathrm{GPa}$, which is 13-times higher. Since the resonance frequency of the film is increased with increased Young's modulus, the PLA film has a higher resonance frequency as well.

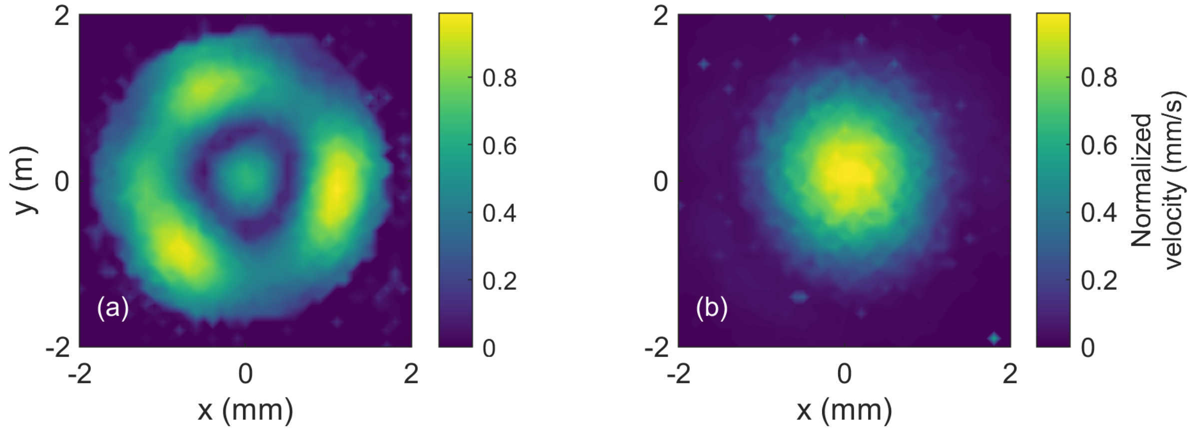

Figure 6.12: The LDPE film creates a [0,2] mode (a), whereas the PLA film creates a [0,1] mode (b).

In order to shift the systems resonance to $40\,\mathrm{kHz}$ a frequency response measurements was conducted at the center of the transducer. Therefore, the grid in front of the transducer was removed. First, the transducer was characterized without the waveguide. Its resonance frequency is $39.3\,\mathrm{kHz}$ with an amplitude of $176\,\mathrm{mm/s} \pm 1.2\,\mathrm{mm/s}$ [Figure 6.13(a)]. When applying the waveguide to the system two resonances occur [Figure 6.13(a)]. The first resonance is at $39.3\,\mathrm{kHz} \pm 0.05\,\mathrm{kHz}$ and reaches an amplitude of $179\,\mathrm{mm/s} \pm 1.2\,\mathrm{mm/s}$. The second resonance is at $40.2\,\mathrm{kHz} \pm 0.05\,\mathrm{kHz}$ and has nearly the same amplitude with $190\,\mathrm{mm/s} \pm 1.2\,\mathrm{mm/s}$. Both resonances increase the amplitude, since they can be seen as Helmholtz resonators. However, they amplify the wrong frequencies. Next, the PLA film is applied to the waveguide. Again two resonances occur at higher frequencies when compared to the single waveguide measurement $+0.3\,\mathrm{kHz} \pm 0.05\,\mathrm{kHz}$ [Figure 6.13(a)]. However, the first resonance has an increased amplitude of 28% compared to the single waveguide and an increase of 30% compared to the transducer. On the other hand, at $40\,\mathrm{kHz}$ a minimum is located which has a reduced amplitude of 42% compared to the waveguide and 31% compared to the transducer.

The two resonances occur, since the system consists of two mechanical oscillators which are coupled via the acoustic compliance of the waveguide. The dominating parts of the system are the two masses of the transducer and the film. The two resonances can be combined by increasing the damping between the masses. Thus, the masses oscillate in phase and amplify frequencies between the previous two resonances. In order to increase the damping inside the waveguide, the thermoviscous effects must be increased. This can be realised by increasing the hydraulic radius of the waveguide. To this extent, the aspect ratio between the perimeter and the cross-sectional area is increased which increases the effective friction surface between the air and the inner surface of the waveguide. The increased hydraulic radius was achieved by exchanging the round waveguide with a waveguide which has a star-shape as a cross-sectional area. Again, the transducer without the waveguide is measured. The transducer has the same resonance frequency of $40\,\text{kHz} \pm 0.05\,\text{kHz}$ and a velocity of $179\,\text{mm/s} \pm 1.2\,\text{mm/s}$ [Figure 6.13(b)]. Next, the star-shaped waveguide is applied to the transducer. Again, two resonances can be observed. In comparison to the round waveguide, the resonances occur at higher frequencies $+0.3\,\text{kHz} \pm 0.05\,\text{kHz}$ [Figure 6.13(b)]. The amplitudes retained the same as well with $159\,\text{mm/s} \pm 1.2\,\text{mm/s}$ and $187\,\text{mm/s} \pm 1.2\,\text{mm/s}$. Last, the PLA film is applied to the star-shaped waveguide. Now, the resonance with the highest amplitude is at $40.1\,\text{kHz} \pm 0.05\,\text{kHz}$ instead of $39.6\,\text{kHz} \pm 0.05\,\text{kHz}$ with the round waveguide [Figure 6.13(b)]. In addition, the amplitude is the same compared to the maximum amplitude of the round waveguide with the PLA film.

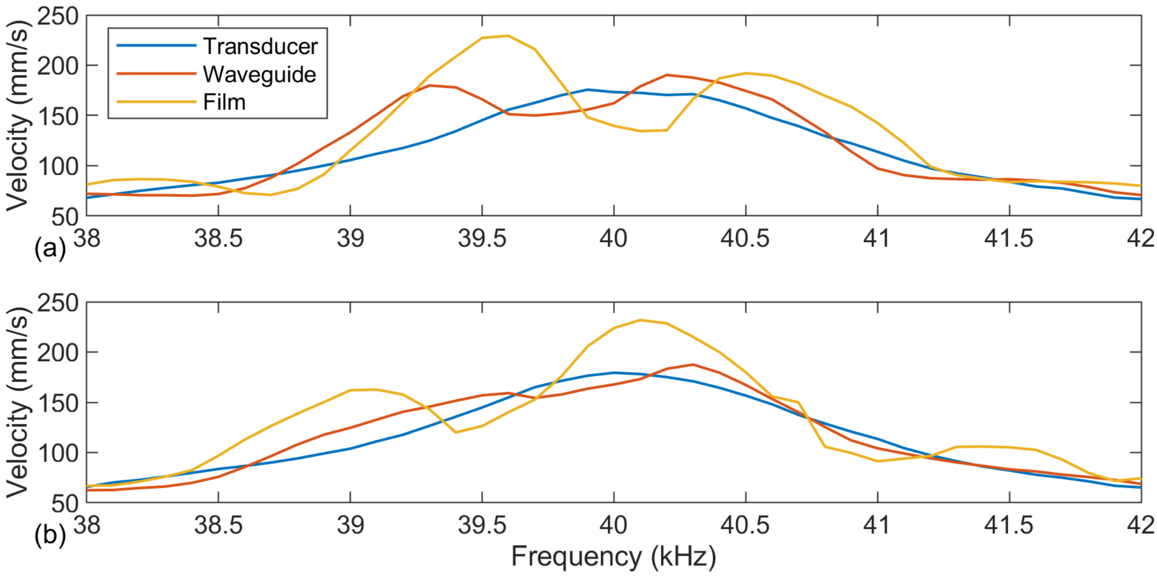

Figure 6.13: The frequency response of the round waveguide including the PLA film is measured (a). However, its resonance frequency is at the wrong frequencies. By applying a star shape to the cross-section of the waveguide, this frequency can be shifted to the desired $40\,\text{kHz}$.

In order to determine the influence of the PLA film on the waveguide, calibrated measurements in an anechoic chamber were conducted. During the experiment, the temperature was $16.4°\text{C} \pm 0.5°\text{C}$, the ambient pressure was $101529\,\text{hPa} \pm 1\,\text{hPa}$ and the humidity was $36.6\% \pm 2\%$. Again, the transducer is driven with $20\,\text{V}_{\text{pp}}$ at $40\,\text{kHz}$ and 80 cycles. For this experiment, the cycles were increased, because the envelope of the time signal is analyzed. Hence, the influence of the film on the rise and decay time can be observed.

In general, the PLA film does not affect the shape of the envelope. Thus, there are no additional time delays due to the film itself. This result was also shown in the directivity pattern of the phased array which retained unaltered due to the use of a thin film. In addition, the PLA film slightly increased the absolute pressure by $0.4\,\text{dB}$. However, the measurement accuracy of the system is $\pm 1\text{dB}$ for microphone measurements. Thus, the PLA film has no significant influence on the SPL of the waveguide.

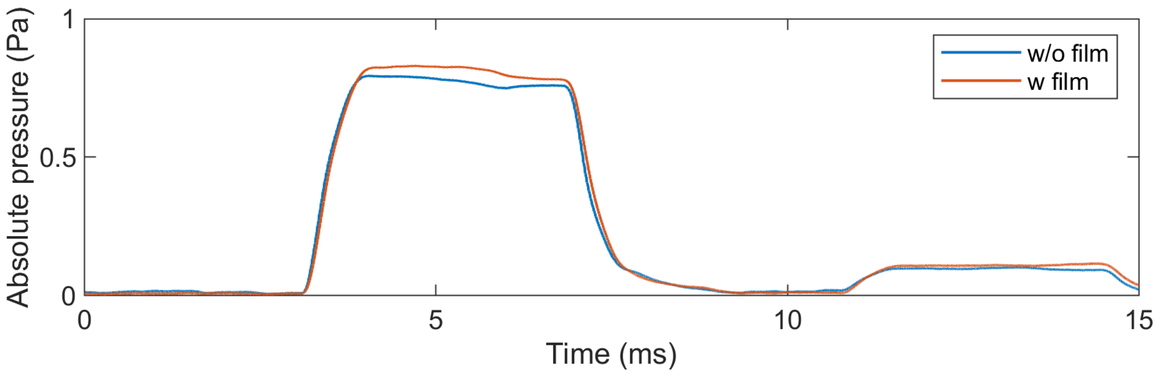

Figure 6.14: The absolute pressure of the waveguide without and with the PLA film is compared. With the PLA film, there is a minor increased SPL of 0.4 dB.

In general, the integration of a PLA film into an FDM process using PLA is possible. Even with predefined printing settings, the print finished without drawbacks such as layer shifts. In the experiments, it is proven that the PLA film leads to minor acoustic effects. These effects were even lower compared to a hydrophobic fabric, when the film is in the right position inside the waveguide, has the right mechanical pre-strain and the entire system is tuned to the right resonance frequency. However, since the positioning of the film inside the waveguide influences the losses, temperature deviations will have an impact on these IL as well. In this case, the hydrophobic fabric has advantages since it is less sensitive to variable positions inside the waveguide and thus less sensitive to temperature changes.

7 Conclusion and future work

In this work, the wave propagation inside acoustic waveguides was investigated for air-coupled ultrasonic phased arrays. First, suitable modeling methods were presented and discussed for the given waveguide geometry at $40\,\text{kHz}$. The approaches are divided in analytic and numeric models and lossless and thermoviscous models. Thermoviscous models are especially of high interest, since the theory recommends them for a valid model. However, they add complexity to the system because energy conservation is add to the set of equations. Thermoviscous losses lead to acoustic shearing at the boundary and thermal conduction. As a result, one of the most crucial parameters is the hydraulic diameter of the waveguide which defines the aspect ratio of the cross-sectional area and the circumference. However, since the cross-section of the waveguides is round, the effect of the thermoviscous losses have just a minor impact on the sound pressure level of $1.7\,\text{dB}$.

On the other hand, the comparison between analytic and numeric models showed a significant difference. In general, analytic models assume plane wave propagation inside the waveguide. However, since the output ports are opened the end-correction of the waveguide needs to be considered. In addition, the diameter of the input section of the waveguide is bigger than the wavelength. Thus, analytic models have big disadvantages when it comes to bent waveguides. As a result, the best way to simulate the directivity pattern of waveguided phased arrays for the given geometry and frequency is the use of the boundary element method. This method provides sufficient accuracy and a reasonable calculation time. Furthermore, it is applicable for 3D simulations, since only the surfaces are meshed and not the air volume.

Additionally, this work presents a method to validate numerical models of phased arrays in free-field. Furthermore, it is suitable to characterize phased arrays in transmit, receive and pulse-echo mode. In transmit, a calibrated microphone is used to capture the ultrasound. The entire signal chain has a noise floor of $60\,\text{dB}$ at a sampling rate of $500\,\text{kSa/s}$ without averaging. This noise floor can be further reduced by increasing the averaging. As the theory predicts, each time the averaging is doubled, the noise floor is reduced by $3\,\text{dB}$. However, this increases the capturing time for the signals with $10\,\text{ms}$ per capture. The upper sound pressure level is limited by the microphone itself with $171\,\text{dB}$. This leads to a dynamic range of the measurement setup of $111\,\text{dB}$. In addition, the microphone is tilted by $90°$ which increases its linearity in the frequency spectrum. Furthermore, the goniometer approach offers fast measurements of up to $0.5\,\text{s/point}$ when the measurement points are arranged in a meander shape. Last, using a g-code like convention for the positioning of the 3D stage offers versatile measurements. This way, ultrasonic phased arrays can be characterized in transmit, receive and pulse echo in various directions.

This measurement setup was used to validate the BE-model. In general, the measurements and the simulations are in good agreement. The half power beam width differs by $4°$ and the side lobe level differs by $3\,\text{dB}$. Additionally, the influence of the finite-sized rigid baffle is noticeable in both the simulations and the measurements. In both results, small ripples in the side lobes can be observed. This proofs the results of R. Golinske who compared the Relay integral with the Helmholtz Kirchhoff integral. The amplitude variation of the transducers was not implemented in the simulations causing different zero-crossings compared to the measurements. Last, the entire simulations were conducted on a single CPU server with no need for calculation clusters.

In the next step of this thesis, the waveguide geometries in previous works were questioned. First, the perpendicular structure of the input and output plane was investigated. As a result, only the input surface needs to be perpendicular to the center line of the waveguide. Since this section has a bigger diameter than the wavelength, higher modes occur when the wave-coupling is tilted. In contrast, the output diameter is small compared to the wavelength which only allows for plane wave propagation inside this section. Afterwards, the length of the waveguides were optimized in order to increase the sound pressure level. However, this optimization is only interesting from an academic point of view. For an industrial application, this approach is not applicable, because the temperature variation has the same influence on the waveguide as a length variation. Especially, in a thermal range of $-40°$ to $85°$ multiple maxima and minima are observed in this frequency range. Next, the aperture size was varied to increase the emitted sound pressure level and received pressure. For this reason, rectangular and elliptic shapes are compared. This resulted in rectangle shapes with slightly higher output SPL and receiving SPL, since their acoustical active area is bigger than the area of ellipsis with the same lengths. However, the increased areas have a limit. When the length exceeds 32 mm higher modes occur at the output which decreases the sound pressure. This is caused by different sound propagations between the center line of the waveguide and the edge line. These differences create a phase shift at the output which can be compared to an inefficient mode shape of an loudspeaker. In order to investigate the losses in the waveguide, a numerical model was set up. This model uses the FEM in the time domain including thermoviscous effects. The time domain allows to distinguish between the different types of losses. These are thermoviscous losses, diffraction losses and losses due to reflections at the output of the waveguide. As a result the thermoviscous losses had just a minor influence on the SPL. The major losses occur due to the diffraction because the aperture size of the waveguide is decreased. All the above mentioned results were used to build a new generation of line arrays. This shows in four steps the evolution from an array with equal length waveguides to a compact design which decreases the length of the waveguide from 80 mm to 28 mm. In addition, the SPL is increased by 5 dB. Furthermore, the smaller waveguide provides a reduced blind zone for pulse-echo measurements of 57%.

Jäger proposed to use Bézier-shaped waveguides in order to reduce the assembly time between the transducers and the waveguide. In this work, this approach was validated using experiments and simulations by comparing two waveguides. The first waveguide consists of equal lengths and the second one consists of the proposed Bézier shapes. As a result, the different duct lengths of the Bézier waveguide can be compensated with additional time delays without introducing drawbacks. The steering capabilities, HPBW, SLL and SPL of the two waveguides have minor deviations. These can be explained with the manufacturing tolerances of the transducers used for the arrays.

The last improvement investigated in this work is the increased water resistance of the waveguide. Hydrophobic fabrics and thin films were compared regarding the IP-class, the insertion loss and their influence on the steering capabilities. In general, both solutions showed no significant effect on the beam steering. The HPW, SLL and maximum steering angles retain the same. However, the IP classes differ with IP x7 for the hydrophobic fabric and IP x8 for the thin film. In addition, the IL of the fabric is less temperature depending in comparison to the thin film. In order to decrease the IL of the thin film, the resonance frequency of the entire system including the waveguide, the transducer and the film itself must be tuned accurately. Since the resonance depends on the wavelength, low IL of the thin film can not be provided over an industrial temperature range with this method.

This work shows, the versatility of acoustic waveguides for ultrasonic applications. They are cheap in production, can be easily built and can be freely designed for different geometries. This leads to a new understanding in designing ultrasonic sensors, which separate the transducers aperture from the radiating aperture. The same approach can be observed in various natural structures such as the human hearing tract or the vocal tract.

In future work, not only the waveguide will be 3D-printed but the ultrasonic transducer as well. This approach provides adjustable bandwidth and resonance frequency of the system. This way, fully 3D-printed phased arrays can be built for different applications. For instance, a higher bandwidth lowers the decay time of the sensor, and, thus, reduces the blind zone in pulse echo mode.

One of the first prototypes of a 3D-printed air-coupled ultrasonic transducers using ferroelectrets was published by O. Ben Dali et al. in 2021 [91]. This transducer consists of a 20-µm-thick plate made of polylactic acid (PLA), a 3D-printed PLA back plate and printed holders. The electrical contact is provided by symmetrically evaporating aluminum on the external sides of the backplate (smooth side) and the bulk film. Afterwards, the bulk PLA film is attached to the printed backplate with the printed holder. In contrast, the ferroelectret transducers [92]–[94], the 3D-printed backplate and the vibrating plate build artificial voids which can be geometrically defined. Thus, the resonance frequency of this ferroelectret can be adjusted and does not depend on the natural voids of the polymer.

During charging, an electric field is applied to the metalized surfaces of the ferroelectret, and, thus, generating large electric fields in the air-filled voids causing Paschen breakdown [95]. The generated positive and negative charges are separated by the applied electrostatic field and move towards the polymer walls, where they are quasipermanently trapped. A surface potential difference is provided by the trapped charges at the polymer walls on both sides of the air gap. This effect serves two properties. First, it applies an electrical bias which can be compared to a DC bias for capacitive ultrasonic transducers. Second, it provides a mechanical pre-stress due to the electrostatic force between the two polymers. The PLA vibrating plate is less stiff compared to the printed backplate. Consequently, the bulk PLA plate causes the acoustic vibrations as a result of the driving AC voltage.

At resonance, this transducer reached sound pressure levels of up to 106.5 dB with a driving voltage of 70.7 V_{RMS}. Due to the large vibrating surface of 42 mm, the transducer has a narrow directivity with a half power beamwidth of 8°. In addition, the maximum side lobe level is 24 dB.

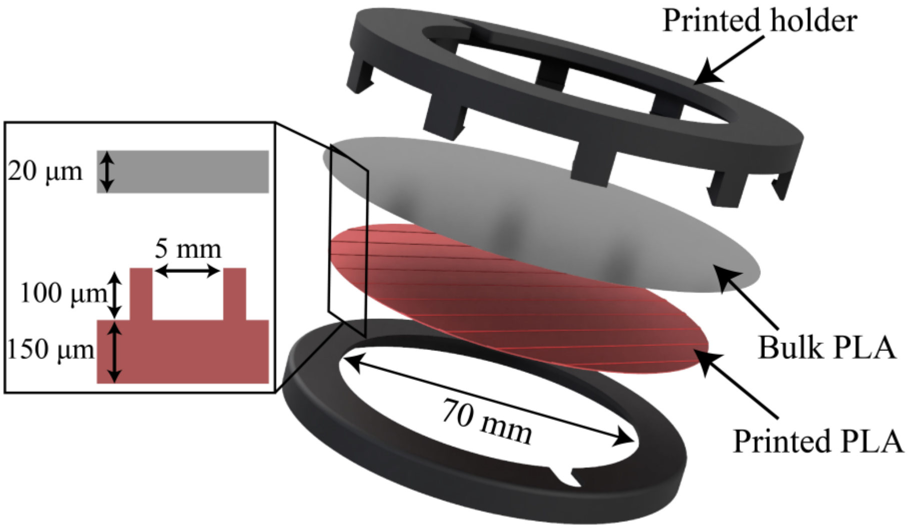

Figure 7.1: The 3D-printed ultrasonic transducer consists of a printed holder, a plate made of bulk PLA and a printed PLA backplate [91].

In order to accelerate the development cycles of the 3D-printed ultrasonic transducer, numerical simulations are planned. Since the ultrasonic transducer consists of an electrical, mechanical and acoustical domain, FEM simulations using COMSOL Multiphysics will be conducted.

First, the back plate needs to be designed. Here, the crucial parameters are the height h_g width w_g and number of grooves n_g. This way, the resonance frequency and its bandwidth can be modified. In addition, the objective is to identify the limits of the groove optimization. For example, one crucial research question is which bandwidths are achievable at which sound pressure levels. Afterwards, the acoustic directivity pattern can be further adjusted with an acoustic waveguide. Therefore, the length l_{duct} and the radius r_{duct} of the waveguide are key for an optimized system and the application optimized directivity.

The numerical model will consist of the following properties. First, a 2D model will be build with a rotational axis. This allows for efficient simulations using the rotational symmetry. Second, the pressure acoustics package and the electromechanical coupling package of COMSOL will be used in the frequency domain. In addition, this model will include the nonlinear geometry package, in order to simulate the displacement of the plate accurately. If this 2D model is not sufficient, a 3D model will be built. However, instead of using the acoustics packages of the FEM the BEM will be used for the 3D calculations.

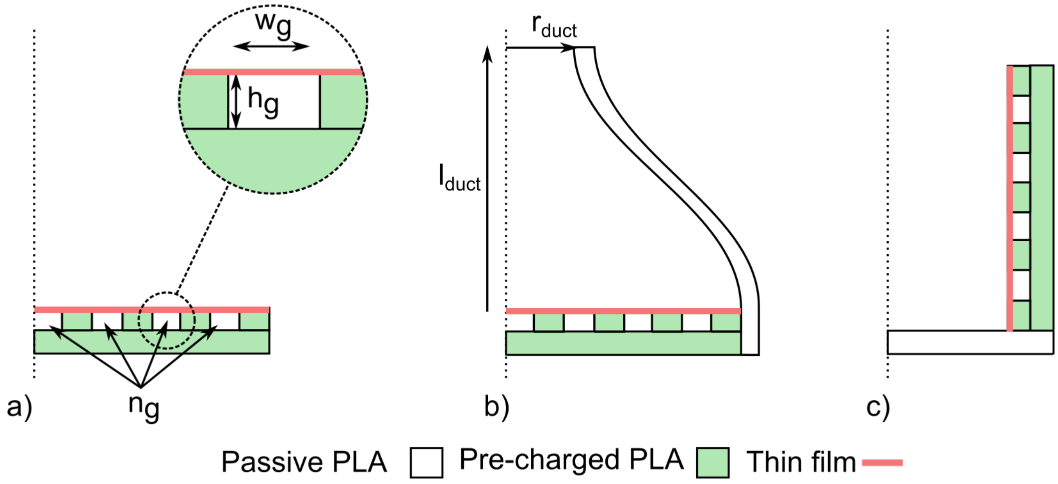

Figure 7.2: The optimization of the 3D-printed ultrasonic transducer will be devided into three steps. First, the backplate will be optimized for maximal bandwidth und SPL. Second, an acoustic waveguide will be attached to the transducer allowing for a versatile directivity. Last, the waveguide itself becomes the acoustic active part of the transducer.

After the simulations, experimental investigations of the mechanical, electrical, and piezoelectric properties of the transducer will be performed as well. Therefore, the acoustic properties will be compared with state of the art CUTs of the company Senscomp. However, without the need of a DC-bias.

This leads to a new generation of air-coupled ultrasonic sensors which are cheap, highly customizable and require simple driving electronics. With this approach, transducers can be easily implemented into the design of complex structures such as car bumpers, ceilings in a warehouse or even robots.

List of used symbols

Symbol	Unit	Description
A_{duct}	m^2	Cross-sectional area inside the duct
A_{Ellipsis}	m^2	Area of an ellipsis
$A_{\text{Rectangle}}$	m^2	Area of a rectangle
B		Auxiliary variable
$B_{\text{0-3}}$	m	Bézier points
$b(t)$	m	Propagation path inside a Bézier-shaped duct
$C_{\text{1-8}}$		Delany-Bazley constants
C_{ac}	m/N	Acoustic compliance
C_{p}	$\text{Jkg}^{-1}\text{K}^{-}1$	Specific heat capacity at constant pressure
C_{v}	$\text{Jkg}^{-1}\text{K}^{-}1$	Specific heat capacity at constant volume
CFL		Courant-Friedrichs-Lewy number
c_{air}	m/s	Speed of sound in air
c_{c}	m/s	Complex speed of sound
d_{Aperture}	m	Diameter of an acoustic aperture
d_{duct}	m	Diameter of an acoustic duct
d_{off}	m	Offset between input surface and output surface of the duct
d_{prot}	m	Position of the protection layer inside the waveguide
$\mathcal{E}$	J	Small change of energy of the system
e		Euler number
F	N	External forces
F_{arb}	N	Arbitrary force function
F_{drag}	N	Drag force at inner wall of ducts
F_{mech}	N	Alternating mechanical force
$F_{\text{mech,0}}$	N	Static mechanical force
$F_{\text{mech,t}}$	N	Total mechanical force
f	Hz	Frequency
f_{n}	Hz	Frequencies of a series of overtones
f_{res}	Hz	Resonance frequency
$f_{\text{r,i}}$	Hz	Relaxation frequency
f_{rN}	Hz	Relaxation frequency of nitrogen
f_{rO}	Hz	Relaxation frequency of oxygen
He		Helmholtz number
h_{aperture}	m	Height of the acoustic aperture
h_{DUT}	m	Height of the device under test from the linear axis
h_{ent}	J	Enthalpy
h_{g}	m	Height of the backplate groove
h_{prot}	m	Height of the pre-strain of the protection layer
h_{rel}	%	Relative humidity

h_{water}	mol/L	Molar concentration of water
I		Unit matrix
i_{el}	A	Electrical current
j	$\sqrt{-1}$	Imaginary number
K_{s}	Pa	Isentropic bulk modulus
K_{t}	Pa	Isothermal bulk modulus
k	$\text{W/m}^{-1}/\text{K}^{-1}$	Thermal conductivity
k_{c}	m^{-1}	Complex wavenumber
k_{eq}	m^{-1}	Equivalent wavenumber
k_{m}	m^{-1}	Wavenumber in radial symmetric systems
k_{wave}	m^{-1}	Wavenumber
L_{ac}	kg/m^4	Acoustic inductance
L_{el}	H	Electrical inductance
L_{p}	dB	Sound pressure level
$l_{\text{correction}}$	m	End correction for a flanged acoustic duct
l_{duct}	m	Length of an acoustic duct
M	kg/s/m^2	Flow source
M_{air}	kg	Air mass
m		Order of wavenumber for radial symmetry
m_{mass}	kg	Mechanical mass
N_{far}	m	Distance of the far-field
n		Integer number
$\mathbf{n}$		Normal vector
n_{cycles}		Number of cycles for the excitation of an ultrasonic transducer
n_{g}		Number of backplate grooves
P_{r}		Prandlt number
p	Pa	Alternating pressure
p_0	Pa	Ambient pressure
$p_{0\text{r}}$	Pa	Ambient reference pressure
p_{BEM}	Pa	Acoustic pressure from the BEM
p_{b}	Pa	Background pressure
p_{FEM}	Pa	Acoustic pressure from the FEM
p_{ref}	Pa	Reference pressure
p_{t}	Pa	Total pressure
p_{+}	Pa	Incident wave inside the duct
p_{-}	Pa	Reflected wave inside the duct
Q	J	Alternating heat
Q_{el}	C	Electrical charge
Q_{m}	Pa	Monopole source
Q_{t}	J	Total heat
Q_0	J	Static heat
q_{d}	Pa	Dipol source
q_{t}	W/m^2	Heat flux
q_{v}	m^3/s	Volume flow rate
R		Reflection coefficient
R_{f}	$\text{rayl}\cdot\text{m}^{-1}$	Flow resistivity of fabrics
R_{gon}	m	Radial coordinate of the goniometer setup

R_t	K/W	Thermal resistance
R_{piston}	rayl/m^2	Acoustic resistance of the piston transducer
R_v	1/k	Viscous resistance
r	m	Radial coordinate in cylindrical systems
r_{duct}	m	Radius of the duct
r_h	m	Hydraulic radius
S	J/K	Entropy
s	J/K	Alternating entropy
s_0	J/K	Ambient entropy
s_{direct}	m	Direct sound path
$s_{indirect}$	m	Indirect sound path
$s_{\mathcal{L}}$		Laplace variable
s_{ratio}		Standing wave ratio
s_t	J/K	Total entropy
T	K	Alternating temperature
$T(z)$	K	Thermal wave in z-direction
T_0	K	Ambient temperature
T_n		nth transducer of the phased array
T_t	K	Total temperature
T_r	K	Reference Temperature
T_{triple}	K	Triple-point isotherm temperature
t	s	Time
U	m^3/s	Volume flow
u_0	m/s	Ambient velocity in x direction
u_{el}	V	Electrical voltage
$u_{(z)}$	m/s	x component of velocity
V_{air}	m^3	Air volume of the acoustic mass
V_{damp}		Exponent for atmospheric daming
v	m/s	Acoustic velocity
v_0	m/s	Ambient velocity
v_n	m/s	Normal velocity
v_t	m/s	Total velocity
$W_{p,V}$	J	Pressure-volume work
$w_{aperture}$	m	Width of the acoustic aperture
w_g	m	Width of the backplate groove
Wo		Wormsley number
X_{piston}	rayl/m^2	Acoustic reactance of the piston transducer
x	m	Coordinate perpendicular to sound-propagation direction
x_{dis}	m	Mechanical displacement
x_{in}	m	x-coordiante of the input point of the duct
x_{mesh}	m	Meshing size
x_{out}	m	x-coordiante of the output point of the duct
y	m	Coordinate perpendicular to sound-propagation direction
y_{in}	m	y-coordiante of the input point of the duct
y_{out}	m	y-coordiante of the output point of the duct
Z_{ac}	rayl/m^2	Acoustic impedance
$Z_{ac,0}$	rayl/m^2	Acoustic characteristic impedance

$Z_{\mathrm{ac,t}}$	rayl/m^2	Acoustic termination impedance
Z_{close}	rayl/m^2	Acoustic impedance for closed duct
Z_{open}	rayl/m^2	Acoustic impedance for opened duct
Z_{piston}	rayl/m^2	Acoustic impedance of piston transducer
Z'_{ac}	rayl/m^2	Infinitesimal section of acoustic impedance of a duct
z	m	Coordinate along sound-propagation direction
z_{in}	m	z-coordiante of the input point of the duct
z_{out}	m	z-coordiante of the output point of the duct
α_{atm}	m^{-1}	Atmospheric attenuation coefficient
α_{cl}	m^{-1}	Classical absorption
α_{gon}	$^\circ$	α-coordinate of the goniometer setup
α_{p}	K^{-1}	Isobaric coefficient of thermal expansion
α_{rot}	m^{-1}	Rotational relaxation
α_{trans}	$^\circ$	Tilt angle of the transducer
$\alpha_{\mathrm{vib,i}}$	m^{-1}	Vibrational relaxation
β_{gon}	$^\circ$	β-coordinate of the goniometer setup
β_{s}	Pa^{-1}	Isentropic or adiabatic compressibility
β_{T}	Pa^{-1}	Isobaric coefficient of isothermal compressibility
β_{trans}	$^\circ$	Rotation angle of the transducer
γ		Ratio of isobaric to isochoric specific heats
δ_{t}	m	Thermal penetration depth
δ_{v}	m	Viscous penetration depth
ϵ	J/kg	Energy per mass unit of the system
κ		Ratio between specific heat capacity at constant pressure and constant volume
λ	m	Wavelength of the ultrasound
λ_{t}	m	Wavelength of the thermal wave
λ_{v}	m	Wavelength of the viscous wave
μ	Ns/m^2	Dynamic viscosity
μ_{B}	Ns/m^2	Bulk viscosity
Π_{duct}	m	Perimeter of the duct
π		Circular number
ρ	kg/m^3	Alternating density
ρ_{t}	kg/m^3	Total density
ρ_{c}	kg/m^3	Complex density
ρ_0	kg/m^3	Ambient density of the air
σ	N/m^2	Viscous-stress tensor
$\sigma(x)$	s^{-1}	Damping coefficient in x-direction in frequency domain
σ_{error}	dB	Standard error
τ	Ns/m^2	Viscous tensor
Φ	m/s	Velocity potential
∇		Nabla operator
ω	s^{-1}	Angular frequency

Acronyms and abbreviations

AC	Alternating current
BEM	Boundary element method
CAD	Computer-aided design
CUT	Capacitive ultrasonic transducer
DC	Direct current
DoF	Degrees of freedom
FDM	Fused deposition modeling
FEA	Finite element analysis
FEM	Finite element method
FPGA	Field programmable fated array
GPU	Graphics processing unit
HPBW	Half power beam width
IL	Insertion loss
IP	International protection
LDPE	Low density polyethylene
LDVM	Laser Doppler Vibrometer Measurements
MSL	Maximum side lobe level
PCB	Printed circuit board
PLA	Polylactic acid
PP	Peak-to-peak
RAM	Random access memory
RMS	Root mean square
SLL	Side lobe level
SNR	Signal to noise ratio
SPL	Sound pressure level

Bibliography

[1] L. D. Pohlmann, "Biomimicry—Innovations Inspired by Nature by Janine M. Benyus US-NY William Morrow. [Hardback 1997, Paperback 2002] (ISBN: 0-688-10699-9)", *INSIGHT*, vol. 19, no. 3, pp. 78–78, 2016, ISSN: 2156-4868. DOI: 10.1002/inst.12116. [Online]. Available: https://onlinelibrary.wiley.com/doi/abs/10.1002/inst.12116 (visited on 01/13/2022).

[2] D. Ramoo, "2.2 The Articulatory System", *Psychology of Language*, Oct. 29, 2021. [Online]. Available: https://opentextbc.ca/psyclanguage/chapter/the-articulatory-system/ (visited on 01/13/2022).

[3] R. D. Kent, "Vocal tract acoustics", *Journal of Voice*, The Voice Foundation's 22nd Annual Symposium, vol. 7, no. 2, pp. 97–117, Jun. 1, 1993, ISSN: 0892-1997. DOI: 10.1016/S0892-1997(05)80339-X. [Online]. Available: https://www.sciencedirect.com/science/article/pii/S089219970580339X (visited on 01/13/2022).

[4] J. Mullen, D. Howard, and D. Murphy, "Waveguide physical modeling of vocal tract acoustics: Flexible formant bandwidth control from increased model dimensionality", *IEEE Transactions on Audio, Speech and Language Processing*, vol. 14, no. 3, pp. 964–971, May 2006, ISSN: 1558-7916. DOI: 10.1109/TSA.2005.858052. [Online]. Available: http://ieeexplore.ieee.org/document/1621208/ (visited on 01/13/2022).

[5] "Figure 3.1. Schematic of the auditory system with its primary...", ResearchGate. (), [Online]. Available: https://www.researchgate.net/figure/Figure-31-Schematic-of-the-auditory-system-with-its-primary-components-including_fig1_322343133 (visited on 01/13/2022).

[6] M. R. Stinson and S. M. Khanna, "Sound propagation in the ear canal and coupling to the eardrum, with measurements on model systems", *The Journal of the Acoustical Society of America*, vol. 85, no. 6, pp. 2481–2491, Jun. 1989, ISSN: 0001-4966. DOI: 10.1121/1.397743. pmid: 2745873.

[7] R. Jorge, "Nonlinear Acoustics – Perturbation Theory and Webster's Equation", Nov. 17, 2013. arXiv: 1311.4238 [physics, physics:quant-ph]. [Online]. Available: http://arxiv.org/abs/1311.4238 (visited on 03/30/2022).

[8] R. Lerch, G. Sessler, and D. Wolf, *Technische Akustik*. Berlin, Heidelberg: Springer Berlin Heidelberg, 2009, ISBN: 978-3-540-23430-2 978-3-540-49833-9. DOI: 10.1007/978-3-540-49833-9. [Online]. Available: http://link.springer.com/10.1007/978-3-540-49833-9 (visited on 03/31/2020).

[9] A. Bell and N. H. Fletcher, "The cochlear amplifier as a standing wave: "squirting" waves between rows of outer hair cells?", *The Journal of the Acoustical Society of America*, vol. 116, no. 2, pp. 1016–1024, Aug. 2004, ISSN: 0001-4966. DOI: 10.1121/1.1766053. pmid: 15376668.

[10] "Acoustics of Organ Pipes - Judit Angster, Péter Rucz, András Miklós", Acoustics Today. (Jan. 27, 2017), [Online]. Available: https://acousticstoday.org/acoustics-organ-pipes-judit-angster/ (visited on 01/14/2022).

[11] "The Acoustics of Woodwind Musical Instruments - Joe Wolfe", Acoustics Today. (Mar. 8, 2018), [Online]. Available: https://acousticstoday.org/acoustics-woodwind-musical-instruments/ (visited on 01/17/2022).

[12] L. L. Beranek and D. T. Blackstock, "Acoustics, 1986 edition by Leo L. Beranek", *The Journal of the Acoustical Society of America*, vol. 83, no. 3, pp. 1206–1207, Mar. 1, 1988, ISSN: 0001-4966. DOI: 10.1121/1.396027. [Online]. Available: https://asa.scitation.org/doi/10.1121/1.396027 (visited on 01/18/2022).

[13] B. A. R., "A Non-resonant-Loudspeaker Enclosure .Non-resonant-Loudspeaker Enclosure Design. Transmission line", Wireless World, Oct. 1965. [Online]. Available: https://fdocuments.in/document/a-non-resonant-loudspeaker-enclosure-non-resonant-loudspeaker-enclosure-design.html (visited on 01/18/2022).

[14] Potente and Daniel, "General Design Principles for an Automotive Muffler Potente", *Proceedings of ACOUSTICS*, 2005. [Online]. Available: https://www.semanticscholar.org/paper/General-Design-Principles-for-an-Automotive-Muffler-Potente-Daniel/72b763683b5e60bee35650f788804727370135d5 (visited on 01/18/2022).

[15] L. Kang, A. Feeney, and S. Dixon, "Flow measurement based on two-dimensional flexural ultrasonic phased arrays", *Proceedings of Meetings on Acoustics*, vol. 32, no. 1, p. 045 012, Dec. 18, 2017. DOI: 10.1121/2.0000708. [Online]. Available: https://asa.scitation.org/doi/abs/10.1121/2.0000708 (visited on 03/31/2020).

[16] C. Haugwitz, A. Jäger, G. Allevato, *et al.*, "Flow Metering of Gases Using Ultrasonic Phased-Arrays at High Velocities", in *2019 IEEE International Ultrasonics Symposium (IUS)*, Oct. 2019, pp. 1129–1132. DOI: 10.1109/ULTSYM.2019.8925568.

[17] T. Carter, S. Seah, B. Long, B. Drinkwater, and S. Subramanian, "UltraHaptics: Multi-point mid-air haptic feedback for touch surfaces", presented at the UIST 2013 - Proceedings of the 26th Annual ACM Symposium on User Interface Software and Technology, Oct. 8, 2013, pp. 505–514. DOI: 10.1145/2501988.2502018.

[18] J. F. Pazos-Ospina, J. L. Ealo, and E. E. Franco, "Characterization of phased array-steered acoustic vortex beams", *The Journal of the Acoustical Society of America*, vol. 142, no. 1, pp. 61–71, Jul. 2017, ISSN: 0001-4966. DOI: 10.1121/1.4985194. [Online]. Available: http://asa.scitation.org/doi/10.1121/1.4985194 (visited on 10/18/2019).

[19] D. O. Ballinger, "Phased array for ultrasonic transducer", *The Journal of the Acoustical Society of America*, vol. 79, no. 3, pp. 888–888, Mar. 1, 1986, ISSN: 0001-4966. DOI: 10.1121/1.393737. [Online]. Available: https://asa.scitation.org/doi/abs/10.1121/1.393737 (visited on 03/31/2020).

[20] J. A. Kaiser Jr., "Spiral membrane speaker enclosure", *The Journal of the Acoustical Society of America*, vol. 58, no. 2, pp. 446–450, Aug. 1, 1975, ISSN: 0001-4966. DOI: 10.1121/1.380689. [Online]. Available: https://asa.scitation.org/doi/10.1121/1.380689 (visited on 03/31/2020).

[21] Y. Li, X. Jiang, B. Liang, J.-c. Cheng, and L. Zhang, "Metascreen-Based Acoustic Passive Phased Array", *Physicla review applied*, vol. 4, 2015. [Online]. Available: https://journals.aps.org/prapplied/pdf/10.1103/PhysRevApplied.4.024003 (visited on 03/31/2020).

[22] Y. Li, S. Qi, and B. Assouar, "Theory of metascreen-based acoustic passive phased array", *New Journal of Physics*, vol. 18, p. 043 024, Apr. 18, 2016. DOI: 10.1088/1367-2630/18/4/043024.

[23] G. Allevato, M. Rutsch, J. Hinrichs, E. Sarradj, M. Pesavento, and M. Kupnik, "Spiral Air-Coupled Ultrasonic Phased Array for High Resolution 3D Imaging", in *2020 IEEE International Ultrasonics Symposium (IUS)*, Sep. 2020, pp. 1–4. DOI: `10.1109/IUS46767.2020.9251675`.

[24] F. J. Pompei and S.-C. Wooh, "Phased array element shapes for suppressing grating lobes", *The Journal of the Acoustical Society of America*, vol. 111, no. 5, pp. 2040–2048, May 1, 2002, ISSN: 0001-4966. DOI: `10.1121/1.1460924`. [Online]. Available: `https://asa.scitation.org/doi/10.1121/1.1460924` (visited on 03/31/2020).

[25] E. Sarradj, "A GENERIC APPROACH TO SYNTHESIZE OPTIMAL ARRAY MICROPHONE ARRANGEMENTS", p. 12, 2016.

[26] A. Langen, "Ein Verfahren zur Konstruktion anwendungsoptimierter Ultraschallsensoren auf der Basis von Schallkanälen", Frauenhofer-Institut für Produktionstechnik und Automatisierung (IPA), Stuttgart, 1993.

[27] S. Igarashi and S. Takeuchi, "Control of Ultrasonic Acoustic Fields by Multiple Acoustic Waveguides and Piezoelectric Transducers", 2014. [Online]. Available: `https://www.semanticscholar.org/paper/Control-of-Ultrasonic-Acoustic-Fields-by-Multiple-Igarashi-Takeuchi/f5616e66f5be1a32015caa3561fb42b178706781` (visited on 03/31/2020).

[28] T. Takahashi, R. Takahashi, and S. Jeong, "Ultrasonic phased array sensor for electric travel aids for visually impaired people", in *ICMIT: Mechatronics and Information Technology*, 2007. DOI: `10.1117/12.783988`.

[29] E. Konetzke, M. Rutsch, M. Hoffmann, *et al.*, "Phased array transducer for emitting 40-kHz air-coupled ultrasound without grating lobes", in *2015 IEEE International Ultrasonics Symposium (IUS)*, Oct. 2015, pp. 1–4. DOI: `10.1109/ULTSYM.2015.0019`.

[30] A. Unger, "Air Coupled Ultrasonic Transducers for Industrial Applications", Ph.D. dissertation, Technische Universität, Darmstadt, Jul. 30, 2019. [Online]. Available: `https://tuprints.ulb.tu-darmstadt.de/8974/` (visited on 01/24/2022).

[31] M. Rutsch, E. Konetzke, A. Unger, *et al.*, "Extending the receive performance of phased ultrasonic transducer arrays in air down to 40 kHz and below", in *2015 IEEE International Ultrasonics Symposium (IUS)*, Oct. 2015, pp. 1–4. DOI: `10.1109/ULTSYM.2015.0095`.

[32] A. Unger, E. Konetzke, M. Rutsch, *et al.*, "Versatile air-coupled phased array transducer for sensor applications", in *2015 IEEE SENSORS*, Nov. 2015, pp. 1–4. DOI: `10.1109/ICSENS.2015.7370187`.

[33] D. M. Kupnik and D. B. Henning, "Phased Arrays für luftgekoppelten Ultraschall", p. 116,

[34] A. Jäger, D. Großkurth, M. Rutsch, *et al.*, "Air-coupled 40-KHZ ultrasonic 2D-phased array based on a 3D-printed waveguide structure", in *2017 IEEE International Ultrasonics Symposium (IUS)*, Sep. 2017, pp. 1–4. DOI: `10.1109/ULTSYM.2017.8091892`.

[35] G. Allevato, J. Hinrichs, M. Rutsch, *et al.*, "Real-Time 3D Imaging using an Air-Coupled Ultrasonic Phased-Array", *IEEE Transactions on Ultrasonics, Ferroelectrics, and Frequency Control*, pp. 1–11, 2020, ISSN: 1525-8955. DOI: `10.1109/TUFFC.2020.3005292`.

[36] R. Golinske, "Modellierung und Simulation der Schallwellenausbreitung von luftgekoppelten Ultraschall Gruppenwandlern", Ph.D. dissertation, Technische Universität, Darmstadt, Feb. 4, 2020. DOI: `10.25534/tuprints-00011377`. [Online]. Available: `https://tuprints.ulb.tu-darmstadt.de/11377/` (visited on 01/24/2022).

[37] R. Golinske, M. Hoffmann, E. Konetzke, A. Unger, M. Rutsch, and M. Kupnik, “Diffraction loss calculation based on boundary element method for an air-coupled phased array”, in *2015 IEEE International Ultrasonics Symposium (IUS)*, Oct. 2015, pp. 1–4. DOI: 10.1109/ULTSYM.2015.0375.

[38] D. Pereira, G. Haiat, J. Fernandes, and P. Belanger, “Simulation of acoustic guided wave propagation in cortical bone using a semi-analytical finite element method”, *The Journal of the Acoustical Society of America*, vol. 141, no. 4, pp. 2538–2547, Apr. 1, 2017, ISSN: 0001-4966. DOI: 10.1121/1.4979695. [Online]. Available: https://asa.scitation.org/doi/10.1121/1.4979695 (visited on 03/31/2020).

[39] D. Pereira, G. Haïat, J. Fernandes, and P. Belanger, “Effect of intracortical bone properties on the phase velocity and cut-off frequency of low-frequency guided wave modes (20–85 kHz)”, *The Journal of the Acoustical Society of America*, vol. 145, no. 1, pp. 121–130, Jan. 1, 2019, ISSN: 0001-4966. DOI: 10.1121/1.5084731. [Online]. Available: https://asa.scitation.org/doi/full/10.1121/1.5084731 (visited on 03/31/2020).

[40] Z. Sun, H. Jia, Y. Chen, Z. Wang, and J. Yang, “Design of an underwater acoustic bend by pentamode metafluid”, *The Journal of the Acoustical Society of America*, vol. 143, no. 2, pp. 1029–1034, Feb. 1, 2018, ISSN: 0001-4966. DOI: 10.1121/1.5024351. [Online]. Available: https://asa.scitation.org/doi/10.1121/1.5024351 (visited on 03/31/2020).

[41] H.-S. Kwon and B.-I. Popa, “Design and experimental demonstration of broadband acoustic pressure enhancing passive metafluids”, *The Journal of the Acoustical Society of America*, vol. 145, no. 6, pp. 3633–3639, Jun. 1, 2019, ISSN: 0001-4966. DOI: 10.1121/1.5112501. [Online]. Available: https://asa.scitation.org/doi/full/10.1121/1.5112501 (visited on 03/31/2020).

[42] R. Kirby, “Modeling sound propagation in acoustic waveguides using a hybrid numerical method”, *The Journal of the Acoustical Society of America*, vol. 124, no. 4, pp. 1930–1940, Oct. 1, 2008, ISSN: 0001-4966. DOI: 10.1121/1.2967837. [Online]. Available: https://asa.scitation.org/doi/10.1121/1.2967837 (visited on 03/31/2020).

[43] S. Félix, J.-B. Doc, and M. A. Boucher, “Modeling of the multimodal radiation from an open-ended waveguide”, *The Journal of the Acoustical Society of America*, vol. 143, no. 6, pp. 3520–3528, Jun. 1, 2018, ISSN: 0001-4966. DOI: 10.1121/1.5041268. [Online]. Available: https://asa.scitation.org/doi/full/10.1121/1.5041268 (visited on 03/31/2020).

[44] A.-C. Hladky-Hennion, “FINITE ELEMENT ANALYSIS OF THE PROPAGATION OF ACOUSTIC WAVES IN WAVEGUIDES”, 1996. DOI: 10.1006/jsvi.1996.0349.

[45] R. Ahmad, T. Kundu, and D. Placko, “Modeling of phased array transducers”, *The Journal of the Acoustical Society of America*, vol. 117, no. 4, pp. 1762–1776, Apr. 1, 2005, ISSN: 0001-4966. DOI: 10.1121/1.1835506. [Online]. Available: https://asa.scitation.org/doi/10.1121/1.1835506 (visited on 03/31/2020).

[46] M. D. Cahill and A. C. Baker, “Numerical simulation of the acoustic field of a phased-array medical ultrasound scanner”, *The Journal of the Acoustical Society of America*, vol. 104, no. 3, pp. 1274–1283, Sep. 1, 1998, ISSN: 0001-4966. DOI: 10.1121/1.424336. [Online]. Available: https://asa.scitation.org/doi/10.1121/1.424336 (visited on 03/31/2020).

[47] H. Mestouri, A. Loussert, and G. Keryer, “Finite Element Modeling of 2-D Transducer Arrays”, *The Journal of the Acoustical Society of America*, vol. 123, no. 5, pp. 3116–3116, May 1, 2008, ISSN: 0001-4966. DOI: 10.1121/1.2933020. [Online]. Available: https://asa.scitation.org/doi/10.1121/1.2933020 (visited on 03/31/2020).

[48] M. Rutsch, A. Jäger, A. Unger, T. Kaindl, and M. Kupnik, "Wave propagation in an acoustic waveguide for ultrasonic phased arrays", in *2019 IEEE International Ultrasonics Symposium (IUS)*, Oct. 2019, pp. 796–799. DOI: 10.1109/ULTSYM.2019.8926307.

[49] T. Maier, G. Allevato, M. Rutsch, and M. Kupnik, "Single Microcontroller Air-coupled Waveguided Ultrasonic Sonar System", in *2021 IEEE Sensors*, Oct. 2021, pp. 1–4. DOI: 10.1109/SENSORS47087.2021.9639849.

[50] M. Rutsch, A. Unger, G. Allevato, *et al.*, "Waveguide for air-coupled ultrasonic phased-arrays with propagation time compensation and plug-in assembly", *The Journal of the Acoustical Society of America*, vol. 150, no. 5, pp. 3228–3237, Nov. 2021, ISSN: 0001-4966. DOI: 10.1121/10.0006969. [Online]. Available: https://asa.scitation.org/doi/full/10.1121/10.0006969 (visited on 03/24/2022).

[51] M. Rutsch, G. Allevato, J. Hinrichs, and M. Kupnik, "Protection layer for air-coupled waveguide ultrasonic phased arrays", in *2020 IEEE International Ultrasonics Symposium (IUS)*, Sep. 2020, pp. 1–4. DOI: 10.1109/IUS46767.2020.9251728.

[52] M. Rutsch, F. Krauß, G. Allevato, J. Hinrichs, C. Hartmann, and M. Kupnik, "Simulation of protection layers for air-coupled waveguided ultrasonic phased-arrays", in *2021 IEEE International Ultrasonics Symposium (IUS)*, Sep. 2021, pp. 1–4. DOI: 10.1109/IUS52206.2021.9593561.

[53] *COMSOL Acoustics Module User's Guide*.

[54] "Fundamentals of Physical Acoustics | Wiley", Wiley.com. (), [Online]. Available: https://www.wiley.com/en-us/Fundamentals+of+Physical+Acoustics-p-9780471319795 (visited on 01/12/2022).

[55] *Foundations of Engineering Acoustics*. Elsevier, 2001, ISBN: 978-0-12-247665-5. DOI: 10.1016/B978-0-12-247665-5.X5000-0. [Online]. Available: https://linkinghub.elsevier.com/retrieve/pii/B9780122476655X50000 (visited on 03/31/2020).

[56] G. W. Swift, "Waves", in *Thermoacoustics: A Unifying Perspective for Some Engines and Refrigerators*, G. W. Swift, Ed., Cham: Springer International Publishing, 2017, pp. 77–116, ISBN: 978-3-319-66933-5. DOI: 10.1007/978-3-319-66933-5_4. [Online]. Available: https://doi.org/10.1007/978-3-319-66933-5_4 (visited on 11/16/2021).

[57] G. W. Swift, "Beyond Rott's Thermoacoustics", in *Thermoacoustics: A Unifying Perspective for Some Engines and Refrigerators*, G. W. Swift, Ed., Cham: Springer International Publishing, 2017, pp. 171–229, ISBN: 978-3-319-66933-5. DOI: 10.1007/978-3-319-66933-5_7. [Online]. Available: https://doi.org/10.1007/978-3-319-66933-5_7 (visited on 11/16/2021).

[58] F. Jacobsen, "PROPAGATION OF SOUND WAVES IN DUCTS", p. 72,

[59] H. Levine and J. Schwinger, "On the Radiation of Sound from an Unflanged Circular Pipe", *Physical Review*, vol. 73, no. 4, pp. 383–406, Feb. 15, 1948. DOI: 10.1103/PhysRev.73.383. [Online]. Available: https://link.aps.org/doi/10.1103/PhysRev.73.383 (visited on 12/21/2021).

[60] G. W. Swift, "Simple Oscillations", in *Thermoacoustics: A Unifying Perspective for Some Engines and Refrigerators*, G. W. Swift, Ed., Cham: Springer International Publishing, 2017, pp. 59–76, ISBN: 978-3-319-66933-5. DOI: 10.1007/978-3-319-66933-5_3. [Online]. Available: https://doi.org/10.1007/978-3-319-66933-5_3 (visited on 11/16/2021).

[61] H. Patil and P. V. Jeyakarthikeyan, "Mesh convergence study and estimation of discretization error of hub in clutch disc with integration of ANSYS", *IOP Conference Series: Materials Science and Engineering*, vol. 402, p. 012 065, Oct. 1, 2018. DOI: 10.1088/1757-899X/402/1/012065.

[62] D. Gilbarg and N. S. Trudinger, "Boundary Gradient Estimates", in *Elliptic Partial Differential Equations of Second Order*, D. Gilbarg and N. S. Trudinger, Eds., Berlin, Heidelberg: Springer, 2001, pp. 333–358, ISBN: 978-3-642-61798-0. DOI: 10.1007/978-3-642-61798-0_14. [Online]. Available: https://doi.org/10.1007/978-3-642-61798-0_14 (visited on 03/31/2022).

[63] E. J. Rickley, G. G. Fleming, and C. J. Roof, *Simplified Procedure for Computing the Absorption of Sound by the Atmosphere*, John A. Volpe National Transportation Systems Center (U.S.), Ed. Oct. 31, 2007. [Online]. Available: https://rosap.ntl.bts.gov/view/dot/9810 (visited on 01/11/2022).

[64] "ANSI/ASA S1.26:2014 (R2019)", Normadoc. (), [Online]. Available: https://www.normadoc.com/english/ansi-asa-s1-26-2014-r2019.html (visited on 01/11/2022).

[65] F. Fahy, "8 - Sound in Waveguides", in *Foundations of Engineering Acoustics*, F. Fahy, Ed., London: Academic Press, Jan. 1, 2001, pp. 181–235, ISBN: 978-0-12-247665-5. DOI: 10.1016/B978-012247665-5/50009-6. [Online]. Available: https://www.sciencedirect.com/science/article/pii/B9780122476655500096 (visited on 11/03/2021).

[66] M. Hoffmann, A. Unger, M.-C. Ho, K. K. Park, B. T. Khuri-Yakub, and M. Kupnik, "Volumetric characterization of ultrasonic transducers for gas flow metering", in *2013 IEEE International Ultrasonics Symposium (IUS)*, Jul. 2013, pp. 1315–1318. DOI: 10.1109/ULTSYM.2013.0336.

[67] "Datasheet 1/8" Pressure-field Microphone - Type 4138", *Brüel & Kjaer*, 2008. [Online]. Available: https://www.bksv.com/-/media/literature/Product-Data/bp2030.ashx (visited on 03/27/2020).

[68] M. Hoffmann, A. Unger, A. Jäger, and M. Kupnik, "Effect of transducer port cavities in invasive ultrasonic transit-time gas flowmeters", in *2015 IEEE International Ultrasonics Symposium (IUS)*, Oct. 2015, pp. 1–4. DOI: 10.1109/ULTSYM.2015.0272.

[69] "GL Gonio Spectrometer GLG 4-500", GL Optic | Light quality control. (), [Online]. Available: https://gloptic.com/de/products/gl-gonio-spectrometer-glg-4-500/ (visited on 02/24/2022).

[70] A. Collette, "H5py Documentation", p. 76,

[71] R. Bolejko and A. Dobrucki, "FEM amd BEM computing costs for acoustical problems", *Archives of Acoustics*, vol. 31, no. 2, pp. 193–212, 2 2006, ISSN: 2300-262X. [Online]. Available: https://acoustics.ippt.gov.pl/index.php/aa/article/view/668 (visited on 03/31/2020).

[72] J. Hinrichs, Y. Bendel, M. Rutsch, *et al.*, "Schlieren photography of 40 kHz leaky Lamb waves in air", in *2020 IEEE International Ultrasonics Symposium (IUS)*, Sep. 2020, pp. 1–4. DOI: 10.1109/IUS46767.2020.9251532.

[73] J. E. Piercy, T. F. W. Embleton, and L. C. Sutherland, "Review of noise propagation in the atmosphere", *The Journal of the Acoustical Society of America*, vol. 61, no. 6, pp. 1403–1418, Jun. 1, 1977, ISSN: 0001-4966. DOI: 10.1121/1.381455. [Online]. Available: https://asa.scitation.org/doi/10.1121/1.381455 (visited on 11/03/2021).

[74] "MA40S4S|Ultrasonic Sensors|Sensors|Murata Manufacturing Co., Ltd." (), [Online]. Available: https://www.murata.com/en-eu/products/productdetail?partno=MA40S4S (visited on 05/27/2021).

[75] R. H. Bartels, J. C. Beatty, B. A. Barsky, and A. R. Forrest, *An Introduction to Splines for Use in Computer Graphics and Geometric Modeling*. M. Kaufmann Publishers, 1987, 512 pp., ISBN: 978-0-934613-27-9. Google Books: 3AcPAAAAMAAJ.

[76] G. Farin, "Chapter 5 - Bézier Curve Topics", in *Curves and Surfaces for Computer-Aided Geometric Design (Third Edition)*, G. Farin, Ed., Boston: Academic Press, Jan. 1, 1993, pp. 65–81, ISBN: 978-0-12-249052-1. DOI: 10.1016/B978-0-12-249052-1.50010-6. [Online]. Available: https://www.sciencedirect.com/science/article/pii/B9780122490521500106 (visited on 11/03/2021).

[77] J. E. Piercy, T. F. W. Embleton, and L. C. Sutherland, "Review of noise propagation in the atmosphere", *The Journal of the Acoustical Society of America*, vol. 61, no. 6, pp. 1403–1418, Jun. 1, 1977, ISSN: 0001-4966. DOI: 10.1121/1.381455. [Online]. Available: https://asa.scitation.org/doi/10.1121/1.381455 (visited on 03/31/2020).

[78] R. Kerstens, D. Laurijssen, and J. Steckel, "eRTIS: A Fully Embedded Real Time 3D Imaging Sonar Sensor for Robotic Applications", in *2019 International Conference on Robotics and Automation (ICRA)*, May 2019, pp. 1438–1443. DOI: 10.1109/ICRA.2019.8794419.

[79] S. Delrue, V. Aleshin, M. Sørensen, and L. D. Lathauwer, "Simulation Study of the Localization of a Near-Surface Crack Using an Air-Coupled Ultrasonic Sensor Array", *Sensors*, vol. 17, no. 4, p. 930, 4 Apr. 2017. DOI: 10.3390/s17040930. [Online]. Available: https://www.mdpi.com/1424-8220/17/4/930 (visited on 08/27/2021).

[80] R. J. Kazys, A. Vilpisauskas, and J. Sestoke, "Application of Air-Coupled Ultrasonic Arrays for Excitation of a Slow Antisymmetric Lamb Wave", *Sensors*, vol. 18, no. 8, p. 2636, 8 Aug. 2018. DOI: 10.3390/s18082636. [Online]. Available: https://www.mdpi.com/1424-8220/18/8/2636 (visited on 08/27/2021).

[81] A. Price and B. Long, "Fibonacci Spiral Arranged Ultrasound Phased Array for Mid-Air Haptics", in *2018 IEEE International Ultrasonics Symposium (IUS)*, Oct. 2018, pp. 1–4. DOI: 10.1109/ULTSYM.2018.8580072.

[82] J. Sanders, "Venting assembly and microporous membrane composite", U.S. Patent 9,317,068 B2. [Online]. Available: https://patentimages.storage.googleapis.com/21/72/ef/145191ab95cd6d/US9317068.pdf (visited on 03/27/2020).

[83] D. J. Weber and N. Matsuyuki, "Hydrophobic Mesh Cover", U.S. Patent 9,573,165 B2.

[84] M. A. Kuczmarski and J. C. Johnston, "Acoustic Absorption in Porous Materials", *NASA Center for Aerospace Information*, p. 27, 2011.

[85] Q. Yu, R. Xiong, C. Li, and M. G. Pecht, "Water-Resistant Smartphone Technologies", *IEEE Access*, vol. 7, pp. 42 757–42 773, 2019, ISSN: 2169-3536. DOI: 10.1109/ACCESS.2019.2904654.

[86] D. Repolle and F. Principe, "Protective cover assembly having sound transmission characteristics", pat. WO 97/45829. [Online]. Available: https://patentimages.storage.googleapis.com/7a/0c/db/af770bb30c9138/WO1997045829A1.pdf (visited on 03/27/2020).

[87] V. Milenkovic and S. Raynor, "Reflection of a Plane Acoustic Step Wave from an Elastic Spherical Membrane", *The Journal of the Acoustical Society of America*, vol. 39, no. 3, pp. 556–563, Mar. 1966, ISSN: 0001-4966. DOI: 10.1121/1.1909928. [Online]. Available: http://asa.scitation.org/doi/10.1121/1.1909928 (visited on 03/27/2020).

[88] "ISO 20653 - 2013-02 - Beuth.de". (), [Online]. Available: https://www.beuth.de/de/norm/iso-20653/180368530 (visited on 03/07/2022).

[89] *Acoustics - Determination of airflow resistance - Part 1: Static airflow method (ISO 9053-1:2018); German version EN ISO 9053-1:2018*.

[90] D. D. Ganji and S. H. H. Kachapi, “Chapter 7 - Nanofluid Flow in Porous Medium”, in *Application of Nonlinear Systems in Nanomechanics and Nanofluids*, ser. Micro and Nano Technologies, D. D. Ganji and S. H. H. Kachapi, Eds., Oxford: William Andrew Publishing, Jan. 1, 2015, pp. 271–316, ISBN: 978-0-323-35237-6. DOI: 10.1016/B978-0-323-35237-6.00007-8. [Online]. Available: https://www.sciencedirect.com/science/article/pii/B9780323352376000078 (visited on 04/26/2021).

[91] O. B. Dali, S. Zhukov, M. Rutsch, *et al.*, “Biodegradable 3D-printed ferroelectret ultrasonic transducer with large output pressure”, in *2021 IEEE International Ultrasonics Symposium (IUS)*, Sep. 2021, pp. 1–4. DOI: 10.1109/IUS52206.2021.9593738.

[92] A. Jiménez, Á. Hernández, J. Ureña, *et al.*, “EMFi-based ultrasonic transducer for robotics applications”, *Sensors and Actuators A: Physical*, vol. 148, no. 1, pp. 342–349, Nov. 4, 2008, ISSN: 0924-4247. DOI: 10.1016/j.sna.2008.07.024. [Online]. Available: https://www.sciencedirect.com/science/article/pii/S0924424708004160 (visited on 12/15/2021).

[93] A. Jiménez Martín, Á. Hernández Alonso, D. Ruíz, *et al.*, “EMFi-Based Ultrasonic Sensory Array for 3D Localization of Reflectors Using Positioning Algorithms”, *IEEE Sensors Journal*, vol. 15, no. 5, pp. 2951–2962, May 2015, ISSN: 1558-1748. DOI: 10.1109/JSEN.2014.2384197.

[94] J. Q. Aguilar, T. G. Álvarez-Arenas, and L. Svilainis, “Ferroelectret Hydrophone”, in *2021 IEEE International Ultrasonics Symposium (IUS)*, Sep. 2021, pp. 1–4. DOI: 10.1109/IUS52206.2021.9593895.

[95] Y. P. Raizer, *Gas Discharge Physics*. Berlin; New York: Springer-Verlag, 1991, ISBN: 978-0-387-19462-2 978-3-540-19462-0.

List of Figures

List of Tables